



HAL
open science

Molecular mobility and aging of chiral amorphous compounds

Bienvenu Atawa

► **To cite this version:**

Bienvenu Atawa. Molecular mobility and aging of chiral amorphous compounds. Materials. Normandie Université, 2018. English. NNT : 2018NORMMR125 . tel-02067560

HAL Id: tel-02067560

<https://theses.hal.science/tel-02067560>

Submitted on 14 Mar 2019

HAL is a multi-disciplinary open access archive for the deposit and dissemination of scientific research documents, whether they are published or not. The documents may come from teaching and research institutions in France or abroad, or from public or private research centers.

L'archive ouverte pluridisciplinaire **HAL**, est destinée au dépôt et à la diffusion de documents scientifiques de niveau recherche, publiés ou non, émanant des établissements d'enseignement et de recherche français ou étrangers, des laboratoires publics ou privés.



Normandie Université

THÈSE

Pour obtenir le diplôme de doctorat

Spécialité Physico-chimie des matériaux

Préparée au sein de « l'Université de Rouen Normandie »

Mobilité Moléculaire et Vieillessement Physique des Composés Amorphes Chiraux

Présentée et soutenue par
Bienvenu ATAWA

Thèse soutenue publiquement le (06/12/2018) devant le jury composé de		
M Marc DESCAMPS	PR UMET Université de Lille 1	Rapporteur
Mme Madalena Dionisio	PR Université Nouvelle de Lisbonne	Rapporteur
M Gérard COQUEREL	PR Université de Rouen Normandie	Examinateur
Mme Emeline DUDOGNON	MCF Université de Lille 1	Examinatrice
M Nicolas COUVRAT	IR Université de Rouen Normandie	Co-encadrant de thèse
Mme Allisson SAITER	PR Université de Rouen Normandie	Directrice de thèse

Thèse dirigée par Allisson SAITER professeur des Universités au laboratoire Groupe de physique des matériaux (UMR 6634) et Co-encadré par Nicolas COUVRAT, ingénieur de recherche au laboratoire Sciences et Méthodes Séparatives (EA 3233)





Normandie Université

Phd Thesis

In view to obtain the degree of Doctor of Philosophy in Science

Specialty: Physical chemistry of materials

Submitted to the Faculty of Science - University of Rouen Normandy in partial fulfillment of the requirements for the degree

Molecular Mobility and aging of chiral amorphous compounds

Presented and defended by

Bienvenu ATAWA

**Thesis defended publicly on Thursday December 06th 2018
in presence of the dissertation committee composed of**

M Marc DESCAMPS	PR University of Lille	Reviewer
Mme Madalena Dionisio	PR New University of Lisbon	Reviewer
M Gérard COQUEREL	PR Université de Rouen Normandie	President
Mme Emeline DUDOGNON	MCF University of Lille	Examiner
M Nicolas COUVRAT	IR University of Rouen Normandy	Advisor
Mme Allisson SAITER	PR University of Rouen Normandy	Supervisor

Thesis supervised by Allisson SAITER professor of Universities in Groupe de physique des matériaux (GPM UMR 6634) laboratory and mentored by Nicolas COUVRAT, research engineer in Sciences et Méthodes Séparatives (SMS EA 3233) laboratory.



TABLE OF CONTENTS

TABLE OF CONTENTS	i
TABLE OF FIGURES	v
DEDICATION	xiv
ACKNOWLEDGEMENTS	xv
ABSTRACT	xix
INTRODUCTION	1
CHAPTER I: THE PHYSICS OF AMORPHOUS STATE AND CHIRALITY	9
I- Generalities on the glassy state	11
I.1 Vitrification processes and crystallization mechanisms.....	11
I.1.1 Vitrification processes	11
I.1.2 Crystallization mechanism: nucleation and crystal growth phenomena	13
a) Nucleation	13
b) Crystal growth	16
I.2 Glass Forming Ability (GFA)	18
I.3 The glass transition phenomenon	20
I.4 The glass transition models	23
a) The Kauzmann Paradox	23
b) Adam-Gibbs (AG) theory	25
I.5 Molecular Mobility in glass forming liquids by broadband dielectric spectroscopy	26
a) Structural Relaxation α	28
b) Molecular mobility in the glassy state: secondary relaxation processes	31
c) Peculiar Debye relaxation in some glass forming liquids	32
I.6 Physical aging phenomenon.....	44
II- Chirality	47
II.1 A Brief History of Chirality	47
II.2 Stereochemical Nomenclature of Chiral Compounds	51
II.3 Thermodynamics of chiral compounds	53
II.3.1 Gibbs phase rule and binary phase diagram between two enantiomers	53
II.3.2 Binary phase diagram between both enantiomers.....	54
III- Impact of chirality in amorphous state: state of art	61
III.1 Glass forming ability and crystallization from amorphous state.....	61
III.2 Molecular mobility in chiral amorphous compounds.....	64
III - CONCLUSION	67

References	68
CHAPTER II: MATERIALS AND METHODS	77
A- 5ethyl-5-methylhydantoin (12H).....	79
1- Structural and thermal properties of 12H.....	80
B- N-acetyl- α -methyl-benzylamine (Nac-MBA): synthesis and purification.....	81
1- Structural and thermal characterization	82
a) Description of the pure enantiomer structure.....	83
b) Description of the racemic compound structure	84
II- Experimental Techniques.....	86
A- Differential scanning calorimetry (DSC)	86
B- Modulated temperature DSC (MT-DSC).....	89
C- Fast Scanning calorimetry (FSC)	92
D- Temperature Resolved X-Ray Diffraction (TR-XRD).....	96
E- Dielectric relaxation Spectroscopy.....	98
1. Principe and basics on dielectrics.....	98
2. Relaxation models	102
3. Dielectric Measurements and Calibration.....	104
a. Low frequency range 0.1 Hz – 1 MHz	104
b - High frequency range 1 MHz – 1 GHz	105
4- Molecular Dynamics Simulations (MDS)	106
References	107
CHAPTER III: CHIRALITY EFFECTS ON AMORPHOUS 5-ETHYL-5-METHYLHYDANTOIN	111
I- Calorimetric investigations of 12H	113
1- Classical DSC Measurements.....	113
2- FSC Measurements.....	115
3- Pure Enantiomer	116
a) Amorphization vs Crystallization: case of enantiopure 12H	116
b) Maxima of nucleation and growth rates of pure enantiomer	118
4- Scalemic Composition ($0 \leq ee < 100\%$)	119
a) Amorphization vs Crystallization: case of scalemic 12H	119
b) Maxima of nucleation and growth rates: scalemic 12H.....	121
c) Thermal lag verification and sampling limitations	123
5- Physical aging and crystallization propensity	126
II- Discussion	132

1- High Crystallization propensity of 12H	132
2- Thermal lag and glass Transition temperature vs ee	133
3- Impact of enantiomeric composition on GFA and crystallization propensity in the glassy state.....	134
4- Impact of chirality upon physical aging.....	136
5- Possible metastable equilibria	137
III - Conclusions.....	138
References	140

CHAPTER IV: CHIRALITY EFFECTS ON AMORPHOUS N-ACETYL-A-METHYLBENZYLAMINE 145

I- Heterogeneous equilibria and vitrification	147
1- Thermal and structural characterizations of both pure enantiomer and racemic Nac-MBA upon heating	147
2- Vitrification and GFA of Nac-MBA versus ee: A kinetic competition	149
3- Thermal behavior upon heating from the amorphous state	151
4- High cooling rate and size effects from FSC measurements.....	154
II- Amorphous Nac-MBA and physical Aging.....	157
1- Thermal and kinetic properties of amorphous Nac-MBA	157
III - Conclusions.....	168
References	169

CHAPTER V: MOLECULAR MOBILITY OF AMORPHOUS N-ACETYL-A-METHYLBENZYLAMINE AND IMPACT OF CHIRALITY EVIDENCED BY DIELECTRIC RELAXATION SPECTROSCOPY AND MOLECULAR DYNAMIC SIMULATIONS.....171

I- Molecular mobility of Nac-MBA.....	173
A- Dielectric Relaxation Spectroscopy (DRS): Molecular mobility characterization of Nac-MBA (ee = 50%).....	173
1- Glassy state ($T < T_g$)	173
2- Supercooled liquid ($T > T_g$).....	174
B- MD simulations investigations	188
1- Static dipolar properties.....	188
2- Dynamic dipolar properties.....	191
3- Hydrogen bonding structures.....	192
II- Impact of chirality.....	195
A- Chirality effects on the molecular mobility below T_g	196
B- Chirality effects on the molecular mobility above T_g	197

Table of Contents

C- Relaxation Map.....	201
III - Conclusions.....	205
References	208
CONCLUSIONS AND PROSPECTS.....	214
ANNEXES.....	221

TABLE OF FIGURES

Chapter I

- Figure 1: Various routes to the glassy state, roughly indicating the energies of the initial states relative to the final glassy states. Adapted from [23] 12
- Figure 2: Schematic TTT diagram adapted from [19] 13
- Figure 3: Gibbs free energy of formation of a cluster of n molecules, ΔG , as a function of n . The critical size, n^* , the critical work of formation, $\Delta G n^* = \Delta G^*$, and the critical region (within which $\Delta G n - \Delta G^* \leq kBT$) are indicated. Below n^* clusters are on average dissolving; above n^* they are on average growing. From [24] 15
- Figure 4: Temperature dependence of the nucleation rate I C involving a thermodynamic and a mobility contribution 16
- Figure 5: Temperature dependence of the growth rate C involving a thermodynamic and a mobility contribution 17
- Figure 6: Schematically time evolution of nucleation and growth temperature region for a) good GFA and b) poor GFA 19
- Figure 7: Schematically temperature evolution of a) enthalpy, H and corresponding b) heat capacity, C_p at different cooling rates $Q_c(1)$, $Q_c(2)$ and $Q_c(3)$ 21
- Figure 8: Schematic illustration of the vibrational and configurational contribution of C_p in both crystalline and glassy phases. Some specific molecules are numbered in order to identify their position after the conformational change occurs 22
- Figure 9: Schematic entropy S evolution as function of temperature of a liquid and its corresponding crystalline phase. ΔS_m is the melting entropy. The extrapolated liquid entropy equals the crystal entropy at the Kauzmann temperature T_K 24
- Figure 10: Schematic evolution of the dielectric loss peak at two temperatures $T_1 < T_2$ over 20 decades in the frequency range (top figure) and its analogous temporal evolution illustrating different possible relaxation modes in a glass forming liquid (bottom figure). Adapted from [37] 27
- Figure 11: Evolution of the viscosity (log scale) as a function of the scaled temperature T_g/T of different glass formers exhibiting either a strong or a fragile behavior. 29
- Figure 12: Evolution of the fragility index m as function of the stretching parameter βKWW for several subsystems of glass forming materials at a time scale of 100s. The minimum fragility value $m = 16$ is indicated by the dashed line while the solid lines are calculated according to equation 8. From [62] 30
- Figure 13: Activation traces of the three dielectric loss peaks of 2-ethyl-1-hexanol 2E1H. Symbols are experimental results; lines are guides only. The inset shows the loss

- spectrum at $T = 166$ K equivalent to the dashed vertical line in the main figure and identifies the correlation with the activation traces. Process I, II and III refers as the Debye, α and β processes respectively. From Huth et al [86] 33
- Figure 14: Illustration of the interconversion between the two non-equivalent chair configurations. Adapted from Mandanici et al. [95] 33
- Figure 15: Temperature dependence of the relaxation frequency of the structural relaxation and secondary processes in ethylcyclohexane (ECH) revealed by mechanical and dielectric spectroscopies. The Debye process revealed by mechanical spectroscopy is indicated by the arrow. The characteristic temperatures T_b , T_m and T_g refer as the boiling point, the melting point, and the glass transition temperature respectively. More details are reported in ref [96] 34
- Figure 16: Dielectric loss peak of 2-ethyl-1-hexanol [84] and a mixture of N-methylacetamide with N-methylformamide as a function of the frequency [89] 35
- Figure 17: Loss components ϵ'' and C_p'' for 2E1H vs temperature, both measured at a frequency of $= 10$ Hz. The C_p'' curve is shifted arbitrarily along the ordinate scale. The dashed lines separate the dielectric signal into the Debye (I) and non-Debye (II) contributions. From Huth et al [86] 36
- Figure 18: Master plots for the real part (scale on the right side) and the imaginary part (scale on the left side) of $G^*(\nu)$ showing normalized shear moduli for (a) 4M3H and (b) 2E1H. From Gainaru et al. [97] 37
- Figure 19: X-ray diffraction patterns of (a) $(4M3H)_x(2B1O)_{1-x}$ and (b) $(2E1H)_x(2M1B)_{1-x}$ recorded at room temperature for several concentrations x . The compositional evolution of the prepeaks as well as of the mainpeaks of the two mixture series is different. The arrows highlight how the prepeak and mainpeak maxima evolve for increasing concentrations x . From [110]. 38
- Figure 20: Characteristic clusters for methanol showing cyclic and linear configurations. From [104] 39
- Figure 21: Sketch of a potential energy barrier separating two di-rections (Y ; Y^*) of the permanent dipole moment l , and sketch of a bifurcated hydrogen bond (bfhb) in a chain-like alcohol cluster. The dashed curve shows the reduction in the potential energy ΔE due to the additional neighbor near the chain and the bfhb situation. from Kaatze et al [115]. 39
- Figure 22: Schematic representation of chains with segmental dipole moments parallel to the polymer chain backbone. Correlation of dipole vector $\underline{\mu}_n$ with displacement vector \underline{r}_n from [119] 40
- Figure 23: Schematic illustration of the transient chain model. Mutually bonded OH groups are shown in color. The sequence of frames is meant to visualize how molecules attach to the chain and detach from it. The dotted arrows highlight the end-to-end

vector of the self- restructuring, transient chain. Its reorientation, corresponding to the Debye process, is obviously very slow on the scale set by the elementary steps. From [118]	41
Figure 24: Ibuprofen real (open circles) and imaginary (filled circles) parts of complex permittivity at (a) 243 K, and (b) 273 K. The solid lines represent the overall fit and the dashed lines the individual fit-functions. From [90]	42
Figure 25: Schematic representation of the two conformations of the O=C-O-H group. From [93]	43
Figure 26: a) Enthalpy vs time evolution of an aged glass at T_a for three aging times (t_0 , t_1 and t_∞) b) Temperature evolution of the heat flow after aging is accomplished at T_a for t_0 , t_1 and t_∞ .	45
Figure 27: Calculation of T_f by application of the “equal area rule” on $C_p(T)$ curve.	46
Figure 28: The left hand and the right hand are image of each other in a mirror but cannot superimposed [141].	47
Figure 29: Hemihedral crystals of sodium ammonium tartrates by Pasteur. From [136]	49
Figure 30: a) Hemihedral crystals of tartaric acid b) Holohedral crystals of racemic acid adapted from [136]	50
Figure 31: Absolute configurations of enantiomers of 2-hydroxypropanoic acid according to the CIP priority rule [145].	51
Figure 32: Fisher projection of L- and D- Glucose [145]	52
Figure 33: Schematic representation of the molecular arrangements and binary phase diagrams in three types of racemic species in absence of partial solid solution and solid/solid transition. Adapted from [148]	54
Figure 34: Energetics of phase equilibria in a binary eutectic of a conglomerate a) system at three temperatures b) T_1 , c) T_2 , d) T_3 . G_{min} represents the minimum Gibbs free energy when equilibrium is reached. Adapted from [150]	57
Figure 35: phase diagram of opposite enantiomers crystallizing as a stable racemic compound. Adapted from [150]	58
Figure 36: Binary phase diagram illustrating two solid-solid transitions between a conglomerate and a racemic compound leading to a) the formation of a racemic compound b) decomposition of a racemic compound. Adapted from [149].	59
Figure 37: Different types of solid solutions between enantiomers a) ideal solid solutions, b) solid solutions with a maximum, c) solid solutions with a minimum [148].	60
Figure 38: a) Thermal signature of the recrystallization behavior of diprophylline at different enantiomeric compositions Adapted from [155]. b) Pressure evolution of the crystallization half time (main), overall crystallization rate (lower inset), and Avrami	

<i>parameter (upper inset) for S-ketoprofen and RS-ketoprofen crystallized along the same isochrones Adapted from [35].</i>	62
<i>Figure 39: a) Stable equilibria between enantiomers of limonene. b) Temperature of the glass transition temperature T_g versus enantiomeric composition and metastable equilibria exhibiting a single complete solid solution between chiral components. The upper part of the figure depicts the developed formulae of both enantiomers of limonene; adapted from [157].</i>	64
<i>Figure 40: relaxation map in both racemic and enantiopure composition of diprophylline (top figure) and ibuprofen (bottom figure) respectively</i>	65
<i>Figure 41: (a) α-relaxation times plotted as a function of temperature for S-ketoprofen, RS-ketoprofen and Me-RS-ketoprofen. Inset enlarges $\tau_\alpha(T)$ dependencies for RS-ketoprofen and S-ketoprofen in vicinity of the glass transition, and shows that both dynamics start to diverge close to T_g. (b) Temperature dependences of τ_α for RSketoprofen and S-ketoprofen plotted versus each other. The linear fit with the slope $s=0.95$ indicates that τ_α for S-ketoprofen changes slightly weaker with the temperature than for RS-ketoprofen. On increased pressure the correlation between τ_α dependencies for RS and S-ketoprofen weakens ($s=0.92$). (c) Comparison of the normalized dielectric loss spectra ϵ'' for Me-RS-ketoprofen, RSketoprofen and S-ketoprofen taken at different temperatures, but with very similar value of ν_{max}. From [159]</i>	66
Chapter II	
<i>Figure 1: a) Molecular formulae of 12H ($C_6H_{10}N_2O_2$) and b) isovaline ($C_5H_{11}NO_2$)</i>	79
<i>Figure 2: Projection of the crystal structure of 12H along a-axis showing molecular ribbons running along the b-axis. From [3]</i>	80
<i>Figure 3: Binary phase diagram between 12H enantiomers</i>	81
<i>Figure 4: Developed formula of Nac-MBA enantiomers ($C_{10}H_{13}NO$)</i>	82
<i>Figure 5: Experimental phase diagram between R and S Nac-MBA. From [5]</i>	83
<i>Figure 6: Projection along c axis of (004) slice in the (R) enantiomer structure of Nac-MBA showing the CHBMs along the 110 direction. Adapted from [7]</i>	84
<i>Figure 7: a) Projection along b axis of the racemic compound structure; homochiral chains are displayed with different colors. b) Alternative rotation around c axis of the side chain plane from the (100) plane</i>	85
<i>Figure 8: Power compensation DSC principle. From [10]</i>	87
<i>Figure 9: Heat-flux DSC principle. T_S and T_R are the sample and reference temperatures respectively. From [10]</i>	87

Figure 10: Illustration of heating ramps in MT-DSC experiment with corresponding heat-only (green), heat-iso (cyan), heat-cool (blue) and linear ramp (orange) mode. The modulation amplitude, the period and the scanning rate are [0.318 K; 90 s; 2 K/min], [0.318 K; 60 s; 2 K/min], [1 K; 60 s; 2 K/min] for the three modes displayed, respectively. From [18]	90
Figure 11: a) Illustration of twin-type chip sensor based on MEMS technology. b) Sample placed on the center of the sample area. From [18,19]	93
Figure 12: XRPD patterns recorded at room temperature from Bicolotymol samples. Top purple diffractogram corresponds to crystalline stable Form I. Bottom blue diffractogram corresponds to melt-quenched sample. From [22]	96
Figure 13: Pathway of the X-Ray beam inside a χ diffractometer	97
Figure 14: Dipole orientations of a dielectric material in absence and presence of an external perturbation hereby an electric field E	98
Figure 15: Time evolution of the polarization P(t) due to an applied external rectangular impulse of the electric field E(t)	100
Figure 16: Schematic frequency evolution of both imaginary and real permittivities for a Debye relaxation, $\vec{\mu}$ is the permanent dipole moment vector, $\epsilon_S = \lim_{\omega \rightarrow 0} \epsilon'(\omega)$, $\epsilon_\infty = \lim_{\omega \rightarrow \infty} \epsilon'(\omega)$ and ω_D is the half height width of the dielectric loss peak	101
Figure 17: Simulated master curves of dielectric loss illustrating the symmetric and asymmetric broadening of the loss peak	103

Chapter III

Figure 1: Heating and cooling curves of a) pure enantiomer and b) racemic mixture in classical DSC	114
Figure 2: Premelted samples with different geometric parameters. Sample (a) 19 ng, (b) 35 ng, (c) 50 ng, (d) 120 ng.	116
Figure 3: Thermal events of enantiopure 12H upon a) cooling and b) second heating at variable cooling and heating rates.	117
Figure 4: FSC scans of pure enantiomer recorded upon heating at 3000 °C/s after the melt was cooled at different isothermal temperatures T_a (from -50 °C to 80 °C) and annealed for 30 min. N(T) and G(T) refers as the nucleation growth temperature region respectively	119
Figure 5: a) Thermal events upon cooling and b) upon heating for the sample at a scalemic composition	120
Figure 6: FSC melting curves of both 12H enantiomers	121

<i>Figure 7: FSC curves of scalemic 12H recorded upon heating at 3000 °C/s after the melt was cooled at different isothermal temperatures T_a (from -50 °C to 70°C) and annealed for 30 min. N (T) and G (T) refers as the nucleation growth temperature region respectively</i>	122
<i>Figure 8: Glass transition signature at 1000 °C/s and 1500 °C/s for three samples (scalemic composition) with increasing masses.</i>	123
<i>Figure 9: Heating curves from the amorphous state at 500 °C/s for seven samples coming from the racemic batch. ΔT represents the temperature between the onset of the crystallization peak and the onset of the first endothermal event. The arrow indicates samples with larger ee.</i>	125
<i>Figure 10: a, b) FSC heating scans at 1000 °C/s as a function of aging temperature for an aging time 60s after cooling at 1000 °C/s for pure enantiomer and scalemic 12H respectively. c) Evolution of the enthalpy excess value as function of the difference ($T_a - T_g$).</i>	127
<i>Figure 11: a, b) FSC heating scans of enantiopure 12H at 1000 °C/s as function of aging time for $T_a = -20^\circ\text{C}$ and -10°C respectively after cooling at 1000 °C/s</i>	128
<i>Figure 12: FSC heating curves of pure enantiomer at 1000 °C/s composition after aging the amorphous samples for 4h at $T_g - 36^\circ\text{C}$.</i>	129
<i>Figure 13 a, b) FSC heating scans of scalemic 12H at 1000 °C/s as function of aging time for $T_a = -20^\circ\text{C}$ and -10°C respectively after cooling at 1000 °C/s.</i>	130
<i>Figure 14: Evolution of the difference ($T_f - T_a$) as function of aging time.</i>	131
<i>Figure 15: Projection of the crystal structure of 12H along a-axis showing molecular ribbons running along the b-axis from C. Gervais et al.[25]</i>	133
<i>Figure 16: Binary phase diagram of 12H enantiomers, suggesting a possible metastable racemic compound.</i>	137

Chapter IV

<i>Figure 1: DSC Heating scans of pure enantiomer and racemic mixture at 10 K/min</i>	148
<i>Figure 2: TR-XRD of the stable conglomerate showing a progressive evolution of the conglomerate towards the racemic compound upon heating. The black arrows point out the characteristic peaks of the racemic compound.</i>	149
<i>Figure 3: Thermal behavior upon cooling of both pure enantiomer and racemic mixture</i>	150
<i>Figure 4: Thermal behavior upon cooling at 10 K/min for several ee</i>	151
<i>Figure 5: Heating at 10 K/min from amorphous state of samples at several ee</i>	152

Figure 6: Metastable binary phase diagram between the two chiral antipodes, established from heating the glassy states. T_g and T_{cr} are the glass transition temperature and the onset of crystallization	153
Figure 7: TR-XRD of the amorphous sample recrystallizing as a racemic compound upon heating.	154
Figure 8: Heating scans at 1000 K/s of both conglomerate and racemic compound crystals	155
Figure 9: Thermal signature upon heating at 1000 K/s after an annealing step at several temperatures ranging from -15°C up to 5°C by step of 5°C	156
Figure 10: Reversing specific heat capacity as a function of temperature at a heating rate of 2 K/min, oscillation amplitude of $\pm 0.318^{\circ}\text{C}$ and a period of 60 s for several ee	157
Figure 11: Kinetic behavior of the glass transition observed by DSC and FSC analyses for the same cooling and heating rates ranging from 0.17 K/s up to 1500 K/s	158
Figure 12: FSC heating scans at 1500 K/s of amorphous enantiomer (ee=100%) annealed at variable temperatures in the vicinity of T_g for 5s.	159
Figure 13: Normalized heat flow curves recorded after physical aging during heating ramps (20 K/min) as a function of ee%. $\Delta T_a = (T_g - T_a) = 6^{\circ}\text{C}$ and 11°C with $T_g = -31 \pm 1^{\circ}\text{C}$	162
Figure 14: Normalized heat flow curves recorded after physical aging during heating ramps as a function of ee%. $\Delta T_a = (T_g - T_a) = 6^{\circ}\text{C}$ and 16°C with $T_g = -22 \pm 0.5^{\circ}\text{C}$	163
Figure 15: FSC and DSC experiments. Time evolution of the fictive temperature in function of several ee at $\Delta T_a = 6^{\circ}\text{C}$, 11°C and 16°C .	164
Figure 16: DSC and FSC time evolution of the difference between ΔH_{∞} and ΔH_t for the aged samples in function of ee at $\Delta T_a = 6^{\circ}\text{C}$	167

Chapter V

Figure 1: Temperature dependence behavior of dielectric loss ϵ'' in the glassy state (Below T_g) over 7 decades of frequency	174
Figure 2: a) Frequency dependence evolution of the dielectric loss ϵ'' in the supercooled liquid state, b) the dielectric real permittivity ϵ' and c) the derivative loss ϵ''_{der}	175
Figure 3: Frequency dependence of a) the real permittivity ϵ' and its b) derivative ϵ''_{der} in the high frequency region [1MHz – 1GHz] from 383 K up to 283 K	176
Figure 4: Fitting procedure of the dielectric loss peak in the glassy state (a) 203 K and b) 232 K) and the supercooled liquid (c) 259 K). The dash-dot lines represent the fitting functions.	178
Figure 5: a) Temperature evolution of the dielectric strength and b) the product $T\Delta\epsilon$ for D and α processes. c) $\Delta\epsilon$ as a function $1000/T$ for β and γ processes.	180

- Figure 6: Relaxation map depicting the temperature evolution of the relaxation time τ for all the different processes from DRS and MD simulations (black layer) and cooling rate (dark gray layer) as a function of the inverse temperature determined from FSC. The data in blue were obtained from MD simulations and those in light gray from FSC. The orange star represents the JG relaxation time calculated at T_g from the Coupling Model. The dash-dot lines give the fit of the Arrhenius and VFTH equations to the corresponding data (same color as the data) 181
- Figure 7: FSC heating curves of Nac-MBA obtained at $q_h = 1500$ K/s after cooling from the supercooled liquid state down to the glassy state at q_c ranging from 5 K/s to 1500 K/s 185
- Figure 8: Temperature evolution of the logarithmic time scale decoupling ratio $\log_{10}(\tau_D/\tau_\alpha)$ plotted from DRS and MD data 187
- Figure 9: Temperature evolution of the Kirkwood correlation factor G_K of Nac-MBA determined from MD simulations 189
- Figure 10: Snapshot extracted from an MD simulation run at $T = 400$ K showing an HB aggregate composed of $n = 6$ Nac-MBA molecules. This HB aggregate possesses a linear shape and the net dipole $\langle \mu_6 \rangle$ of this aggregate is also schematically represented. Intermolecular HB are displayed as bold line 190
- Figure 11: Time-dependent of the total dipole correlation function $\Phi_{Mt} = M_t \cdot M_0$ for Nac-MBA represented at different temperatures $T = 340, 360, 400, 450,$ and 500 K. The solid lines indicate a fit with the function $\Phi_{Mt} = AD(MD)\exp(-\tau_D(MD)) + Afast(MD)\exp(-\tau_{fast}(MD))\beta_{fast}(MD)$ where the index "D" and "fast" refer to the long time single exponential decay (D process) and to the fast relaxational process ($10 < t < 100$ ps) respectively (see text) 192
- Figure 12: Evolution of the population P_n (bottom), the average net dipole $\langle \mu_n \rangle$ (middle) and the product $P_n \cdot \mu_n$ (top) for HB aggregate made of n Nac-MBA molecules at $T = 340$ and 500 K 194
- Figure 13: Temperature evolution of the real dielectric permittivity at several ee at $f=11\text{Hz}$ 195
- Figure 14: Frequency evolution of the dielectric loss at various ee in the glassy state a) $T = 203$ K, b) $T = 234$ K. 196
- Figure 15: Isothermal frequency evolution of the dielectric loss in the supercooled liquid state for several ee and temperatures a) 247 K, b) 313 K and 363 K 197
- Figure 16: temperature dependence of the dielectric strength at several ee of a) the two secondary γ and β_{JG} processes b) α process c) D process in the low temperature region and d) D process in the high temperature region 199
- Figure 17: Temperature dependency of the relaxation time of the four processes at different ee . Each color is attributed to an ee , black for $ee=100\%$, green for $ee=75\%$, blue for $ee=50\%$ and red for $ee=0$ The orange star represents the JG relaxation time

calculated at T_g from the Coupling Model. The dash-dot lines give the fit of the Arrhenius and VFTH equations to the corresponding data (same color as the data)

Dedication

À mes parents Sodje & Deguewa

À mes grands-parents

Djayam, Zadala, Cheye, Ngougé & Maya

À mes frères & sœurs

Moïse, Clément & Azack

Paulette, Reine-de-Guerre, Duplexe & Leslie

À mon ami de toujours "Lucy"

Acknowledgements

Et voici venu le temps de dire en ces quelques mots toute ma gratitude et ma reconnaissance aux personnes qui ont participées de près ou de loin à mon épanouissement scientifique, personnel et mieux encore à l'aboutissement de ce travail.

Comme le chante le psalmiste, "je te rends grâce Seigneur de tout mon cœur, tu as entendu les paroles de ma bouche" merci pour la santé, pour la sérénité et la sagesse que tu me procures devant l'épreuve, la fatigue et le découragement.

Je veux exprimer mes sincères remerciements à ma directrice de thèse Professeur Allisson Saiter du laboratoire GPM, pour son encadrement efficace, sa disponibilité constante, ses petits coups de pression et surtout sa confiance. J'ai passé, trois années de recherche intenses, avec certes des doutes et une remise en question permanente de soi, des interrogations qui forgent le jeune esprit scientifique mais surtout trois années enrichissantes et passionnantes et tu y as participé pleinement. Je vais peut-être m'arrêter là car tu attends des mesures hautes fréquences et hautes pressions.

Je voudrais dire un merci tout particulier à mon encadrant de thèse Dr Nicolas Couvrat du laboratoire SMS. Merci de m'avoir permis de découvrir le monde de la chiralité et de la "petite" synthèse chimique. Je vais te l'avouer, je n'ai pas "tout" compris. Mais je crois avoir appris beaucoup au sein des deux laboratoires. Merci pour ta disponibilité sans faille, ta volonté contagieuse à percer le mystère de l'état l'amorphe des conglomerats. Merci pour tes petites phrases du style "il faut prendre de la hauteur" qui m'ont toujours boostées à creuser le sujet d'avantage au point de m'y perdre un peu dans des "idées hautement spéculatives" (confère un des reviewers de la publication sur la 12H).

Je veux doublement remercier le Professeur Gérard Coquerel directeur du laboratoire SMS pour m'avoir accueilli au sein de son laboratoire et d'avoir accepté de présider mon jury de soutenance.

J'exprime mes sincères remerciements au Professeur Eric Dargent pour m'avoir accueilli et facilité mon intégration au sein de l'équipe EIRCAP du laboratoire GPM.

Comment ne pas exprimer toute ma gratitude et ma reconnaissance au projet de bourse Erasmus Mundus ACP II grâce auquel j'ai pu obtenir mon Master 2 à l'université de Lille. Je joins mes sincères remerciements au personnel scientifique et administratif ayant mené ce projet à bon port et ainsi participé à ma réussite académique.

Acknowledgements

Je tiens également à remercier très particulièrement la région Normandie et l'UE pour avoir financé le projet FEDER MACHI qui m'a permis d'effectuer dans des meilleures conditions ma thèse de doctorat au sein des laboratoires SMS et GPM.

Mes remerciements vont également à l'endroit du professeur Frédéric Affouard et du Dr Natalia Correia pour toutes leurs petites attentions, les innombrables conseils reçus tant sur l'aspect scientifique que personnel. Merci pour votre collaboration sincère et fructueuse, j'espère continuer à bénéficier de votre belle attention.

J'exprime également toute ma reconnaissance envers les membres du jury de ma thèse pour l'intérêt qu'ils ont manifesté en acceptant de participer à ce jury de thèse.

Toute ma gratitude à l'endroit des rapporteurs de cette thèse, les Professeurs Marc Descamps de l'Université de Lille et Madalena Dionisio de la nouvelle Université de Lisbonne pour leur disponibilité et les échanges enrichissants que nous avons eu avant et pendant la soutenance de thèse. Un merci tout particulier au Dr Emeline Dudognon d'avoir accepté de participer au jury de thèse en sa qualité d'examinatrice. J'aime à lui rappeler que les premières notions apprises sur la mobilité moléculaire dans les matériaux formateurs de verre m'ont été dispensés par elle. Encore merci pour tout.

Un profond remerciement va à l'endroit des permanents de l'équipe Eircap du laboratoire GPM pour les conseils reçus, les échanges scientifiques et les bons moments de convivialité.

Un grand Merci aux docteurs Laurent Delbreilh, Antonella Esposito et Nicolas Delpouve. Merci à Marie Rose Garda, Eric Dontzoff et Clément Démarest pour leur simplicité et leur grande disponibilité.

Je tiens également à remercier tous les permanents du Laboratoire SMS pour m'avoir accueilli et permis de découvrir le monde de la chiralité et des équilibres hétérogènes. Merci aux Professeurs Samuel Petit et Pascal Cardinael, aux docteurs Valerie Dupray, Valérie Agasse, Yohan Cartigny, Ivo rietveld, Gabin Gbabode, Clément Brandel. Un merci particulier à Morgan Sanselme pour les figures des structures cristallographiques et les verres partagés en terrasse l'été. Merci à Marie Vaccaro pour son aide efficace dans les analyses de chromatographie.

J'exprime également toute ma reconnaissance et mes amitiés aux doctorants des deux laboratoires. Pour tous les moments resto, laser game, dancing party, ballades, bowling, jeu de société... Merci à Quentin Viel, pour sa disponibilité et ses petites attentions, merci à Benjamin Schammé et Emilie Bobo pour leur simplicité et les encouragements. Merci à Steven, Xavier (Mr Flash), Sélim, Clément de Saint Jores, FX pour votre aide et votre disponibilité.

Acknowledgements

Merci à ceux qui ont partagés les mêmes bureaux que moi durant ces trois années de thèse pour la bonne ambiance et les belles discussions: FX, Grace, Simon, Lina Yuan (thank you so much for your friendship) Manon, Chloé, Nagihan, Quentin Lozay, Clément Fosse et Alexandre (Vive l'ADDED et bien sûr Petit Pays). Merci également à Aurélie et Sareh pour votre amitié, bon courage à toutes les deux pour la fin de vos thèses. Merci à Esteve et à Bindu pour les conseils reçus lors de la préparation de ma soutenance. Merci à Antoine, Lina H, Aliou Ryusei, KangLi, Marine, Aurelien pour votre soutien et vos mots d'encouragement.

Merci au corps enseignant de l'université de Yaoundé 1 plus particulièrement ceux du département de physique pour la formation reçue et l'esprit forgé. Je pense de façon naturelle à vous Pr Jean-Marie Bienvenu Ndjaka, merci pour votre amitié paternelle et vos multiples conseils de vie.

Je veux remercier de façon particulière les amis de la chorale et de l'aumônerie pour tous les moments d'amitié de fraternité de déconnade mais aussi de prière passé ensemble. C'est aussi grâce à vous que j'ai réussi à tenir avec sourire ces trois années. Je pense particulièrement au père Robert (merci pour ce que vous m'apportez au quotidien) à Thomas H, Rémi, Vincent, Thomas R, Etienne D (la famille tenor), Aymeric (mon colloc préféré), Eugénie (le big boss) Anne (la cheffete adorée), Claire S, Margerie, Thomas C (Mr le prof), Marie, Marie L, Marie J, Sylvain, Thibault (pour la belle musique), Appoline, Martin, Jeanne et bien sûr toi Solenne (pour nos discussions interminables "ah le temps passe si vite"). Merci à toi maman Nicole pour la générosité, l'affection et l'attention que tu as su me manifester pendant la période de préparation de ma soutenance. Merci à toute la communauté de Spiritus, les paroissiens et les sœurs qui ont partagés la plupart de mes soirées du mercredi. Merci à vous Chloé et Paul pour la joie et l'assurance que vous m'apportez, vous êtes géniaux. Merci à vous Danièle et Christelle pour votre amitié fraternelle et fidèle ainsi que pour toute votre aide dans la préparation de mon pot de thèse. Merci les filles.

Merci aux amis de Roméro (Lille) pour cette fraternité indélébile qui nous lie : merci à vous Danielle, Aigline, Herman, Eric et Lydia.

Merci à toi Thierry pour ta disponibilité, tes multiples conseils et pour tous les moments antistress passés autour de tes histoires de vie (très drôles).

Merci à vous camarades et amis Clinton, Ibrahim, Roméo, Césaire, Martin, Derrick, Achille, Fabrice, William pour votre amitié. Merci à toi Ernesto (Lucy) pour ton amitié débordante et le lien de confiance.

Acknowledgements

Merci à toute ma famille pour l'amour et la confiance qu'elle me porte. Merci pour vos encouragements, vos petits messages de réconfort, je suis certes loin de vous mais je pense fortement à vous. Merci Papa et maman même si je ne le dit pas très souvent je vous aime.

Résumé

Dans le cadre de cette thèse, nous avons réalisé l'étude de systèmes amorphes moléculaires chiraux en évaluant leur vieillissement, leur mobilité ainsi que leur capacité à recristalliser en fonction de la composition énantiomérique du matériau. Pour limiter les facteurs additionnels à la chiralité, ce travail s'est concentré sur des systèmes modèles formant des conglomerats stables : N-acetyl- α -methylbenzylamine (Nac-MBA) et 5-ethyl-5-methylhydantoin (12H).

De ces travaux il ressort que l'impact le plus spectaculaire de la chiralité est exprimé dans la propension à la cristallisation ou l'habilité à former un verre (qui augmente de façon inversement proportionnelle de l'excès énantiomérique (ee)). Les cinétiques de vieillissement sont implicitement impactées par l'ee : Celles-ci sont plus lentes pour les ee importants. Enfin, il semble que les processus de relaxation ainsi que les temps associés soient identiques quelle que soit l'ee, bien que le comportement à la cristallisation soit lui significativement impacté. A noter que la signature la plus manifeste de la chiralité dans l'état amorphe du Nac-MBA s'exprime dans l'intensité diélectrique des processus D et α .

Mots Clés : Chiralité, Mobilité Moléculaire, Etat Vitreux, Transition Vitreuse, Vieillissement Physique, Relaxation Debye, DSC, FSC, Spectroscopie de relaxation Diélectrique (DRS).

Abstract

In the framework of this thesis, we carried out the study of amorphous chiral molecular systems by evaluating their molecular mobility, the evolution of physical properties during aging and the recrystallization behavior as function of the initial enantiomeric excess (ee). In order to avoid factors additional to chirality itself, we focused on enantiomeric systems forming stable conglomerates (full chiral discrimination in the solid state) by choosing two model compounds: 5-ethy-5-methylhydantoin (12H) and N-acetyl- α -methylbenzylamine (Nac-MBA).

From this thesis it was shown that the most spectacular effects of chirality in the amorphous state is expressed in the GFA or the crystallization propensity. The GFA increases as the ee decreases. The kinetics of physical aging is implicitly impacted by chirality. Glassy pure enantiomer requires more time to reach equilibrium than that of an intermediate composition. This situation is hypothetically due to constraints effects mostly resulting from a strong nucleation behavior in the glass state at high ee. Furthermore, the time scale of all the processes (D , α , β_{JG} , γ) and the evolution of their temperature dependency are approximatively identical even though the crystallization behavior is highly impacted by ee. It seems that molecular mobility would not be a key parameter in the crystallization behavior of Nac-MBA. The main expression of chirality in amorphous Nac-MBA is evidenced in the signature of the dielectric strength of both D and α processes.

Keywords: Chirality, molecular mobility, glassy state, glass transition, physical aging, Debye relaxation, Fast Scanning Calorimetry (FSC) Dielectric relaxation spectroscopy (DRS).

Introduction

Chirality is an important feature for molecular recognition in biology and chemical physics. Amino acids (as found in proteins) and monosaccharides (as found in RNA or DNA) possess forms that are each nonsuperimposable to their respective mirror images. In general, laboratory synthesis of a given chiral compound will yield a racemic mixture, i.e., an equal proportion of its two chiral forms identified typically as L- or D- enantiomers. However, all naturally occurring chiral proteinogenic amino acids exist exclusively as L-enantiomers, as identified by the chirality of their α -carbon, while most naturally occurring monosaccharides exist as D-enantiomers, as identified by the chirality of the carbon furthest removed from the carbonyl group [1–3]. Chirality as well as its stereochemical, structural and thermodynamic implications, play an important role in many biological and physicochemical processes. It is well established that the opposite enantiomer of a chiral drug often differs significantly in its pharmacological, toxicological, pharmacodynamics and pharmacokinetic properties [2]. Specific examples include the tuberculosis drug ethambutol, which possesses an enantiomer that lacks antimicrobial activity and the morning sickness as well as cancer drug thalidomide, which possesses an enantiomer known to cause birth defects. Accordingly, the pharmaceutical industry pursues the development of design principles for asymmetric synthesis [2,4] or efficient separation [5] of chirality-tailored compounds. Additionally to the few pharmaceutical applications, chirality is of primary importance in advanced photonic applications [6,7] (such as alternative routes to negative refraction), in low-power display technologies [8,9] and in the processing of amorphous pharmaceuticals [10]. A specific example relevant to processing concerns the area of pressure induced crystallization [11]. Whereas high pressures increase the rate of crystallization of supercooled achiral and enantiopure liquids, recent experiments have shown the opposite effect for racemic mixtures of analgesic drugs such as ketoprofen and ibuprofen [12,13].

More than 50% of pharmaceutical marketed drugs are chiral. Usually Active Pharmaceutical Ingredients (API) are formulated in the crystalline state for obvious reasons of structural purity, high physical and chemical stability. Their physicochemical properties remain stable after long storage time. However, they are concerned by the problematic of poor solubility raised by the biopharmaceutical classification system. The biopharmaceutical classification

system (BCS) categorizes oral medications into four groups on the basis of their solubility and permeability characteristics. The problem of poor solubility of APIs is a huge headache for pharmaceutical industries. About 40% of commercialized drugs are poorly water soluble and a more disturbing feature is that almost 75% of future drugs candidates will have this deficit of solubility in water. This deficit in solubility could be skirted by converting the crystalline API to the disordered amorphous solid considering that thermodynamic properties of the amorphous products present higher dissolution rate leading to better oral absorption [14]. Many studies have been carried out on the amorphous state of API, investigating the molecular mobility (relaxation processes and their time scale), the recrystallization behavior at ambient and variable pressure, the structural or enthalpy relaxation time evolution and so on [14,15]. But when it comes to the impact of chirality in the amorphous state, very few studies are reported. The thesis of Dr Quentin Viel (defended in 2017) realized in SMS and GPM laboratories of “Université de Rouen Normandie” was entirely devoted to the understanding of the amorphous state and relaxation phenomena in chiral compounds (diprophylline) as function of the initial enantiomeric composition. The work of Dr Viel aimed to complete the very few studies on this area [12,13,16,17]. It revealed that the glass transition temperature and the characteristic size of cooperative movements, appear to be independent of the ratio of enantiomers (in accordance to Gordon Taylor Law), whereas the differences of relaxation processes and relaxation rates were due to the presence of very few molar percentage of theophylline impurities rather than from chirality itself [18]. In the framework of MACHI (Materials and Chirality) FEDER project, we proposed to carry on the work initiated by Dr Viel on chiral amorphous molecular compounds by evaluating their aging, their mobility and their ability to form glass or the propensity to crystallize as function of the enantiomeric composition. In order to characterize the aging and storage effects, it was necessary to avoid factors additional to chirality that may influenced these effects. We therefore focused on enantiomeric systems forming stable conglomerates (full chiral discrimination in the solid state). Indeed in almost 95% of chiral systems, the crystallization of a racemic compound is favored from a thermodynamic point of view; this is the case of diprophylline. The appearance of this compound in the binary diagram between both enantiomers could thus influence the aging and relaxation behavior. Conversely, in the case of stable conglomerates, the counter enantiomer will act as an impurity (of the same chemical nature) until reaching a maximum of 50% which could impact the relaxation rates in the

amorphous state. This project therefore focused on the glass forming ability, the recrystallization tendency, the physical aging phenomenon, and the phenomena of relaxation at several enantiomeric excess (ee) of the following organic chiral glasses: 5-ethyl-5-methylhydantoin (12H, stable conglomerate), N-acetyl- α -methylbenzylamine (NAC-MBA, conglomerate stable below 64 °C, racemic compound stable above). The characterization of the amorphous states were carried out by mean of calorimetric techniques (such as Differential Scanning Calorimetry (DSC) Fast Scanning Calorimetry (FSC), Temperature modulated DSC (MTDSC)), structural characterization (Temperature Resolved X-ray diffraction), dielectric spectroscopy and molecular dynamic simulations.

The modelling and molecular mobility analyses were performed in the framework of collaboration with Pr Frédéric Affouard and Dr Natália Correia of UMET Laboratory in “Université de Lille”.

The compiled results have the aim to shed light into the following interrogations:

- i) At which extent the amorphous state of a pure enantiomer differs from that of an equimolar composition of the two enantiomers in conglomerate forming systems?
- ii) Upon storage, is the viability of the amorphous state identical or strongly differ when considering an enantiomerically pure sample or samples presenting variable concentrations of both enantiomers?
- iii) At what extent the molecular mobility can influence the crystallization behavior of pure enantiomer or racemic mixtures?
- iv) Regarding the pharmaceutical interest to obtain purely active enantiomers, could the amorphous state be a pathway towards the crystallization of new polymorphic forms crystallizing as conglomerates?

The manuscript is organized into five chapters and presented as follow:

Chapter I is devoted to generalities on the physics of condensed matter specifically the glassy state and some background and vocabulary notions on chirality.

Chapter II is subdivided into two sections. The first section details the thermal and structural properties of the investigated materials. The second section explicit the different experimental and modelling facilities used to probe the amorphous state of the studied systems.

Chapter III is entirely devoted to the calorimetric characterization by Fast Scanning Calorimetry and Differential Scanning Calorimetry of the amorphous of a stable conglomerate namely 5-ethyl-5-methylhydantoin (12H). An attention is paid the glass forming ability, the recrystallization behavior from the amorphous state, the propensity of crystallization and the viability of the amorphous state upon physical aging as function of the ee.

Chapter IV details the thermal characterization of the amorphous state of the second model system namely N-acetyl- α -methylbenzylamine (Nac-MBA), a stable conglomerate below 64°C. A special interest is attached to the determination of the binary phase diagram after recrystallization from the glassy state, the evaluation of the glass forming ability and the kinetic of enthalpy recovery upon physical aging as function of the ee.

The last chapter is devoted to molecular mobility investigation in Nac-MBA probe by dielectric relaxation spectroscopy and molecular dynamic simulations. The relaxational landscape of Nac-MBA is therefore investigated as function of the enantiomeric composition and direct implications of the expression of chirality in the amorphous Nac-MBA are explored.

At last, a general recall of the main results of this thesis are presented and some prospects regarding the amorphous state of chiral molecular compounds, the impact of chirality and possible pharmaceutical applications are proposed.

At the end of the manuscript, few annexes are proposed to the reader concerning some enthalpy recovery analysis performed by FSC at 500 K/s for several ee at different aging temperature and some published articles concerning this thesis.

References

- [1] F. Latinwo, F.H. Stilling, P.G. Debenedetti, Molecular model for chirality phenomena, *J. Chem. Phys.* 145 (2016) 154503. doi:10.1063/1.4964678.
- [2] I.K. Reddy, R. Mehvar, *Chirality in Drug Design and Development*, CRC Press, 2004.
- [3] *Chirality in Natural and Applied Science* Edited by W. J. Lough and I. W. Wainer Blackwell/CRC Press: Oxford. 2003. 313 pp. £95. ISBN 0-632-05435-2., *Org. Process Res. Dev.* 9 (2005) 374–374. doi:10.1021/op050037+.
- [4] R.A. Sheldon, *Asymmetric Catalysis in Organic Synthesis*. Ryoji Noyori. John Wiley & Sons, Chichester, 1994. xvii + 378 pp., £45.50. ISBN 0-471-57267-5, *Recl. Trav. Chim. Pays-Bas.* 115 (1996) 155–155. doi:10.1002/recl.19961150216.
- [5] A.M. Stalcup, Chiral separations, *Annu. Rev. Anal. Chem.* Palo Alto Calif. 3 (2010) 341–363. doi:10.1146/annurev.anchem.111808.073635.
- [6] J.B. Pendry, A Chiral Route to Negative Refraction, *Science.* 306 (2004) 1353–1355. doi:10.1126/science.1104467.
- [7] P.F. Damasceno, A.S. Karas, B.A. Schultz, M. Engel, S.C. Glotzer, Controlling Chirality of Entropic Crystals, *Phys. Rev. Lett.* 115 (2015) 158303. doi:10.1103/PhysRevLett.115.158303.
- [8] C. Tschierske, Development of structural complexity by liquid-crystal self-assembly, *Angew. Chem. Int. Ed Engl.* 52 (2013) 8828–8878. doi:10.1002/anie.201300872.
- [9] H.H. Wensink, G. Jackson, Generalized van der Waals theory for the twist elastic modulus and helical pitch of cholesterics, *J. Chem. Phys.* 130 (2009) 234911. doi:10.1063/1.3153348.
- [10] S.F. Swallen, K.L. Kearns, M.K. Mapes, Y.S. Kim, R.J. McMahon, M.D. Ediger, T. Wu, L. Yu, S. Satija, Organic Glasses with Exceptional Thermodynamic and Kinetic Stability, *Science.* 315 (2007) 353–356. doi:10.1126/science.1135795.
- [11] K. Adrjanowicz, K. Kaminski, M. Paluch, K.L. Ngai, L. Yu, Study of dynamics and crystallization kinetics of 5-methyl-2-[(2-nitrophenyl)amino]-3-thiophenecarbonitrile at ambient and elevated pressure, *J. Chem. Phys.* 136 (2012) 234509. doi:10.1063/1.4728162.
- [12] K. Adrjanowicz, K. Kaminski, Z. Wojnarowska, M. Dulski, L. Hawelek, S. Pawlus, M. Paluch, W. Sawicki, Dielectric Relaxation and Crystallization Kinetics of Ibuprofen at Ambient and Elevated Pressure, *J. Phys. Chem. B.* 114 (2010) 6579–6593. doi:10.1021/jp910009b.
- [13] K. Adrjanowicz, K. Kaminski, M. Paluch, K. Niss, Crystallization Behavior and Relaxation Dynamics of Supercooled S-Ketoprofen and the Racemic Mixture along an Isochrone, *Cryst. Growth Des.* 15 (2015) 3257–3263. doi:10.1021/acs.cgd.5b00373.

- [14] M. Rams-Baron, R. Jachowicz, E. Boldyreva, D. Zhou, W. Jamroz, M. Paluch, Amorphous Drug Formulation, in: M. Rams-Baron, R. Jachowicz, E. Boldyreva, D. Zhou, W. Jamroz, M. Paluch (Eds.), *Amorph. Drugs Benefits Chall.*, Springer International Publishing, Cham, 2018: pp. 159–223. doi:10.1007/978-3-319-72002-9_6.
- [15] M. Descamps, J.-F. Willart, Some Facets of Molecular Disorder in Crystalline and Amorphous Pharmaceuticals, in: *Disord. Pharm. Mater.*, Wiley-Blackwell, 2016: pp. 1–56. doi:10.1002/9783527652693.ch1.
- [16] H. E. Gallis, J.C. van Miltenburg, H.A. J. Oonk, Polymorphism of mixtures of enantiomers: A thermodynamic study of mixtures of D - and L-limonene, *Phys. Chem. Chem. Phys.* 2 (2000) 5619–5623. doi:10.1039/B005603K.
- [17] T.H. Kim, T. Shibata, S. Kojima, D.-M. Shin, Y.-H. Hwang, J.-H. Ko, Comparison of thermal and elastic properties of glassy racemic and enantiomeric ibuprofen studied by Brillouin light scattering and modulated differential scanning calorimetry, *Curr. Appl. Phys.* 14 (2014) 965–969. doi:10.1016/j.cap.2014.05.001.
- [18] Q. Viel, L. Delbreilh, G. Coquerel, S. Petit, E. Dargent, Molecular Mobility of an Amorphous Chiral Pharmaceutical Compound: Impact of Chirality and Chemical Purity, *J. Phys. Chem. B.* 121 (2017) 7729–7740. doi:10.1021/acs.jpcc.7b05667

CHAPTER I:

THE PHYSICS OF AMORPHOUS STATE AND CHIRALITY

The present chapter partitioned into three main sections encounters theoretical and fundamental notions on the physics of condensed matter, chirality and the state of art of chirality in the amorphous state respectively. The first section devoted to the glassy state hold on five parts. Section I.1 and I.2 explicit the phenomena implicated in glass formation and crystallization. The glass transition and several thermodynamics and kinetic models are presented in section I.3 and I.4 respectively. Since the glassy state is an out of equilibrium state, a high point is mentioned on its instability character and the implications related to molecular mobility or time dependent properties such as physical aging and relaxation phenomena (see section I.5). The second main topic is dedicated to chirality and subdivided into three parts: a brief history of chirality, the stereochemical nomenclature used, and the thermodynamics of chiral systems respectively. In the last section, few available studies on the impact of chirality in the amorphous state regarding their glass forming ability and crystallization propensity as function of the enantiomeric composition are detailed. Lastly we illustrated some molecular mobility investigations from the glassy state toward the supercooled liquid state over a wide range of frequency at variable temperatures for both pure enantiomer and racemic mixture.

I- Generalities on the glassy state

I.1 Vitrification Processes and Crystallization Mechanisms

I.1.1 Vitrification Processes

Glasses are disordered materials (liquid-like structure) with no long-range translational order or periodicity of crystals but behave mechanically like solids. Glass formation is a generic behavior of matter [1–4]. Several types of materials, with different chemical nature such as metallic alloys [5–8], oxides [9–12], polymers [13–15], chalcogenides [16], halides [17], pharmaceuticals [4,18–20] or small organic molecules [21,22] can form glasses. Numerous routes of glass formation from various initial states are summed up in figure 1. Therefore melt quenching remains one of the most conventional and ancient route for vitrification. Under certain conditions, the melt of several materials can be cooled continuously below the melting point T_m in order to reach the out of equilibrium glassy state. Anyhow amorphous glass can be obtained from melt quenching if crystallization is bypassed upon cooling.

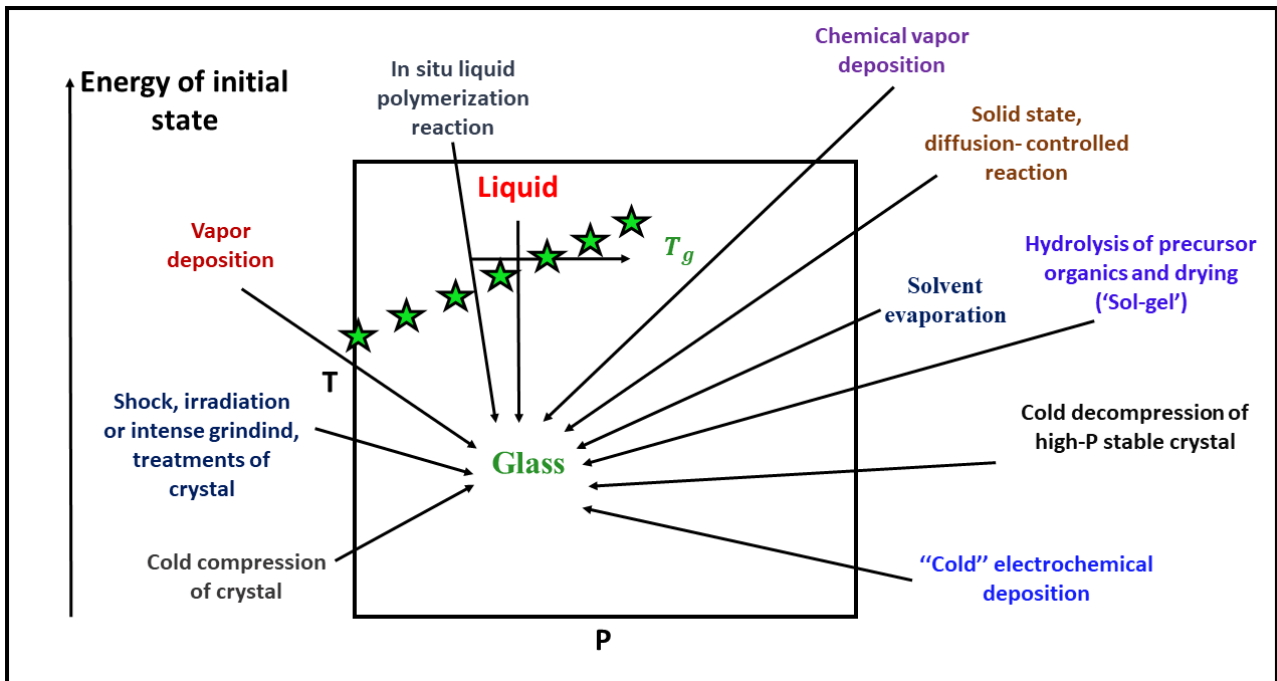


Figure 1: Various routes to the glassy state, roughly indicating the energies of the initial states relative to the final glassy states. Adapted from [23]

Crystallization is a conjugation of two temperature dependent phenomena: nucleation and crystal growth. This process results in a competition between the driven force of crystallization and molecule dynamics. When the melt is cooled down slowly below the melting temperature, the first order transformation from liquid to crystal does not take place spontaneously upon cooling. The supercooled liquid crystallizes at the crystallization temperature T_c . Therefore, if sufficient cooling rate is provided, crystallization can be inhibited even below T_c . At the glass transition temperature T_g the supercooled liquid ‘falls’ in an out of equilibrium state, namely the vitreous state. One of the best ways to illustrate this fact is to schematize a time-temperature-transformation (TTT) diagram, which predicts the amount of crystalline fraction at an annealing temperature after a given time. Figure 2 schematizes a TTT diagram, which illustrates the different pathways that lead either to glass formation or to crystallization. This diagram often presents a nose-shape behavior and the temperature at which crystallization is most probable is located at the nose. Passing rapidly this nose temperature with a critical cooling rate Q_{crit} , may certainly avoid experimentally detectable crystallization, but it does

not necessarily avoid catching some nuclei that are unable to grow within the amorphous matrix [4]

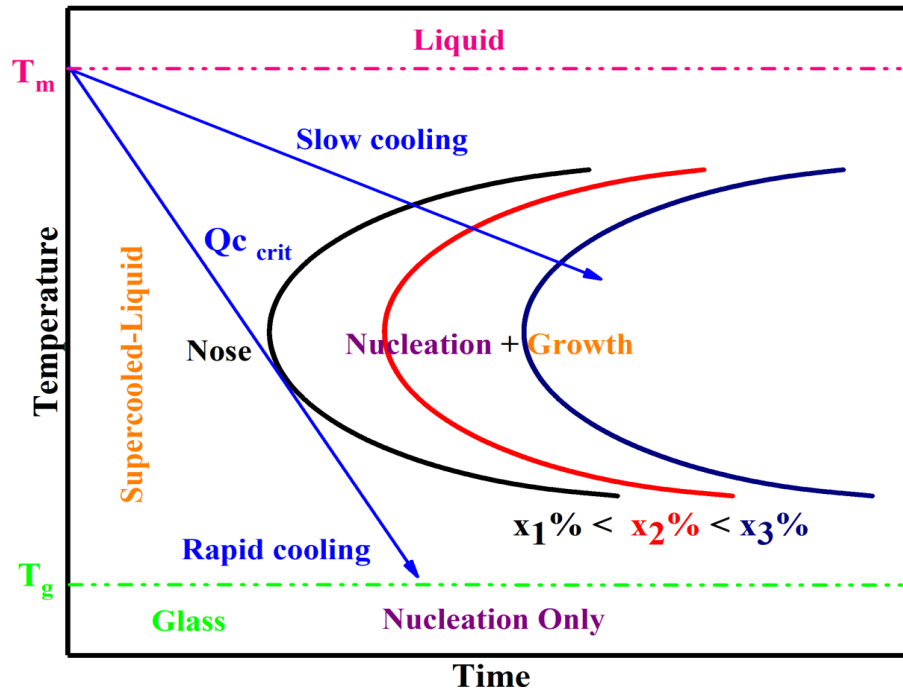


Figure 2: Schematic TTT diagram adapted from [19]

Theoretically, one can understand that crystallization can be avoided when sufficient cooling is provided. Therefore all liquids do not present the same propensity to crystallize or to vitrify. Consequently one can distinguish good, medium and poor glass former depending on how fast enough it is necessary to cool down the liquid in order to reach the glassy state.

I.1.2 Crystallization Mechanism: Nucleation and Crystal Growth Phenomena

From a theoretical point of view, crystallization from the molten or amorphous state is a thermodynamic phenomenon involving complex nucleation and growth stages, each phenomenon having its own specific properties.

a) Nucleation

The most common, and reliable theory that gives a good understanding of the mechanism engaged in nucleation is the classical nucleation theory (CNT). Nucleation is related to the stochastic spontaneous formation of small crystalline nuclei made of few molecules in the liquid. Two types of nucleation are distinguished: homogeneous nucleation, corresponding to

spatially and temporally independent fluctuations of regions of the original phase, and heterogeneous nucleation, which is catalyzed at specific sites [20,24,25]. In this section only homogenous nucleation will be discussed. The characteristic features of homogeneous nucleation - formation of nuclei, able to grow in a homogeneous phase by fluctuation of the atomic structure - have been developed by Volmer and Weber [cited in 25] and also by Becker and Döring [cited in 26]. Statistical fluctuations generate nuclei through the transient appearance and disappearance of small regions of a new phase within an original (or “parent”) phase. Here the “fluctuation” is taken to be a cluster of few molecules in the configuration of the new phase. These fluctuations are localized and are stochastic in both space and time. The probability that a fluctuation occurs is governed by thermodynamic conditions, specifically the minimum work required to create the fluctuation. The lifetime of a fluctuation is related to its size. Only when a “critical” size is exceeded is the dissolution probability small enough for the fluctuation to evolve into a macroscopic region of the new phase. The stochastic behavior of shrinkage and growth is consistent with the existence of a barrier to the phase transition: the nucleation barrier. The nucleation barrier arises from the energy penalty for creating an interface between this cluster and the original phase. The formation of a small volume fraction, which has the structure of the end phase, is connected to a decrease of the Gibbs energy of the system by ΔG_V . Simultaneously, a phase interface appears between the nucleus and the starting phase. The nucleation is thus, connected with an increase in the interfacial Gibbs energy by ΔG_σ . The total change in Gibbs energy ΔG of the system connected to the nucleation is given by:

$$\Delta G = \Delta G_V + \Delta G_\sigma \quad (1)$$

Assuming that the nuclei are of spherical shape, the change of the Gibbs energy during nucleation is then related to the radius r of the nucleus and expressed as follows:

$$\Delta G = \frac{4}{3}\pi r^3 \Delta g_V + 4\pi r^2 \sigma \quad (2)$$

where Δg_V is the Gibbs free energy variation per unit volume for the formation of the new phase, and σ is the interfacial energy per unit area. For a critical cluster, having radius r^* and containing n^* molecules, the Gibbs free energy for new phase formation has a maximum ΔG^* , which constitutes the barrier to nucleation. As clusters grow beyond the critical size, the fraction of molecules in the interfacial region decreases, as does the work of cluster formation (see figure 3). Clusters larger than r^* (or n^*) are therefore favored to grow to complete the

phase transformation [20,24,25]. The critical nucleus size r^* is calculated by solving $(d\Delta G/dr)_r = 0$

$$r^* = \frac{2\sigma}{\Delta g_V} \quad (3)$$

And the activation energy required to reach the critical size, ΔG^* is:

$$\Delta G^* = \frac{16\pi}{3} \frac{\sigma^3}{\Delta g_V^2} \quad (4)$$

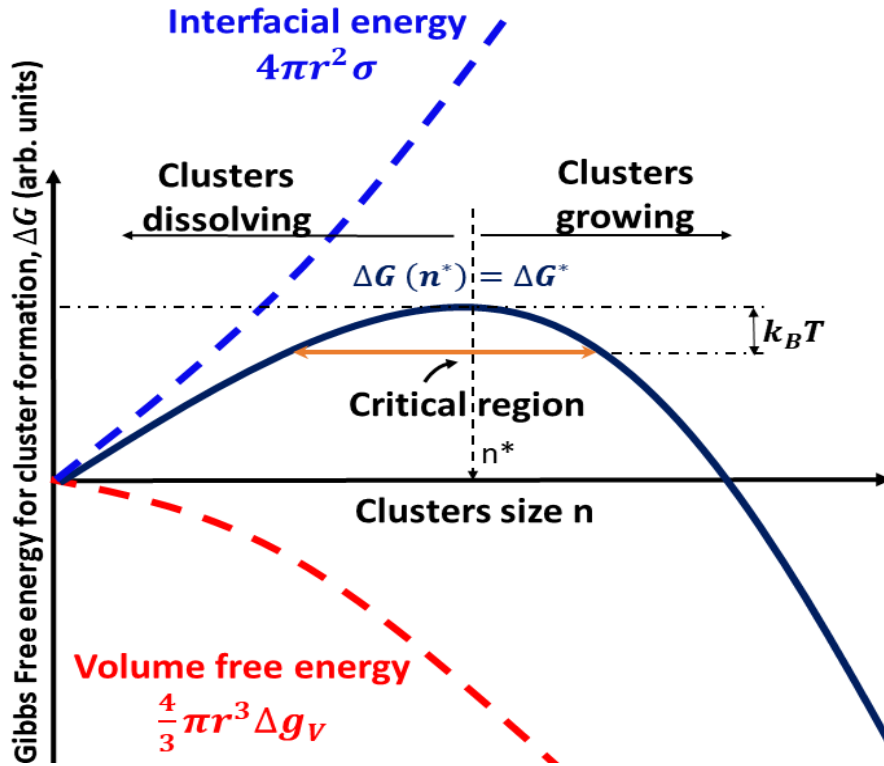


Figure 3: Gibbs free energy of formation of a cluster of n molecules, ΔG , as a function of n . The critical size, n^ , the critical work of formation, $\Delta G(n^*) = \Delta G^*$, and the critical region (within which $\Delta G(n) - \Delta G^* \leq k_B T$) are indicated. Below n^* clusters are on average dissolving; above n^* they are on average growing. From [24]*

Diffusion is also required to make nucleation possible since molecules have to aggregate to form the nucleus. Nucleation is often characterized by the nucleation rate, I (unit $m^{-3} s^{-1}$), which is the number of formed critical nuclei per volume unit and time. It is proportional to the product of two activated processes: (i) the number of critical size nuclei $\sim \exp[-\Delta G^*/k_B T]$ (k_B is the Boltzmann constant) and (ii) the probability for a molecule to migrate across the interface separating the critical size nucleus and the liquid (thus forming a supercritical size nucleus) which is roughly proportional to the diffusivity $D \sim \exp[-A/k_B T]$, where A is the

energy barrier associated with atomic motion. Both probabilities behave in opposite ways as a function of temperature and thus give rise to the bell-shaped dependence of the nucleation rate. The nucleation rate increases sharply with increasing supercooling, yet decreases again at low temperatures, due to the decreasing atomic mobility, described by the diffusion coefficient [20,24,28,29] (see figure 4).

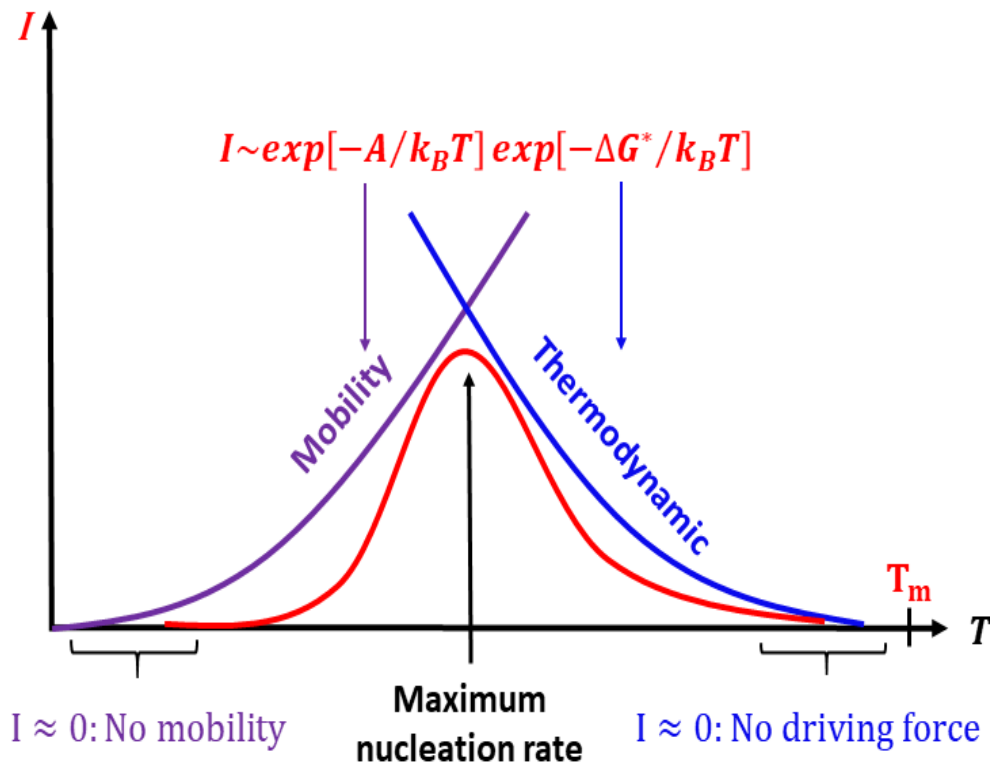


Figure 4: Temperature dependence of the nucleation rate I involving a thermodynamic and a mobility contribution

b) Crystal growth

The second stage in which the supercritical nuclei formed will grow within the liquid phase is the growth stage. It occurs by aggregation of molecules of the phase undergoing a transformation. Crystal growth velocity, C (unit $\text{m}\cdot\text{s}^{-1}$), is a measure of the growing of the crystal surface of the supercritical nuclei. Similarly to the nucleation rate, C is proportional to the product of a thermodynamic term, describing the probabilities of attachment/detachment of the molecules to/from the nuclei $[1 - \exp(-\Delta G_{\text{liq-crys}}/k_B T)]$ and the probability of the molecule diffusion across the interface, which is also roughly proportional to the

diffusivity, $D \sim \exp[-A/k_B T]$ where $\Delta G_{liq-crys}$ is the difference between the Gibbs free energies of the liquid and the solid phases, k_B is the Boltzmann constant and A is the energy barrier associated to atomic motions. The net effect of combining these two terms is that the growth rate must go through a maximum and thus also give rise to a bell-shaped dependence as a function of temperature as displayed in figure 5.

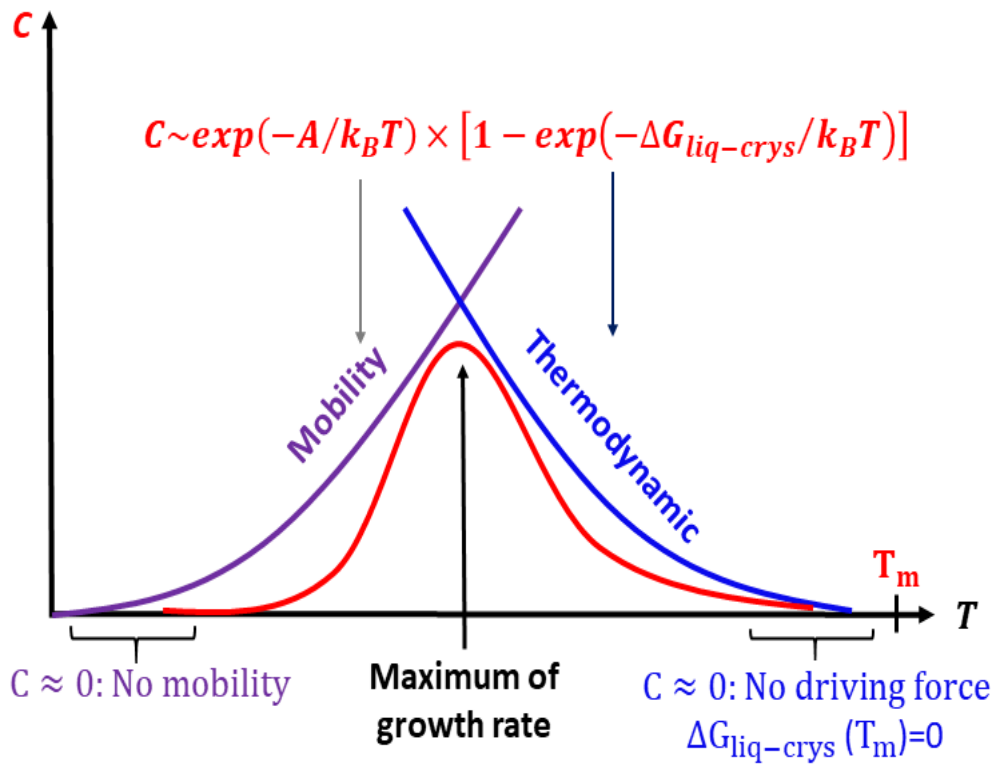


Figure 5: Temperature dependence of the growth rate C involving a thermodynamic and a mobility contribution

I.2 Glass Forming Ability (GFA)

The knowledge of both nucleation and growth rates as a function of temperature thus provides a guideline to predict the crystallization tendency. The glass-forming ability (GFA) of a melt is usually evaluated in terms of the critical cooling rate (Q_{Ccrit}) for glass formation, which is the minimum cooling rate necessary to keep the melt amorphous without precipitation of any crystals during solidification. The smaller Q_{Ccrit} , the higher the GFA of a system should be [30,31]. However, a general or universal understanding of GFA based on structural, dynamic and thermodynamic theories is not yet available [19]. It has been suggested that a good GFA is linked to the complexity of the molecular composition. For many metallic alloys, as the number of components increases the crystallization propensity decreases, consequently GFA increases [32,33]. Low molecular symmetry and high flexibility due to high number of internal degrees of freedom can also improve the GFA [20,34]. The correlation between molecular mobility and GFA is still questionable. Molecular glasses with the same mobility can illustrate different crystallization propensity [35]. From a thermodynamically point of view a low melting entropy, ΔS_m , and a limited range between the melting temperature T_m and T_g appear to be an advantage for GFA [4,7,8,10]. Since the dynamic, thermodynamic and structural properties are mostly interrelated, it is somehow difficult to accurately predict the GFA character of a system. Theoretically, crystallization of the supercooled melt implies nucleation and growth stages, both processes having their own temperature dependence behavior. As illustrated in figure 6, when the temperature dependence curve of nucleation and crystal growth are well separated, crystallization becomes difficult and takes much more time. Conversely, when the two processes overlap, the propensity to crystallize increases consequently the GFA is impacted. The temperature position of both nucleation and growth domains is function of the interfacial energy. Consequently, this parameter may play an essential role in the GFA of glass forming liquids. The interfacial energy can be defined as the necessary energy required to build an interface between the liquid and the solid phases. As long as this energy is of high magnitude, the interface creation becomes costly energetically. Therefore, it seems obvious that crystallization becomes difficult, while vitrification could be favored. Conversely if the interfacial energy is low enough, crystallization is favored.

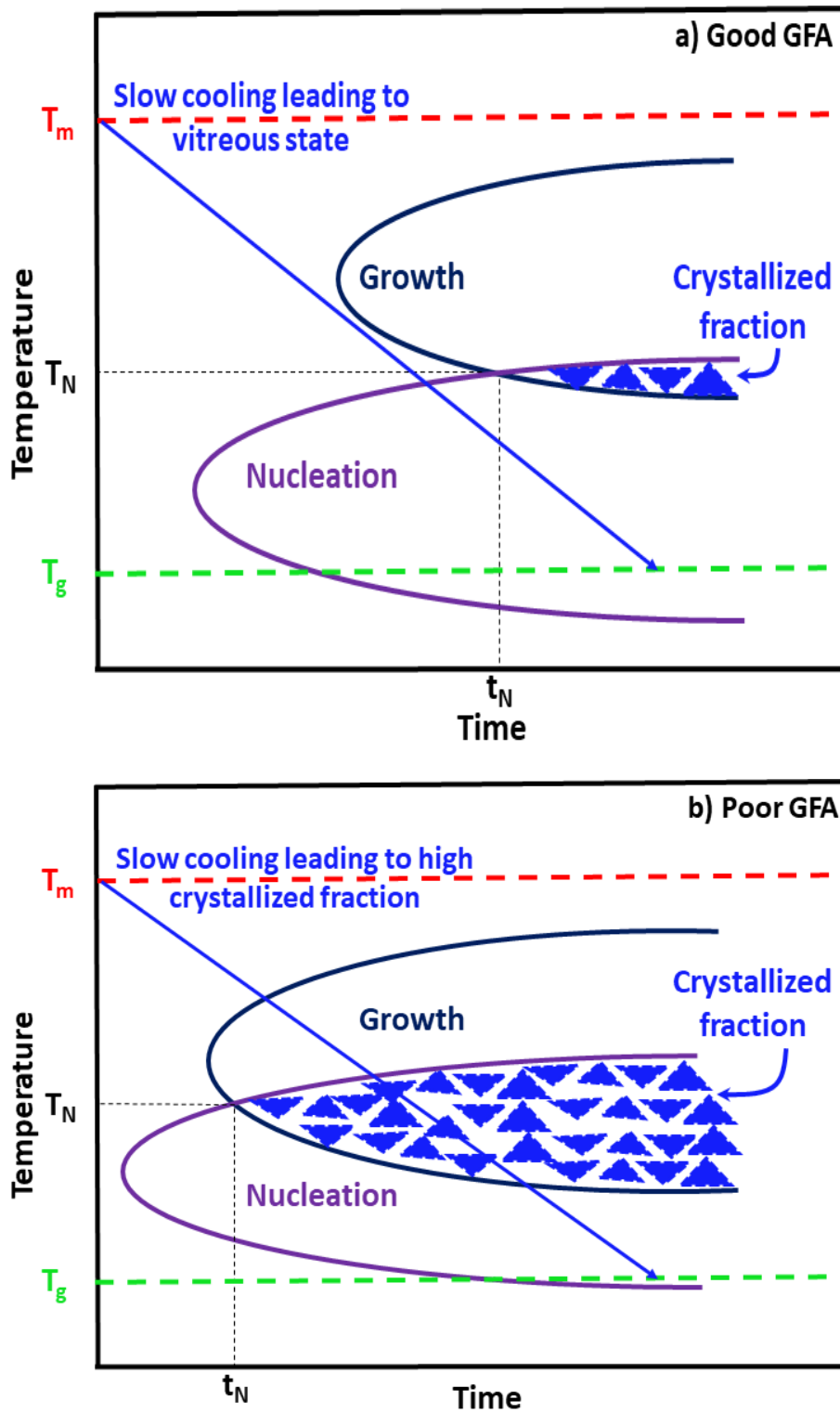


Figure 6: Schematically time evolution of nucleation and growth temperature region for a) good GFA and b) poor GFA

I.3 The glass Transition Phenomenon

Glassy materials are omnipresent in our daily life and play an essential role in modern technology. Even though they have been available since the rise of mankind their physical understanding is still controversial and remains an unresolved problem of condensed matter physics [37]. The glass transition is an important phenomenon for the glass-formers and its fundamental nature is still unclear. Philip W. Anderson, a Nobel Laureate wrote in 1995: “The deepest and most interesting unsolved problem in solid state theory is probably the theory of the nature of glass and the glass transition” [38]. Contrary to melting, glass transition is not a real phase transition but a kinetic phenomenon and vitrification occurs over a narrow temperature interval. Additionally, T_g value depends on the cooling rate: the lower the cooling rate, the lower the T_g value as long as cooling is fast enough for glass formation. Figure 7a) illustrates the thermal behavior that characterizes the cooling of a liquid through the glass transition at different cooling rates. Upon continuous undercooling from the molten state, the enthalpy, H or entropy, S evolution changes continuously across T_g same as the volumetric, V behavior, but the corresponding heat capacity $C_p = \left(\left(\frac{\partial H}{\partial T} \right)_p, \left(\frac{T \partial S}{\partial T} \right)_p \right)$ decreases brutally to a value slightly higher than that of the crystal (see figure 7b)). Likewise the drop of the expansion coefficient α_p results from a change in volume, $V(T) (\alpha_p = \left(\frac{\partial \ln V}{\partial T} \right)_p)$. The drop of C_p at T_g is characterized by its magnitude $\Delta C_p = C_{p,liq} - C_{p,glass}$.

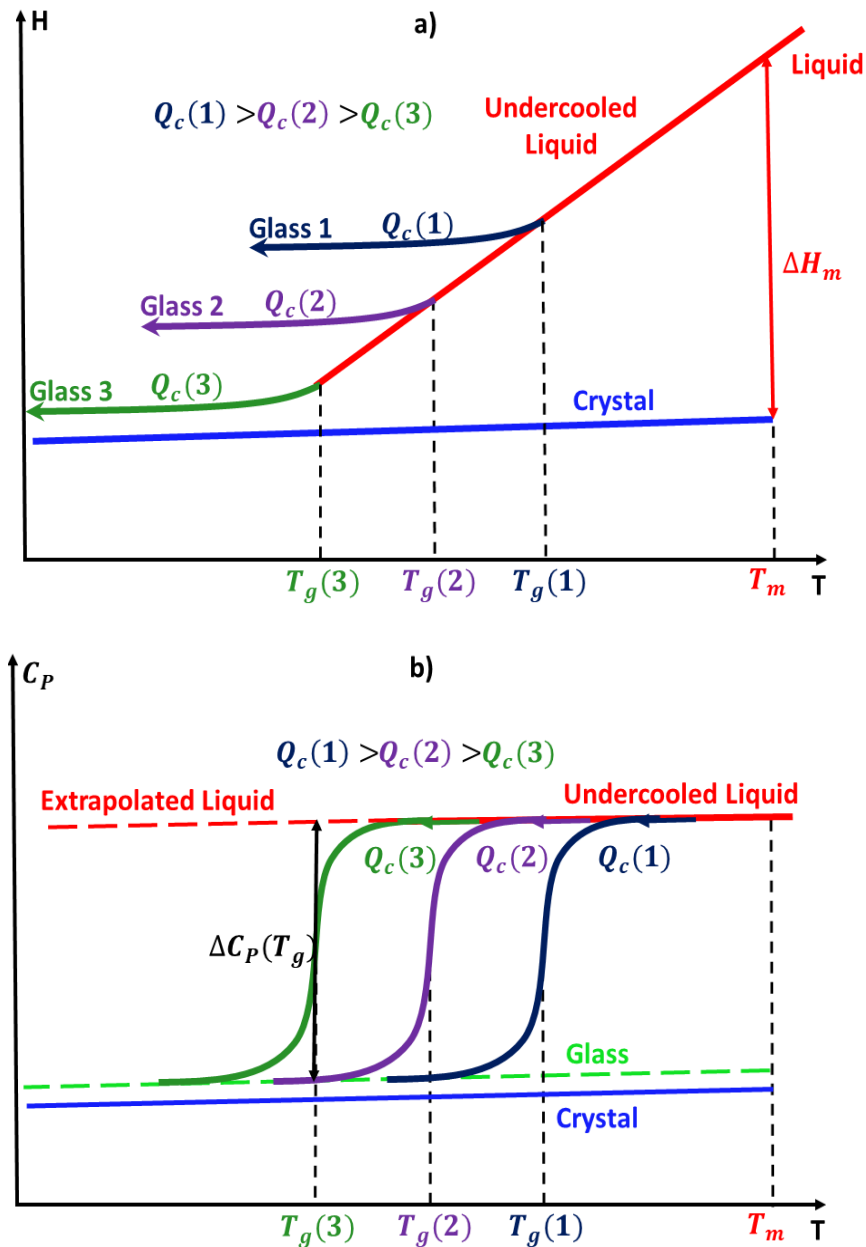


Figure 7: Schematically temperature evolution of a) enthalpy, H and corresponding b) heat capacity, C_p at different cooling rates $Q_c(1)$, $Q_c(2)$ and $Q_c(3)$

C_p increases in relation to the number of degree of freedom consequently, $\Delta C_p > 0$ below and above T_g . Two types of motions contribute to C_p of an ordinary glass forming liquid: very fast vibrational motions (motions localized inside the cage formed by neighboring molecules) and molecular rearrangement processes such as diffusion from the cage and molecular rotation of high angles (See figure 8). Only vibrational motions contribute in the C_p of crystalline solids. A glass differs from a liquid due to the absence of some degrees of freedom frozen at T_g . Even below T_g vibrational and localized relaxation motions can occur in glassy

state. This is the main reason for the slight excess of the specific heat of the glass in comparison with the crystal. The thermodynamic quantities involved in C_p (or H , S ...) can be separated into a vibrational and configurational contribution.

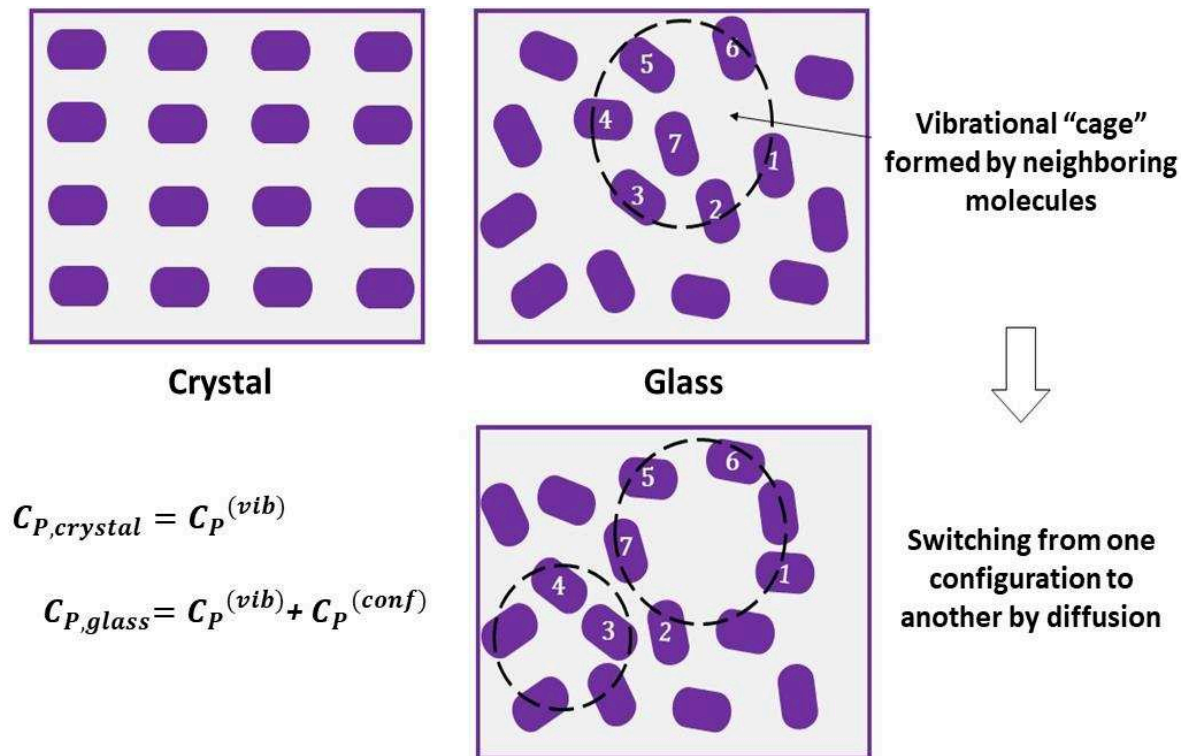


Figure 8: Schematic illustration of the vibrational and configurational contribution of C_p in both crystalline and glassy phases. Some specific molecules are numbered in order to identify their position after the conformational change occurs

The temperature defined by the intersection of the liquid and vitreous portion of the volume or enthalpy vs. temperature curve is the glass transition temperature, T_g . Then, T_g marks the transition from amorphous supercooled liquid to the glassy amorphous state. At this temperature the characteristic time for structural relaxation approaches the time scale of a macroscopic experiment 100 -1000 s. At the same time the viscosity value reaches 10^{12} Pa.s. Therefore molecules rearrange so slowly in such a way that they cannot explore the entire possible sample configurations in the available time permitted by the cooling rate. The supercooled liquid is structurally arrested and falls out of equilibrium [4,37,38]

I.4 The Glass Transition Models

Several theories and models have been proposed to explain the phenomenology and physical fundamentals of the glass transition. They can be classified into two types: a thermodynamic and a dynamic viewpoint. The first considered the glass transition as a kinetically controlled manifestation of an underlying singularity described by thermodynamic properties. This viewpoint concerns the Doolittle [39] or Cohen-Turnbull free volume model [40,41] and the entropy based Gibbs-Di Marzio theory [42]. The second considered vitrification as a purely dynamic singularity described by molecular mobility [38]. The purpose of this section is not to make a catalogue of existing theories on the glass transition but to highlight the link between thermodynamic and dynamic viewpoints. For this reason we will focus on the Kauzmann paradox and the Adam-Gibbs cooperative rearrangement region theory.

a) The Kauzmann Paradox

Kauzmann defined the glassy state as a necessity of matter in these terms “the vitreous or glassy state of liquids evidently only exists because experiments performed by mortal beings must of necessity be of limited duration” [43].

The entropy of a liquid phase, S_{liq} exceeds that of the corresponding crystalline phase S_{cx} at the melting temperature. However, upon cooling S_{liq} decreases more rapidly than S_{cx} . Let's hypothesize that we can undercool the liquid phase ultra-slowly, while avoiding crystallization or vitrification at low temperature. As illustrated in figure 9 at a particular temperature called Kauzmann temperature T_K the entropy difference between the liquid and its corresponding crystalline phase vanishes. Below T_K the entropy of the crystal becomes greater than that of the imaginary liquid. This unphysical result of the glassy state phenomenology is known as the “Kauzmann Paradox”. Experimentally no proof of such behavior has been highlighted since vitrification or crystallization seems unavoidable during undercooling. The Kauzmann paradox has been a permanent theoretical cogitation for many decades. In order to solve this puzzle, Kauzmann proposed the existence of the liquid intrinsic limit of metastability in the vitreous state temperature region. This limit of metastability implies a spontaneous crystallization process at temperature lower than T_K due to a critical decrease of the nucleation barrier [4,43]. Consequently, if vitrification did not occur between T_g and T_K crystallization would

remain inevitable. The second approach considered the opposite reasoning. If crystallization is bypassed upon cooling, the supercooled liquid can only escape the entropy crisis by undergoing a sharp glass transition at a defined temperature T_K . This transformation known as the “ideal glass transition” is a true thermodynamic transition by contrast to the experimental glass transition [38,44].

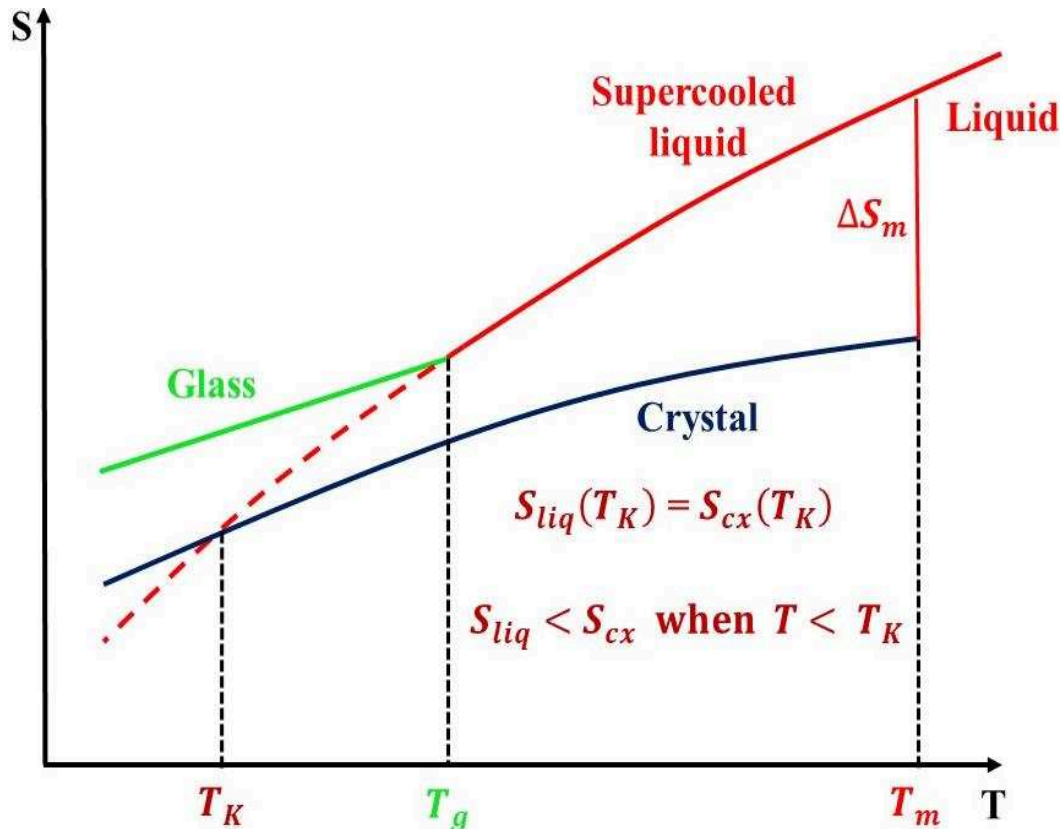


Figure 9: Schematic entropy S evolution as function of temperature of a liquid and its corresponding crystalline phase. ΔS_m is the melting entropy. The extrapolated liquid entropy equals the crystal entropy at the Kauzmann temperature T_K

b) Adam-Gibbs (AG) Theory

The merit of Adam-Gibbs theory is to rationalize the link between the two approaches of the glass transition physics. The foundation of this model is built from the Gibbs and Di Marzio entropy theory. From the latter theory, the entropy of a glass forming liquid can be separated into two contributions: a configurational and a vibrational contribution in such a way that the vibrational part is equal to that of the crystalline solid phase. As the liquid is undercooled, the entropy of the system drastically decreases due to a diminution in accessible configurations. Therefore the configurational entropy (defined as the entropy difference between the undercooled liquid and the crystal) diminishes upon undercooling and vanishes at T_K [38,42]. The latter phenomenological description advances a structural arrest of configurational rearrangements at T_K with the condition that the liquid be undercooled without crystallization or vitrification occurring. Therefore, the AG model theorizes a thermodynamic phase transition to a state of zero configurational entropy and infinite relaxation time at T_K . From this description, the temperature evolution of the relaxation times can be expressed as a function of the configurational entropy S_C [4,45] as follows:

$$\tau = A \exp C/TS_c(T) \quad (5)$$

where C is a constant containing an activation energy term. A fundamental notion developed in AG theory is the concept of “cooperatively rearranging region” defined as a subsystem of molecules that can rearrange itself into a different configuration independently of its surrounding environment resulting from an enthalpy fluctuation. As the liquid is undercooled, the cooperatively rearranging regions grow and relaxations demand the concerted participation of progressively bigger and bigger cooperatively rearranging regions. This increase of cooperativity is reflected by a loss of configurational entropy linked to a decrease of molecular mobility in AG theory [38,45].

I.5- Molecular Mobility in Glass Forming Liquids by Broadband Dielectric Spectroscopy

So far we focused on the thermodynamic description of glass transition manifestation below and above T_g . Therefore one of the fundamental aspects of this process is the out of equilibrium character emphasized by relaxation phenomena from the undercooled liquid to the vitreous state and vice versa. The understanding of the nature and origin of these relaxation motions and their temperature evolution, remain one of the main challenges of condensed matter physics [46,46,47]. These interrogations originate from the complex dynamics in glass forming liquids. Several experimental techniques are used to probe molecular dynamics in such disorder materials by applying a perturbation (electrical, magnetic or mechanical) on the system and monitoring its relaxation toward equilibrium. The most prominent among these are nuclear magnetic resonance techniques [48], mechanical [49], dielectric [50], enthalpy [51] and volume relaxation [52]. When the dynamic of molecules implies the mobility of permanent dipole moments or ionic displacements, broadband dielectric spectroscopy persists as one of the most useful tools to inquest molecular mobility [47,53]. This powerful tool covers over 16 decades in the frequency range which enables measurements of different dynamics from the undercooled liquid to the vitreous state.

I.5.1 Relaxation Processes in Glass Forming Liquids: from the Supercooled Liquid to the Glassy State

The vitrification of a liquid implies a gradual slowing down of molecular motion as temperature decreases with a concomitant increase of viscosity. The dynamical character of such glass forming liquids and thus its relaxational processes, covers a wide frequency range from local vibronic processes around T_m to highly cooperative motions at the vicinity of T_g [54] (see figure 10). Molecular motions in such systems are rather a complex affair. In the liquid state, the molecular motion is governed by a single response time with a temperature dependence reflecting a single activated process, followed by the appearance of at least two processes in the undercooled regime, a slow non exponential and non-linear [46,55] process due to intermolecular cooperativity [45,47,56,57] with a departure from an Arrhenius behavior, and a faster secondary process that remains active even below T_g with an Arrhenius

temperature dependence. In the following sections we will analyze the dynamical behavior and its origins in glass forming liquid from the undercooled liquid to the glassy state by dielectric spectroscopy.

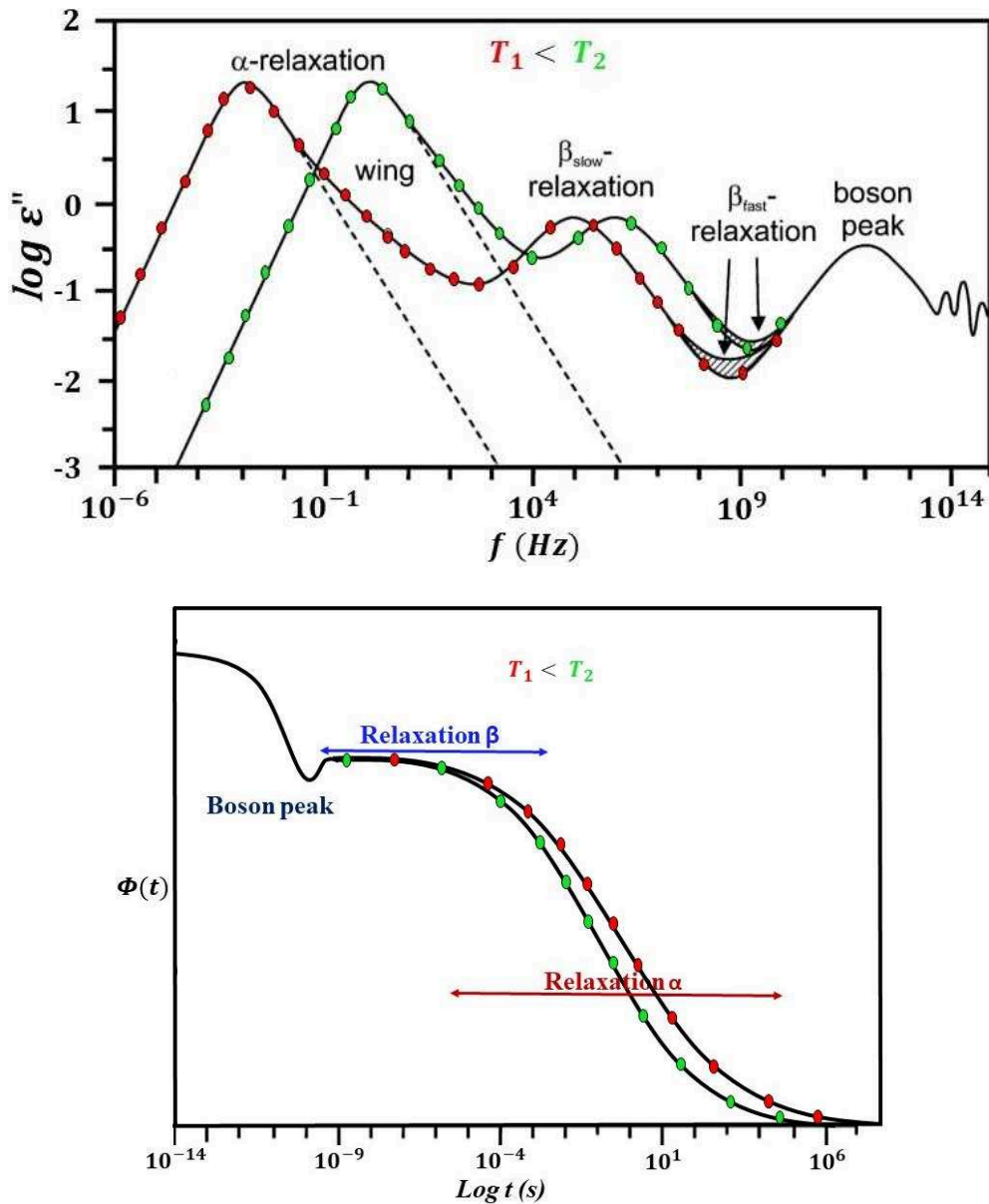


Figure 10: Schematic evolution of the dielectric loss peak ϵ'' at two temperatures $T_1 < T_2$ over 20 decades in the frequency range (top figure) and its analogous temporal evolution $\Phi(t)$ illustrating different possible relaxation modes in a glass forming liquid (bottom figure). Adapted from [47]

a) Structural Relaxation α

The structural relaxation process is a common feature in glass forming liquids associated to the dynamic of glass transition. This process is observed in the undercooled liquid at temperatures higher than T_g . Generally the dielectric loss associated to the α relaxation presents a broad and asymmetric shape with an intensity significantly higher than other processes. According to Adam-Gibbs model of glass transition, this process originates from a cooperative motion in several sub-systems of molecules that can rearrange in a certain environment independently from each other called CRR's. As temperature decreases the relaxation time drastically increases and reaches a value of 100 s at T_g ; this is the dielectric T_g (Approximately equal to the calorimetric T_g). At T_g , the structure of the liquid is frozen and the glassy state is reached. Additionally the structural relaxation time becomes very slow in such a way that extremely long time (low frequency) measurements are required for its detection at lower temperature. This abrupt increase of relaxation time with the temperature decrease induces a nonlinear temperature evolution of the relaxation time. The empirical Vogel-Fulcher-Tamman-Heise (VFTH) [58,59] model is usually used to quantitatively describe the temperature evolution of the α relaxation time. Equation gives the VFTH expression:

$$\tau_\alpha = \tau_\infty \exp\left(\frac{DT_0}{T-T_0}\right) \quad (6)$$

where τ_∞ is the dielectric relaxation time in the high temperature limit with a typical value of about $\tau_\infty = 10^{-13} \text{ s}$ (τ_∞ has the physically reasonable value corresponding to angular attempt frequencies for independent rotation of the molecules at high temperatures) [cited in 34], D is a constant and T_0 is the Vogel temperature interpreted as the glass transition of an ideal glass, ie a glass obtained with infinitely slow cooling rate. Although the VFTH equation is generally in good agreement with the relaxation time temperature dependence behavior derived from experimental measurements, a clear physical meaning of this equation is lacking [60]. As illustrated in figure 11, the temperature evolution of the relaxation time (or viscosity) of all glass former does not express the same deviation from an Arrhenius behavior near the T_g . The quantification of this deviation is at the origin of a classification in glass forming system. The latter classification permitted to distinguish two types of behavior: strong (if the temperature evolution of τ_α is close to an Arrhenius nature when plotting $\log \tau_\alpha$ as function of the scaled temperature T_g/T), and fragile (if the scaled temperature evolution of $\log \tau_\alpha$

deviates strongly from the Arrhenius behavior but fits well with a VFTH law). This deviation near T_g is quantified by the so called fragility parameter m or the steepness index defined by Böhmer and co-workers [61] as follows:

$$m = \left[\frac{d \log \tau_\alpha}{d(T/T_g)} \right]_{T=T_g} = \frac{D(T_0/T_g)}{(1-(T_0/T_g))^2 \ln 10} \quad (7)$$

where D is the strength parameter.

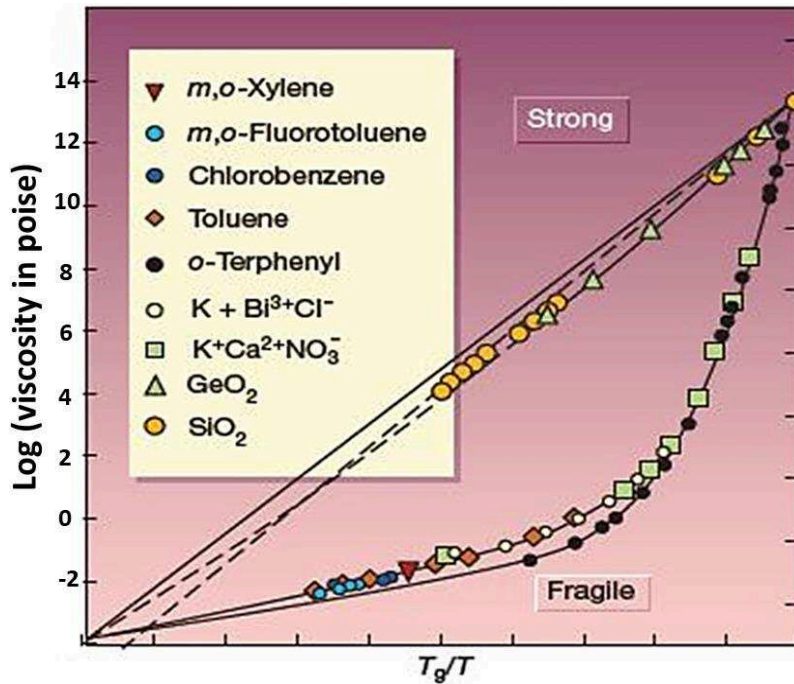


Figure 11: Evolution of the viscosity (log scale) as a function of the scaled temperature T_g/T of different glass formers exhibiting either a strong or a fragile behavior. From [3]

Following the value of the fragility index parameter m , a glass former is considered as strong when $m \leq 30$ and fragile when $m \geq 100$. For the particular case where $30 < m < 100$ the liquid can be considered as an intermediate glass former.

Many attempts were carried out to establish a correlation between the fragility index m and the GFA or the glass stability (GS). It is usually considered that good glass formers mostly present a strong “character”, while fragile systems usually demonstrate marginal GFA [36,62]. This observation is mostly accurate for some classes of material such as metallic and inorganic systems but remains questionable concerning molecular or pharmaceutical compounds [20,63,64]. Due to contradictory features on the hypothetical link between these parameters, no general consensus up to now has been found. Nevertheless, it is universally accepted that strong liquids are resistant to structural change due to temperature fluctuation near T_g ,

whereas fragile systems undergo larger structural reorganization with temperature leading to non-Arrhenius character of the structural relaxation time temperature evolution. Böhmer and coworkers [61] based on a set of experimental results establish a general but rather broad empirical linear relation, linking the structural relaxation KWW shape parameter β_{KWW} to m for several glass forming systems given by:

$$m = 250 (\pm 30) - 230 \beta_{KWW} \quad (8)$$

From equation 8 one can understand that fragile system with high value of m should be characterized by broad relaxation peak (small β_{KWW} value) near T_g , while strong glass former should present low level of non-exponentiality of the dielectric response (β_{KWW} value near 1). As depicted in figure 12 some subgroups of glass forming system deviate from this general trend among which hydrogen bonded organic liquids (mostly aliphatic monohydric alcohols) and orientationally disordered crystals. Therefore there are some special circumstances that rationalize this behavior [61].

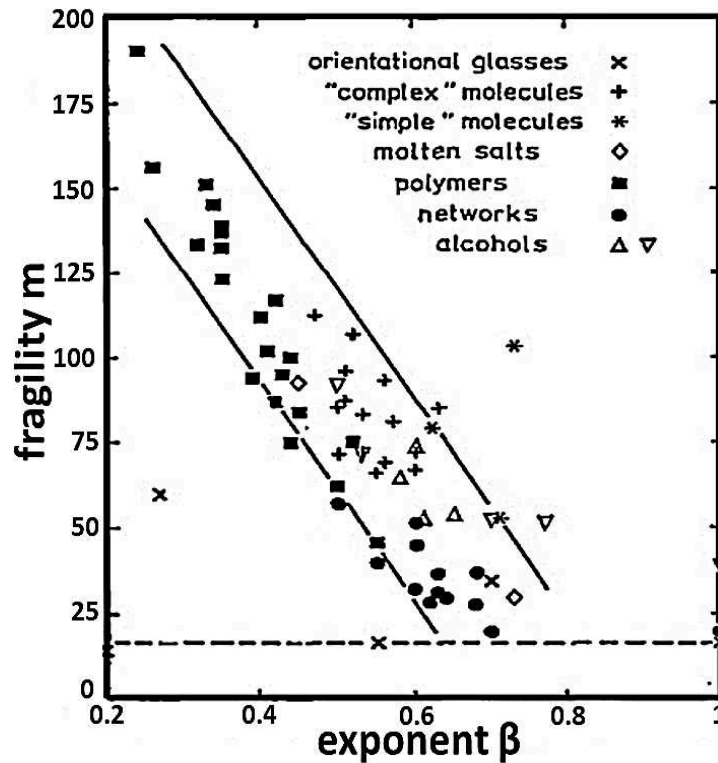


Figure 12: Evolution of the fragility index m as function of the stretching parameter β_{KWW} for several subsystems of glass forming materials at a time scale of 100s. The minimum fragility value $m = 16$ is indicated by the dashed line while the solid lines are calculated according to equation 8. From [61]

b) Molecular mobility in the glassy state: secondary relaxation processes

Upon cooling of an undercooled liquid, the time scale of the structural relaxation process highly increases and becomes extremely long in such a way that it is considered as “frozen” below T_g at the experimental timescale. However, molecular mobility still persists at this low temperature range with characteristic times shorter than that of the α process. These relaxations are mainly called secondary relaxations and known as β, γ, δ and so on (in order of decreasing timescale). Secondary relaxations can also occur in the supercooled liquid state concomitantly with the main α process but at higher frequency or lower temperature. These processes can be related to internal degrees of freedom of the molecule such as reorientation or vibrational motions or side group motions of the constituents [65,66]. The dielectric intensity $\Delta\epsilon$ of secondary relaxation is generally weaker compared to that of α relaxation. Moreover, the shape of the dielectric loss is generally broad and the temperature evolution of the relaxation time follows an Arrhenius law (most clearly below T_g) given by:

$$\tau(T) = \tau_{\infty} \exp\left(\frac{E_A}{k_B T}\right) \text{ or } \tau(T) = \tau_{\infty} \exp\left(\frac{E_A}{RT}\right) \quad (9)$$

where, τ_{∞} is the characteristic time at high temperature limit of the order of atomic vibrations (10^{-11} to 10^{-14} s), E_A is the activation energy of the process representing the potential barrier resisting the molecular rearrangement, k_B is the Boltzmann constant ($k_B = 1.3806488 \times 10^{-23} \text{ m}^2 \text{ kg s}^{-2} \text{ K}^{-1}$) and R is the ideal gas constant ($R = 8.3144621 \text{ J} \cdot \text{mol}^{-1} \text{ K}^{-1}$). Johari and Goldstein (JG) showed that not all secondary relaxations originated from local or internal molecular modes of motions [67,68]. Even molecules lacking flexible branches can present an authentic secondary process. These secondary processes named β Johari Goldstein (β_{JG}) are genuine features in glass former and emanate from the motion of mobile clusters in a frozen environment [21,67,69]. Considering its intramolecular or intermolecular nature, secondary relaxation motions are non-cooperative and localized motions. Yet the nature of these motions and their spatial distribution are still a matter of intense debates from which two main interpretations can arise: according to Johari [21,70] there are structural heterogeneities in the glass and secondary relaxations in general would correspond to motions of molecules situated at local region of low density called “islands of mobility”. The second interpretation considers that the main and secondary processes are continuous and represent the evolution with time of a single process whose long time evolution is assigned to the main process [4,71].

The last interpretation has some affinity with the coupling model introduced by Ngai, in which secondary β_{JG} is considered as located near an independent or primitive process (that implies the motion of the molecule as a whole) precursor of the cooperative main α relaxation [46,72,73]. The characteristic time of the primitive motion τ_0 is approximatively the same as that of β_{JG} motion and expresses as follows:

$$\tau_{JG}(T) \approx \tau_0(T) = t_c^n [\tau_\alpha(T)]^{1-n} \quad (10)$$

where n is the coupling parameter ($n = 1 - \beta_{KWW}$), t_c is the time characterizing the crossover from independent to cooperative fluctuations found to be close to $t_c = 2 \times 10^{-12}$ s for molecular glass formers [70], τ_α is the relaxation time associated to structural relaxation derived from KWW function ($\Phi(t) = \exp\left[-\left(\frac{t}{\tau_{KWW}}\right)^{\beta_{KWW}}\right]$ where $\Phi(t)$ is the dielectric response in the time domain and β_{KWW} the stretching parameter).

c) Peculiar Debye relaxation in some glass forming liquids

Generally, in the supercooled liquid the main motion localized at the lowest frequency range is known as the structural relaxation process associated to the dynamic of glass transition and molecular cooperative motions in an environment of few nanometers [15,74]. However, some glass formers display a slower dielectric relaxation than α process with a Debye like behavior but a non-Arrhenius temperature dependency of the relaxation times as illustrated in figure 13 for 2-ethyl-1-hexanol (2E1H) [75].

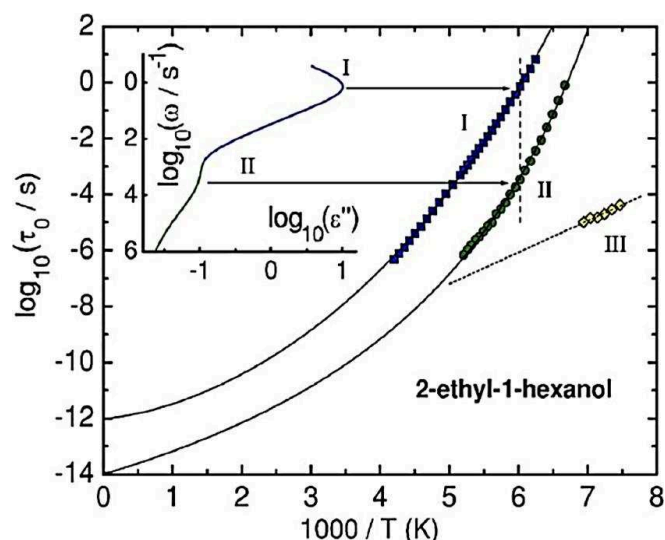


Figure 13: Activation traces of the three dielectric loss peaks of 2-ethyl-1-hexanol 2E1H. Symbols are experimental results; lines are guides only. The inset shows the loss spectrum at $T = 166$ K equivalent to the dashed vertical line in the main figure and identifies the correlation with the activation traces. Process I, II and III refers as the Debye, α and β processes respectively. From Huth et al [75]

The so-called D process has been observed in many hydrogen bonded liquids such as water [76,77], monohydroxy alcohols [78–82], N-mono-substituted amides [83–86], pharmaceuticals [87–90], but also in non-hydrogen-bonded liquids involving rotational isomerism such as methylcyclohexane or other derivatives of cyclohexane highlighted by means of mechanical spectroscopy at ultrasonic frequencies [91]. The latter case originates from interconversion of the cyclohexane ring between two nonequivalent chair conformations, from equatorial to axial orientation of side groups as depicted in figure 14.

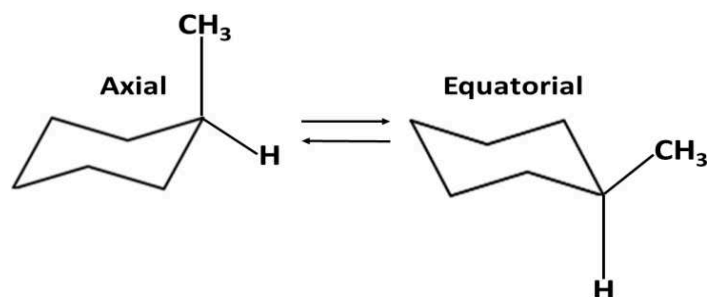


Figure 14: Illustration of the interconversion between the two non-equivalent chair configurations. Adapted from Mandanici et al. [91]

The relaxation time of D-process in cyclohexane derivatives exhibits Arrhenius temperature dependence as shown in figure 15. Thus, the transition from the axial to the equatorial conformation is controlled by an activation enthalpy barrier hindering conformational changes [91]. D-process observed in H-bonded liquids may emanate from different molecular origins compared to those mentioned in cyclohexane derivatives.

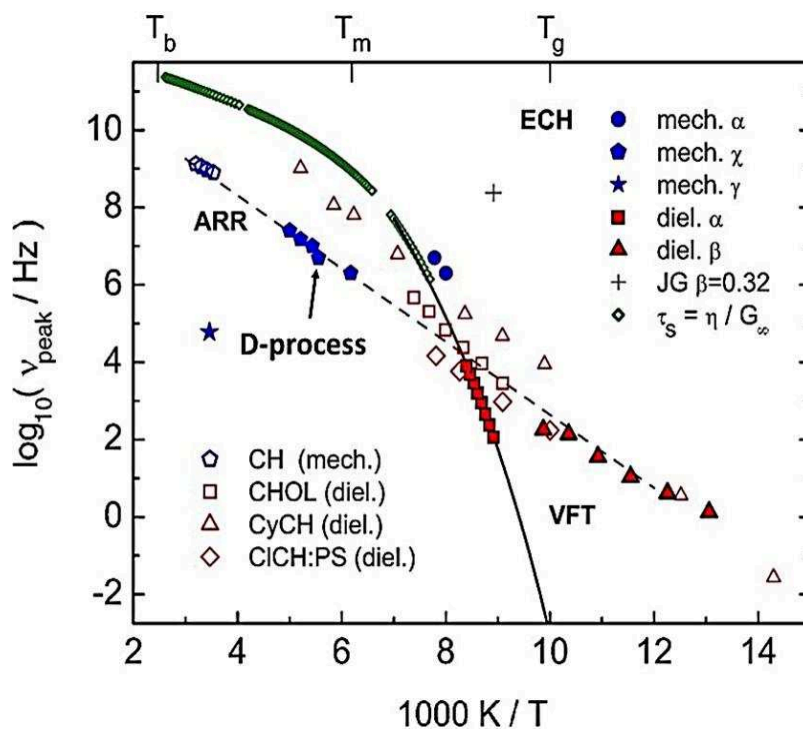


Figure 15: Temperature dependence of the relaxation frequency of the structural relaxation and secondary processes in ethylcyclohexane (ECH) revealed by mechanical and dielectric spectroscopies. The Debye process revealed by mechanical spectroscopy is indicated by the arrow. The characteristic temperatures T_b , T_m and T_g refer as the boiling point, the melting point, and the glass transition temperature respectively. More details are reported in ref [92]

The D-process observed in monohydroxy alcohols (or mixtures) and secondary amides (or mixtures) usually show very high dielectric intensity (almost 90% of the global dielectric polarization). The case of 2-ethyl-1-hexanol (2E1H) [81] and mixture of N-ethylacetamide (NMA) and N-methylformamide (NMF) [86] are displayed in figure 16. Common practice usually attributes the prominent and slowest dielectric process to the structural relaxation. Regarding the exponential nature of the dielectric loss peak and the non-correlation of the relaxation time with the dynamic of structural relaxation, the slowest process in 2E1H and NMA_{0.4}NMF_{0.6} are assigned as the exponential Debye process (single relaxation time).

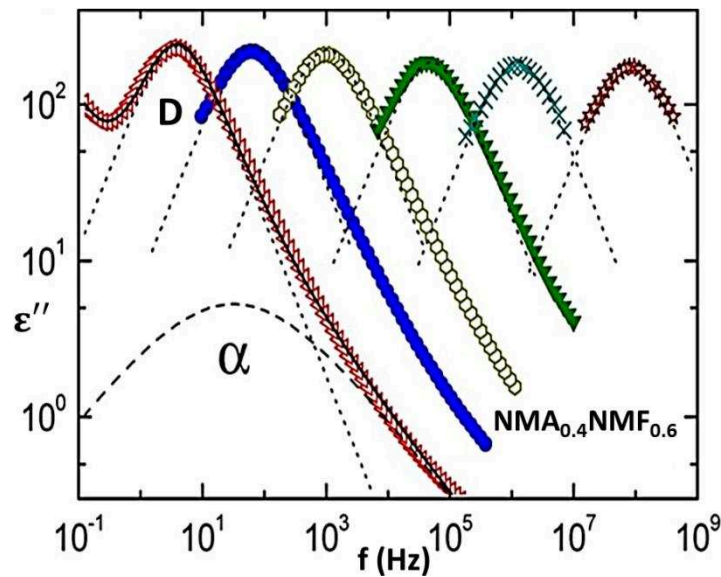
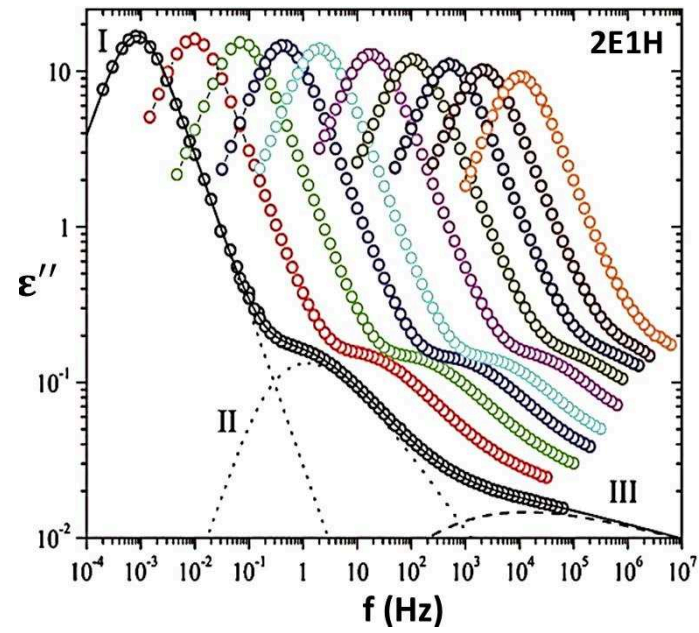


Figure 16: Dielectric loss peak of 2-ethyl-1-hexanol [81] and a mixture of N-methylacetamide with N-methylformamide as a function of the frequency [86]

More surprisingly, even though the dielectric intensity exceeds by many orders of magnitudes that of the structural relaxation, it does not contribute in the calorimetric signal [93] as displayed in figure 17.

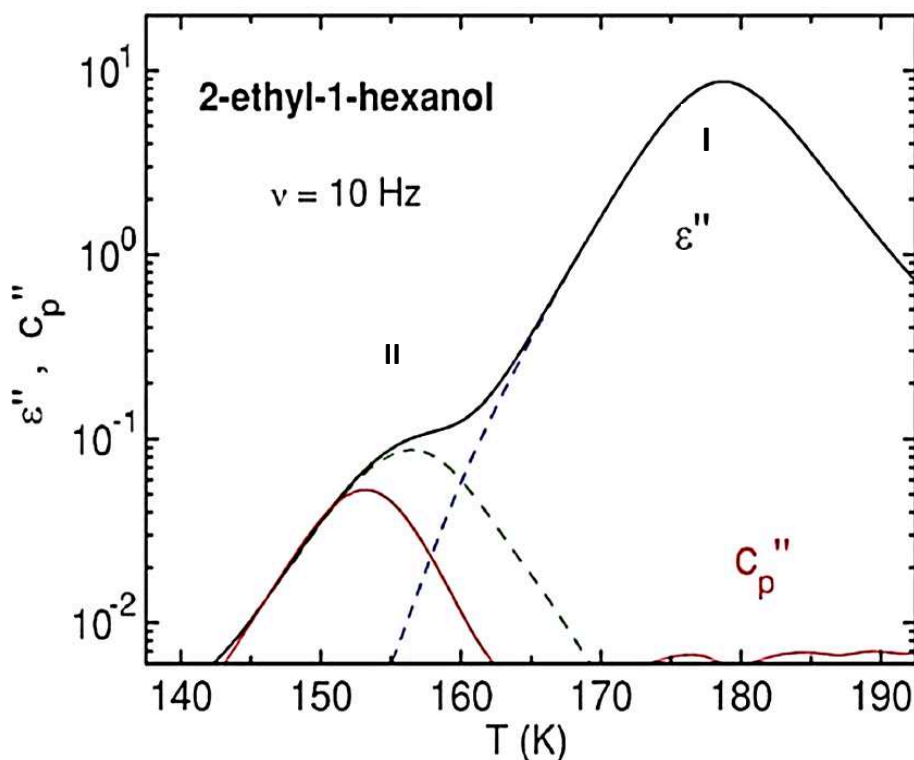


Figure 17: Loss components ϵ'' and C_p'' for 2E1H vs temperature, both measured at a frequency of $\nu = 10$ Hz. The C_p'' curve is shifted arbitrarily along the ordinate scale. The dashed lines separate the dielectric signal into the Debye (I) and non-Debye (II) contributions. From Huth et al. [75]

Unlike the absence of a calorimetric signature, the Debye process can exhibit a mechanical signal. Gainaru and coworkers [94] evidenced by high resolution shear mechanical spectroscopy the mechanical signature of D process in two monohydroxy alcohols (2E1H and 4M3H) close to the glass transition region as shown in figure 18. The dielectric contribution of the structural relaxation process to the global polarization in these systems is lower than 5%, which means that only few molecules contribute to the dynamic of the glass transition (see figure 16). It is counter intuitive to imagine that the orientational diffusion of this small population of molecules can control alone the viscosity or structural relaxation of the supercooled liquid. Nevertheless the origin of D-process and its possible implication in the dynamic of the glass transition is still matter of intense debates even though numerous models have been proposed to explain its microscopic origin.

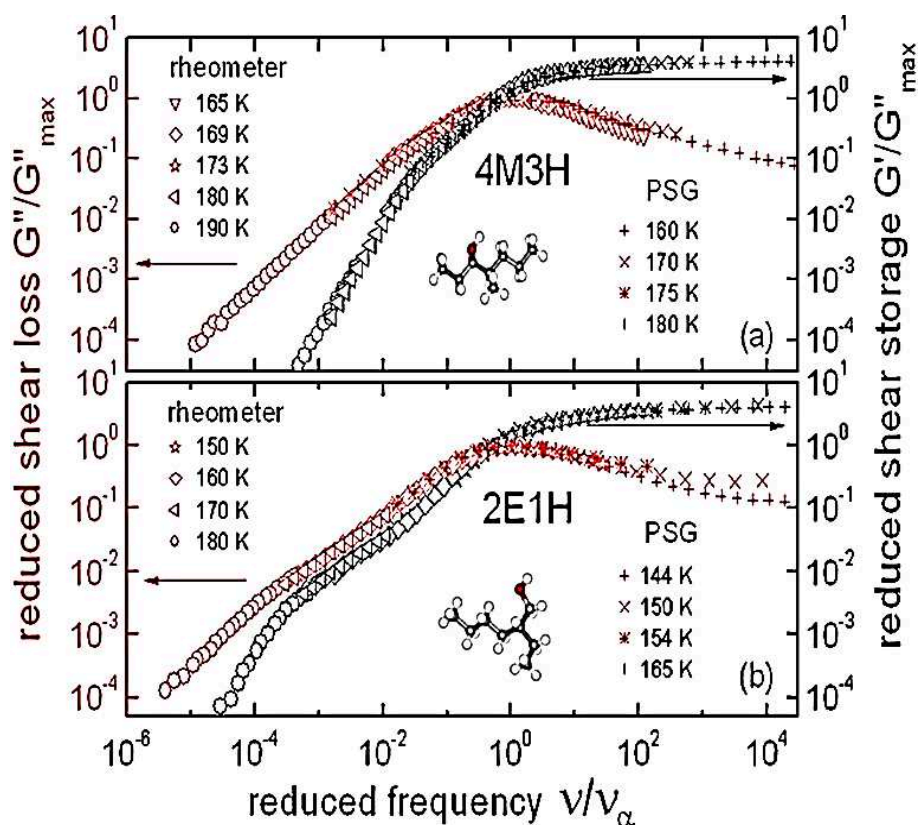


Figure 18: Master plots for the real part (scale on the right side) and the imaginary part (scale on the left side) of $G^(\nu)$ showing normalized shear moduli for (a) 4M3H and (b) 2E1H. From Gainaru et al. [94]*

- **Microscopic origin of Debye Process: Case of Monohydroxy Alcohols and Secondary Amides**

Monohydroxy alcohols and secondary amides can be generalized as HB forming systems. All the available theories and models around the Debye process are based on this general feature. Therefore the above features described for the case of monohydroxy alcohols and secondary amides do not occur in every liquids that involve hydrogen-bonding [95]. For example, Debye peak is not reported in most polyalcohols or diols [96,97]. Moreover, it has been observed that some monohydroxy alcohols can lack this Debye process, e.g., salol, 2-phenyl-1-ethanol [98], 1-phenyl-1-propanol [99], and 1-phenyl-2-propanol [100]. The explanation of these exceptions is based on steric hindrances that prevent the capability of forming an intermolecular hydrogen-bonded network [95]. Consequently, the occurrence of the Debye process implies that the hydroxyl (OH) or amide (NH) groups should be sterically available in order to build intermolecular hydrogen-bonded networks. Additionally associated liquids can

be considered as a special class of liquids. Due to the strong directional hydrogen bonding, they tend to be locally more organized than ordinary liquids [101]. It was recognized early through x-ray diffraction experiments [102], that alcohols have very specific local molecular arrangements that show up as a pre-peak in the structure factor (see figure 19). The existence of the inner peak has been mostly associated with a manifestation of H-bonding tendency in such liquids [93,103]. This viewpoint is also dominantly found in several light scattering experiments [104,105].

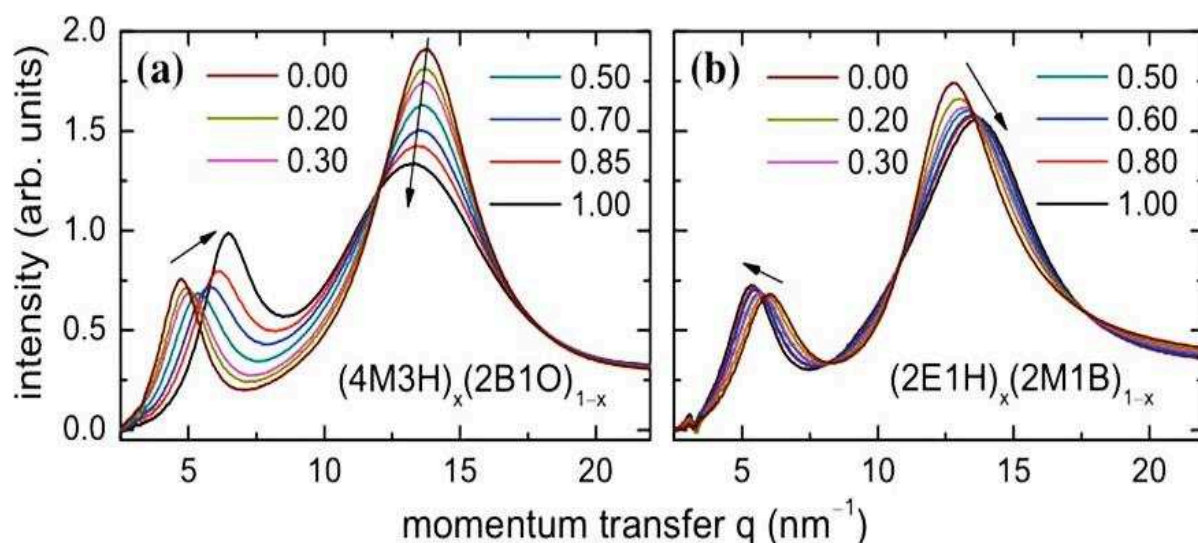


Figure 19: X-ray diffraction patterns of (a) $(4M3H)_x(2B1O)_{1-x}$ and (b) $(2E1H)_x(2M1B)_{1-x}$ recorded at room temperature for several concentrations x . The compositional evolution of the prepeaks as well as of the mainpeaks of the two mixture series is different. The arrows highlight how the prepeak and mainpeak maxima evolve for increasing concentrations x . From [106]

On the other hand, spectroscopic measurements [107] put a clearer accent on clusters as independent entities, seen both in pure and mixed alcohols. From the theoretical side, most approaches are made by simulation techniques [105–108], where the accent is put more on modeling interactions and fitting thermodynamic properties rather than clustering. It is possible to gather some information on the clustering for these systems from quantum calculations [109], and corroborate them with spectroscopic data [107]. Such approaches reveal the rich variety of cluster shapes (see figure 20), usually involving a number of molecules around five [101].

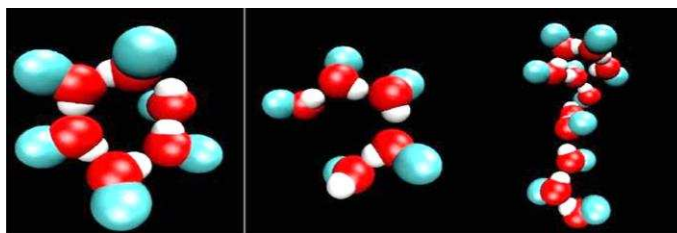


Figure 20: Characteristic clusters for methanol showing cyclic and linear configurations. From [101]

Several models based on dielectric spectroscopy measurements try to give a general account of the microscopic origin of D-process in monohydroxy alcohols and secondary amides regarding the possible structural correlation among neighboring molecules linked by H-Bonds: **The “wait and switch” model [95,110,111]** in which the relaxation time is governed by the period for which a set of hydrogen bond partners (within the hydrogen network) has to wait for favorable conditions. As the energy minimization condition is fulfilled the reorientation of a molecular permanent dipole can exist. These conditions are provided by the reorientation of an additional molecule or group which firstly tends to lower the potential energy barrier for reorientation and at the same time, offers a site for the formation of a new hydrogen bond (see figure 21). By forming a branched (bifurcated) hydrogen bond and offering a site for the formation of a new bond, this neighbor tends to flatten the potential energy barriers [111], as indicated by the dashed energy curve in figure 21.

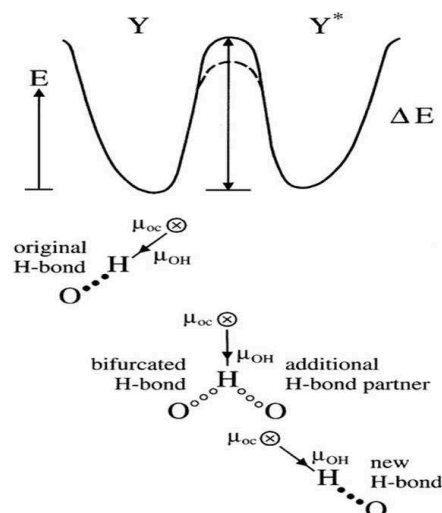


Figure 21: Sketch of a potential energy barrier separating two di-rections (Y ; Y^*) of the permanent dipole moment I , and sketch of a bifurcated hydrogen bond (bfhb) in a chain-like alcohol cluster. The dashed curve shows the reduction in the potential energy ΔE due to the additional neighbor near the chain and the bfhb situation. From Kaatz et al [111].

The “dipole inversion by cooperative rotation of OH groups engaged in the multimers” model [112] assuming that liquid alcohol molecules exist in association equilibria, involving both hydrogen-bonded ring dimers and linear chain n-mers, and each of the n-mers alters or reverses its dipole moment by successive rotation of the individual hydroxyl groups.

“self-restructuring transient-chain” model, where molecules break off from or add to the ends of the chain promoting slow rotations of the effective dipoles of the chain [113,114]. As previously reported, several shapes of clusters formation are possible (cyclic and linear configurations). But regarding the high dielectric intensity of D-process, it is more obvious that the effective dipole responsible of the main dielectric response is made up of linear HB chains. The D-process is analogous to the dynamical behavior of the “normal mode” observed in some polymers [94]. According to Stockmayer model [115], the normal mode reflects the reorientation of the total dipole moment of the entire polymer chain (i.e., the sum of the segmental dipole moments parallel to the polymer chain), which is proportional to the distance vector r between the ends of the polymer chain (see figure 22).

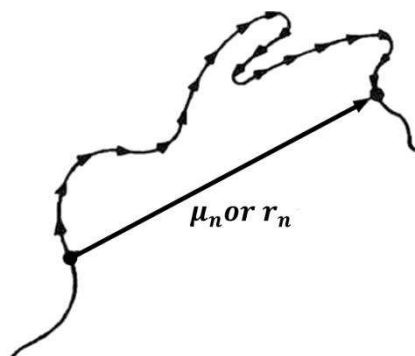


Figure 22: Schematic representation of chains with segmental dipole moments parallel to the polymer chain backbone. Correlation of dipole vector μ_n with displacement vector r_n from [115]

It is important to quote that in polymer the segmental chains are permanently present, while in the case of alcohols or secondary amides the existing chains are transient (the lifetime of an HB being of the order of few picoseconds) [116,117]. The “self-restructuring transient-chain” model proposed by Gainaru *et al.* [114] takes into consideration this transient character of the HB attachment or detachment events (see figure 23).

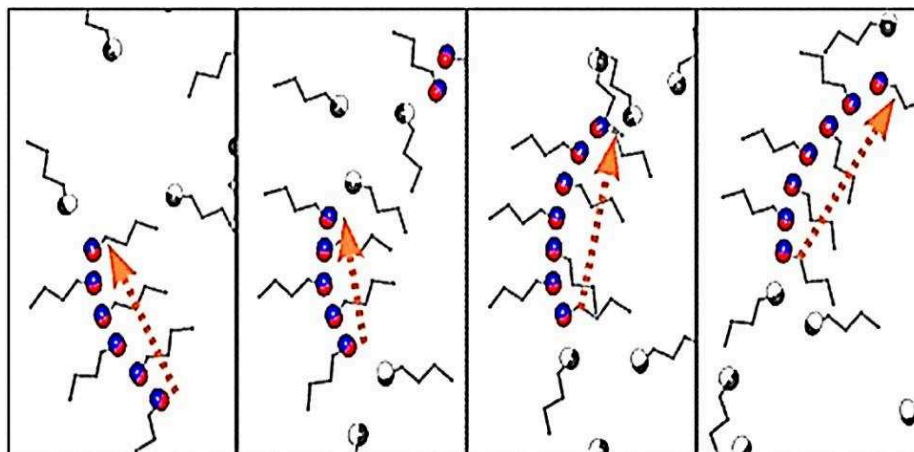


Figure 23: Schematic illustration of the transient chain model. Mutually bonded OH groups are shown in color. The sequence of frames is meant to visualize how molecules attach to the chain and detach from it. The dotted arrows highlight the end-to-end vector of the self-restructuring, transient chain. Its reorientation, corresponding to the Debye process, is obviously very slow on the scale set by the elementary steps. From [114]

For polyalcohols or different HB forming liquids, with each molecule carrying several OH or NH groups, branched structures result. Hence, a well-defined end-to-end vector does not exist. Merely, a component dipole moment may be associated with each temporarily existing branch. However, the unsynchronized OH or NH switching occurring in such a multiple-branch structure will lead to an effective mutual cancellation of the component moments. Thus, with a vanishing net dipole moment a supramolecular dielectric signature does not arise from such branched structures, and a Debye process is not expected in harmony with the experimental situation.

● The D-process in Ibuprofen and Flurbiprofen

The specific case of ibuprofen and flurbiprofen D-relaxation is worth mentioning. The microscopic origin is typically different from the case of monohydroxy alcohols or secondary amides. The Debye process in the profen family is of low magnitude and observed as a weak shoulder at lower frequencies than the structural relaxation as displayed in figure 24. Even though its relaxation time illustrates a non-Arrhenius temperature dependence, this process emanates from physical mechanisms different from what has been presented up to now. From the MD simulations, it was found that the cyclic structures present in ibuprofen or flurbiprofen are characterized by longer lifetimes, smaller dipole moments and low Kirkwood correlation

factors. This might imply that the hydrogen bonded cyclic structures are associated with this Debye peak [87,89,90].

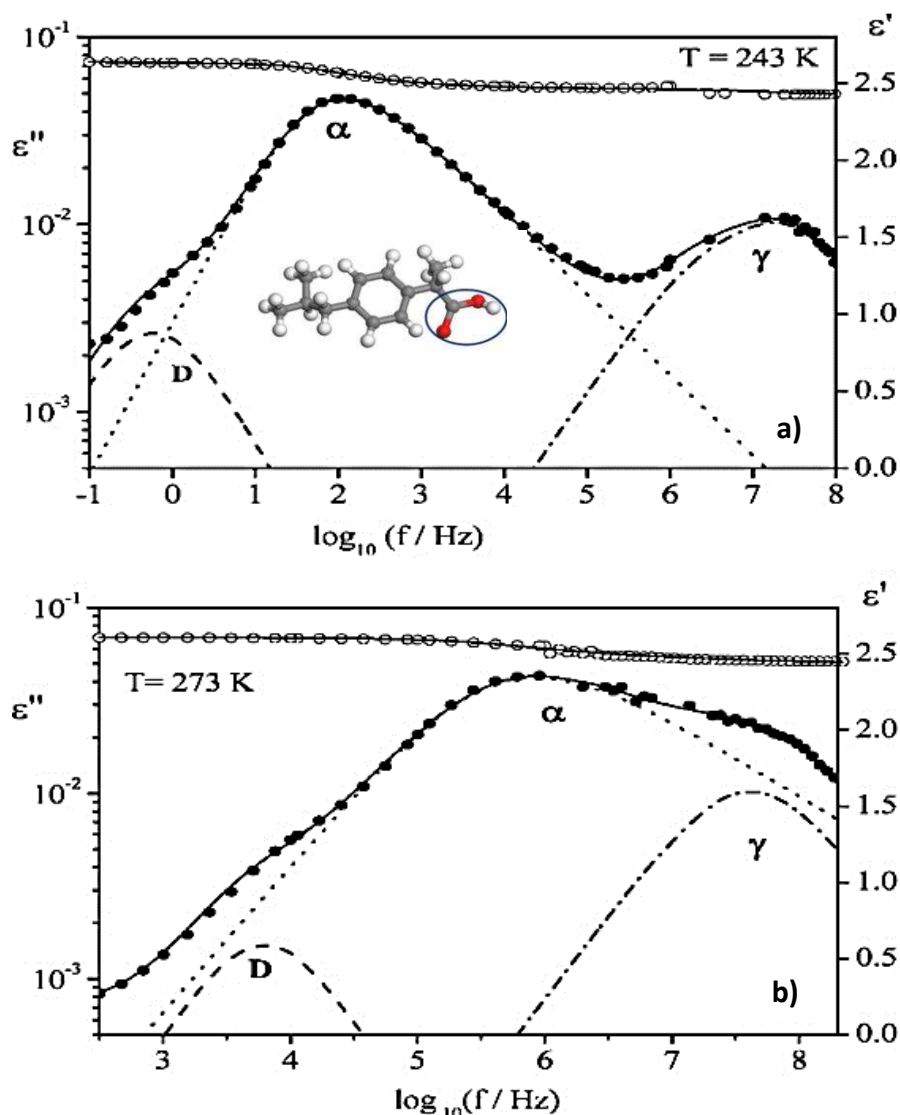


Figure 24: Ibuprofen real (open circles) and imaginary (filled circles) parts of complex permittivity at (a) 243 K, and (b) 273 K. The solid lines represent the overall fit and the dashed lines the individual fit-functions. From [87]

The carboxylic $\text{O}=\text{C}-\text{O}-\text{H}$ group of ibuprofen can take two conformations as illustrated in figure 25. HB intermolecular associations play an important role on the stabilities and interconversion kinetics of the Cis and Trans conformations. Indeed, the Debye-like process is associated to the dynamic of the cis-trans conversion of the carboxyl group influenced by the intermolecular HB associations [89].

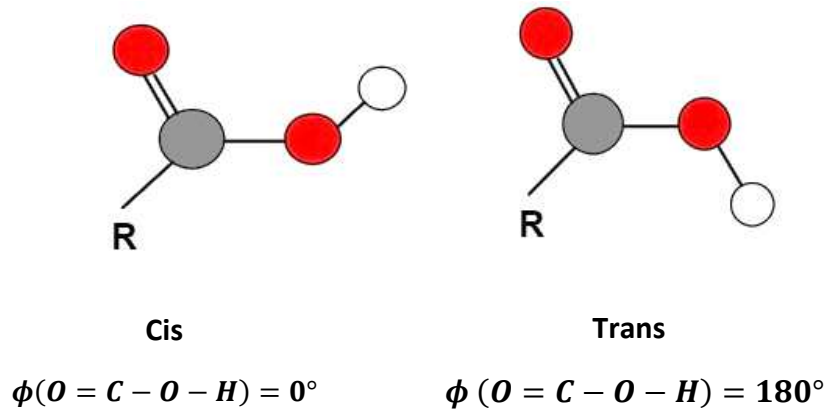


Figure 25: Schematic representation of the two conformations of the O=C-O-H group. From [90]

- **Temperature Dependence of D-Process Relaxation Time**

In most cases the temperature dependence of D-process follows the non-Arrhenius behavior. The model of “fluctuating free volume” developed in the years 60’s successively by Litovitz & Mc Duffie [118], Anderson & Ullman [119], and Johari & Dannhauser [120] brought a physical description of the single exponential correlation time for D-process and the distribution of the relaxation time of the structural relaxation. This model assumes that structural relaxation must be fast compared to dipolar reorientation. In this way the surroundings of all molecules are the same on a time average. This situation leads to a single experimental correlation time which reflects a weighted average of the reorientation probabilities in each of the many environments. However, because of the hydrodynamic aspects of the motion that affects the end-to-end distance and orientation, the correlation time of the chains will be governed for the most part by viscosity and its temperature dependence [121]. As a result, the activation traces of Debye and structural peaks are approximately parallel. Additional temperature effect may result from the temperature-dependent partitioning into different chain lengths, rings, and other structures. Because D process is slow compared with the primary structural relaxation process, dynamical heterogeneities will have averaged out and only a single time constant prevails; i.e., the Debye nature of this polarization process originates from the environmental fluctuation being fast compared with the Debye relaxation time [121].

I.6 Physical Aging Phenomenon

As previously mentioned, molecular mobility in glass forming systems still persists below T_g even though the structure of the liquid is considered as frozen at the laboratory time scale. The glassy state is literally an out of equilibrium state. As a consequence, a variety of intriguing phenomena such as physical aging, memory effect or rejuvenation are observed [4,122]. When stored below T_g , the out-of-equilibrium glass will gradually relax towards an equilibrium state. The relaxation toward equilibrium is a time dependent process that implies a modification in thermodynamic properties [123,124] such as enthalpy (entropy), specific volume, refractive index, and mechanical properties such as density [125,126], brittleness or toughness [127,128], as well as dielectric properties such dielectric strength and dielectric loss [122]. Figure 26 a) illustrates the enthalpy H time evolution for an initially prepared glass, aged for t_1 and t_∞ at a given aging temperature T_a . The initially glass formed presents a high enthalpy value. Therefore when the glass is stored below T_g at an aging temperature T_a it slowly evolves towards equilibrium by lowering its enthalpy, this phenomenon is called physical aging or enthalpy relaxation. For identically prepared glasses, the larger the deviation from T_g , the slower the aging kinetic. Theoretically after long aging time, the aged glass can reach the lowest enthalpy value H_∞ synonym that the liquid equilibrium (liquid enthalpy line extrapolated in the glassy state) has been achieved. As the aging temperature is lowered, longer times are required to reach equilibrium. Calorimetric approaches are usually used when it comes to investigate the kinetics of physical aging. When an aged glass is heated above the glass transition temperature, an overshoot peak referring to enthalpy relaxation is generally observed. As the aging time increases, the overshoot peak is shifted towards higher temperatures and its magnitude increases up to a limit value at which equilibrium is normally reached (generally after very long aging time). The continuous shift of the overshoot peak towards higher temperatures is related to the fact that upon aging some degrees of freedom are lost, the residual free volume and enthalpy are lowered, and thus, the aged glass possesses less molecular mobility compared to the unaged glass. Therefore the lost properties are recovered upon heating at temperature higher than T_g where molecular mobility is high enough to allow it [4]. Figure 26 b) displays the heat flow signals of the unaged (t_0) and aged glasses (for t_1 and t_∞) as a function of temperature. From these curves it is possible to evaluate the recovered enthalpy upon heating which is equivalent to the enthalpy loss during

the storage time. The calculation procedure consists in integrating the difference between the specific heat of the aged and unaged scans according to the following equation [51]:

$$\Delta H(T_a, t_a) = \int_{T_1}^{T_2} [C_p^a(T) - C_p^r(T)] \cdot dT \quad (11)$$

in which $C_p^a(T)$ and $C_p^r(T)$ are the specific heat of aged and unaged samples respectively, and T_1 and T_2 are arbitrary temperatures below and above T_g . Under the assumption that thermodynamic equilibrium is reached for an infinite aging time, the expected enthalpy loss ΔH_∞ extrapolated from the equilibrium melt depends on T_a , T_g and on the heat capacity step at T_g , ΔC_p according to the following relation:

$$\Delta H_\infty = \Delta C_p \cdot (T_g - T_a) \quad (12)$$

The kinetic of enthalpy relaxation can also be investigated in terms of the change in fictive temperature. This notion was introduced by Tool in 1931 [129]

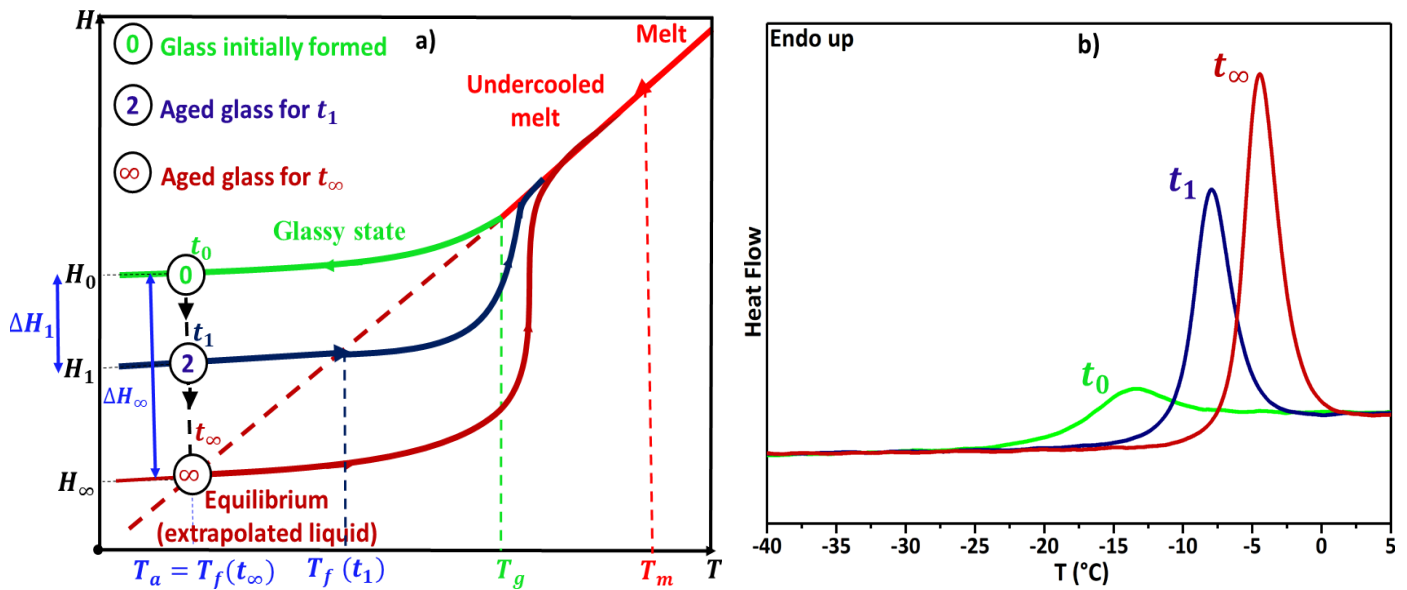


Figure 26: a) Enthalpy vs time evolution of an aged glass at T_a for three aging times (t_0 , t_1 and t_∞) b) Temperature evolution of the heat flow after aging is accomplished at T_a for t_0 , t_1 and t_∞ .

The fictive temperature is defined as the actual temperature T_f of the same compound in the equilibrium, metastable supercooled state whose structure is expected to be similar to that of the glassy state. At T_f , the thermodynamic properties (the enthalpy in the present case) of

the heated glass intercept with those of the metastable equilibrium. As the aging time increases, the glass evolves towards equilibrium while T_f decreases to a limit value equal to that of the aging temperature T_a as equilibrium is reached. The calculation of T_f is performed according to Moynihan's method (see figure 27) by solving equation 13 also known as the equal area rule expressed as follows:

$$\int_{T_f}^{T > T_g} [C_{p,liq} - C_{p,glass}] \cdot dT = \int_{T < T_g} [C_p - C_{p,glass}] \cdot dT \quad (13)$$

Monitoring the time dependency of T_f can therefore give information on the enthalpy recovery kinetic.

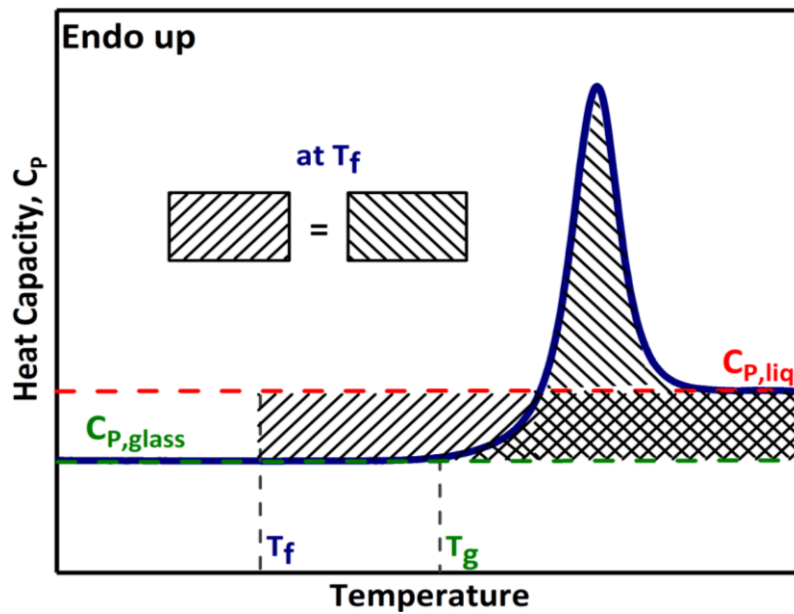


Figure 27: Calculation of T_f by application of the “equal area rule” on $C_p(T)$ curve.

II- Chirality

II.1 A Brief History of Chirality

The term “*chiral*” was introduced for the first time in 1884 by Lord Kelvin (also known as Sir William Thomson) in his Baltimore Lectures on Molecular Dynamics and the Wave Theory of Light. The term was defined in the following manner: “*I call any geometric figure, or group of points, chiral, and say it has chirality, if its image in a plane mirror, ideally realized, cannot be brought to coincide with itself*” [130]. Etymologically the term chiral derived from the Greek “*cheir*” referring to hand. The pair of hand is the most familiar expression of chirality as depicted in figure 28. Some molecules act like hands and are considered to be chiral. A “chiral” molecule and its mirror image are enantiomers of each other. When the image objects can be brought to superimposed they are considered as “achiral”. For a pair of enantiomers, no difference in the interatomic distances exists. Therefore they possess the same geometrical parameters. Consequently, enantiomers cannot be differentiated in terms of geometry but in terms of direction (left, right, clockwise or anticlockwise, etc.), i.e. in terms of vector rather than scalar quantities. Both enantiomers have the same physical properties (melting point, melting enthalpy or entropy, glass transition, solubility in achiral media, refractive index, IR, RMN, Raman, UV spectra, etc) same reactivity in achiral media, but differ in terms of sign and not in magnitude in some vector properties such as optical rotation, optical rotary dispersion and circular dichroism [131]. Therefore, chiral molecules have this particular ability to interact with polarized light: one of the two enantiomers rotates the plan of polarized light to the right (or clockwise), whereas the other enantiomer rotates the plan of the polarized light to the left (or counter clockwise) [130–136].

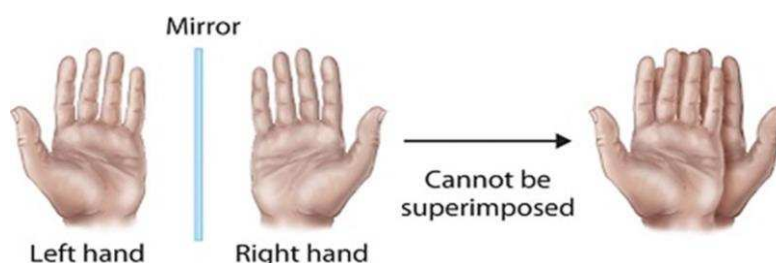


Figure 28: The left hand and the right hand are image of each other in a mirror but cannot superimposed [137].

The highlighting and understanding of chirality result from several experiences and observations over more than 50 years. In 1808 while looking from his home through a calcite crystal at the light from the sunset reflected from a window in Luxembourg Palace, Etienne-Louis Malus discovered that the light that was reflected from the castle windows was polarized. This discovery three years later permitted to Arago to evidence the optical rotation of quartz crystals. One year later inspired by Arago's discovery, Biot showed that there are two forms of quartz, one dextrorotatory and the other levorotatory. In 1815 Biot extended these observations to organic substances in solution such as glucose, tartaric acid, camphor etc. It seemed obvious for him that the optical activity of quartz or other crystals result from the crystalline packing in the solid state while in solution, it results from specific properties of individual molecules [131,135,136]. It is only in 1848 that a clear understanding of the optical activity phenomenon was brought by Louis Pasteur. In 1820 Paul Kestner, a French manufacturer of tartaric acid, synthesized a compound having exactly the same composition than the tartaric acid but which did not rotate the polarized light, contrary to the tartaric acid prepared from wine. Joseph Louis Gay-Lussac gave it the name by which it is now known, racemic acid (*acide racémique*, from the Latin *racemus*, for a bunch of grapes). In 1831 Jöns Jacob Berzelius cited these acids as examples of compounds having the same chemical composition but different properties, a phenomenon that he called *isomeri* (isomerism from the Greek, *isos* and *meros*, composed of equal parts). In 1844 Mitscherlich, one of the most distinguished crystallographers at that time, made the racemic acid enigma to be more mysterious. He examined the sodium ammonium salts of tartaric and racemic acids and found them to be identical in crystalline form except that the former was optically active and the latter was not. Mitscherlich thought that the *"nature, the number, the packing and the distance between the atoms are the same for both samples"*. Therefore, how comes that both compounds are identical and different at the same time? Pasteur noticed an unusual anomaly that Mitscherlich had overlooked and put an end on to this mystery in 1848 [135]. A dozen years after this revolutionary discovery Pasteur recalled it as follows: *"I found...that the tartrate was hemihedral..., but strange to say the paratartrate was hemihedral also. Only the hemihedral faces which in the tartrate were all turned the same way were, in the paratartrates inclined sometimes to the right and sometimes to the left.... I carefully separated the crystals that were hemihedral to the right from those hemihedral to the left, and examined their solutions separately in the polarizing apparatus. I then saw with no less surprise than pleasure*

that the crystals hemihedral to the right deviated the plane of polarization to the right, and that those hemihedral to the left deviated it to the left; and when I took an equal weight of each of the two kinds of crystals, the mixed solution was indifferent towards the light in consequence of the neutralization of the two equal and opposite individual deviations" [132–134]. Pasteur had mechanically separated the two types of sodium ammonium paratartrate (racemate) crystals from an equimolar mixture of dextrorotatory and previously unknown levorotatory tartrates (see figure 29)

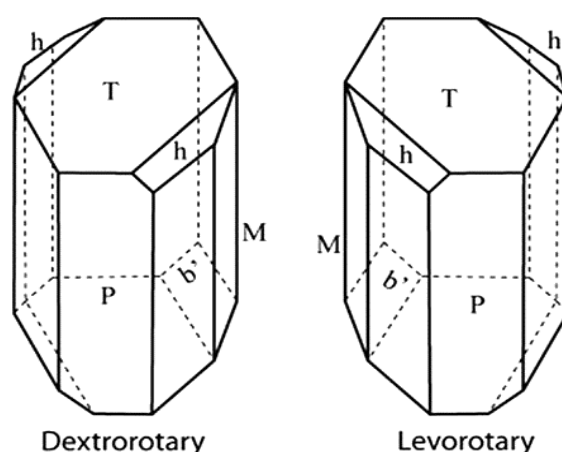


Figure 29: Hemihedral crystals of sodium ammonium tartrates by Pasteur. From [134]

However, there were two elements of sheer luck in his discovery. First, with the possible exception of the sodium potassium salt, the sodium ammonium salt is the only inactive tartrate that undergoes crystallization of the two antipodes in different crystal lattice and can be mechanically resolved in this manner because the two forms of tartaric acid (see figure 30 a)) and the two forms of all its other salts combine to form crystalline racemic acids and racemates, respectively, which show no hemihedrism or optical activity (see figure 30 b)). Secondly, Pasteur carried out his experiment in the moderate Parisian climate rather than in a Mediterranean or tropical hot one. In the latter case he would not have made his revolutionary discovery, for it was later found that the two sodium ammonium tartrates unite to form a single inactive, holohedral racemate at temperatures above 26° C [134].

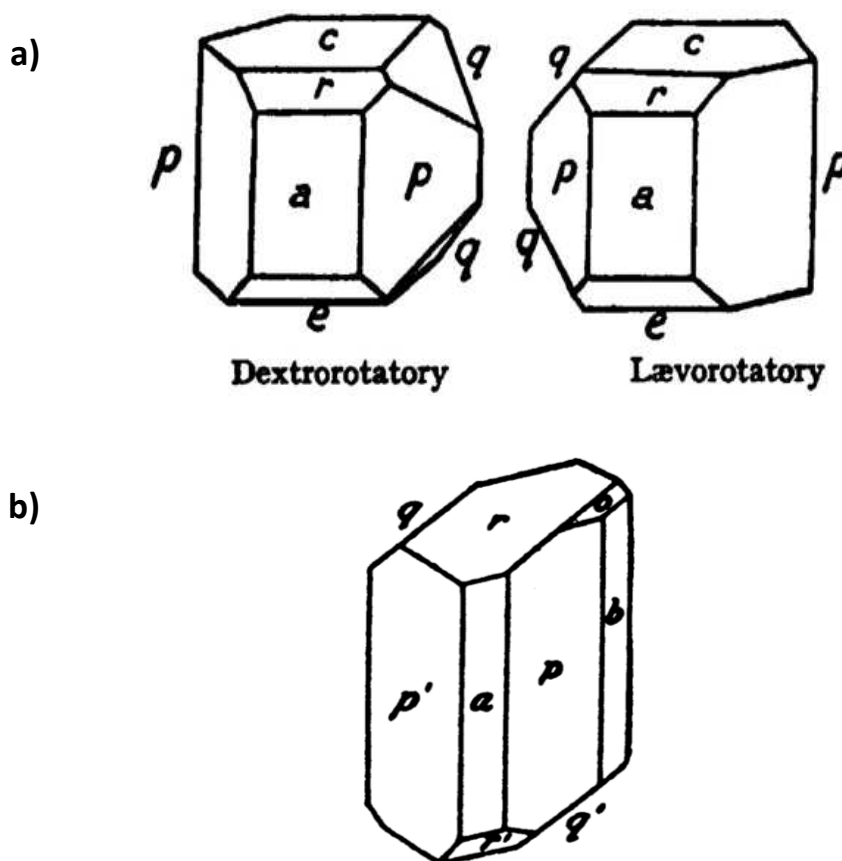


Figure 30: a) Hemihedral crystals of tartaric acid b) Holohedral crystals of racemic acid adapted from [134]

Chirality manifests itself in both molecules and crystals, and its origin lies clearly in molecular architecture. The analogy between crystals and molecules in this context was first caught by Pasteur, who realized that the nonidentity of the crystal (or molecule) with its mirror image was due to what he called dissymmetry. Although Pasteur himself conjectured on different structural arrangements, including tetrahedral, he was unaware of the tetrahedral asymmetric carbon postulated simultaneously and independently by Jacobus Henricus van't Hoff and Joseph Achille Le Bel in 1874. They proposed a structural theory from which chirality was due to a spatial arrangement around a tetrahedral carbon. If a carbon is linked to four different substituents, the tetrahedron will be irregular and therefore become a chiral center [130,135–138].

II.2 Stereochemical Nomenclature of Chiral Compounds

The use of the term “chiral” remained ignored for nearly one century and was reintroduced by Cahn Ingold and Prelog (CIP) around the mid-1960s, to define a geometrical model devoid of certain symmetry elements, with the exception of an axis of rotation [138]. The CIP priority rules named before their authors (Cahn, Ingold and Prelog) established a stereochemical nomenclature in order to describe the configuration of the asymmetric carbon [139]. After the substituents of a stereocenter have been assigned their priorities, the molecule is oriented in space so that the group with the lowest priority is pointed away from the observer. If the substituents are numbered from 1 (highest priority) to 4 (lowest priority), then the sense of rotation of a curve passing through 1, 2 and 3 distinguishes the stereoisomers. A center with a clockwise sense of rotation is an *R* (*rectus*) center and a center with a counterclockwise sense of rotation is an *S* (*sinister*) center [140] (see figure 31). The names are derived from the Latin for 'right' and 'left', respectively.

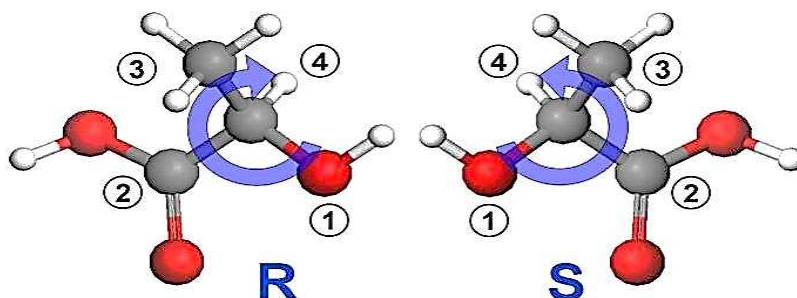


Figure 31: Absolute configurations of enantiomers of 2-hydroxypropanoic acid according to the CIP priority rule [cited in 141].

An enantiomer can be labelled (+) when it rotates the plan of the polarized light to the right, and (-) when it rotates the plan of the polarized light to the left. The (+) and (-) compounds have also been termed d- and l-, respectively for dextrorotatory and levorotatory.

Amino acids and sugars can be labelled *D*- or *L*-, depending on whether the substituent with the highest priority is to the right or to the left in the Fisher projection of the molecule (see figure 32).

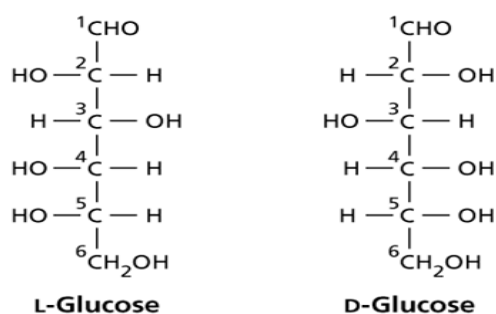


Figure 32: Fisher projection of L- and D- Glucose [cited in 141]

Different experimental methods such as Polarimetry, Optical Rotary Dispersion (ORD), and Circular Dichroism (CD) are used to determine the handedness of a chiral molecule based on the interaction between a chiral stereogenic center and the incident polarized electromagnetic radiation. Historically the oldest method used to determine the amount of each enantiomer for a given sample is polarimetry. Optically active samples deviate the polarization plane over a specific rotation angle α . The rotation angle can be positive (+) or negative (-) depending on whether the rotation is clockwise or counterclockwise relative to an observer placed at the exit of the polarized light. The quantification of the specific rotation is given by Biot law expressed as follows:

$$[\alpha] = \frac{\alpha}{lc} \quad (14)$$

where $[\alpha]$ (deg. cm²/g) is the specific rotation depending on the nature of the solvent, the wavelength of the polarized light and temperature T $[\alpha]_{\lambda}^T$, α measures the rotation expressed in degrees, l is the path length in decimeters, c the concentration of the solution in g/mL. When the specific rotation of an optical pure sample $[\alpha]_0$ is known, it becomes possible to determine the optical purity of a mixture of both enantiomers expressed as follows:

$$\text{Optical Purity} = \frac{\text{observed rotation of the mixture}}{\text{specific rotation of a enantiomer}} \times 100 (\%) \quad (15)$$

The optical purity is thus equal to the percentage excess of the major enantiomer over the minor enantiomer. The term, “enantiomeric excess”, or “ee” for short form, is equivalent to the optical purity and is actually used far more often for expressing the enantiomeric purity of a mixture given by:

$$ee = \frac{|r-s|}{r+s} \times 100 (\%) \quad (16)$$

r and s are the respective mass fraction of R and S enantiomers such that $r + s = 1$. Like the optical purity, the ee is highly dependent of the solvent nature and the temperature of measurement. When the ee=100% the sample contains only one enantiomer, the latter is named enantiopure. For ee=0% the sample contain an equal proportion (50/50 ratio) of both enantiomers and the composition is consider as racemic. If $0\% < ee < 100\%$ the sample is reported to be at the scalemic composition. In the next section we will focus on the thermodynamics of chiral compounds through the study of the main phase equilibria that could exist in the solid state for a pair of nonracemizable enantiomers (nonracemizable: no conversion of an enantiomerically pure mixture to a situation where both enantiomers are presents).

II.3 Thermodynamics of Chiral Compounds

II.3.1 Gibbs Phase Rule and Binary Phase Diagram between two Enantiomers

A system is in equilibrium when thermal, chemical and mechanical equilibria are achieved. That means that for a system of n components, the intensive parameters, i.e. the temperature T (thermal equilibrium), the pressure P (mechanical equilibrium) and the chemical potentials μ_i (chemical equilibrium for the component i), are the same in all phases. Gibbs Phase rule states that "If the equilibrium between any number of phases is not influenced by gravity, or electrical, or magnetic forces, or by surface action, but are influenced only by temperature, pressure and concentration, then the number of degrees of freedom (V: corresponds to the number of intensive variables which can be varied independently without changing the equilibrium between all the phases) of the system is related to the number of components (n) and number of phases (φ : an homogeneous, physically distinct and mechanically separable portion of system, which is separated from other such parts of the system by definite boundary surfaces) by the following phase rule equation:

$$V = n + 2 - \varphi \quad (17)$$

As previously stated, enantiomers present the same physicochemical properties but opposite vector properties [142]. For this symmetric reason the phase diagram describing equilibria between both enantiomers is symmetrical with respect to the vertical axis passing through the racemic composition. The phase rule has to be carefully considered when dealing with

enantiomers. The possible racemization has also to be taken into account. For nonracemizable enantiomers, the perfect symmetry between the two mirror image components leads to amend the Gibbs phase rule [138]. Scott proposed a more generalized rule known as the Gibbs-Scott rule [143] in order to take into account the singularity of chiral compounds by distinguishing symmetric components or phases (n_2, φ_2) from non-symmetric components or phases (n_1, φ_1).

$$V = \frac{n_2}{2} + n_1 + 2 - \frac{\varphi_2}{2} - \varphi_1 \quad \text{with } \varphi_2 \geq 2 \quad (18)$$

When the sample does not undergo thermal degradation before the melting point upon heating, the binary phase diagram between both non racemizable enantiomers can be built from Differential Scanning Calorimetry (DSC), Temperature Resolved X-Ray Diffraction (TRXR), and Temperature Resolved Second-Harmonic Generation (TRSGH) experiments (for structural change investigations).

II.3.2 Binary Phase Diagram between both Enantiomers

Three fundamental types of enantiomer systems, described in a pioneering work of Roozeboom can be identified [144]. The three possibilities are a) conglomerates, b) racemic compounds, and c) solid solutions illustrated in figure 33.

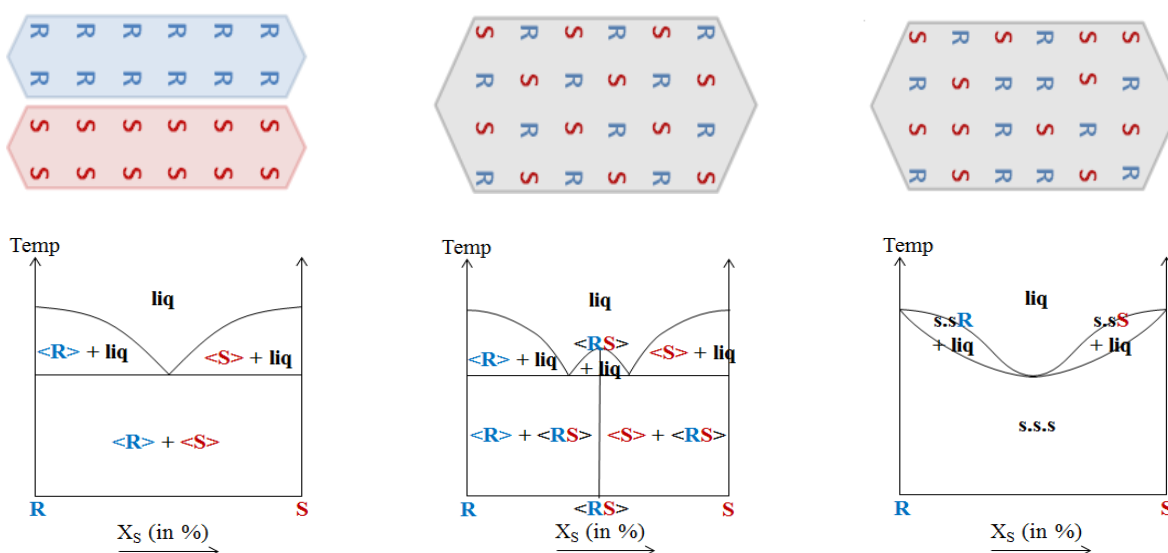


Figure 33: Schematic representation of the molecular arrangements and binary phase diagrams in three types of racemic species in absence of partial solid solution and solid/solid transition. Adapted from [144]

Other variations can be encountered, as mixed situations between a conglomerate and a racemic compound, or polymorphic transition for both pure enantiomer and racemic compound. The binary phase diagram is obtained by plotting the occurrence temperature of the various thermal events obtained from DSC at variable compositions. The liquidus line is therefore obtained by reporting on the diagram the melting point of each analyzed composition. When it is not possible to examine each single composition (e.g. poor quantities), simple conjectures linking temperature T to the composition x (molar fraction of one of the enantiomer in the liquid) can be drawn on thermodynamic basis and depending on the nature of the liquid-solid equilibrium. In a binary system involving a conglomerate, the relation between the temperature T of the system and the composition of the liquid phase is generally described by the simplify Schröder van-Laar equation 19 (case of an ideal mixture). The equation of Prigogine-Defay-Mausser (equation 20) describes the liquidus line of a binary system involving a racemic compound.

$$\ln x = \frac{\Delta H_S^m}{R} \left(\frac{1}{T_S^m} - \frac{1}{T^m} \right) \quad (19)$$

$$\ln(4x(1-x)) = \frac{2\Delta H_{RS}^m}{R} \left(\frac{1}{T_{RS}^m} - \frac{1}{T^m} \right) \quad (20)$$

where:

x is the molar fraction of the enantiomer in excess, $0.5 \leq x \leq 1$

ΔH_S^m is the melting enthalpy of the pure enantiomer (J mol^{-1})

T_S^m is the melting point of the pure enantiomer (K)

T^m is the end point of the melting (K)

ΔH_{RS}^m is the melting enthalpy of the racemic compound (J/mol)

T_{RS}^m is the melting point of the racemic compound (K)

R is the ideal gaz constant ($R=8.31 \text{ J mol}^{-1} \text{ K}^{-1}$)

a) Conglomerate: It is an equimolar eutectic physical mixture of crystals between the two enantiomers. For conglomerate forming systems the two enantiomers crystallize separately; each crystal contains homochiral molecules which in principle can be separated manually. The crystalline structure of the mixture is the same as that of the pure enantiomer since it is a juxtaposition of both enantiomer structures. In fact from a total of 230 available space groups, only 65 of them devoid of inverse symmetry elements are compatible with a single enantiomer in the asymmetric unit for the simple reason that the combination of the different symmetry

operations (of the space group) should respect the chirality of the molecule. Regarding this restriction and from available statistics, approximately 5–10% of crystalline racemic species are of this type [145]. From the phase diagram reported in figure 34 a) one can describe the thermal behavior of a conglomerate at various enantiomeric compositions. For transformations that occur at constant temperature and pressure, the relative stability of a system is determined by its Gibbs free energy. The plotted phase diagram of a conglomerate can be interpreted by the isothermal Gibbs free energy curve as a function of the composition. The equilibrium of the system is evaluated at three temperatures T_1 , T_2 , and T_3 . In a simple eutectic system, where the extent of solid solutions is negligibly small, a mixture of almost pure components always appears. The Gibbs function associated with the solid phases G_{sol} (pure enantiomers) are so steep that they are here considered as vertical [146]. The Gibbs energies of these mixtures are composed of the Gibbs energies of both components according to the lever rule [147].

At the temperature T_1 , both enantiomers participate in the melting equilibrium. Two equivalent regions of solid-liquid (R+liq, S+liq) equilibria are present (see figure 34b).

At the eutectic temperature T_2 the straight line $G_{sol}^R - G_{sol}^S$ itself is the tangent. It touches the $G_{liq}(x)$ curve at a point which corresponds to the composition of the eutectic ($x=0.5$). The phases connected by the tangent are in equilibrium: solid R, liquid with the composition $x=0.5$ and solid S (see figure 34 c)).

Below the eutectic temperature (T_3) all points of the straight line $G_{sol}^R - G_{sol}^S$ lay below the $G_{liq}(x)$ curve. No liquid solution can therefore appear. Only a mechanical mixture of R and S enantiomers is thermodynamically stable in the whole composition range (see figure 34 d)).

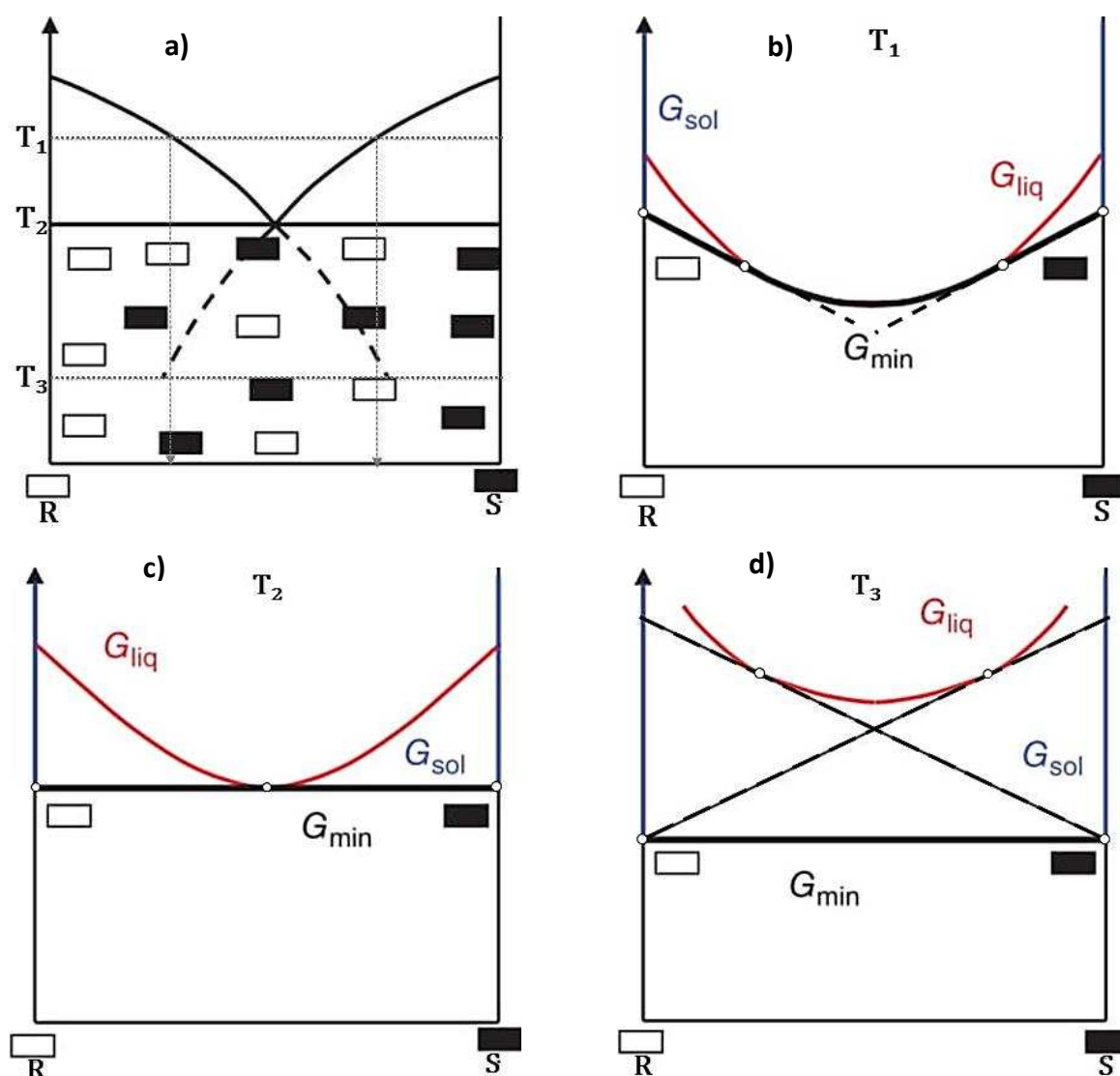


Figure 34: Energetics of phase equilibria in a binary eutectic of a conglomerate a) system at three temperatures b) T₁, c) T₂, d) T₃. G_{min} represents the minimum Gibbs free energy when equilibrium is reached. Adapted from [148]

b) Racemic compound: It is a defined compound formed by a stoichiometric mixture of the two enantiomers. Additionally, it can be seen as a cocrystal containing equimolar quantities of both enantiomers, usually paired up. A racemic compound is a heterochiral crystal, because the unit cell of each crystal contains enantiomeric molecules with opposite chirality. A racemic compound possesses physical properties different from those of the enantiomers. Racemic compounds are the most common racemic species, representing 90–95% of them [135,145,149]. Any one of the 230 space groups is compatible with a racemic compound provided that the number of molecules in the asymmetric unit Z' is consistent with

the crystalline structure. From a crystallographic perspective, the high occurrence must be associated with the preference of centrosymmetric space groups [146,150]. From the phase diagram reported in figure 35 it is possible to give the following descriptions of the system:

At T , $T_E < T < T_m^R$, two phases coexist (liquid-solid) in each of the four biphasic symmetrical regions (in all these regions the system is monovariant). The solid phase is composed of R or S enantiomers or the defined racemic compound.

At T_E the system is considered as invariant considering the coexisting phases: liquid, solid ($\langle R \rangle$, $\langle S \rangle$, $\langle RS \rangle$).

At $T < T_E$ the system is considered as monovariant and the defined racemic compound coexists with crystals of both enantiomers.

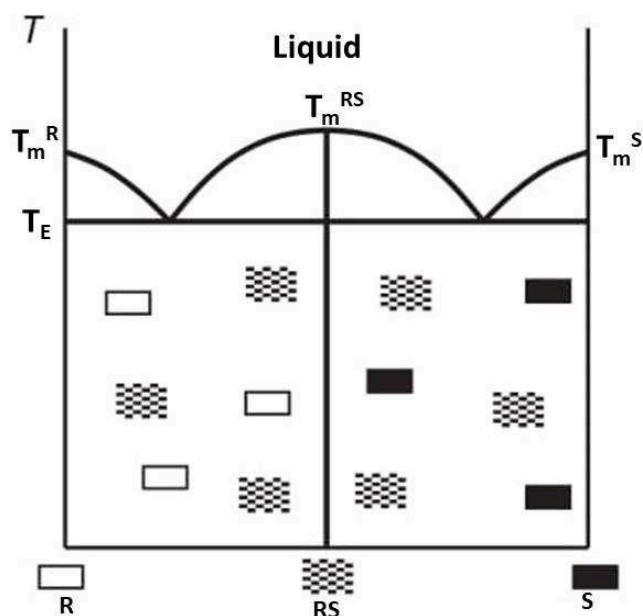


Figure 35: phase diagram of opposite enantiomers crystallizing as a stable racemic compound. Adapted from [148]

The binary phase diagrams of opposite enantiomers are generally complex compared to what have been presented up to now. They can involve metastable equilibria such as solid-solid transition or eutectoid, peritectoid invariants and polymorphic transitions. Racemic compounds can formed or decomposed through reactions involving solid-solid transitions as depicted in figure 36 a) and b) respectively.

At $T=T_E$, a racemic compound forms upon heating engaging a eutectoid reaction as the following equilibrium takes place: $R + S \rightleftharpoons RS$ (figure 36 a)).

At $T=T_{\pi}$, a racemic compound decomposes upon heating during a peritectoid reaction as following equilibrium takes place $RS \rightleftharpoons R + S$ (figure 36 b)).

These solid-solid transition phenomena involve very slow kinetics due to the poor diffusion rate in the solid state. Therefore the thermal detection can be problematic as they may appear as very low magnitude events.

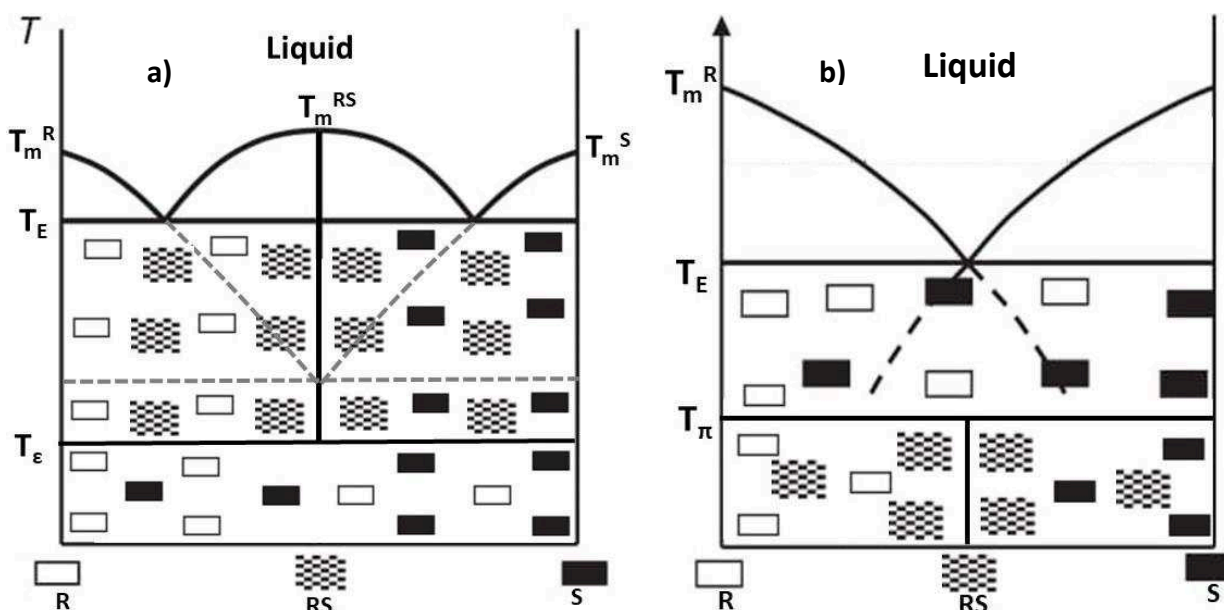


Figure 36: Binary phase diagram illustrating two solid-solid transitions between a conglomerate and a racemic compound leading to a) the formation of a racemic compound b) decomposition of a racemic compound. Adapted from [148]

c) Solid solutions: solid solutions are the rarest type of racemic species formed of equal numbers of molecules of both enantiomers in a more or less random arrangement. Less than 1% of racemic species are solid solutions. As displayed in figure 37, they can form three types of solid solutions defined by Roozeboom [144], which differ in the phase diagrams: type a) ideal solid solutions, type b) solid solutions with a maximum of melting point, type c) solid solutions with a minimum of melting point. In all these cases, both enantiomers form a solid solution in all the binary composition. Consequently both enantiomers are distributed in the same crystalline network but at variable compositions.

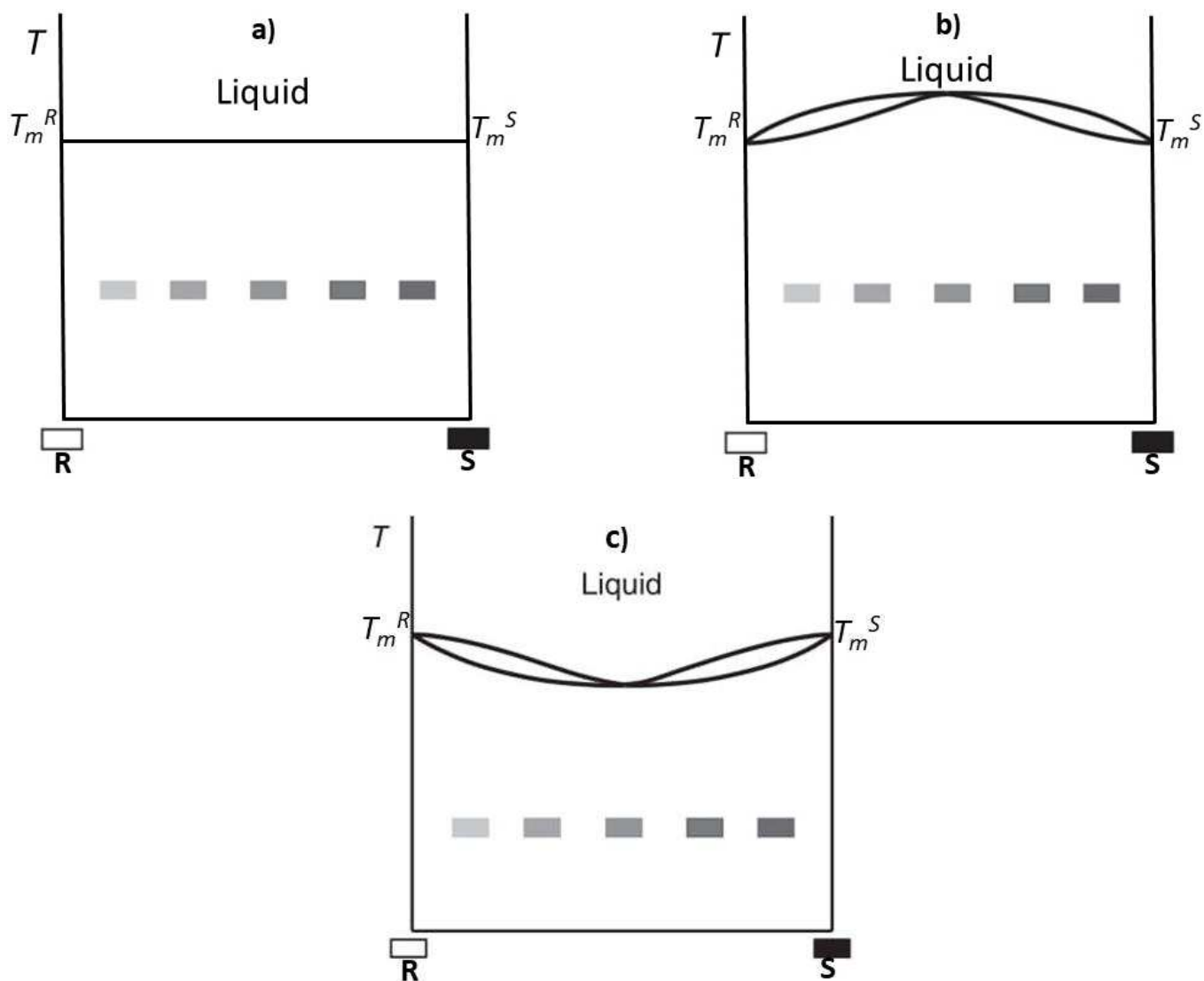


Figure 37: Different types of solid solutions between enantiomers a) ideal solid solutions, b) solid solutions with a maximum, c) solid solutions with a minimum [144]

III- Impact of Chirality in Amorphous State: State of Art

Systematic studies on the amorphous state of molecular compounds with a stereogenic chiral center are largely available in the literature, but when it comes to the influence of chirality in the amorphous state, the literature database is poorly furnish. Consequently many questions are still unsolved and are matter of fixed ideas without strong experimental evidence. The present paragraph summed up the few studies carried out on this subject and raises some unsolved questions. For reasons of clarity and simplicity, this paragraph is organized around two main points: the impact of chirality in the recrystallization behavior from amorphous state and the molecular mobility respectively.

III.1 Glass Forming Ability and Crystallization from Amorphous State

As it is the case for several molecular systems, the glassy state of chiral compounds can be reached using conventional technics such as melt quenching. The GFA is generally strongly impacted by chirality, more precisely by the presence of the counter enantiomer (opposite chirality). Considering that both enantiomers present identical scalar properties, it is obvious that they exhibit the same GFA. However mixture of both enantiomers can considerably modify their initial properties consequently the GFA may be impacted. For example, a pure enantiomer can illustrate a good GFA while the racemic mixture is a poor glass former considering the same cooling conditions. This is the case for numerous set of chiral organic compounds (e.g. alkylamide derived from *trans*-1,2-bis(amino)cyclohexane, diprophylline (figure 38 a)), for which racemic mixture has a much higher propensity to crystallize compared to the enantiomeric counterpart [148]. The same behavior can be mentioned for *RS* and enantiopure ketoprofen. Upon pressure P ($50 \leq P \leq 350$ MPa) application, the inverse situation is observed [35] (figure 38 b)). It is important to notice that the racemic mixtures studied in the mentioned works crystallize as racemic compounds (i.e. both enantiomers crystallize in the same crystal lattice) like more than 90% of racemic species [148]. No study in the literature highlights the case of conglomerate forming systems. One may ask if the behavior reported in racemic compounds is universal for all chiral systems.

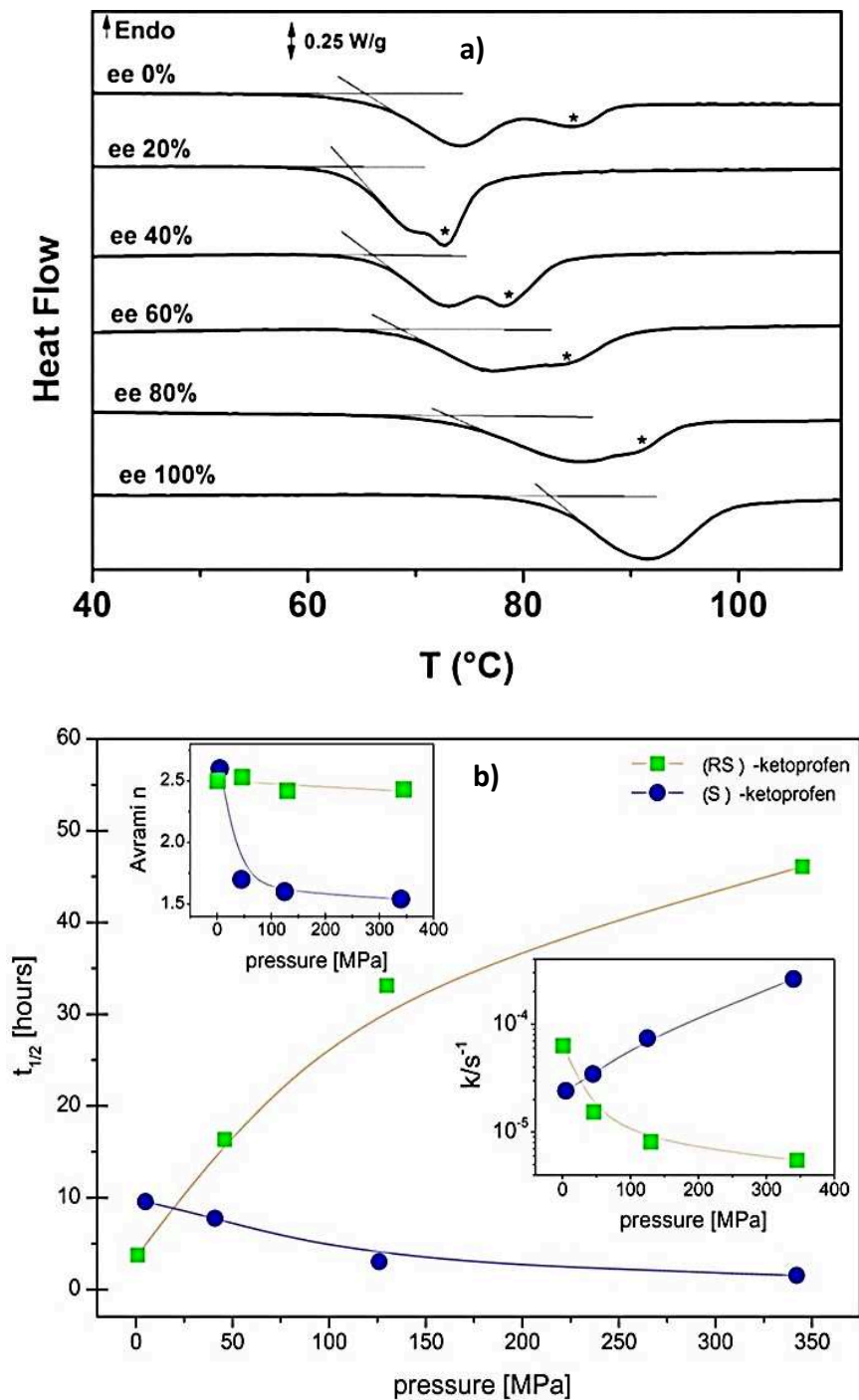


Figure 38: a) Thermal signature of the recrystallization behavior of diprophylline at different enantiomeric compositions Adapted from [151]. b) Pressure evolution of the crystallization half time (main), overall crystallization rate (lower inset), and Avrami parameter (upper inset) for S-ketoprofen and RS-ketoprofen crystallized along the same isochrones Adapted from [152].

Crystallization from amorphous glassy state usually leads to the appearance of highly energetic states or metastable crystalline solids. This tendency is also observed in chiral systems. In the case of Limonene the phase diagram corresponding to the thermodynamically stable state involves the formation of racemic compound (figure 39 a)), whereas the diagram obtained from amorphous state relies on the presence of mixed crystals (including a metastable solid solution, figure 39 b)). This can be understood in the framework of Ostwald rule of stages which states that phase transformations will always proceed through stages of metastable states whenever such metastable states exist. This rule is empirical, yet it is widely observed in phase transformations [153].

Another interesting feature reported in figure 39 b) is the invariability of T_g with the ee. Whatever the enantiomeric composition, T_g value remains constant. The symmetry between both opposite enantiomers induces a degenerate situation which can be detailed in the framework of Gordon Taylor law (excess of entropy neglected) in any R-S binary system as follows:

$$T_g(x) = \frac{xT_{gS} + (1-x)T_{gR}}{x + (1-x)K} \quad (21)$$

With

$$K = \frac{\Delta C_{pR}}{\Delta C_{pS}} = 1$$

Therefore whatever the composition, the following expression is verified:

$$T_g(x) = T_{gS} = T_{gR} \quad (22)$$

Consequently, T_g should be independent of the enantiomeric composition [148].

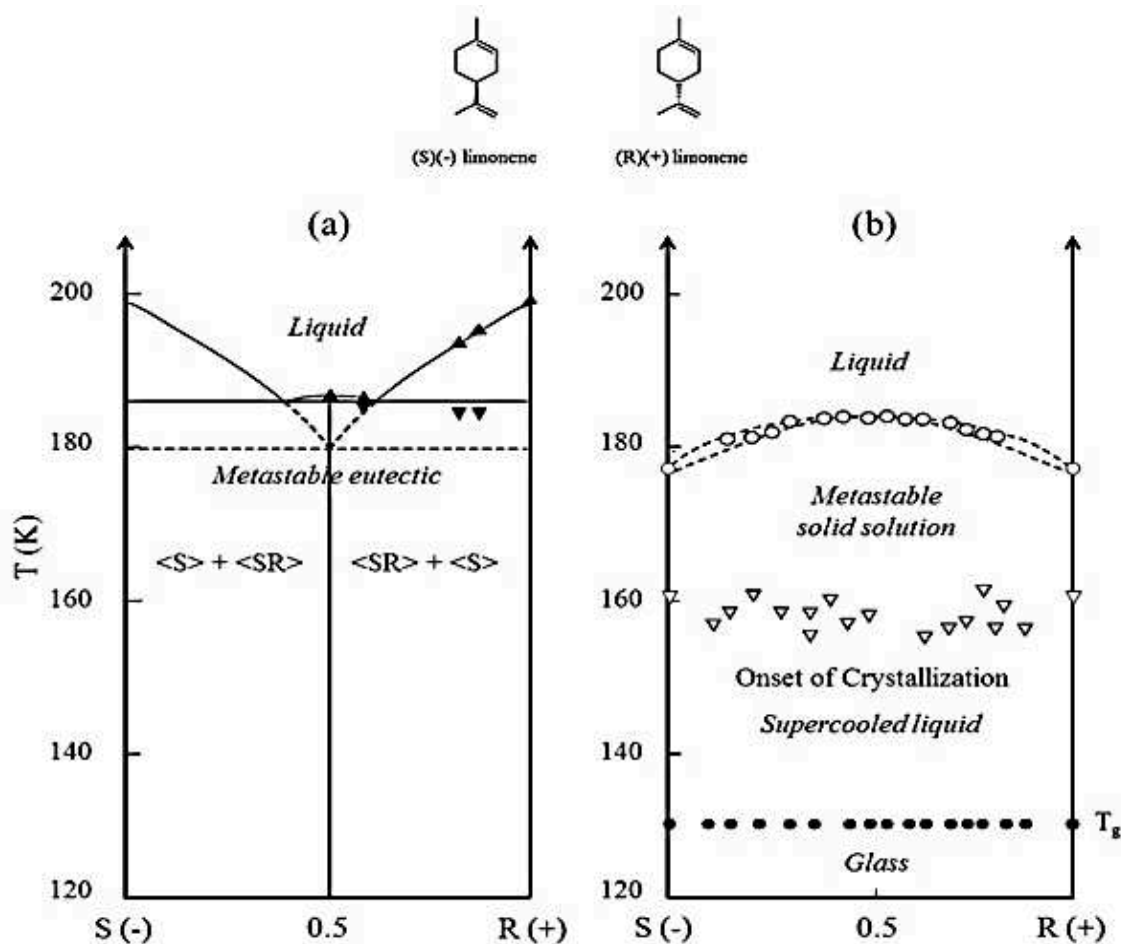


Figure 39: a) Stable equilibria between enantiomers of limonene. b) Temperature of the glass transition temperature T_g versus enantiomeric composition and metastable equilibria exhibiting a single complete solid solution between chiral components. The upper part of the figure depicts the developed formulae of both enantiomers of limonene; adapted from [154]

III.2 Molecular Mobility in Chiral Amorphous Compounds

Intuitively it is expected that the changes in the enantiomeric composition should not produce differences in the dynamic behavior of molecular system since both enantiomers possess identical scalar properties and T_g is composition independent. This intuition seems verified in various enantiomeric systems such as ibuprofen [155], ketoprofen [156], and diprophylline [157]. The relaxation processes are similar such as their rates as illustrated in figure 40. Thus, the molecular mobility of the presented cases is not influenced by chirality.

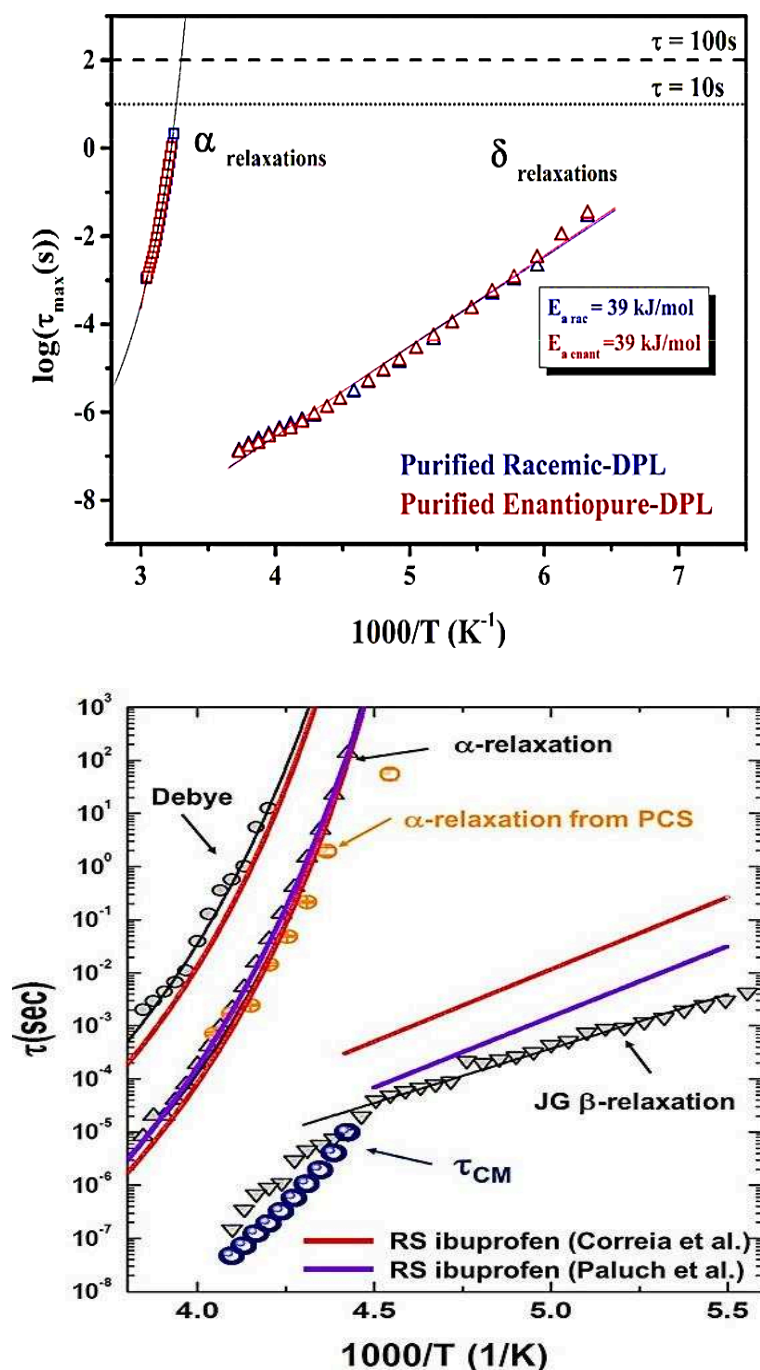


Figure 40: relaxation map in both racemic and enantiopure composition of diprophylline (top figure) [157] and ibuprofen (bottom figure) [155] respectively

These situations may change under pressure application as is shown in figure 41. Intuitively it is expected that the changes in the enantiomeric composition should not produce differences in the dynamic behavior of the molecular system. This result suggest that pressure can modify not only crystallization properties of a chiral molecule but also their glassy dynamics [156].

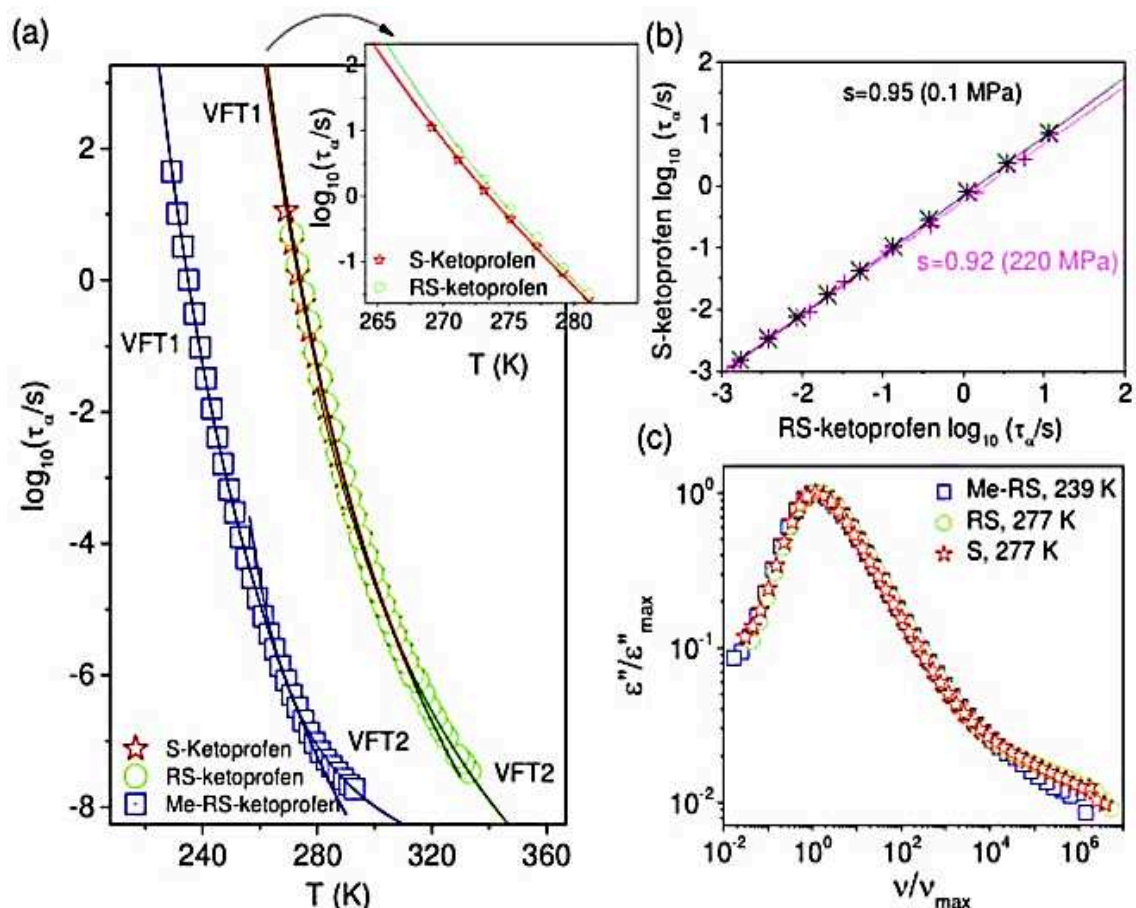


Figure 41: (a) α -relaxation times plotted as a function of temperature for S-ketoprofen, RS-ketoprofen and Me-RS-ketoprofen. Inset enlarges $\tau_{\alpha}(T)$ dependencies for RS-ketoprofen and S-ketoprofen in vicinity of the glass transition, and shows that both dynamics start to diverge close to T_g . (b) Temperature dependences of τ_{α} for RSketoprofen and S-ketoprofen plotted versus each other. The linear fit with the slope $s=0.95$ indicates that τ_{α} for S-ketoprofen changes slightly weaker with the temperature than for RS-ketoprofen. On increased pressure the correlation between τ_{α} dependencies for RS and S-ketoprofen weakens ($s=0.92$). (c) Comparison of the normalized dielectric loss spectra ϵ'' for Me-RS-ketoprofen, RSketoprofen and S-ketoprofen taken at different temperatures, but with very similar value of v_{\max} . From [156]

III - Conclusion

The link between all these enantiomeric systems is the fact that they crystallize as stable racemic compounds such as 95% of enantiomeric systems. From these studies, the most spectacular impact of chirality is expressed in the kinetics of crystallization/vitrification (it seems much easier to crystallize a racemic mixture than a pure enantiomer). As already reported in the introduction, we are interested in the case of two conglomerate forming systems: N-acetyl- α -methylbenzylamine (Nac-MBA) and 5-ethyl-5-methylhydantoin (12H). In this chiral species, one enantiomer acts like a chemical impurity of same chemical nature as its counterpart. We will evaluate their GFA, recrystallization tendency, molecular mobility and their behavior upon physical ageing at variable ee.

The following chapter gives some details about the investigated systems (12H and Nac-MBA) and the set of experimental and modelling techniques used to fulfill the goal of our work.

References

- [1] J. Jackle, Models of the glass transition, *Rep. Prog. Phys.* 49 (1986) 171. doi:10.1088/0034-4885/49/2/002.
- [2] C.A. Angell, Perspective on the glass transition, *J. Phys. Chem. Solids.* 49 (1988) 863–871. doi:10.1016/0022-3697(88)90002-9.
- [3] P.G. Debenedetti, F.H. Stillinger, Supercooled liquids and the glass transition, *Nature.* (2001). doi:10.1038/35065704.
- [4] M. Descamps, J.-F. Willart, Some Facets of Molecular Disorder in Crystalline and Amorphous Pharmaceuticals, in: *Disord. Pharm. Mater.*, Wiley-Blackwell, 2016: pp. 1–56. doi:10.1002/9783527652693.ch1.
- [5] A. Peker, W.L. Johnson, A highly processable metallic glass: Zr_{41.2}Ti_{13.8}Cu_{12.5}Ni_{10.0}Be_{22.5}, *Appl. Phys. Lett.* 63 (1993) 2342–2344. doi:10.1063/1.110520.
- [6] D. Xu, B. Lohwongwatana, G. Duan, W.L. Johnson, C. Garland, Bulk metallic glass formation in binary Cu-rich alloy series – Cu_{100-x}Zr_x (x=34, 36, 38.2, 40 at.%) and mechanical properties of bulk Cu₆₄Zr₃₆ glass, *Acta Mater.* 52 (2004) 2621–2624. doi:10.1016/j.actamat.2004.02.009.
- [7] M.F. Ashby, A.L. Greer, Metallic glasses as structural materials, *Scr. Mater.* 54 (2006) 321–326. doi:10.1016/j.scriptamat.2005.09.051.
- [8] A. Inoue, B. Shen, N. Nishiyama, Development and Applications of Late Transition Metal Bulk Metallic Glasses, in: *Bulk Met. Glas.*, Springer, Boston, MA, 2008: pp. 1–25. doi:10.1007/978-0-387-48921-6_1.
- [9] H. Dislich, New Routes to Multicomponent Oxide Glasses, *Angew. Chem. Int. Ed. Engl.* 10 (1971) 363–370. doi:10.1002/anie.197103631.
- [10] H. Namikawa, Characterization of the diffusion process in oxide glasses based on the correlation between electric conduction and dielectric relaxation, *J. Non-Cryst. Solids.* 18 (1975) 173–195. doi:10.1016/0022-3093(75)90019-8.
- [11] B.A. Shakhmatkin, N.M. Vedishcheva, M.M. Shultz, A.C. Wright, The thermodynamic properties of oxide glasses and glass-forming liquids and their chemical structure, *J. Non-Cryst. Solids.* 177 (1994) 249–256. doi:10.1016/0022-3093(94)90538-X.
- [12] T. Komatsu, Design and control of crystallization in oxide glasses, *J. Non-Cryst. Solids.* 428 (2015) 156–175. doi:10.1016/j.jnoncrysol.2015.08.017.
- [13] R.N. Haward, Introduction, in: *Phys. Glas. Polym.*, Springer, Dordrecht, 1973: pp. 1–53. doi:10.1007/978-94-010-2355-9_1.
- [14] U.W. Gedde, The Glassy Amorphous State, in: *Polym. Phys.*, Springer, Dordrecht, 1999: pp. 77–98. doi:10.1007/978-94-011-0543-9_5.
- [15] A. Saiter, H. Couderc, J. Grenet, Characterisation of structural relaxation phenomena in polymeric materials from thermal analysis investigations, *J. Therm. Anal. Calorim.* 88 (2007) 483–488. doi:10.1007/s10973-006-8117-x.
- [16] K. Tanaka, K. Shimakawa, Introduction, in: *Amorph. Chalcogenide Semicond. Relat. Mater.*, Springer, New York, NY, 2011: pp. 1–28. doi:10.1007/978-1-4419-9510-0_1.
- [17] J.D. Mackenzie, Structure of Glass Forming Halides. I. Liquid Beryllium Fluoride, *J. Chem. Phys.* 32 (1960) 1150–1152. doi:10.1063/1.1730864.
- [18] B.C. Hancock, S.L. Shamblin, G. Zografi, Molecular Mobility of Amorphous Pharmaceutical Solids Below Their Glass Transition Temperatures, *Pharm. Res.* 12 (1995) 799–806. doi:10.1023/A:1016292416526.
- [19] J.A. Baird, B. Van Eerdenbrugh, L.S. Taylor, A Classification System to Assess the Crystallization Tendency of Organic Molecules from Undercooled Melts, *J. Pharm. Sci.* 99 (2010) 3787–3806. doi:10.1002/jps.22197.
- [20] J. Gerges, F. Affouard, Predictive Calculation of the Crystallization Tendency of Model Pharmaceuticals in the Supercooled State from Molecular Dynamics Simulations, *J. Phys. Chem. B.* 119 (2015) 10768–10783. doi:10.1021/acs.jpcc.5b05557.

- [21] G.P. Johari, Intrinsic mobility of molecular glasses, *J. Chem. Phys.* 58 (1973) 1766–1770. doi:10.1063/1.1679421.
- [22] M. Vogel, P. Medick, E.A. Rössler, Secondary Relaxation Processes in Molecular Glasses Studied by Nuclear Magnetic Resonance Spectroscopy, in: G.A. Webb (Ed.), *Annu. Rep. NMR Spectrosc.*, Academic Press, 2005: pp. 231–299. doi:10.1016/S0066-4103(05)56005-8.
- [23] C.A. Angell, Formation of Glasses from Liquids and Biopolymers, *Science*. 267 (1995) 1924–1935. doi:10.1126/science.267.5206.1924.
- [24] K.F. Kelton, A.L. Greer, Chapter 2 - The Classical Theory, in: K.F. Kelton, A.L. Greer (Eds.), *Pergamon Mater. Ser.*, Pergamon, 2010: pp. 19–54. doi:10.1016/S1470-1804(09)01502-8.
- [25] M. Descamps, E. Dudognon, Crystallization from the Amorphous State: Nucleation–Growth Decoupling, Polymorphism Interplay, and the Role of Interfaces, *J. Pharm. Sci.* 103 (n.d.) 2615–2628. doi:10.1002/jps.24016.
- [26] J. Lothe, G.M. Pound, Reconsiderations of Nucleation Theory, *J. Chem. Phys.* 36 (1962) 2080–2085. doi:10.1063/1.1732832.
- [27] D. Turnbull, J.C. Fisher, Rate of Nucleation in Condensed Systems, *J. Chem. Phys.* 17 (1949) 71–73. doi:10.1063/1.1747055.
- [28] D. Zhou, G.G.Z. Zhang, D. Law, D.J.W. Grant, E.A. Schmitt, Thermodynamics, molecular mobility and crystallization kinetics of amorphous griseofulvin, *Mol. Pharm.* 5 (2008) 927–936. doi:10.1021/mp800169g.
- [29] M.D. Ediger, P. Harrowell, L. Yu, Crystal growth kinetics exhibit a fragility-dependent decoupling from viscosity, *J. Chem. Phys.* 128 (2008) 034709. doi:10.1063/1.2815325.
- [30] Z.P. Lu, C.T. Liu, A new glass-forming ability criterion for bulk metallic glasses, *Acta Mater.* 50 (2002) 3501–3512. doi:10.1016/S1359-6454(02)00166-0.
- [31] I. Avramov, E.D. Zanotto, M.O. Prado, Glass-forming ability versus stability of silicate glasses. II. Theoretical demonstration, *J. Non-Cryst. Solids*. 320 (2003) 9–20. doi:10.1016/S0022-3093(03)00081-4.
- [32] Z.P. Lu, T.T. Goh, Y. Li, S.C. Ng, Glass formation in La-based La–Al–Ni–Cu–(Co) alloys by Bridgman solidification and their glass forming ability, *Acta Mater.* 47 (1999) 2215–2224. doi:10.1016/S1359-6454(99)00058-0.
- [33] S. Guo, Z.P. Lu, C.T. Liu, Identify the best glass forming ability criterion, *Intermetallics*. 18 (2010) 883–888. doi:10.1016/j.intermet.2009.12.025.
- [34] C. Alba, L.E. Busse, D.J. List, C.A. Angell, Thermodynamic aspects of the vitrification of toluene, and xylene isomers, and the fragility of liquid hydrocarbons, *J. Chem. Phys.* 92 (1990) 617–624. doi:10.1063/1.458411.
- [35] K. Adrjanowicz, K. Kaminski, M. Paluch, K. Niss, Crystallization Behavior and Relaxation Dynamics of Supercooled S-Ketoprofen and the Racemic Mixture along an Isochrone, *Cryst. Growth Des.* 15 (2015) 3257–3263. doi:10.1021/acs.cgd.5b00373.
- [36] H. Tanaka, Relationship among glass-forming ability, fragility, and short-range bond ordering of liquids, *J. Non-Cryst. Solids*. 351 (2005) 678–690. doi:10.1016/j.jnoncrysol.2005.01.070.
- [37] M. Goldstein, Viscous liquids and the glass transition. V. Sources of the excess specific heat of the liquid, *J. Chem. Phys.* 64 (1976) 4767–4774. doi:10.1063/1.432063.
- [38] P.G. Debenedetti, *Metastable Liquids: Concepts and Principles*, Princeton University Press, 1996.
- [39] A.K. Doolittle, Studies in Newtonian Flow. II. The Dependence of the Viscosity of Liquids on Free-Space, *J. Appl. Phys.* 22 (1951) 1471–1475. doi:10.1063/1.1699894.
- [40] M.H. Cohen, D. Turnbull, Molecular Transport in Liquids and Glasses, *J. Chem. Phys.* 31 (1959) 1164–1169. doi:10.1063/1.1730566.
- [41] D. Turnbull, M.H. Cohen, Free-Volume Model of the Amorphous Phase: Glass Transition, *J. Chem. Phys.* 34 (1961) 120–125. doi:10.1063/1.1731549.
- [42] J.H. Gibbs, E.A. DiMarzio, Nature of the Glass Transition and the Glassy State, *J. Chem. Phys.* 28 (1958) 373–383. doi:10.1063/1.1744141.
- [43] W. Kauzmann, The Nature of the Glassy State and the Behavior of Liquids at Low Temperatures., *Chem. Rev.* 43 (1948) 219–256. doi:10.1021/cr60135a002.

- [44] C.A. Angell, J.C. Tucker, Heat capacities and fusion entropies of the tetrahydrates of calcium nitrate, cadmium nitrate, and magnesium acetate. Concordance of calorimetric and relaxational ideal glass transition temperatures, *J. Phys. Chem.* 78 (1974) 278–281. doi:10.1021/j100596a018.
- [45] G. Adam, J.H. Gibbs, On the Temperature Dependence of Cooperative Relaxation Properties in Glass-Forming Liquids, *J. Chem. Phys.* 43 (1965) 139–146. doi:10.1063/1.1696442.
- [46] K.L. Ngai, Introduction to the Problems of Relaxation and Diffusion in Complex Systems, in: *Relax. Diffus. Complex Syst.*, Springer, New York, NY, 2011: pp. 1–47. doi:10.1007/978-1-4419-7649-9_1.
- [47] F. Kremer, A. Schönhal, The Scaling of the Dynamics of Glasses and Supercooled Liquids, in: *Broadband Dielectr. Spectrosc.*, Springer, Berlin, Heidelberg, 2003: pp. 99–129. doi:10.1007/978-3-642-56120-7_4.
- [48] U. Tracht, M. Wilhelm, A. Heuer, H. Feng, K. Schmidt-Rohr, H.W. Spiess, Length Scale of Dynamic Heterogeneities at the Glass Transition Determined by Multidimensional Nuclear Magnetic Resonance, *Phys. Rev. Lett.* 81 (1998) 2727–2730. doi:10.1103/PhysRevLett.81.2727.
- [49] J.C. Qiao, J.M. Pelletier, Dynamic Mechanical Relaxation in Bulk Metallic Glasses: A Review, *J. Mater. Sci. Technol.* 30 (2014) 523–545. doi:10.1016/j.jmst.2014.04.018.
- [50] F. Stickel, E.W. Fischer, R. Richert, Dynamics of glass-forming liquids. II. Detailed comparison of dielectric relaxation, dc-conductivity, and viscosity data, *J. Chem. Phys.* 104 (1996) 2043–2055. doi:10.1063/1.470961.
- [51] I.M. Hodge, Enthalpy relaxation and recovery in amorphous materials, *J. Non-Cryst. Solids.* 169 (1994) 211–266. doi:10.1016/0022-3093(94)90321-2.
- [52] R. Gardon, O.S. Narayanaswamy, Stress and Volume Relaxation in Annealing Flat Glass, *J. Am. Ceram. Soc.* 53 (1970) 380–385. doi:10.1111/j.1151-2916.1970.tb12137.x.
- [53] G. Smith, A.P. Duffy, J. Shen, C.J. Olliff, Dielectric relaxation spectroscopy and some applications in the pharmaceutical sciences, *J. Pharm. Sci.* 84 (1995) 1029–1044. doi:10.1002/jps.2600840902.
- [54] M. Dionísio, J.F. Mano, Chapter 7 - Electric Techniques, in: M.E. Brown, P.K. Gallagher (Eds.), *Handb. Therm. Anal. Calorim.*, Elsevier Science B.V., 2008: pp. 209–268. doi:10.1016/S1573-4374(08)80010-6.
- [55] K.L. Ngai, Coupling model explanation of salient dynamic properties of glass-forming substances, *IEEE Trans. Dielectr. Electr. Insul.* 8 (2001) 329–344. doi:10.1109/94.933340.
- [56] R. Richert, A. Blumen, Disordered Systems and Relaxation, in: *Disord. Eff. Relaxational Process.*, Springer, Berlin, Heidelberg, 1994: pp. 1–7. doi:10.1007/978-3-642-78576-4_1.
- [57] K. Grzybowska, K. Adrjanowicz, M. Paluch, Application of Broadband Dielectric Spectroscopy to Study Molecular Mobility in Pharmaceutical Systems, in: *Disord. Pharm. Mater.*, Wiley-Blackwell, 2016: pp. 301–360. doi:10.1002/9783527652693.ch11.
- [58] G.S. Fulcher, Analysis of Recent Measurements of the Viscosity of Glasses, *J. Am. Ceram. Soc.* 8 (1925) 339–355. doi:10.1111/j.1151-2916.1925.tb16731.x.
- [59] G. Tammann, W. Hesse, Die Abhängigkeit der Viskosität von der Temperatur bei unterkühlten Flüssigkeiten, *Z. Für Anorg. Allg. Chem.* 156 (1926) 245–257. doi:10.1002/zaac.19261560121.
- [60] G.A. Schwartz, E. Tellechea, J. Colmenero, Á. Alegría, Correlation between temperature–pressure dependence of the α -relaxation and configurational entropy for a glass-forming polymer, *J. Non-Cryst. Solids.* 351 (2005) 2616–2621. doi:10.1016/j.jnoncrysol.2005.03.058.
- [61] R. Böhmer, K.L. Ngai, C.A. Angell, D.J. Plazek, Nonexponential relaxations in strong and fragile glass formers, *J. Chem. Phys.* 99 (1993) 4201–4209. doi:10.1063/1.466117.
- [62] K. Kawakami, T. Harada, Y. Yoshihashi, E. Yonemochi, K. Terada, H. Moriyama, Correlation between Glass-Forming Ability and Fragility of Pharmaceutical Compounds, *J. Phys. Chem. B.* 119 (2015) 4873–4880. doi:10.1021/jp509646z.
- [63] L.-M. Wang, R. Richert, Glass Transition Dynamics and Boiling Temperatures of Molecular Liquids and Their Isomers, *J. Phys. Chem. B.* 111 (2007) 3201–3207. doi:10.1021/jp0688254.
- [64] O.N. Senkov, Correlation between fragility and glass-forming ability of metallic alloys, *Phys. Rev. B.* 76 (2007) 104202. doi:10.1103/PhysRevB.76.104202.

- [65] W. Gotze, L. Sjogren, Relaxation processes in supercooled liquids, *Rep. Prog. Phys.* 55 (1992) 241. doi:10.1088/0034-4885/55/3/001.
- [66] J. Heijboer, Secondary Loss Peaks in Glassy Amorphous Polymers, *Int. J. Polym. Mater. Polym. Biomater.* 6 (1977) 11–37. doi:10.1080/00914037708075218.
- [67] G.P. Johari, M. Goldstein, Viscous Liquids and the Glass Transition. II. Secondary Relaxations in Glasses of Rigid Molecules, *J. Chem. Phys.* 53 (1970) 2372–2388. doi:10.1063/1.1674335.
- [68] K.L. Ngai, *Relaxation and Diffusion in Complex Systems*, Springer-Verlag, New York, 2011. //www.springer.com/fr/book/9781441976482 (accessed May 7, 2018).
- [69] G.P. Johari, Glass Transition and Secondary Relaxations in Molecular Liquids and Crystals, *Ann. N. Y. Acad. Sci.* 279 (1976) 117–140. doi:10.1111/j.1749-6632.1976.tb39701.x.
- [70] K.L. Ngai, M. Paluch, Classification of secondary relaxation in glass-formers based on dynamic properties, *J. Chem. Phys.* 120 (2003) 857–873. doi:10.1063/1.1630295.
- [71] C.J. Reid, M.W. Evans, Dielectric and far infrared study of solutions in the glassy state from 100 Hz to 10 THz: Discovery and characterization of the universal γ process, *J. Chem. Phys.* 76 (1982) 2576–2584. doi:10.1063/1.443235.
- [72] K.L. Ngai, Relation between some secondary relaxations and the α relaxations in glass-forming materials according to the coupling model, *J. Chem. Phys.* 109 (1998) 6982–6994. doi:10.1063/1.477334.
- [73] K.L. Ngai, An extended coupling model description of the evolution of dynamics with time in supercooled liquids and ionic conductors, *J. Phys. Condens. Matter.* 15 (2003) S1107. doi:10.1088/0953-8984/15/11/332.
- [74] B. Rijal, J.A. Soto Puentes, B. Atawa, L. Delbreilh, K. Fatyeyeva, A. Saiter, E. Dargent, Correlated and cooperative motions in segmental relaxation: Influence of constitutive unit weight and intermolecular interactions, *Phys. Rev. E.* 94 (2016) 062502. doi:10.1103/PhysRevE.94.062502.
- [75] H. Huth, L.-M. Wang, C. Schick, R. Richert, Comparing calorimetric and dielectric polarization modes in viscous 2-ethyl-1-hexanol, *J. Chem. Phys.* 126 (2007) 104503. doi:10.1063/1.2539105.
- [76] M.A. Floriano, C.A. Angell, On the relaxation between Debye and nonexponential relaxation in supercooled monohydric alcohols and water: A solution study, *J. Chem. Phys.* 91 (1989) 2537–2543. doi:10.1063/1.457013.
- [77] U. Kaatze, Dielectric and structural relaxation in water and some monohydric alcohols, *J. Chem. Phys.* 147 (2017) 024502. doi:10.1063/1.4991850.
- [78] W. Dannhauser, Dielectric Study of Intermolecular Association in Isomeric Octyl Alcohols, *J. Chem. Phys.* 48 (1968) 1911–1917. doi:10.1063/1.1668989.
- [79] F. Stickel, E.W. Fischer, R. Richert, Dynamics of glass-forming liquids. II. Detailed comparison of dielectric relaxation, dc-conductivity, and viscosity data, *J. Chem. Phys.* 104 (1996) 2043–2055. doi:10.1063/1.470961.
- [80] O.E. Kalinovskaya, J.K. Vij, The exponential dielectric relaxation dynamics in a secondary alcohol's supercooled liquid and glassy states, *J. Chem. Phys.* 112 (2000) 3262–3266. doi:10.1063/1.480909.
- [81] D. Fragiadakis, C.M. Roland, R. Casalini, Insights on the origin of the Debye process in monoalcohols from dielectric spectroscopy under extreme pressure conditions, *J. Chem. Phys.* 132 (2010) 144505. doi:10.1063/1.3374820.
- [82] G. Power, M. Nagaraj, J.K. Vij, G.P. Johari, Debye process and dielectric state of an alcohol in a nonpolar solvent, *J. Chem. Phys.* 134 (2011) 044525. doi:10.1063/1.3543713.
- [83] S.J. Bass, W.I. Nathan, R.M. Meighan, R.H. Cole, Dielectric Properties of Alkyl Amides. II. Liquid Dielectric Constant and Loss, *J. Phys. Chem.* 68 (1964) 509–515. doi:10.1021/j100785a011.
- [84] M. Kunst, D. van Duijn, P. Bordewijk, Association of Alcohols in Carbon Tetrachloride and Alkanes, *Berichte Bunsenges. Für Phys. Chem.* 83 (1979) 840–847. doi:10.1002/bbpc.19790830814.
- [85] L.-M. Wang, R. Richert, Identification of dielectric and structural relaxations in glass-forming secondary amides, *J. Chem. Phys.* 123 (2005) 054516. doi:10.1063/1.1997135.

- [86] C. Gainaru, S. Bauer, E. Vynokur, H. Wittkamp, W. Hiller, R. Richert, R. Böhmer, Dynamics in Supercooled Secondary Amide Mixtures: Dielectric and Hydrogen Bond Specific Spectroscopies, *J. Phys. Chem. B.* 119 (2015) 15769–15779. doi:10.1021/acs.jpcc.5b10034.
- [87] A.R. Brás, J.P. Noronha, A.M.M. Antunes, M.M. Cardoso, A. Schönhals, F. Affouard, M. Dionísio, N.T. Correia, Molecular Motions in Amorphous Ibuprofen As Studied by Broadband Dielectric Spectroscopy, *J. Phys. Chem. B.* 112 (2008) 11087–11099. doi:10.1021/jp8040428.
- [88] M. Rams-Baron, Z. Wojnarowska, M. Dulski, A. Ratuszna, M. Paluch, Evidence of slow Debye-like relaxation in the anti-inflammatory agent etoricoxib, *Phys. Rev. E.* 92 (2015) 022309. doi:10.1103/PhysRevE.92.022309.
- [89] M.T. Ottou Abe, N.T. Correia, J.M.B. Ndjaka, F. Affouard, A comparative study of ibuprofen and ketoprofen glass-forming liquids by molecular dynamics simulations, *J. Chem. Phys.* 143 (2015) 164506. doi:10.1063/1.4933430.
- [90] M.T. Ottou Abe, N.T. Correia, L.-C. Valdes, J.M.B. Ndjaka, F. Affouard, Local molecular organizations of ibuprofen, flurbiprofen and ketoprofen in the liquid phase: Insights from molecular dynamics simulations, *J. Mol. Liq.* 205 (2015) 74–77. doi:10.1016/j.molliq.2014.08.015.
- [91] A.M. and, M. Cutroni*, Multiple Mechanical Relaxations in Ethylcyclohexane above the Glass Transition Temperature, (2007). doi:10.1021/jp071202l.
- [92] A. Mandanici, W. Huang, M. Cutroni, R. Richert, Dynamics of glass-forming liquids. XII. Dielectric study of primary and secondary relaxations in ethylcyclohexane, *J. Chem. Phys.* 128 (2008) 124505. doi:10.1063/1.2844797.
- [93] A.H. Narten, A. Habenschuss, Hydrogen bonding in liquid methanol and ethanol determined by x-ray diffraction, *J. Chem. Phys.* 80 (1984) 3387–3391. doi:10.1063/1.447093.
- [94] C. Gainaru, R. Figuli, T. Hecksher, B. Jakobsen, J.C. Dyre, M. Wilhelm, R. Böhmer, Shear-Modulus Investigations of Monohydroxy Alcohols: Evidence for a Short-Chain-Polymer Rheological Response, *Phys. Rev. Lett.* 112 (2014) 098301. doi:10.1103/PhysRevLett.112.098301.
- [95] L.P. Singh, C. Alba-Simionesco, R. Richert, Dynamics of glass-forming liquids. XVII. Dielectric relaxation and intermolecular association in a series of isomeric octyl alcohols, *J. Chem. Phys.* 139 (2013) 144503. doi:10.1063/1.4823998.
- [96] J.L. Salefran, G. Vicq, S. Delbos, Y. Dutuit, A.M. Bottreau, Etude des spectres de relaxation dielectrique de quelques diols, *Adv. Mol. Relax. Interact. Process.* 16 (1980) 63–79. doi:10.1016/0378-4487(80)80007-0.
- [97] D.W. Davidson, Dielectric Relaxation in Liquids: II. Isomeric Pentanediols, *Can. J. Chem.* 39 (1961) 2139–2154. doi:10.1139/v61-286.
- [98] S.S.N. Murthy, Dielectric Relaxation in Monohydroxy Alcohols and Its Connection to the Glass Transition Process, *J. Phys. Chem.* 100 (1996) 8508–8517. doi:10.1021/jp953596z.
- [99] G.P. Johari, O.E. Kalinovskaya, J.K. Vij, Effects of induced steric hindrance on the dielectric behavior and H bonding in the supercooled liquid and vitreous alcohol, *J. Chem. Phys.* 114 (2001) 4634–4642. doi:10.1063/1.1346635.
- [100] O.E. Kalinovskaya, J.K. Vij, G.P. Johari, Mechanism of the Major Orientation Polarization in Alcohols, and the Effects of Steric Hindrance-, and Dilution-Induced Decrease on H-Bonding, *J. Phys. Chem. A.* 105 (2001) 5061–5070. doi:10.1021/jp0040695.
- [101] L. Zoranić, F. Sokolić, A. Perera, Microstructure of neat alcohols: A molecular dynamics study, *J. Chem. Phys.* 127 (2007) 024502. doi:10.1063/1.2753482.
- [102] G.W. Stewart, E.W. Skinner, X-Ray Diffraction in Liquids: A Comparison of Certain Primary Normal Alcohols and their Isomers, *Phys. Rev.* 31 (1928) 1–9. doi:10.1103/PhysRev.31.1.
- [103] K.S. Vahvaselkä, R. Serimaa, M. Torkkeli, Determination of Liquid Structures of the Primary Alcohols Methanol, Ethanol, 1-Propanol, 1-Butanol and 1-Octanol by X-ray Scattering, *J. Appl. Crystallogr.* 28 (1995) 189–195. doi:10.1107/S0021889894010149.
- [104] T. WEITKAMP, J. NEUEFEIND, H.E. FISCHER, M.D. ZEIDLER, Hydrogen bonding in liquid methanol at ambient conditions and at high pressure, *Mol. Phys.* 98 (2000) 125–134. doi:10.1080/00268970009483276.

- [105] T. YAMAGUCHI, K. HIDAKA, A.K. SOPER, The structure of liquid methanol revisited: a neutron diffraction experiment at $-80\text{ }^{\circ}\text{C}$ and $+25\text{ }^{\circ}\text{C}$, *Mol. Phys.* 96 (1999) 1159–1168. doi:10.1080/00268979909483060.
- [106] S.P. Bierwirth, J. Bolle, S. Bauer, C. Sternemann, C. Gainaru, M. Tolan, R. Böhmer, Scaling of Suprastructure and Dynamics in Pure and Mixed Debye Liquids, in: F. Kremer, A. Loidl (Eds.), *Scaling Relax. Process.*, Springer International Publishing, Cham, 2018: pp. 121–171. doi:10.1007/978-3-319-72706-6_5.
- [107] D. ZIMMERMANN, T. HÄBER, H. SCHAAL, M.A. SUHM, Hydrogen bonded rings, chains and lassos: the case of t-butyl alcohol clusters, *Mol. Phys.* 99 (2001) 413–425. doi:10.1080/00268970010017009.
- [108] L. Bianchi, A.K. Adya, O.N. Kalugin, C.J. Wormald, The structure of liquid methanol: a molecular dynamics study using a six-site model, *J. Phys. Condens. Matter.* 11 (1999) 9151. doi:10.1088/0953-8984/11/47/303.
- [109] R. Ludwig, The Structure of Liquid Methanol, *ChemPhysChem.* 6 (n.d.) 1369–1375. doi:10.1002/cphc.200400663.
- [110] M.W. Sagal, Dielectric Relaxation in Liquid Alcohols and Diols, *J. Chem. Phys.* 36 (1962) 2437–2442. doi:10.1063/1.1732905.
- [111] U. Kaatze, R. Behrends, R. Pottel, Hydrogen network fluctuations and dielectric spectrometry of liquids, *J. Non-Cryst. Solids.* 305 (2002) 19–28. doi:10.1016/S0022-3093(02)01084-0.
- [112] R. Böhmer, C. Gainaru, R. Richert, Structure and dynamics of monohydroxy alcohols—Milestones towards their microscopic understanding, 100 years after Debye, *Phys. Rep.* 545 (2014) 125–195. doi:10.1016/j.physrep.2014.07.005.
- [113] F.X. Hession, R.H. Cole, Dielectric Properties of Liquid Ethanol and 2-Propanol, *J. Chem. Phys.* 23 (1955) 1756–1761. doi:10.1063/1.1740575.
- [114] C. Gainaru, R. Meier, S. Schildmann, C. Lederle, W. Hiller, E.A. Rössler, R. Böhmer, Nuclear-Magnetic-Resonance Measurements Reveal the Origin of the Debye Process in Monohydroxy Alcohols, *Phys. Rev. Lett.* 105 (2010) 258303. doi:10.1103/PhysRevLett.105.258303.
- [115] W.H. Stockmayer, Dielectric dispersion in solutions of flexible polymers, *Pure Appl. Chem.* 15 (1967) 539–554. doi:10.1351/pac196715030539.
- [116] J. Šponer, J. Leszczynski, P. Hobza, Hydrogen Bonding and Stacking of DNA Bases: A Review of Quantum-chemical ab initio Studies, *J. Biomol. Struct. Dyn.* 14 (1996) 117–135. doi:10.1080/07391102.1996.10508935.
- [117] S. Woutersen, Y. Mu, G. Stock, P. Hamm, Hydrogen-bond lifetime measured by time-resolved 2D-IR spectroscopy: N-methylacetamide in methanol, *Chem. Phys.* 266 (2001) 137–147. doi:10.1016/S0301-0104(01)00224-5.
- [118] T.A. Litovitz, G.E. McDuffie, Comparison of Dielectric and Mechanical Relaxation in Associated Liquids, *J. Chem. Phys.* 39 (1963) 729–734. doi:10.1063/1.1734316.
- [119] J.E. Anderson, R. Ullman, Molecular Relaxation in a Fluctuating Environment, *J. Chem. Phys.* 47 (1967) 2178–2184. doi:10.1063/1.1712250.
- [120] G.P. Johari, W. Dannhauser, Effect of Pressure on Dielectric Relaxation in Isomeric Octanols, *J. Chem. Phys.* 50 (1969) 1862–1876. doi:10.1063/1.1671282.
- [121] L.P. Singh, R. Richert, Watching Hydrogen-Bonded Structures in an Alcohol Convert from Rings to Chains, *Phys. Rev. Lett.* 109 (2012) 167802. doi:10.1103/PhysRevLett.109.167802.
- [122] P. Lunkenheimer, R. Wehn, U. Schneider, A. Loidl, Glassy Aging Dynamics, *Phys. Rev. Lett.* 95 (2005) 055702. doi:10.1103/PhysRevLett.95.055702.
- [123] B.C. Hancock, S.L. Shamblin, G. Zografi, Molecular Mobility of Amorphous Pharmaceutical Solids Below Their Glass Transition Temperatures, *Pharm. Res.* 12 (1995) 799–806. doi:10.1023/A:1016292416526.
- [124] R. Wungtanagorn, S.J. Schmidt, Thermodynamic Properties and Kinetics of the Physical Ageing of Amorphous Glucose, Fructose, and Their Mixture, *J. Therm. Anal. Calorim.* 65 (2001) 9–35. doi:10.1023/A:1011574031179.

- [125] A. Tanaka, K. Nitta, R. Maekawa, T. Masuda, T. Higashimura, Effects of Physical Aging on Viscoelastic and Ultrasonic Properties of Poly[1-(trimethylsilyl)-1-propyne] Films, *Polym. J.* 24 (1992) 1173–1180. doi:10.1295/polymj.24.1173.
- [126] S. Mukherjee, S.A. Jabarin, Aging characteristics of oriented poly(ethylene terephthalate), *Polym. Eng. Sci.* 35 (1995) 1145–1154. doi:10.1002/pen.760351404.
- [127] J.C. Arnold, The effects of physical aging on the brittle fracture behavior of polymers, *Polym. Eng. Sci.* 35 (1995) 165–169. doi:10.1002/pen.760350207.
- [128] J. Yang, Y. Yang, J. Hou, X. Zhang, W. Zhu, M. Xu, M. Wan, Polypyrrole—polypropylene composite films: preparation and properties, *Polymer.* 37 (1996) 793–798. doi:10.1016/0032-3861(96)87255-7.
- [129] A.Q. Tool, C.G. Eicitlin, Variations Caused in the Heating Curves of Glass by Heat Treatment¹, *J. Am. Ceram. Soc.* 14 (n.d.) 276–308. doi:10.1111/j.1151-2916.1931.tb16602.x.
- [130] W. Thomson, B. Kelvin, Baltimore Lectures on Molecular Dynamics and the Wave Theory of Light, 2010. <http://adsabs.harvard.edu/abs/2010blmd.book.....T>.
- [131] Capillary Electrophoresis in Chiral Analysis, Wiley.Com. (n.d.). <https://www.wiley.com/en-us/Capillary+Electrophoresis+in+Chiral+Analysis-p-9780471974154> (accessed July 19, 2018).
- [132] L. PASTEUR, Memoires sur la relation qui peut exister entre la forme cristalline et al composition chimique, et sur la cause de la polarization rotatoire, *Compt Rend.* 26 (1848) 535–538.
- [133] L. Pasteur, Leçons de chimie (et de physique) professée en 1860, La Hachette & C°, 1861.
- [134] G.B. Kauffman, R.D. Myers, Pasteur’s Resolution of Racemic Acid: A Sesquicentennial Retrospect and a New Translation, *Chem. Educ.* 3 (1998) 1–4. doi:10.1007/s00897980257a.
- [135] A. Collet, J. Crassous, J.-P. Dutasta, *Molécules chirales*, EDP Sciences, 2012.
- [136] S.F. Mason, ed., *Optical Activity and Chiral Discrimination*, Springer Netherlands, 1979. [//www.springer.com/fr/book/9789027709820](http://www.springer.com/fr/book/9789027709820) (accessed July 19, 2018).
- [137] stereochemistry - Are our hands really chiral?, *Chem. Stack Exch.* (n.d.). <https://chemistry.stackexchange.com/questions/66024/are-our-hands-really-chiral> (accessed December 14, 2018).
- [138] C. Viedma, G. Coquerel, P. Cintas, 22 - Crystallization of Chiral Molecules, in: T. Nishinaga (Ed.), *Handb. Cryst. Growth Second Ed.*, Elsevier, Boston, 2015: pp. 951–1002. doi:10.1016/B978-0-444-56369-9.00022-8.
- [139] R.S. Cahn, C. Ingold, V. Prelog, Specification of Molecular Chirality, *Angew. Chem. Int. Ed. Engl.* 5 (n.d.) 385–415. doi:10.1002/anie.196603851.
- [140] Cahn–Ingold–Prelog priority rules, Wikipedia. (2018). https://en.wikipedia.org/w/index.php?title=Cahn%E2%80%93Ingold%E2%80%93Prelog_priority_rules&oldid=846728357.
- [141] Q. Viel, De l’amorphe au cristal : etude d’un composé pharmaceutique chiral, thesis, Normandie, 2017. <http://www.theses.fr/2017NORMR048> (accessed December 14, 2018).
- [142] H.D. Flack, *Absolute-Structure Determination: Past, Present and Future*, (2014). doi:info:doi/10.2533/chimia.2014.26.
- [143] R.L. Scott, Modification of the phase rule for optical enantiomers and other symmetric systems, *J. Chem. Soc. Faraday Trans. 2 Mol. Chem. Phys.* 73 (1977) 356–360. doi:10.1039/F29777300356.
- [144] H.W.B. Roozeboom, Löslichkeit und Schmelzpunkt als Kriterien für racemische Verbindungen, pseudoracemische Mischkristalle und inaktive Konglomerate, *Z. Für Phys. Chem.* 28U (1899) 494–517. doi:10.1515/zpch-1899-2832.
- [145] J. Jacques, A. Collet, S.H. Wilen, *Enantiomers, racemates, and resolutions*, Wiley, 1981. <http://agris.fao.org/agris-search/search.do?recordID=US201300332512> (accessed July 24, 2018).
- [146] Coquerel Gerard, Tamura Rui, “Enantiomeric Disorder” *Pharmaceutically Oriented, Disord. Pharm. Mater.* (2016). doi:10.1002/9783527652693.ch5.
- [147] B. Predel, M. Hoch, M.J. Pool, *Phase Diagrams and Heterogeneous Equilibria: A Practical Introduction*, Springer-Verlag, Berlin Heidelberg, 2004. [//www.springer.com/gp/book/9783540140115](http://www.springer.com/gp/book/9783540140115) (accessed July 26, 2018).

- [148] G. Coquerel, R. Tamura, "Enantiomeric Disorder" Pharmaceutically Oriented, in: rc Descamps (Ed.), *Disord. Pharm. Mater.*, Wiley-VCH Verlag GmbH & Co. KGaA, 2016: pp. 135–160. doi:10.1002/9783527652693.ch5.
- [149] I.K. Reddy, R. Mehvar, *Chirality in Drug Design and Development*, CRC Press, 2004.
- [150] G. Coquerel, Review on the heterogeneous equilibria between condensed phases in binary systems of enantiomers, *Enantiomer*. 5 (2000) 481–498.
- [151] Q. Viel, C. Brandel, Y. Cartigny, M.E.S. Eusébio, J. Canotilho, V. Dupray, E. Dargent, G. Coquerel, S. Petit, Crystallization from the Amorphous State of a Pharmaceutical Compound: Impact of Chirality and Chemical Purity, (2016). doi:10.1021/acs.cgd.6b01566.
- [152] K. Adrjanowicz, K. Kaminski, M. Paluch, K. Niss, Crystallization Behavior and Relaxation Dynamics of Supercooled S-Ketoprofen and the Racemic Mixture along an Isochrone, *Cryst. Growth Des.* 15 (2015) 3257–3263. doi:10.1021/acs.cgd.5b00373.
- [153] A. Keller, M. Hikosaka, S. Rastogi, A. Toda, P.J. Barham, G. Goldbeck-Wood, An approach to the formation and growth of new phases with application to polymer crystallization: effect of finite size, metastability, and Ostwald's rule of stages, *J. Mater. Sci.* 29 (1994) 2579–2604. doi:10.1007/BF00356806.
- [154] H.E. Gallis, J.C. van Miltenburg, H.A.J. Oonk, Polymorphism of mixtures of enantiomers: A thermodynamic study of mixtures of D- and L-limonene, *Phys. Chem. Chem. Phys.* 2 (2000) 5619–5623. doi:10.1039/B005603K.
- [155] T.H. Kim, T. Shibata, S. Kojima, D.-M. Shin, Y.-H. Hwang, J.-H. Ko, Comparison of thermal and elastic properties of glassy racemic and enantiomorphous ibuprofen studied by Brillouin light scattering and modulated differential scanning calorimetry, *Curr. Appl. Phys.* 14 (2014) 965–969. doi:10.1016/j.cap.2014.05.001.
- [156] K. Adrjanowicz, K. Kaminski, M. Tarnacka, K. Szutkowski, L. Popenda, G. Bartkowiak, M. Paluch, The effect of hydrogen bonding propensity and enantiomeric composition on the dynamics of supercooled ketoprofen – dielectric, rheological and NMR studies, *Phys. Chem. Chem. Phys.* 18 (2016) 10585–10593. doi:10.1039/C6CP00578K.
- [157] Q. Viel, L. Delbreilh, G. Coquerel, S. Petit, E. Dargent, Molecular Mobility of an Amorphous Chiral Pharmaceutical Compound: Impact of Chirality and Chemical Purity, *J. Phys. Chem. B.* 121 (2017) 7729–7740. doi:10.1021/acs.jpcc.7b05667.

CHAPTER II:

MATERIALS AND METHODS

This chapter presents in the first section the investigated materials namely 5-ethyl-5-methylhydantoin (12H) and N-acetyl- α -methyl-benzylamine (Nac-MBA). Some details on the synthesis and purification steps of Nac-MBA are provided. The second section is devoted to the description of the experimental and simulation tools used to probe the thermal, structural and dynamic behaviors of both 12H and Nac-MBA systems.

I- Materials

A- 5-ethyl-5-methylhydantoin (12H)

5-ethyl-5-methylhydantoin ($C_6H_{10}N_2O_2$ see figure 1a) is a chiral derivative of hydantoin and used for its antibacterial and antifungal activities [1,2]. Additionally, the ring opening of this 5, 5-disubstituted hydantoin leads to isovaline (2-amino-2-methylbutanoic acid) (see figure 1b)) which is an important α, α disubstituted glycine derivative. As it is the case for other aminoacids, its incorporation into small up to medium size peptides is able to induce specific conformational constraints and improve their resistance to hydrolases [2].



Figure 1: a) Molecular formulae of 12H ($C_6H_{10}N_2O_2$) and b) isovaline ($C_5H_{11}NO_2$)

Racemic mixture of 5-ethyl-5-methylhydantoin was supplied by ABCR GmbH, and analyses were carried out without further chemical treatment. The pure enantiomer was obtained by an optical resolution procedure, namely Auto-Seeded Programmed Polythermic Preferential Crystallization method (AS3PC), performed in SMS laboratory by Beilles and co-workers [2]. The obtained white crystals were grinded and mixed with the racemic sample in order to prepare different enantiomeric compositions.

1- Structural and thermal properties of 12H

The structural resolution of enantiopure 12H has been reported previously by S. Beilles and co-authors [2] and highlighted the presence of infinite H-bond chains along b-axis. These strong molecular ribbons (two H-bonds per molecule involving N1, O2 and N3, see figure 2) are held together by means of van der Waals contacts [2], [3]. Both enantiomers and racemic 12H crystallize in $P2_12_12_1$ space group, having identical parameters of crystal unit cell. This fact is consistent with the conglomerate nature of 12H.

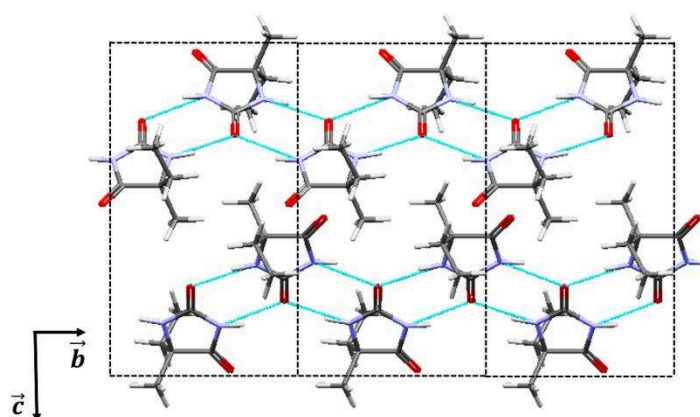


Figure 2: Projection of the crystal structure of 12H along a-axis showing molecular ribbons running along the b-axis. From [3]

The crystallographic parameters of 12H are summed up in table 1:

Table 1: Crystallographic parameters and thermal characteristics of 12H. From [2–4]

Formula	C ₆ H ₁₀ N ₂ O ₂
Crystal Class	Orthorhombic
Space group	$P2_12_12_1$
a (Å)	7.980 (2)
b (Å)	7.219 (2)
c (Å)	12.818 (3)
Volume (Å³)	738.4 (3)
d	1.28
Z', Z	1, 4

The melting point of the pure enantiomer is reference at $T_m=175^\circ\text{C}$ with an enthalpy $\Delta H_m(\text{R or S})=21.9\text{ kJ/mol}$ ($\Delta S_m(\text{R or S})=48.9\text{ (J/(mol.K))}$). Racemic 12H melts at 141°C with an enthalpy of 21.3 kJ/mol ($\Delta S_m(\text{RS})=51.4\text{ (J/(mol.K))}$). Hydantoin derivative 12H, crystallizes as a stable conglomerate without any detectable metastable racemic compound or solid solution (see figure 3). So far, neither polymorph nor solvate of 12H has been identified.

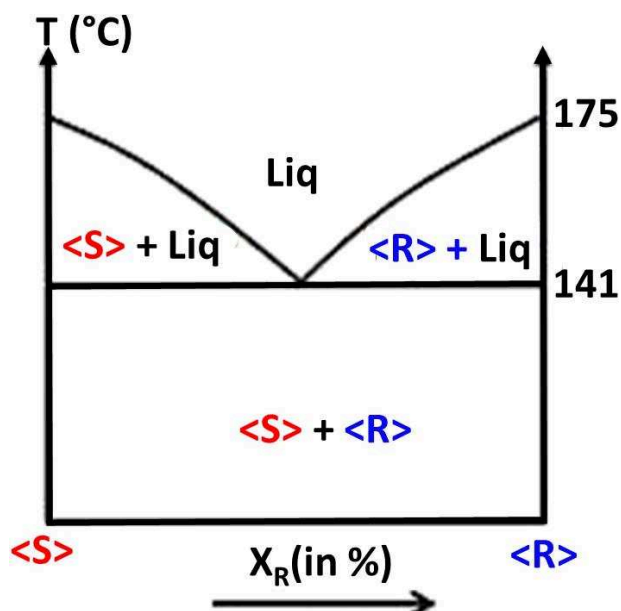


Figure 3: Binary phase diagram between 12H enantiomers

B- N-acetyl- α -methylbenzylamine (Nac-MBA): synthesis and purification

Nac-MBA is a derivative from α -methylbenzylamine, a widely used chiral resolving agent for optical resolution procedures. At the end of the year fifties Nerdel and Liebig [cited in 5] realized the acetylation of α -methylbenzylamine by means of acetic anhydride. This acetylation reaction can also be operated by acetyl chloride as inspired by Brown and Moudachirou [6]. Optically pure and racemic Nac-MBA were synthesized by acetylation of pure and racemic α -methylbenzylamine purchased from Aldrich (99%) using either acetic anhydride or acetyl chloride. The last methods consist to dilute the amine in dichloromethane and mix the diluted solution with an aqueous solution of sodium carbonate initially prepared. Slight excess of diluted acetyl chloride in dichloromethane is slowly added to the previous solution. After stirring, the reaction mixture is decanted and the unreacted products are removed by successive washings with acid and basic aqueous solutions. The washed solution

is dried with MgSO_4 and evaporated (yield almost 90%). The white powder obtained from synthesis is doubly recrystallized from toluene or purified by column chromatography (the developed formula is presented in figure 4). Samples of several ee were prepared by physical mixtures of both enantiomers. For example, an ee = 0% contains the same amount of both enantiomers (i.e. racemic), when an ee = 100 % is enantiomerically pure. The optical purity was verified by polarimetry using a Perkin Elmer model 341 polarimeter dotted with a Na and Hg source lamps. Experiments were carried out at ambient temperature by dissolving 5 mg of Nac-MBA opposite enantiomers in 1mL of ethanol.

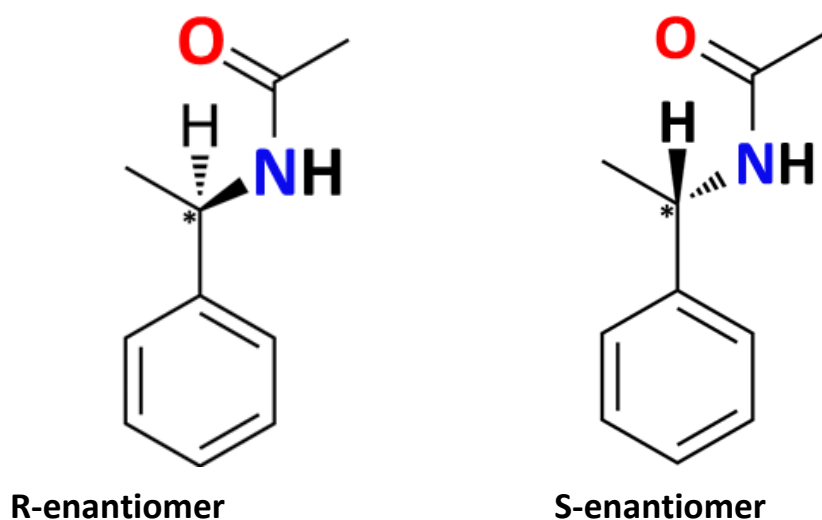


Figure 4: Developed formula of Nac-MBA enantiomers ($\text{C}_{10}\text{H}_{13}\text{NO}$)

1- Structural and thermal characterization

According to the phase diagram established by Druot and coworkers (see figure 5) [5], Nac-MBA is reported as a stable conglomerate below 64°C. At this temperature a eutectoid invariant takes place; the conglomerate transforms into a racemic compound. Hypothetically, the metastable eutectic refers as the melting of residual R and S enantiomers that did not undergo the eutectoid transition. The racemic compound melts at $T_m(\text{RS}) = 79^\circ\text{C}$ with an enthalpy $\Delta H_m(\text{RS}) = 19 \pm 3 \text{ kJ/mol}$ (melting entropy $\Delta S_m(\text{RS}) = 54 \text{ J/(mol}\cdot\text{K)}$) and the pure enantiomer melts at $T_m(\text{R or S}) = 100^\circ\text{C}$ with an enthalpy $\Delta H_m(\text{R or S}) = 25 \pm 4 \text{ kJ/mol}$ (melting entropy $\Delta S_m(\text{R}) = 66 \text{ J/(mol}\cdot\text{K)}$) [7].

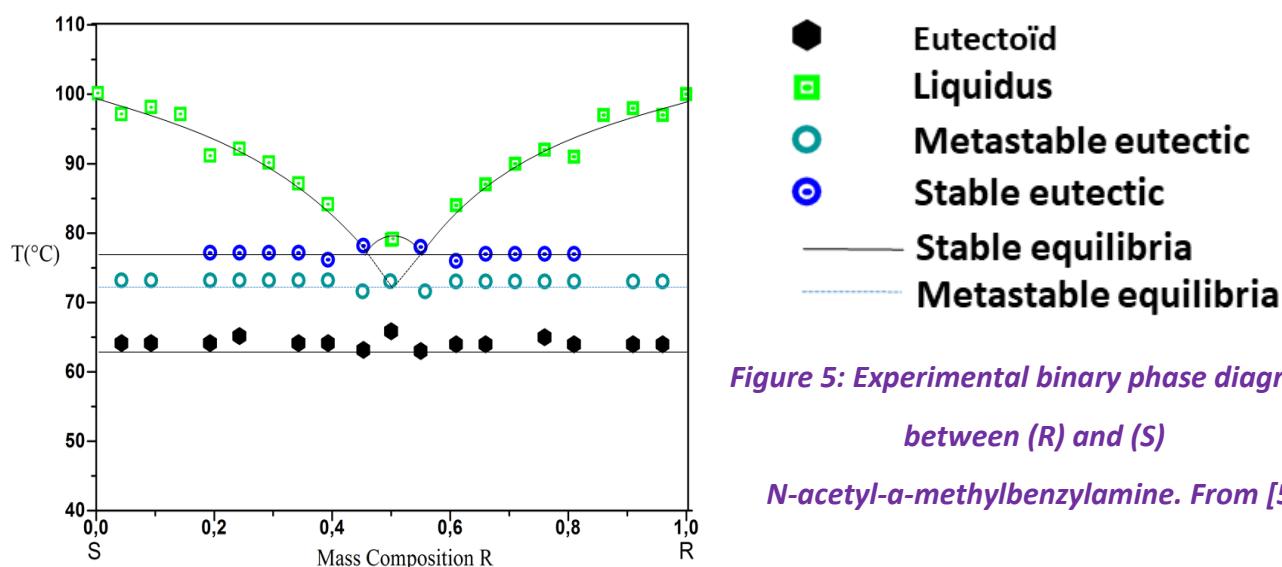


Figure 5: Experimental binary phase diagrams between (R) and (S) *N*-acetyl- α -methylbenzylamine. From [5]

The pure enantiomer crystallographic structure was firstly resolved by Aubry and coworkers in 1980 [8]. In 1996 Druot and coworkers [5] resolved the structure of the racemic compound. The pure enantiomers crystallize in the tetragonal $P4_12_12$ space group and the racemic compound in the $P2_1/c$ monoclinic system.

a) Description of the pure enantiomer structure

The side chain plane defined by the *N*-Acetyl group and the chiral center is 86.2° from the phenyl ring plane; and the Carbon of the CH_3 group linked to the chiral carbon is 0.54 \AA from the side chain plane. The strongest intermolecular link is a hydrogen bond between $N - H \cdots O$ atoms in such a way that: $d(N - O) = 2.86 \text{ \AA}$; $d(H \cdots O) = 2.03 \text{ \AA}$ and $(N - H \cdots O) = 175.0^\circ$. As a consequence, the main feature of the structure is infinite and isotactic Chains of H-Bonded Molecules (CHBMs) alternately parallel to $\langle 110 \rangle$ and $\langle 1\bar{1}0 \rangle$ in successive (004) slices. The side chains involved in CHBMs form series of corrugated planes which are 25.7° apart, with the row (441) as a common edge (see figure 6).

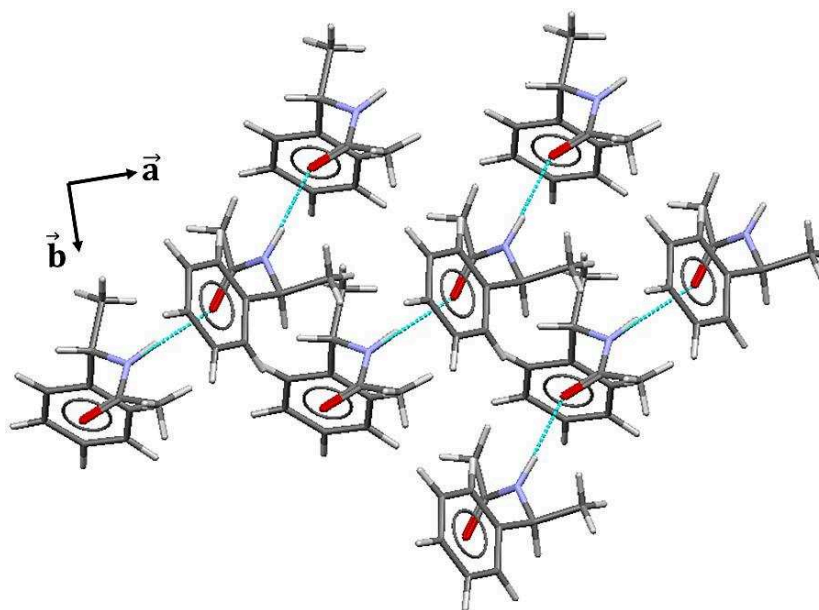


Figure 6: Projection along \vec{c} axis of (004) slice in the (R) enantiomer structure of Nac-MBA showing the CHBMs along the $\langle 110 \rangle$ direction. Adapted from [5]

b) Description of the racemic compound structure

The side chain plane defined by the N-Acetyl group and the chiral center is 88.6° from the phenyl ring plane; and the Carbon of the methyl group linked to the chiral carbon is 0.62 \AA from the side chain plane. The hydrogen bond has almost the same characteristics as in the structure of the enantiomer: $d(N - O) = 2.87 \text{ \AA}$; $d(H \cdots O) = 2.10 \text{ \AA}$ and $(N - H \cdots O) = 171.8^\circ$. Nevertheless, the resulting CHBMs are syndiotactic (figure 7 a)). They have the same periodicity ($c = 9.471 \text{ \AA}$, at 20°C) than those in the enantiomer structure ($2d_{110} = 9.543 \text{ \AA}$ at 20°C). The side chain planes of successive molecules are rotated around c axis by alternately $+34^\circ$ or -34° from the (100) plane (figure 7b)). These chains are stacked along b, and the cohesion is mainly due to weak interactions (the aromatic rings are too far apart)

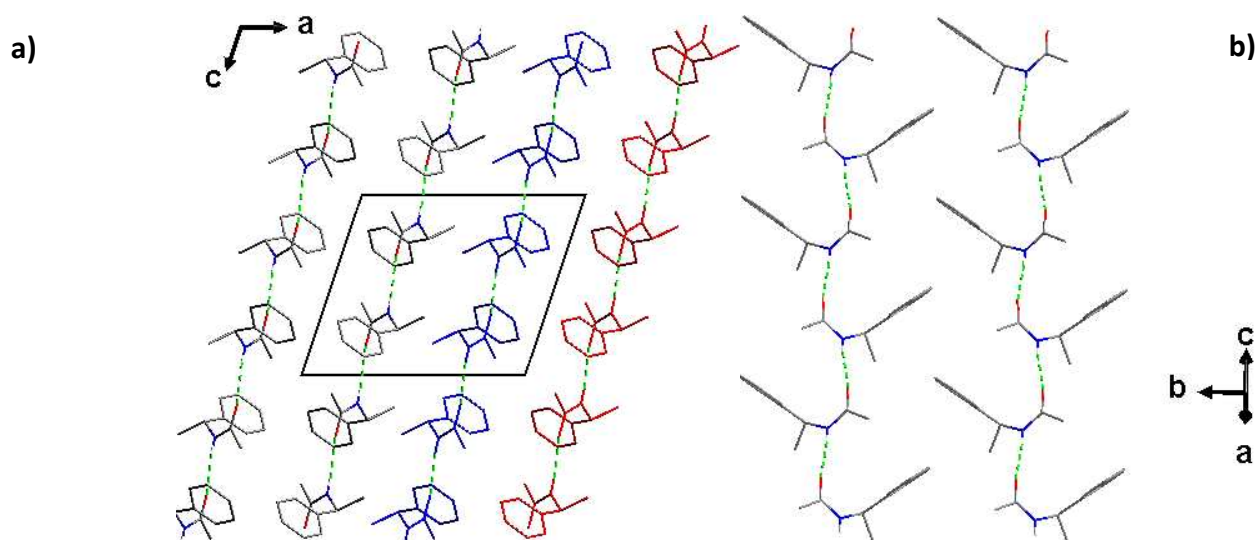


Figure 7: a) Projection along \vec{b} axis of the racemic compound structure; homochiral chains are displayed with different colors. b) Alternative rotation around \vec{c} axis of the side chain plane from the (100) plane

The crystallographic parameters are summed up in table 2.

Table 2: Crystallographic characteristics for (R) Nac-MBA and (rac) Nac-MBA [5]

	R enantiomer Nac-MBA	Racemic compound Nac-MBA
Formula	$C_{10}H_{13}NO$	$C_{10}H_{13}NO$
Crystal Class	tetragonal	Monoclinic
Space group	$P4_1 2_1 2$	$P2_1/C$
a (Å)	6.748 (2)	11.209 (4)
b (Å)	6.748 (2)	9.519 (2)
c (Å)	41.815 (12)	9.519 (2)
Volume (Å ³)	1904 (2)	668 (2)
d	1.14	1.13
Z	8	4

II- Experimental Techniques

In order to characterize and understand the thermal, structural and dynamical behavior of Nac-MBA, different experimental techniques were used. In the following section, we report some details about the experimental tools.

A- Differential scanning calorimetry (DSC)

Differential scanning calorimetry (DSC) is a thermal technique used to study thermodynamic phase transformations, such as crystallization, melting or oxidation, as well as time evolution properties of materials, such as physical aging [9,10]. DSC is used in many industries including pharmaceuticals, polymers, food, paper, printing, manufacturing, agriculture, semiconductors, and electronics as most materials exhibit some sort of transitions. For example for pharmaceutical purposes, DSC is used in order to define processing parameters. For instance, if it is necessary to deliver a drug in the amorphous form, it is required to process the drug below the crystallization temperature domain.

DSC measures the energy necessary to establish a nearly zero temperature difference between a substance and an inert reference material, as the two specimens are subjected to identical temperature regimes in a controlled environment, heated or cooled at a controlled rate. Conventionally one distinguishes two main types of DSC systems: a power-compensation and heat flux DSC. In this work DSC measurements were performed using Q 100 from TA, DSC Polyma 214 from Netzsch (Heat- Flux DSC) and DSC 8500 of Perkin Elmer (Power-Compensation DSC).

In power-compensation DSC (see figure 8) the temperatures of the sample (T_s) and reference (T_R) are controlled independently using separate, identical furnaces. The temperatures of the sample and reference are made identical (ΔT = temperature difference between the sample and the reference) by varying the power input to the two furnaces (ΔP = power difference applied by both furnaces); the energy required to do this is a measure of the enthalpy or heat capacity changes in the sample relative to the reference.

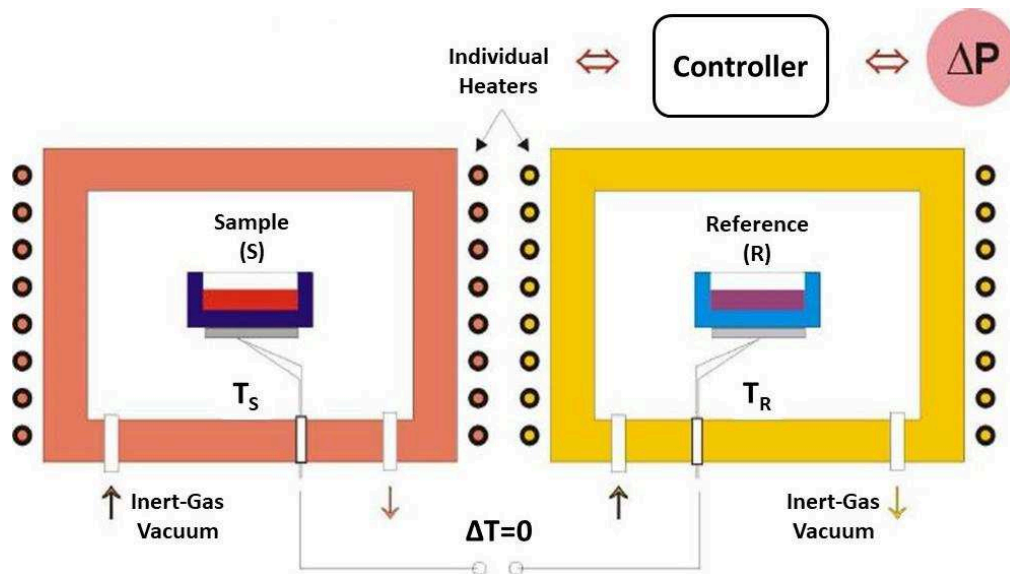


Figure 8: Power compensation DSC principle. From [9]

In heat-flux DSC (see figure 9), the sample and reference are connected by a low-resistance heat-flow path (a metal disc). The assembly is enclosed in a single furnace. Enthalpy or heat capacity changes in the sample causes a difference in its temperature relative to the reference (ΔT).

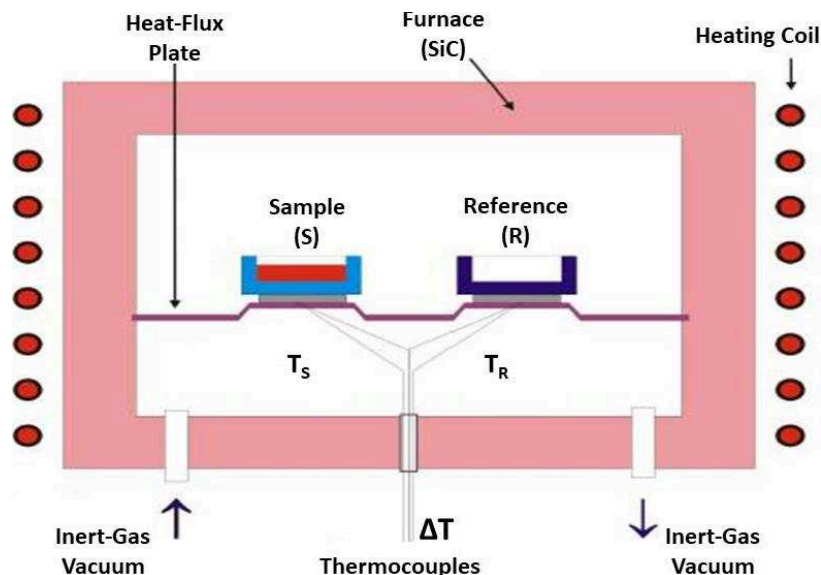


Figure 9: Heat-flux DSC principle. T_S and T_R are the sample and reference temperatures respectively. From [9]

The temperature ramp applied to the sample and the reference is linear:

$$T_b(t) = T_i + qt \quad (1)$$

in which T is the temperature at the time t , T_i the initial temperature and q the scanning rate.

The temperature difference is recorded and indirectly related to enthalpy change regarding Newton law. The heat flow absorbed or emitted by the sample is defined as follows:

$$dQ/dt = (dQ_S)/dt - (dQ_R)/dt \quad (2)$$

Where $(dQ_S)/dt$ and $(dQ_R)/dt$ are the heat flow provided to the sample and the reference respectively and expressed as follows:

$$(dQ_S)/dt = 1/R_S (T_b - T_S) \quad (3)$$

$$(dQ_R)/dt = 1/R_R (T_b - T_R) \quad (4)$$

Where T_b , T_R and T_S are the temperature of the furnace, the reference and the sample respectively. R_S and R_R are the thermal resistance associated to the sample and the reference respectively. In such set up, both resistance values are equals ($R_S = R_R = R$). Therefore considering equations (3) and (4), (2) can be simplified as following:

$$dQ/dt = K (T_R - T_S) \quad (5)$$

with $K = 1/R$.

Some specifications have to be precised in the case of the DSC Q100 based on the Tzero TM technology. Such technology uses more complex equations of the heat flow. Thermal resistances R_{SCP} and R_{RCP} , and heat capacities C_{SCP} and C_{RCP} of the sample and the reference cell platforms, respectively, are taken into account in the heat flow expression. Thus, by measuring the temperatures T_S and T_R as a function of a fixed temperature T_0 , the measured heat flow can be expressed as:

$$\frac{dQ}{dt} = K (T_R - T_S) + (T_0 - T_S)(1/R_{SCP} - 1/R_{RCP}) + (C_{RCP} - C_{SCP})\frac{dT_S}{dt} - C \frac{d\Delta T}{dt} \quad (6)$$

As a consequence, a specific calibration procedure was used with the Tzero TM technology. First, a constant heating rate experiment was performed without sample and pan, namely an empty furnace. A second constant heating rate experiment was performed with sapphire disks directly placed on the sample and reference platform. These experiments figure out the resistance and capacitance R_{RCP} , R_{SCP} , C_{RCP} and C_{SCP} of the cell platforms. Then, the calibration in temperature and energy were carried out using standard of indium, by matching the melting temperature ($T_m = 156.6 \text{ }^\circ\text{C}$) and enthalpy ($\Delta H_m = 28.6 \text{ J/g}$) associated. A second

standard, benzophenone ($T_m = 48.0\text{ }^\circ\text{C}$), was used to calibrate the cell in a temperature range from $-70\text{ }^\circ\text{C}$ to $200\text{ }^\circ\text{C}$. The calibrations in temperature and energy have to be repeated if the scanning rate is changed. To ensure a good signal/noise ratio, masses of samples were ranged between 5 and 10 mg. Scanning rate was selected to promote the resolution of investigated thermal events, namely 10 - 20 K/min. All experiments were carried out under nitrogen atmosphere.

B- Modulated temperature DSC (MT-DSC)

During standard DSC experiments, samples generally undergo phase transformations (manifested by a change in the heat flow) that change their physical and/or chemical properties during heating or cooling steps. These transformations include glass transition, crystallization, melting, oxidation, as well as curing, evaporation and so on [11–13], as listed in the previous section. Those reactions may occur at the same time or in the same range of temperature. Thus, the respective heat flows may overlap and become undistinguishable from each other by standard DSC. In MT-DSC measurements, the usually linear temperature program is modulated by a small perturbation, in this case a sine wave (see figure 10) and a mathematical treatment is applied to the resultant data in order to deconvolute the sample response to the perturbation from its response to the underlying heating protocol. In this way the reversible (within the time scale of the perturbation) and irreversible natures of a thermal event can be probed. The advantages include disentangling overlapping phenomena, improving resolution and enhancing sensitivity [11]. The original idea was conceived demonstrated and developed by M. Reading [14].

The sinusoidal temperature profile is superimposed on the underlying linear heating ramp so that the temperature at any time, t , is given by:

$$T_b(t) = T_i + qt + A\sin(\omega t) \quad (7)$$

T_i : initial temperature

q : linear scanning rate (it can vary from 0.01 K/min up to 10 K/min)

A : amplitude of the modulation (it can vary from 0 up to 10 K)

ω : the angular frequency of the temperature modulation (the period of oscillation, $p = 2\pi/\omega$ can vary from 10 to 100 seconds). The three last parameters have to be chosen adequately in order to allow the sample to follow the imposed thermal oscillation and also according to the

nature of the event that is investigated [12]. As reported in figure 10, three temperature modulation modes exist: named heat-only, heat-iso and heat-cool. Heat-only is advised to investigate the coupling of different thermal events such as glass transition and cold crystallization and melting. Heat-iso is advised to investigate melting while heat-cool is advised to investigate the glass transition and the molecular mobility in this region. In this work the heat-only modulation mode was selected.

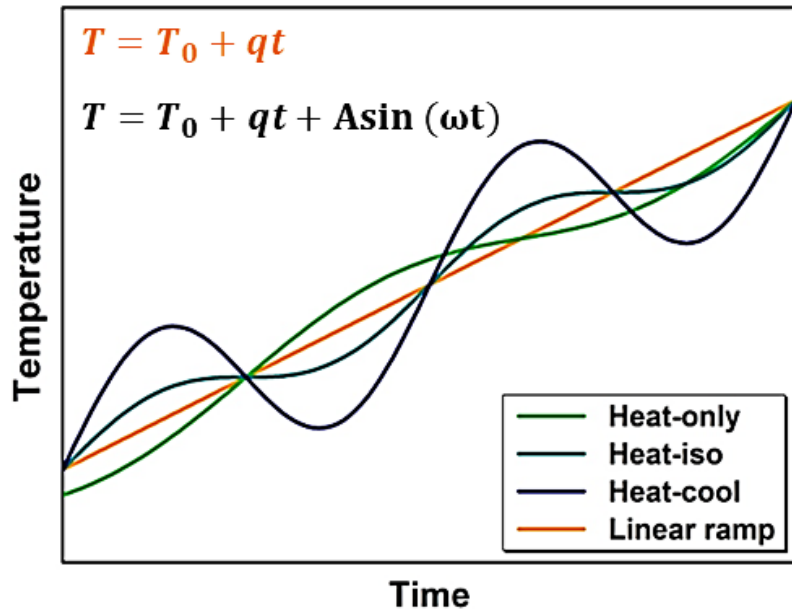


Figure 10: Illustration of heating ramps in MT-DSC experiment with corresponding heat-only (green), heat-iso (cyan), heat-cool (blue) and linear ramp (orange) mode. The modulation amplitude, the period and the scanning rate are [0.318 K; 90 s; 2 K/min], [0.318 K; 60 s; 2 K/min], [1 K; 60 s; 2 K/min] for the three modes displayed, respectively. From [15]

The thermal perturbation felt by the sample can be expressed in term of the derivative of the furnace modulated temperature:

$$d(T_b)/dt = \dot{T}_b(t) = q + \dot{T}_0 \cos(\omega t) \quad (8)$$

With $\dot{T}_0 = A\omega$ the amplitude of the modulation heating rate. Regarding equation (5) the modulated heat flow can be expressed as follows:

$$d(Q(t))/dt = \dot{Q}(t) = \dot{Q}(q) + \dot{Q}_0 \cos(\omega t - \varphi) \quad (9)$$

Where φ is the phase lag between the heating modulation $\dot{T}_b(t)$ and the calorimeter response function $\dot{Q}(t)$. The temporal average of the modulated heat flow is considered identical to the heat flow obtained without modulating (Classical DSC) so that it becomes possible to separate

the mean heat flow $\dot{Q}(q)$ associated to the average scanning rate and the purely modulation contribution.

From Reading original approach [11], the purely modulated contribution of the heat flow thus provides an independent estimation of the specific heat through the expression:

$$C_p = \dot{Q}_0 / \dot{T}_0 \quad (10)$$

Let consider the case of a system where the thermodynamic behavior is governed solely by its heat capacity (defined here as that due to the energy stored in the vibrational, rotational and translational motions of the sample) and independent of time, one can write:

$$(dQ(t))/dt = C_p dT/dt \quad (11)$$

In the case where the system additionally undergoes kinetic evolutions due to chemical reactions or phase transformations (such as recrystallization or enthalpy relaxation) equation (11) becomes:

$$(dQ(t))/dt = C_p dT/dt + f(t, T) \quad (12)$$

where $f(t, T)$ is a kinetical function of time and temperature that governs the kinetic response of any physical or chemical transformation. The first term in equation (12) is the reversible part of the heat flux: it can be measured both in cooling and heating steps. The second term is the irreversible contribution of the heat flow: it is not measured upon cooling. The measurement of the specific heat C_p allows the determination of the so-called "reversible" heat flow by multiplying \dot{Q}_0 / \dot{T}_0 by the average scanning rate q . The "non-reversible" heat flow is obtained by subtracting the "reversible" heat flow from the average heat flow [16].

The MT-DSC experiments were performed with a heat-flux calorimeter DSC Q100 from Thermal Analysis Instruments. The MT-DSC calibration procedure is consists of three different steps. The two first steps are identical to that of classical DSC calibration procedure and was detailed in section II. A. The calibration of the reversing heat capacity is then carried out using sapphire as a heat capacity standard. The sapphire is used as a reference sample for this calibration because it does not undergo any transition in the temperature range scanned for all analyses. The heat capacity of sapphire as a function of temperature is very stable and its value known precisely. Any change to the experimental conditions such as modulation period, heating rate etc. necessitates re-calibration. A correction factor namely K_{Cp} can then be calculated (using the experimental and theoretical specific heat capacity values of sapphire) as a function of temperature according to the giving equation:

$$K_{Cp}(T) = Cp_{sapphire,theoretical}(T)/Cp_{sapphire,experimental}(T) \quad (13)$$

In this way, errors that arise from an imperfect baseline and those derived from inaccuracies in the calibration can be corrected. The calibration factor can be then used to correct the apparent heat capacity of the sample.

Measurements were performed only for Nac-MBA at various enantiomeric excess (since 12H demonstrated a strong crystallization tendency) with a modulation amplitude of 0.318 K, a period of 60 s and a scanning rate of 2 K/min under nitrogen atmosphere at a flow of 20 mL/min. Cooling was ensured by a refrigerated cooling system RCS90 (TA Instruments) equipped with a station of information (Thermal Analysis 2100).

C- Fast Scanning calorimetry (FSC)

Fast Scanning Calorimetry or FSC hereafter device is based on a calorimeter chip using a MultiSTAR UFS 1 sensor provided by METTLER TOLEDO [17]. As illustrated in figure 11 a) the sensor is a micro-calorimeter based on MEMS technology (MEMS: Micro-Electro-Mechanical Systems) and made of two separate identical calorimeters (for sample and reference) made in silicon nitride membranes. FSC operates like a conventional power compensation DSC but without the need of crucibles [18–21]. The membranes of approximately $1.6 \times 1.6 \text{ mm}^2$ area and $2 \text{ }\mu\text{m}$ thickness are suspended in a $300 \text{ }\mu\text{m}$ thick silicon frame. As shown in figure 11 b) the sample area with a diameter of 0.5 mm is in the middle of the membrane. In order to achieve a homogeneous temperature profile the sample area is coated with aluminum. Eight thermocouples polysilicon thermopile measure the temperature elevation of the sample area with respect to the silicon frame, which acts as heat sink. Each sample area has two heater resistances, a main heater for realizing the general temperature scan program and a compensation heater to allow operation in power compensation mode. FSC measurement system can accurately provide cooling from 1 to 4000 K/s and heating scans up to 40.000K/s in a wide range of temperature (from -95°C up to 450°C). These high scanning rates could therefore permit to model industrial production processes for which cooling rates between 1 and 10.000 K/s are required. For example the materials (polymers, aluminum alloys, metallic glasses, etc.) resulting from such industrial processing can be in the form of supersaturated solutions, nanostructures, polymorphic phases, glasses, or other metastable structures. These

metastable materials can also show diffusion or reorganization effects at the typical low scanning rates upon heating, which can lead to misinterpretation of conventional DSC measurements [17]. Furthermore considering the high cooling rate values achieved by this technique, it could permit to avoid recrystallization of most highly crystallogenic systems, and probe the vitreous state or amorphous sample or nucleation and growth phenomena in such compounds.

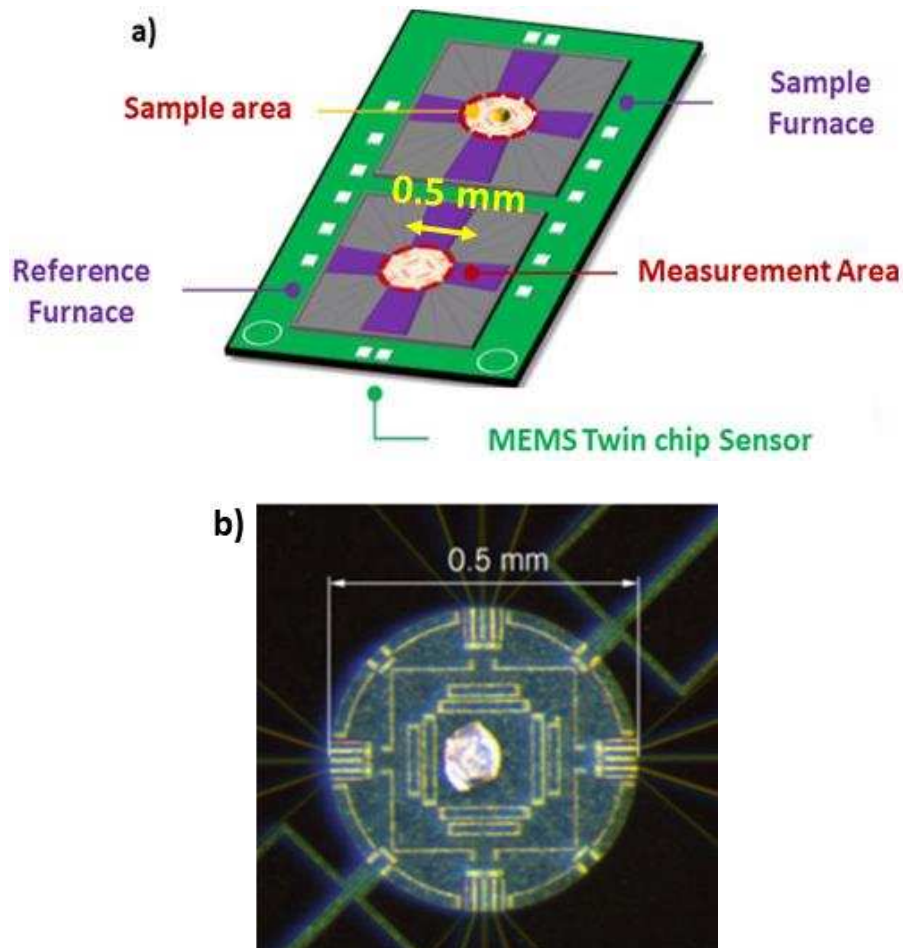


Figure 11: a) Illustration of twin-type chip sensor based on MEMS technology. b) Sample placed on the center of the sample area. From [15,17]

This high scanning rate facilities are made possible thanks to, the less than 1ms time constant of the sensor signal, the small size of the calorimeter (low heat capacity), the low temperature of the surrounding gas and the small value of the thermal resistance. Thus, the sample have to fulfill some requirements [17]:

- In order to follow the fast temperature changes, the sample has to have a good thermal contact to both the calorimeter and the surrounding gas and the heat capacity must be sufficiently small.
- If the bulk behavior of the sample should be measured, surface-induced effects must be suppressed. This requires sufficiently large sample volumes.
- A good thermal contact between the calorimeter and the sensor is also necessary
- To measure the sample temperature: small temperature gradients inside the sample require sufficiently thin samples. In all FSC measurements, the sample thickness was estimated to be $\leq 10 \mu\text{m}$.

Since the applied power compensation principle allows direct measurement of the excess heat flow, and by virtue of the small time constants of the sensor, a calorimetric accuracy of 1–3% can be achieved. Conditioning and correction of the chip were performed according to the manufacturer and prior to measurements. The calibration of the Flash DSC 1 consists of conditioning and correction procedures. The conditioning procedure checks the proper behavior of the sensor. Potential memory effects from its production are erased by heating the sensor to the maximum temperature (450 °C). Then, the correction temperature is performed in order to correct the thermocouple signal with respect to the sensor support temperature. The correction is done by comparing the signal of the thermocouples with the temperature behavior of the heating resistances, which was determined during production. For FSC measurements cooling was ensured down to -70°C by a Huber TC100 intracooler at variable rates. The powder sample was submitted to a nitrogen purge gas flow at a rate of 20 ml/min and placed on the sample chip area (0.5mm of diameter) by the mean of an optical microscope and a long fiber for sample positioning.

Preparation of the sample: a first chip was used for the pure enantiomer and a second for the samples taken from the racemic batch or mixtures of both. Despite a pre-milling (manually) of the powder to ensure homogenization, the experimental constraints on the sample size cannot permit to isolate or ensure an equimolar proportion between enantiomers during the sampling from the racemic batch. Thus, the sampling from the racemic batch may lead to samples at scalemic compositions (*i.e.* ee is different from 0% and 100%) and only the thermal signature of the samples could give an approximation of their enantiomeric compositions (this will be detailed in the result chapter). Measurements: A first pre-melting step was launched

to ensure a good thermal contact between the sample and the sensor. The sample mass was estimated using an equivalence DSC- FSC based on the thermal properties of the liquid or the glassy state linked to the sample mass. These properties can be either the melting enthalpy, ΔH_m or the heat capacity jump at the glass transition region, ΔC_p [17]. In this work, the sample mass used for FSC analyses was determined using either equation (14) or (15):

$$m (FSC) = \frac{\Delta H_m(FSC)}{\Delta H_m(DSC)} \times m (DSC) \quad (14)$$

Or

$$m (FSC) = \frac{\Delta C_p(FSC)}{\Delta C_p(DSC)} \times m (DSC) \quad (15)$$

Where ΔH_m (or ΔC_p) represents the area of the melting pic (or the heat capacity jump at T_g) normalized by the cooling rate and $m (DSC)$ the sample mass used for DSC analysis. In this work, the glass forming ability, the kinetical behavior of the glass transition, the structural enthalpy relaxation and the recrystallization behavior of both 12H and Nac-MBA systems were analyzed at different enantiomeric compositions. The results are presented and discussed in chapter III, the main point being the impact of chirality in the recrystallization behavior and the kinetic of enthalpy recovery.

D- Temperature Resolved X-Ray Diffraction (TR-XRD)

This technique is generally used for structural identification of crystallized solid. By comparing the angular position and the peak intensity, it can be conceived as a “fingerprint” of this specific crystalline packing. In case of an amorphous material, the powder diagram obtained does not exhibit any fine and intense peak, but a large maximum of low intensity (see figure 12). Other applications can be explored, like the quantifications of mixtures, or, in favored cases, the structure determination. The principle of XRD consists in the diffraction of an incident X-ray beam by the crystallographic planes of the crystal structure. When a monochromatic beam of X-rays, wavelength λ , reaches a crystal, it is diffracted by the atoms regularly packed in the structure. The direct consequence is the appearance of constructive or destructive interferences, which results in increasing or decreasing the intensity of the diffracted beam. The intensity of the diffracted beam is recorded as a function of the diffraction angle θ . For a given incidence angle of X-rays, some crystallographic planes will therefore satisfy the Bragg condition. The intensity of this beam will be non-zero only at those diffraction angles at which the Bragg condition is satisfied: $n\lambda = 2d_{hkl}\sin(\theta)$, where d_{hkl} is the spacing of the crystalline lattice planes with indices hkl and n is an integer. Thus, an analysis inside a sufficient range of Bragg angle (θ) will give a specific pattern, characteristic of a solid phase (for example, polymorphs of a given molecule can be differentiated by this technique).

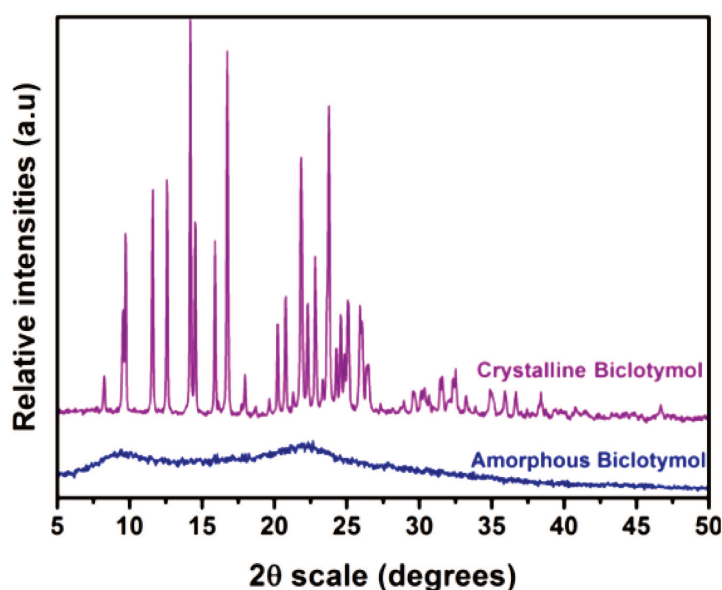
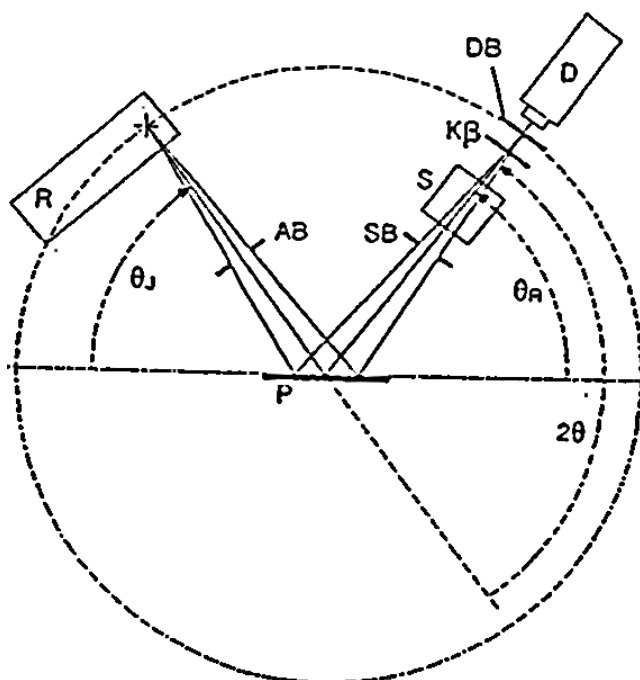


Figure 12: XRPD patterns recorded at room temperature from Bicletymol samples. Top purple diffractogram corresponds to crystalline stable Form I. Bottom blue diffractogram corresponds to melt-quenched sample. From [22]

In this work, X-ray diffraction data were recorded on a model D5005 diffractometer (Siemens-Bruker). The X-Ray tube is equipped with a copper anticathode and a $k\beta$ filter (Ni). The analysis step was set at 0.08° with a counting time of 4s / step in the range 3 to 30° (2θ). These analyzes were resolved in temperature by means of a heating plate TTK 450 (Anton Paar) coupled with a Lauda RP890 intracooler for low temperatures. At each temperature, the analysis lasted 22 minutes and the heating rate between each temperature step was fixed at $2K / \text{min}$. The set-up of a diffractometer is displayed in figure 13



Caption:

- | | |
|---------------------------------|--------------------------------|
| R: X- Ray tube; | θ_J : incidence angle; |
| AB: incidence beam diaphragm; | P: sample; |
| θ_R : diffraction angle; | SB: diffracted beam diaphragm; |
| S: Soller slot; | K_β : filter; |
| D: detector; | DB: detector diaphragm. |

Figure 13: Pathway of the X-Ray beam inside a θ/θ diffractometer. From [23]

E- Dielectric Relaxation Spectroscopy

1. Principle and basics on dielectrics

In dielectric measurements, the material is submitted to an alternating electric field created by application of a voltage. Therefore, a symmetric distribution of electric charge results from the application of the field; this phenomenon is known as electric polarization \vec{P} . It originates from two main microscopic processes: the induced or deformation and orientational polarizations. The induced polarization \vec{P}_{ind} arises from small displacements of electrons (electronic polarization) \vec{P}_e and nuclei (atomic polarization) \vec{P}_n under the influence of an external applied electric field, while the orientational polarization \vec{P}_{or} emanates from the rotational motions of permanent dipoles under the effect of an external applied field. In a system of freely floating dipoles there are no restoring forces tending to impose a preferred direction to the dipole vectors, only the randomizing influence of the thermal agitation. In such conditions the polarization is zero. Conversely, when an electric field is applied to a system of freely floating dipoles, a preferred direction will be imposed to the dipoles, thus creating a given amount of orientational and induced polarizations. Figure 14 illustrates the behavior of the dipoles in a dielectric material in absence and presence of an external electric field E [25,26].

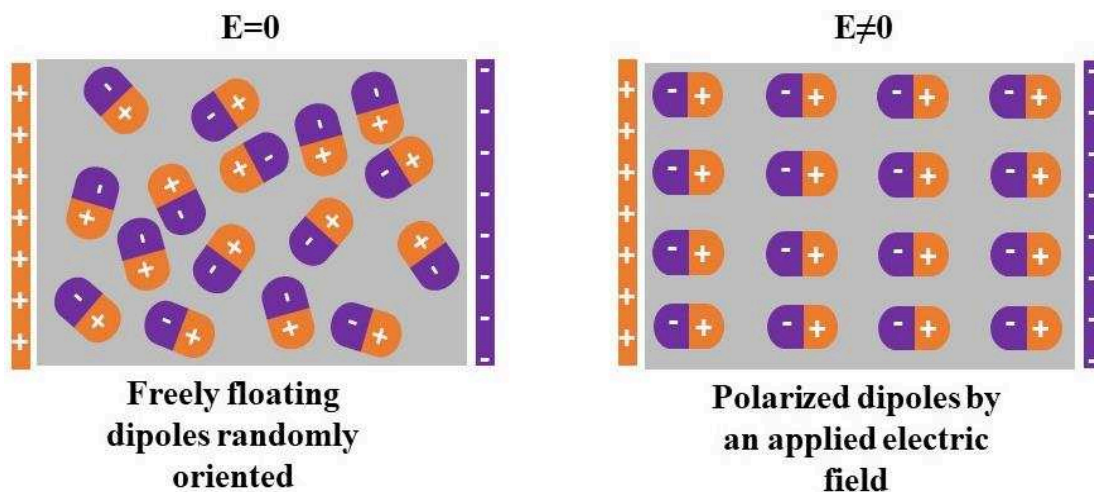


Figure 14: Dipole orientations of a dielectric material in absence and presence of an external perturbation hereby an electric field E

Consequently, in the presence of a steady electric field, the total polarization is given by equation (16):

$$\vec{P} = \vec{P}_{ind} + \vec{P}_{or} \quad (16)$$

For moderate electric fields (negligible nonlinear effects) the total created polarization is directly proportional to the field intensity.

$$\vec{P}(\omega) = \epsilon_0 (\epsilon_r - 1) \vec{E}(\omega) \quad (17)$$

where ϵ_0 is the permittivity of vacuum, ϵ_r the relative permittivity.

Considering an applied electric field, switched at a moment $t = t_1$, the induced polarization P_{ind} increases suddenly, while the orientational polarization P_{or} increases much more slowly (due to intermolecular frictions) and reaches a maximum value P_s at $t = t_2$ in such a way that:

$$P_{ind} = \epsilon_0 (\epsilon_\infty - 1) E \quad (18)$$

and

$$P_s = \epsilon_0 (\epsilon_s - 1) E \quad (19)$$

where ϵ_∞ and ϵ_s are the dielectric permittivity in the high frequency limit and static permittivity of the material respectively. Therefore from these two expressions one can obtain the saturated orientation polarization as:

$$P_o = \epsilon_0 (\epsilon_s - \epsilon_\infty) E \quad (20)$$

Let's switch off the field at $t = t_2$, the induced polarization decreases rapidly while the orientation polarization requires sufficiently long time to completely decay. The phenomenon of decrease and increase in the orientational polarization is known as dielectric relaxation [24,25]. Mathematically we can describe the increase in $P_o(t)$ in the time domain by the following differential equation:

$$\tau_D \frac{dP_{or}(t)}{dt} = P_o - P_{or}(t) \quad (21)$$

τ_D is a characteristic relaxation time, which is the same for all molecules in the material. This differential equation is a conventional feature in mathematic physics. A solution is given by:

$$P_{or}(t) = P_o [1 - \exp(-t/\tau_D)] \quad (22)$$

The latter situation describing the time evolution of the polarization is illustrated in figure 15.

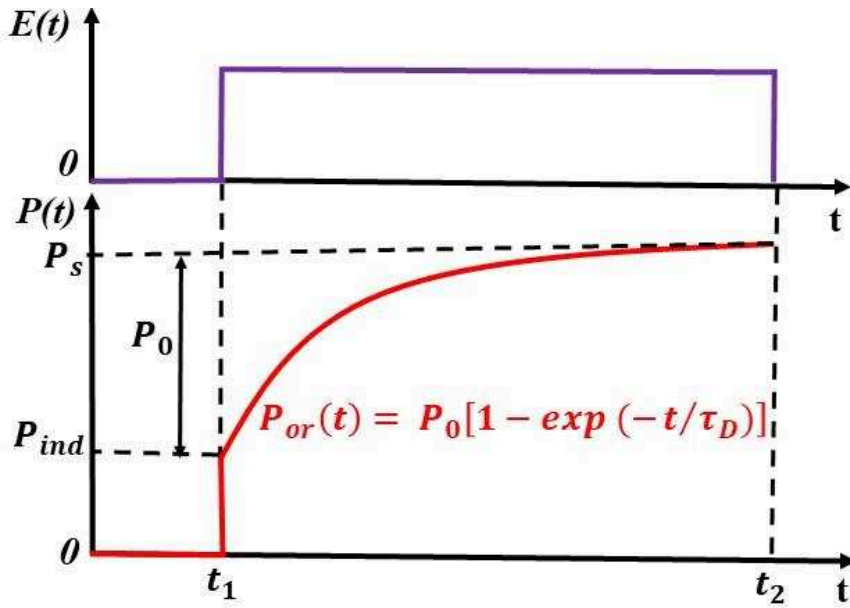


Figure 15: Time evolution of the polarization $P(t)$ due to an applied external rectangular impulse of the electric field $E(t)$

Now, let's consider an electric alternating electric field of the complex form $E_0 e^{i\omega t}$ (applied field $(t) = E_0 \cos(\omega t)$), the validity of equation 21 is not questionable and can be rewritten as follows:

$$\tau_D \frac{dP_{or}^*(t)}{dt} = \epsilon_0 (\epsilon_s - \epsilon_\infty) E_0 e^{i\omega t} - P_{or}^*(t) \quad (23)$$

A solution of this equation is:

$$P_{or}^*(t) = \frac{\epsilon_0 (\epsilon_s - \epsilon_\infty)}{1 + i\omega\tau_D} E_0 e^{i\omega t} \quad (24)$$

From equations 18 and 24 the total polarization is:

$$P^*(t) = \epsilon_0 (\epsilon_\infty - 1) E^*(t) + \frac{\epsilon_0 (\epsilon_s - \epsilon_\infty)}{1 + i\omega\tau_D} E^*(t) \quad (25)$$

Taking into consideration equations 23 and 25, the response of a dielectric sample submitted to an external alternating electric field can be described in terms of complex dielectric permittivity expressed as:

$$\epsilon^*(\omega) = \epsilon'(\omega) - i\epsilon''(\omega) = \epsilon_\infty + \frac{\epsilon_s - \epsilon_\infty}{1 + i\omega\tau_D} \quad (26)$$

where $\epsilon'(\omega)$ and $\epsilon''(\omega)$ are the real and imaginary parts of the complex permittivity representing the dielectric dispersion and absorption respectively. This is the simplest model of dipole relaxation known as the Debye model.

Considering a dipole molecular motion characterized by a relaxation time τ , and assuming that the frequency of the alternating field is low enough so that $\omega\tau \ll 1$, the field is allowed to fully polarize the orientational part of the polarization, and the real part of the relative permittivity $\epsilon'(\omega)$ (in-phase with the field) is the static relative permittivity, ϵ_s . Additionally, since the total polarization is in phase with the electric field, the imaginary part of permittivity $\epsilon''(\omega)$ is zero. On the contrary if the frequency of the field is high enough in such a way that $\omega\tau \gg 1$, the dipoles do not have sufficient time to polarize and the observed low dielectric constant denoted ϵ_∞ , is only due to induced effects and deformation. As it was in the previous case, $\epsilon''(\omega)$ is also zero because the induced polarization is in-phase with the polarizing field. At last when $\omega\tau \cong 1$ (namely the dispersion region) there is a decrease of $\epsilon'(\omega)$ from ϵ_s to ϵ_∞ . At the same time $\epsilon''(\omega)$ will show values different from zero since in these conditions, part of the polarization is out of phase with the field (See figure 16) [24].

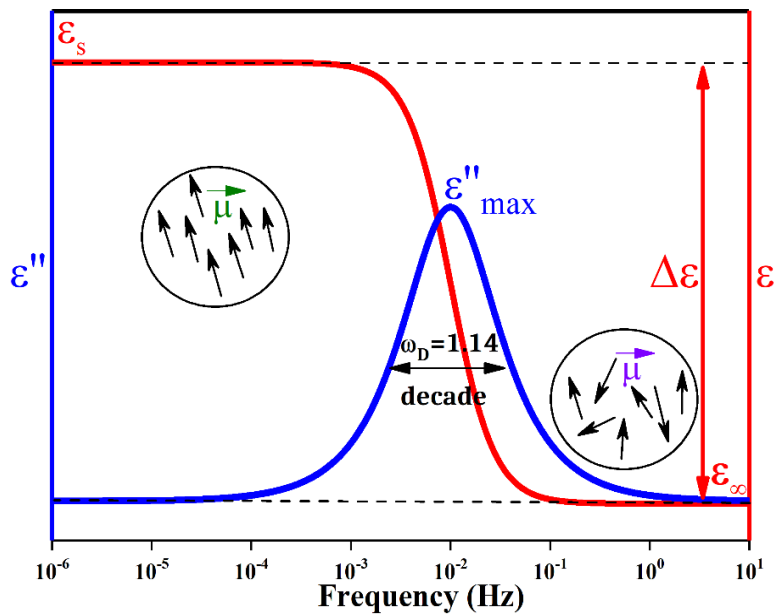


Figure 16: Schematic frequency evolution of both imaginary and real permittivities for a Debye relaxation, $\vec{\mu}$ is the permanent dipole moment vector, $\epsilon_s = \lim_{\omega \rightarrow 0} \epsilon'(\omega)$,

$\epsilon_\infty = \lim_{\omega \rightarrow \infty} \epsilon'(\omega)$ and ω_D is the half height width of the dielectric loss peak

From the Debye model of single dipolar molecular motion [26] it can be shown that:

$$\epsilon'(\omega) = \epsilon_\infty + \frac{\epsilon_s - \epsilon_\infty}{1 + (\omega\tau_D)^2} \quad (27)$$

$$\epsilon''(\omega) = (\epsilon_s - \epsilon_\infty) \frac{\omega\tau_D}{1 + (\omega\tau_D)^2} \quad (28)$$

As illustrated in figure 16 $\varepsilon''(\omega)$ presents a peak, the so called dielectric loss peak, with a half-height width of 1.14 decades in frequency and a maximum at f_{max} related to the characteristic relaxation time of the reorienting dipoles τ_D ($\tau_D = 1/2\pi f_{max}$). The location of this peak provides the easiest way of obtaining the relaxation time from experimental results. The dielectric strength $\Delta\varepsilon = \varepsilon_s - \varepsilon_\infty$ defined as the difference between the dielectric constant measured at low and high frequencies gives the magnitude of the relaxation process. This parameter is related to the permanent dipole moment $\vec{\mu}$ and the number of relaxing dipoles per unit of volume, N through the Onsager relation $\Delta\varepsilon \sim N\mu^2$ [cited in 26].

2. Relaxation models

The Debye model is usually suitable for simple polar liquids but rapidly becomes inappropriate in more complex systems. For the latter, the dielectric functions are broader and more asymmetric than a Debye function. Consequently, the molecular motions of all dipoles in the sample cannot be characterized by the single relaxation time τ_D . A phenomenological approach to deal with the broadening is to consider that the enlargement in the response is due to the heterogeneity of the environment nearest to the reorienting dipoles. From this heterogeneity concept, molecular motions can be seen as a distribution of single Debye processes with different relaxation times [24,27–29]. The concept of dynamical heterogeneities was also investigated by Berthier and defined as special variations in the local relaxation rate instead as a distribution of single Debye processes [30]. Hoang and coworkers proposed recent contributions to the understanding of this concept of dynamical heterogeneities [31,32]. Even though this concept of heterogeneity is largely used to explain the apparent stretching of the α -relaxation function, Arbe and coworkers [33] showed that the stretching is mostly due to sublinear diffusion than to heterogeneities itself. Different empirical functions are proposed to describe experimental dielectric spectra presenting a non-Debye behavior in the frequency domain. This function helps to extract valuable information about the relaxation process. The top three most used empirical equations are Cole-Cole, Cole-Davidson and Havriliak-Negami functions. They can be generalized as follows:

$$\varepsilon^*(\omega) = \varepsilon_\infty + \frac{\varepsilon_s - \varepsilon_\infty}{[1 + (i\omega\tau)^x]^y} \quad (29)$$

When $y = 1$ and $0 < x \leq 1$ Cole-Cole (CC) function [34].

When $x = 1$ and $y = \beta$ ($0 < \beta \leq 1$) Cole-Davidson (CD) function [35].

When $x = 1 - \alpha$ and $y = \beta$ ($0 \leq \alpha < 1$) and ($0 < \beta \leq 1$) Havriliak-Negami (HN) function [36]. As depicted in figure 17, α value (symmetric broadening parameter) is related to the broadness of the distribution of relaxation times, while β to its asymmetry. The Debye model is obtained when $x = y = 1$. The Havriliak-Negami model is a generalization of the Debye, Cole-Cole and Cole-Davidson models. Since it has two adjustable parameters, it can describe with greater success isolated relaxation process. Usually many relaxation processes occur at the same temperature over several decades. In these cases the experimental data can be fitted with a sum of HN functions, while considering each function associated to each process. The shape parameter $\alpha_{HN} = 1 - \alpha$ and $\beta_{HN} = \beta$ describe the slope of the dielectric loss peak ϵ'' in the low and high frequency limits with reference to f_{max} : $\alpha_{HN} = \frac{\partial \log \epsilon''}{\partial \ln \omega}$ for $f \ll f_{max}$ and $\alpha_{HN}\beta_{HN} = -\frac{\partial \log \epsilon''}{\partial \ln \omega}$ for $f \gg f_{max}$. The characteristic relaxation rate $\tau_{max} = 1/2\pi f_{max}$, where f_{max} is the frequency of the outer electric field at which a maximum in ϵ'' occurs, can be easily obtained from the fitted τ_{HN} and shape parameters from the HN function through the equation:

$$\tau_{max} = \tau_{HN} \left[\sin \left(\frac{\alpha_{HN}\pi}{2+2\beta_{HN}} \right) \right]^{-\left(\frac{1}{\alpha_{HN}}\right)} \left[\sin \left(\frac{\alpha_{HN}\beta_{HN}\pi}{2+2\beta_{HN}} \right) \right]^{\left(\frac{1}{\alpha_{HN}}\right)} \quad (30)$$

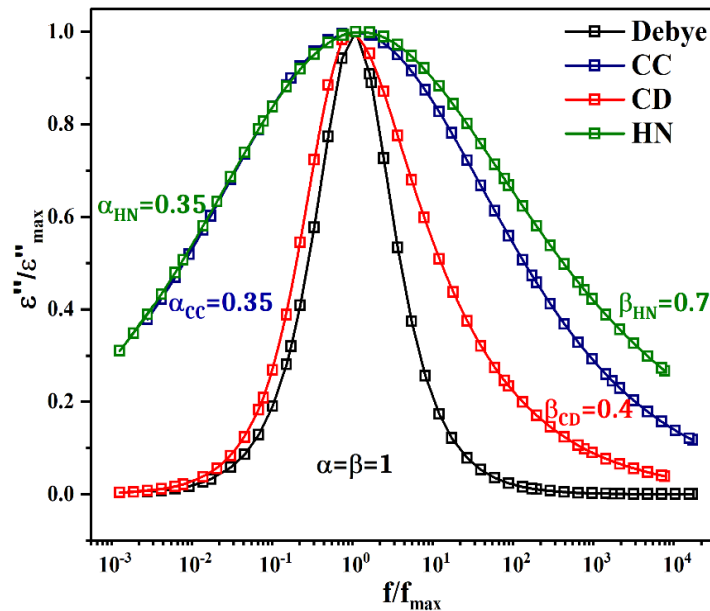


Figure 17: Simulated master curves of dielectric loss illustrating the symmetric and asymmetric broadening of the loss peak

Dielectric spectra can be described not only in the frequency domain but also in the time domain. The most empirical model used for this purpose is the Kohlrausch-Williams-Watts function (KWW) known as the stretched exponential law given by:

$$\Phi(t) = \exp\left[-\left(\frac{t}{\tau_{KWW}}\right)^{\beta_{KWW}}\right] \quad (31)$$

where τ_{KWW} is the characteristic KWW relaxation time, and the exponent $0 < \beta_{KWW} \leq 1$ gives the deviation of the time-dependent relaxation from the Debye exponential function ($\beta_{KWW} = 1$). The stretched exponential function behavior matches with the idea of an asymmetric response described in the framework of the HN model. A relationship among the two parameters of both models is suggested by the fact that both models yield an accurate description of real data. Alegria and co-workers [37] proposed a comparison relation between the fitting parameters of both models expressed by equations 32 and 33:

$$\beta_{KWW} \approx (\alpha_{HN} \beta_{HN})^{\frac{1}{1.23}} \quad (32)$$

and

$$\ln\left[\frac{\tau_{HN}}{\tau_{KWW}}\right] = 2.6(1 - \beta_{KWW})^{0.5} \exp(3\beta_{KWW}) \quad (33)$$

3. Dielectric Measurements and Calibration

a. Low frequency range 0.1 Hz – 1 MHz

Dielectric measurements were performed using high quality interdigitated gold plated electrodes, IE (BDS1410-20-150) purchased from Novocontrol GmbH. The electrode is a round shape 20 mm diameter gold plated copper layers with 35 μm thickness and a comb structure for convenient sample attachment. The spacing between the comb fingers and their width are both 150 μm . Prior to sample deposition, the electrode was calibrated by measuring its respective geometric (empty cell) capacity, C_0 , and substrate capacity, C_{su} , through measurement of a standard material with known permittivity (B-oil; Vacuubrand). As the substrate material of the IE has a low loss factor ($\tan \delta = 0.001$) and the substrate real part permittivity being approximately constant over frequency and temperature, the calibration procedure [38] can be simplified if the permittivity of the electrode substrate ϵ_{su}^* is approximated by a real constant ϵ_{su} . For a selected frequency (*e.g.* 10 kHz), the capacity of the empty electrode without sample material attached $C_e^*(\omega)$ and the capacity of the

electrode with the calibration oil attached C_c^* (permittivity ϵ_s^*) are measured. The total capacity is determined considering that the upper and lower electrodes constitute two independent volumes generating two independent capacitors [39,40] with a total capacity of:

$$C_m^* = C_0(\epsilon_s^*(\omega) + \epsilon_{su}(\omega)) \quad (34)$$

with

$$C_0 = \frac{C_c^*(\omega) - C_e^*(\omega)}{\epsilon_c^*(\omega)} \quad (35)$$

The complex frequency-dependent permittivity ($\epsilon^*(f) = \epsilon'(f) - i\epsilon''(f)$, where $f = \omega/2\pi$ is the frequency, ϵ' is the storage permittivity, and ϵ'' is the loss permittivity) was measured over the range 10^{-1} Hz – 2MHz using an Alpha-A analyzer from Novocontrol Technologies GmbH. Sample preparation and amorphization steps were performed *ex situ*. Almost 150 mg of the crystalline powder was deposited on the IE then heated above the liquidus temperature at 110°C and annealed 5 min to guarantee complete melting. The melt was then promptly quenched in liquid nitrogen in order to ensure total amorphization. Dielectric spectra were collected isothermally from -120°C up to 0°C with a suitable consecutive step.

b - High frequency range 1 MHz – 1 GHz

Measurements were performed in the range 1 MHz – 1 GHz by means of a coaxial line reflectometer based on the impedance analyzer HP 4191 from Novocontrol Technologies GmbH. Prior to measurements, two successive calibration steps were achieved: Line and sample cell calibrations. Samples were prepared in parallel plate geometry between two gold-plated electrodes of 10 mm diameter, separated by silica spacers of 50 μ m thickness. The prepared sample was connected to the end of the coaxial line, and then melted *in situ* and annealed for 5min at 110°C. Isothermal frequency scans were carried out from 110 °C down to 20 °C, in steps of 10 °C. A Quatro Cryosystem (Novocontrol Technologies GmbH) was used to control the temperature with a stability of ± 0.2 K for both low and high frequency domains.

4- Molecular Dynamics Simulations (MDS)

Molecular dynamics (MD) simulations have been performed using the DL_POLY package [41] and the GAFF force field (General Amber Force Field) [42]. This force field was chosen due to its capability of reproducing successfully large number of experimental data of low molecular weight molecules [43]. As recommended for the GAFF force field [42], atomic partial charges were calculated from ab-initio computations using the Gaussian 03 programme [44] at the HF/6-31G* level with the restrained electrostatic potential (RESP) fitting approach. For the electrostatic interactions, a pairwise damped shifted method developed by Wolf [45] was used. For both van der Waals and electrostatic interactions, the same cutoff radius of 10 Å was employed. Periodic boundary conditions were applied in all directions. The time step to integrate Newton's equation of motion was chosen to 0.001 ps. The MD simulations were performed only for Nac-MBA system. The modelled system possesses a total number of N = 64 molecules composed of (-) Nac-MBA and (+) Nac-MBA molecules in order to obtain an enantiomeric excess of 0%, 50%, 75% and 100% respectively. Simulations have been conducted either in the NPT or NVT statistical ensemble where P is the pressure, T the temperature and V the volume. Pressure and temperature were controlled with a Nose-Hoover barostat and thermostat respectively. All NPT simulations were realized at atmospheric pressure. The Nosé Hoover thermostat and barostat relaxation times have been set at 0.2 and 2.0 ps respectively. The equilibrated volume of the simulation box during the NPT simulation was considered to compute the averaged density of system and used to perform the subsequent production simulation in the NVT ensemble. MD simulations were performed at five temperatures 500K, 450K, 400K, 360K and 340K. The equilibration/production times range from 10/200 ns to 20/800 ns from the highest to the lowest investigated temperature.

The following chapter details some calorimetric results on the amorphous state of chiral 12H at several enantiomeric compositions by means of DSC and FSC.

References

- [1] N. Takamura, S. Terashima, K. Achiwa, S. Yamada, Studies on optically active amino acids. XV. Studies on alpha-alkyl-alpha-amino acids. 8. Absolute configuration of optically active alpha-methylserine and 2-amino-2-methyl-3-butenoic acid, *Chem. Pharm. Bull. (Tokyo)*. 15 (1967) 1776–1784.
- [2] S. Beilles, P. Cardinael, E. Ndzié, S. Petit, G. Coquerel, Preferential crystallisation and comparative crystal growth study between pure enantiomer and racemic mixture of a chiral molecule: 5-ethyl-5-methylhydantoin, *Chem. Eng. Sci.* 56 (2001) 2281–2294. doi:10.1016/S0009-2509(00)00442-5.
- [3] C. Gervais, S. Beilles, P. Cardinaël, S. Petit, G. Coquerel, Oscillating Crystallization in Solution between (+)- and (-)-5-Ethyl-5-methylhydantoin under the Influence of Stirring, *J. Phys. Chem. B.* 106 (2002) 646–652. doi:10.1021/jp012622s.
- [4] E. Ndzie, Etude de la nucléation et de la croissance cristalline au cours du dédoublement par cristallisation préférentielle auto-ensemencée de dérivés 5-méthyl-5-alkyl (ou 5-aryl) hydantoïnes, thesis, Rouen, 1998. <http://www.theses.fr/1998ROUES072> (accessed January 2, 2019).
- [5] S. Druot, M.N. Petit, S. Petit, G. Coquerel, N.B. Chanh, Experimental Data and Modelling of the Interactions in Solid State and in Solution between (R) and (S) N-Acetyl- α -Methylbenzylamine. Influence on Resolution by Preferential Crystallization, *Mol. Cryst. Liq. Cryst. Sci. Technol. Sect. Mol. Cryst. Liq. Cryst.* 275 (1996) 271–291. doi:10.1080/10587259608034081.
- [6] E. Brown, M. Moudachirou, Agents de dédoublement. 2. Synthèse d'aryluréthanes de l'acide (S)-lactique et leur utilisation dans le dédoublement de bases racémiques, *Tetrahedron*. 50 (1994) 10309–10320. doi:10.1016/S0040-4020(01)81763-4.
- [7] S. Druot Houllémare, Influence des interactions homo- et heterochirales lors du dédoublement par cristallisation préférentielle de deux dérivés de l' α -methylbenzylamine: le n-acetamide et le chloroacetate, thesis, Caen, 1999. <http://www.theses.fr/1999CAEN2029> (accessed January 2, 2019).
- [8] A. Aubry, J. Protas, M.T. Cung, M. Marraud, Conformation et interactions moléculaires à l'état solide de la (-)-(S)-N-(phényl-1 éthyl)-acetamide (C₁₀H₁₃NO), *Acta Crystallogr. Sect. B.* 36 (1980) 1861–1864. doi:10.1107/S0567740880007376.
- [9] K. Kv, A. Sr, Y. Pr, P. Ry, B. Vu, Differential Scanning Calorimetry: A Review., *Res. Rev. J. Of Pharmaceutical Anal.* 3 (2014) 11–22.
- [10] S.-D. Clas, C.R. Dalton, B.C. Hancock, Differential scanning calorimetry: applications in drug development, *Pharm. Sci. Technol. Today.* 2 (1999) 311–320. doi:10.1016/S1461-5347(99)00181-9.
- [11] M. Reading, A. Luget, R. Wilson, Modulated differential scanning calorimetry, *Thermochim. Acta.* 238 (1994) 295–307. doi:10.1016/S0040-6031(94)85215-4.

- [12] O. Bustin, Relaxation structurale des matériaux vitrifiables par calorimétrie à balayage modulé, thesis, Lille 1, 1999. <http://www.theses.fr/1999LIL10116> (accessed January 2, 2019).
- [13] M. Reading, D.J. Hourston, eds., Modulated Temperature Differential Scanning Calorimetry: Theoretical and Practical Applications in Polymer Characterisation, Springer Netherlands, 2006. [//www.springer.com/de/book/9781402037498](http://www.springer.com/de/book/9781402037498) (accessed January 2, 2019).
- [14] M. Reading, B.K. Hahn, B.S. Crowe, Method and apparatus for modulated differential analysis, US5224775A, 1993. <https://patents.google.com/patent/US5224775A/en> (accessed January 2, 2019).
- [15] X. Monnier, Mobilité moléculaire dans des systèmes polymères complexes anisotropes et confinés, thesis, Normandie, 2017. <http://www.theses.fr/2017NORMR021> (accessed January 2, 2019).
- [16] B. Wunderlich, Y. Jin, A. Boller, Mathematical description of differential scanning calorimetry based on periodic temperature modulation, *Thermochim. Acta.* 238 (1994) 277–293. doi:10.1016/S0040-6031(94)85214-6.
- [17] J.E.K. Schawe, S. Pogatscher, Material Characterization by Fast Scanning Calorimetry: Practice and Applications, in: C. Schick, V. Mathot (Eds.), *Fast Scanning Calorim.*, Springer International Publishing, Cham, 2016: pp. 3–80. doi:10.1007/978-3-319-31329-0_1.
- [18] E. Zhuravlev, C. Schick, Fast scanning power compensated differential scanning nanocalorimeter: 1. The device, *Thermochim. Acta.* 505 (2010) 1–13. doi:10.1016/j.tca.2010.03.019.
- [19] E. Zhuravlev, C. Schick, Fast scanning power compensated differential scanning nanocalorimeter: 2. Heat capacity analysis, *Thermochim. Acta.* 505 (2010) 14–21. doi:10.1016/j.tca.2010.03.020.
- [20] S. van Herwaarden, E. Iervolino, F. van Herwaarden, T. Wijffels, A. Leenaers, V. Mathot, Design, performance and analysis of thermal lag of the UFS1 twin-calorimeter chip for fast scanning calorimetry using the Mettler-Toledo Flash DSC 1, *Thermochim. Acta.* 522 (2011) 46–52. doi:10.1016/j.tca.2011.05.025.
- [21] V. Mathot, M. Pyda, T. Pijpers, G. Vanden Poel, E. van de Kerkhof, S. van Herwaarden, F. van Herwaarden, A. Leenaers, The Flash DSC 1, a power compensation twin-type, chip-based fast scanning calorimeter (FSC): First findings on polymers, *Thermochim. Acta.* 522 (2011) 36–45. doi:10.1016/j.tca.2011.02.031.
- [22] B. Schammé, Mobilité moléculaire, mécanismes de cristallisation et stabilité physique de composés pharmaceutiques amorphes : impact des méthodes de préparation, thesis, Rouen, 2016. <http://www.theses.fr/2016ROUES049> (accessed January 7, 2019).
- [23] N. Couvrat, Four case studies on the impact of the heterogeneous equilibria on physicochemical behaviour of organic solids, 2011. <http://www.theses.fr/s149502> (accessed January 3, 2019).

- [24] M.S.C. Dionísio, H.P. Diogo, J.P.S. Farinha, J.J. Moura-Ramos, Rotational Mobility in a Crystal Studied by Dielectric Relaxation Spectroscopy. An Experiment for the Physical Chemistry Laboratory, *J. Chem. Educ.* 82 (2005) 1355. doi:10.1021/ed082p1355.
- [25] K. Grzybowska, K. Adrjanowicz, M. Paluch, Application of Broadband Dielectric Spectroscopy to Study Molecular Mobility in Pharmaceutical Systems, in: *Disord. Pharm. Mater.*, Wiley-Blackwell, 2016: pp. 301–360. doi:10.1002/9783527652693.ch11.
- [26] C.J.F. Böttcher, CHAPTER V - THE DIELECTRIC CONSTANT IN THE CONTINUUM APPROACH TO THE ENVIRONMENT OF THE MOLECULE, in: *Theory Electr. Polariz. Second Ed.*, Elsevier, Amsterdam, 1973: pp. 159–204. doi:10.1016/B978-0-444-41019-1.50011-0.
- [27] K. Grzybowska, K. Adrjanowicz, M. Paluch, Application of Broadband Dielectric Spectroscopy to Study Molecular Mobility in Pharmaceutical Systems, in: *Disord. Pharm. Mater.*, Wiley-Blackwell, 2016: pp. 301–360. doi:10.1002/9783527652693.ch11.
- [28] F. Kremer, A. Schönhals, The Scaling of the Dynamics of Glasses and Supercooled Liquids, in: *Broadband Dielectr. Spectrosc.*, Springer, Berlin, Heidelberg, 2003: pp. 99–129. doi:10.1007/978-3-642-56120-7_4.
- [29] M. Dionísio, J.F. Mano, Chapter 7 - Electric Techniques, in: M.E. Brown, P.K. Gallagher (Eds.), *Handb. Therm. Anal. Calorim.*, Elsevier Science B.V., 2008: pp. 209–268. doi:10.1016/S1573-4374(08)80010-6.
- [30] L. Berthier, Dynamic heterogeneity in amorphous materials, *Physics*. 4 (2011). doi:10.1103/Physics.4.42.
- [31] K. Paeng, H. Park, D.T. Hoang, L.J. Kaufman, Ideal probe single-molecule experiments reveal the intrinsic dynamic heterogeneity of a supercooled liquid, *Proc. Natl. Acad. Sci.* (2015) 201424636. doi:10.1073/pnas.1424636112.
- [32] V. Van Hoang, V. Teboul, T. Odagaki, New Scenario of Dynamical Heterogeneity in Supercooled Liquid and Glassy States of 2D Monatomic System, *J. Phys. Chem. B.* 119 (2015) 15752–15757. doi:10.1021/acs.jpcc.5b08912.
- [33] A. Arbe, J. Colmenero, M. Monkenbusch, D. Richter, Dynamics of Glass-Forming Polymers: “Homogeneous” versus “Heterogeneous” Scenario, *Phys. Rev. Lett.* 81 (1998) 590–593. doi:10.1103/PhysRevLett.81.590.
- [34] K.S. Cole, R.H. Cole, Dispersion and Absorption in Dielectrics I. Alternating Current Characteristics, *J. Chem. Phys.* 9 (1941) 341–351. doi:10.1063/1.1750906.
- [35] D.W. Davidson, R.H. Cole, Dielectric Relaxation in Glycerol, Propylene Glycol, and n-Propanol, *J. Chem. Phys.* 19 (1951) 1484–1490. doi:10.1063/1.1748105.
- [36] S. Havriliak, S. Negami, A complex plane analysis of α -dispersions in some polymer systems, *J. Polym. Sci. Part C Polym. Symp.* 14 (n.d.) 99–117. doi:10.1002/polc.5070140111.
- [37] F. Alvarez, A. Alegria, J. Colmenero, Relationship between the time-domain Kohlrausch-Williams-Watts and frequency-domain Havriliak-Negami relaxation functions, *Phys. Rev. B.* 44 (1991) 7306–7312. doi:10.1103/PhysRevB.44.7306.

- [38] Novocontrol Interdigitated Electrodes, (n.d.). https://www.novocontrol.de/php/sa_cell_interd.php (accessed January 7, 2019).
- [39] Z. Chen, A. Sepúlveda, M.D. Ediger, R. Richert, Dielectric spectroscopy of thin films by dual-channel impedance measurements on differential interdigitated electrode arrays, *Eur. Phys. J. B.* 85 (2012) 268. doi:10.1140/epjb/e2012-30363-0.
- [40] A. Dhotel, Z. Chen, J. Sun, B. Youssef, J.-M. Saiter, A. Schönhals, L. Tan, L. Delbreilh, From monomers to self-assembled monolayers: the evolution of molecular mobility with structural confinements, *Soft Matter.* 11 (2014) 719–731. doi:10.1039/C4SM01893A.
- [41] W. Smith, T.R. Forester, DL_POLY_2.0: A general-purpose parallel molecular dynamics simulation package, *J. Mol. Graph.* 14 (1996) 136–141. doi:10.1016/S0263-7855(96)00043-4.
- [42] J. Wang, R.M. Wolf, J.W. Caldwell, P.A. Kollman, D.A. Case, Junmei Wang, Romain M. Wolf, James W. Caldwell, Peter A. Kollman, and David A. Case, 'Development and testing of a general amber force field' *Journal of Computational Chemistry*(2004) 25(9) 1157–1174, *J. Comput. Chem.* 26 (2005) 114–114. doi:10.1002/jcc.20145.
- [43] C. Caleman, P.J. van Maaren, M. Hong, J.S. Hub, L.T. Costa, D. van der Spoel, Force Field Benchmark of Organic Liquids: Density, Enthalpy of Vaporization, Heat Capacities, Surface Tension, Isothermal Compressibility, Volumetric Expansion Coefficient, and Dielectric Constant, *J. Chem. Theory Comput.* 8 (2012) 61–74. doi:10.1021/ct200731v.
- [44] M. Frisch, G. Trucks, H. Schlegel, G. Scuseria, M. Robb, J. Cheeseman, J. Montgomery, T. Vreven, K. Kudin, J. Burant, J. Millam, S. Iyengar, J. Tomasi, V. Barone, B. Mennucci, M. Cossi, G. Scalmani, N. Rega, G. Petersson, H. Nakatsuji, M. Hada, M. Ehara, K. Toyota, R. Fukuda, J. Hasegawa, M. Ishida, T. Nakajima, Y. Honda, O. Kitao, H. Nakai, M. Klene, X. Li, J. Knox, H. Hratchian, J. Cross, V. Bakken, C. Adamo, J. Jaramillo, R. Gomperts, R. Stratmann, O. Yazyev, A. Austin, R. Cammi, C. Pomelli, J. Ochterski, P. Ayala, K. Morokuma, G. Voth, P. Salvador, J. Dannenberg, V. Zakrzewski, S. Dapprich, A. Daniels, M. Strain, O. Farkas, D. Malick, A. Rabuck, K. Raghavachari, J. Foresman, J. Ortiz, Q. Cui, A. Baboul, S. Clifford, J. Cioslowski, B. Stefanov, G. Liu, A. Liashenko, P. Piskorz, I. Komaromi, R. Martin, D. Fox, T. Keith, A. Laham, C. Peng, A. Nanayakkara, M. Challacombe, P. Gill, B. Johnson, W. Chen, M. Wong, C. Gonzalez, J. Pople, Gaussian 03, Revision C.02, (n.d.).
- [45] D. Wolf, P. Keblinski, S.R. Phillpot, J. Eggebrecht, Exact method for the simulation of Coulombic systems by spherically truncated, pairwise r^{-1} summation, *J. Chem. Phys.* 110 (1999) 8254–8282. doi:10.1063/1.478738.

CHAPTER III:

CHIRALITY EFFECTS ON AMORPHOUS 5-ETHYL-5-METHYLHYDANTOIN

The highlights of this chapter have been published in international journal of pharmaceutics: Impact of chirality on the glass forming ability and the recrystallization from the amorphous state of 5-ethyl-5-methylhydantoin, a chiral poor glass former [1].

In this work, the investigation of the glassy state of 5-ethyl-5methylhydantoin (*i.e.* 12H) was attempted by Differential Scanning Calorimetry (DSC) and Fast Scanning Calorimetry (FSC). This study aims thus at isolating amorphous states of enantiopure and racemic 12H, in order to determine their physical differences in terms of glass forming ability and, crystallization propensity (and by extension to predict chirality implications on the glassy state of conglomerate forming systems).

I- Calorimetric investigations of 12H

1- Classical DSC Measurements

Figure 1 displays the thermal behavior of both pure enantiomer and racemic mixture upon heating and cooling (at 10 °C/min and 50 °C/min respectively). Upon heating, only a single thermal event corresponding to the melting of each compound is mentioned. The melting point of both pure enantiomer and racemic composition are, $T_m(\text{R or S}) = 173 \pm 2^\circ\text{C}$ and $T_m(\text{RS}) = 140 \pm 2^\circ\text{C}$ respectively. The melting enthalpies are $\Delta H_m(\text{R or S}) = 21 \pm 1 \text{ kJ}\cdot\text{mol}^{-1}$ ($\Delta S_m(\text{R or S}) = 47 \text{ J}\cdot\text{mol}^{-1}\cdot\text{K}^{-1}$) and $\Delta H_m(\text{RS}) = 18 \pm 1 \text{ kJ}\cdot\text{mol}^{-1}$ ($\Delta S_m(\text{RS}) = 50.8 \text{ J}\cdot\text{mol}^{-1}\cdot\text{K}^{-1}$) for the pure enantiomer and racemic composition respectively (and the corresponding melting entropy). All these results are in accordance with the literature data [2]. Upon cooling, recrystallization was not inhibited despite the applied cooling rate. These observations support the highly crystallogenic character of this molecule. Other attempts to vitrify the liquid by applying higher cooling rates in the range [100 - 250] °C/min resulted in failure. Another possibility remained quenching directly (manually) the melt of both samples in liquid nitrogen. Nevertheless, this possibility was quickly put aside. Actually, during the quenching, an extremely fast crystal growth occurred leaving no chance for vitrification.

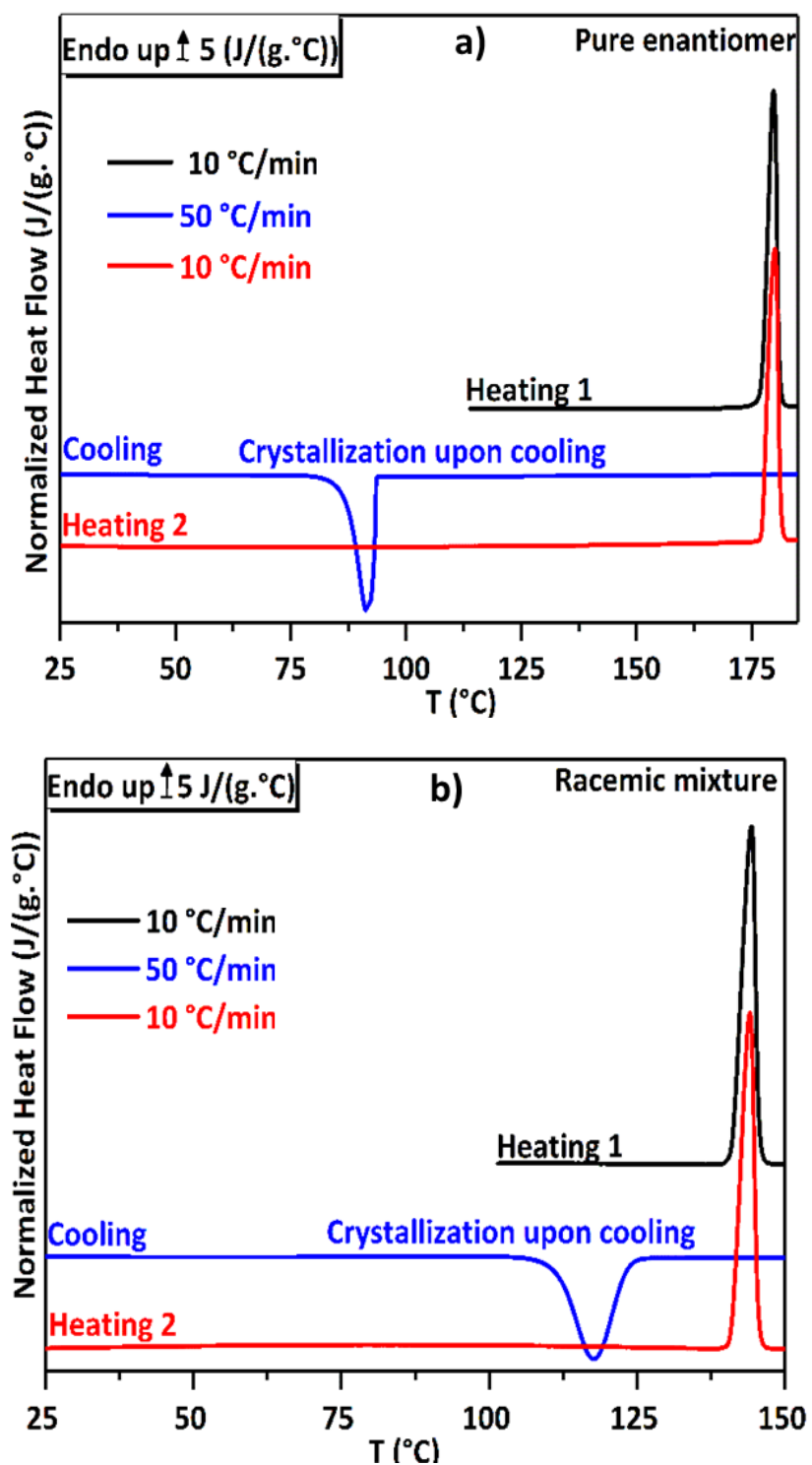


Figure 1: Heating and cooling curves of a) pure enantiomer and b) racemic mixture in classical DSC

Considering that the glass formation probability increases when fast cooling is provided [3–5], vitrification and crystallization propensities of 12H were apprehended by FSC.

2- FSC Measurements

In FSC analyses, the sample is directly deposited on the chip and is heated from the bottom part in contact with the chip. Hence, there is a thermal gradient dependent from sample thermal conductivity and size [6]. Dynamic and static temperature gradients linked to the sample size and the high scanning rate during FSC experiments are reported in literature [7]. The dynamic thermal lag at the glass transition is corrected by averaging T_g values on cooling and on heating. This dynamic thermal lag can be neglected for small organic compounds if three conditions are fulfilled: i) a good thermal contact is ensured between the sample and the sensor, ii) the sample thickness is lower than 10 μm and iii) the heating rate is low enough (circa 1000 °C/s) [6]. The static thermal gradient is essentially due to the temperature difference between the furnace and its immediate environment. This effect is mostly impacted by the sample thickness. As reported in the case of polystyrene [7], the static thermal lag becomes obvious when the thickness of the sample is > 10 μm. Thickness calculation was purchased based on simple geometric considerations. We assume that the samples are 3D cylindrical objects with different geometrical bases. The sample volume can be determined knowing the density of the crystal lattice (d=1.28) and the sample mass. Consequently knowing the area occupied by the sample on the chip, one can determine its thickness. Figure 2 depicts images of four samples of different masses (from 19 to 120 ng) noted (a), (b), (c), (d) and table 1 summarizes the sample geometrical characteristics.

Table 1: Geometrical characteristics of samples (a), (b), (c) and (d)

Sample mass (ng)	Volume 10 ¹ (μm ³)	Surface (μm ²)	Thickness (μm)
(a) 19	1484	2294	6.5
(b) 35	2734	3853	7.0
(c) 50	3906	8482	4.6
(d) 120	9375	10993	8.5

In this study, all sample thicknesses were estimated below 10 μm and thermal lag effects were then considered as negligible.

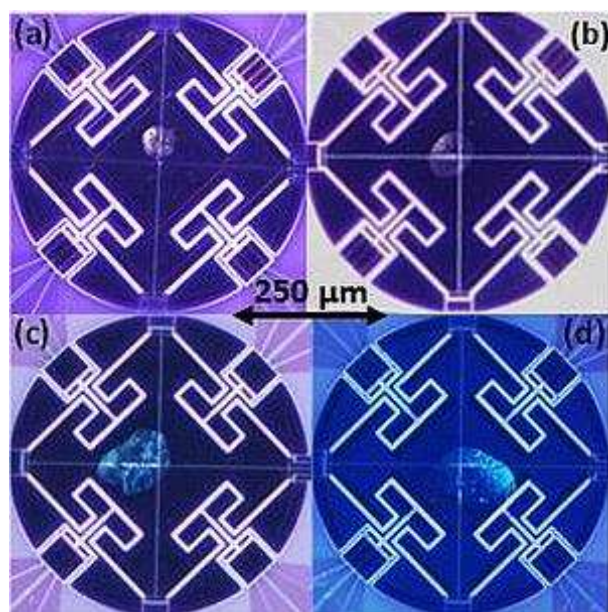


Figure 2: Premelted samples with different geometric parameters. Sample (a) 19 ng, (b) 35 ng, (c) 50 ng, (d) 120 ng.

3- Pure Enantiomer

a) Amorphization vs Crystallization: case of enantiopure 12H

Figure 3 illustrates the thermal signature of pure enantiomer upon cooling and the second heating at the same rates. First, the recorded melting temperature was consistent with the value obtained by classical DSC (175°C) as shown in figure 3. Thus, cooling rates higher than 500 °C/s were required to inhibit recrystallization and fully amorphize enantiopure 12H. The thermal signature of the glass transition was well illustrated by an endothermal steep jump of the heat flow at T_g . The latter was measured on cooling and no obvious cooling rate dependency was noticed: $T_{g(\text{onset})} = 16 \pm 2^\circ\text{C}$. Nevertheless, at cooling rates of 300 °C/s and 500 °C/s, partial crystallization was evidenced. Cold crystallization remained unavoidable when the compound was heated from the amorphous state, even at 3000 °C/s. Cold crystallization was always followed by an endothermal peak corresponding to the melting of enantiopure 12H.

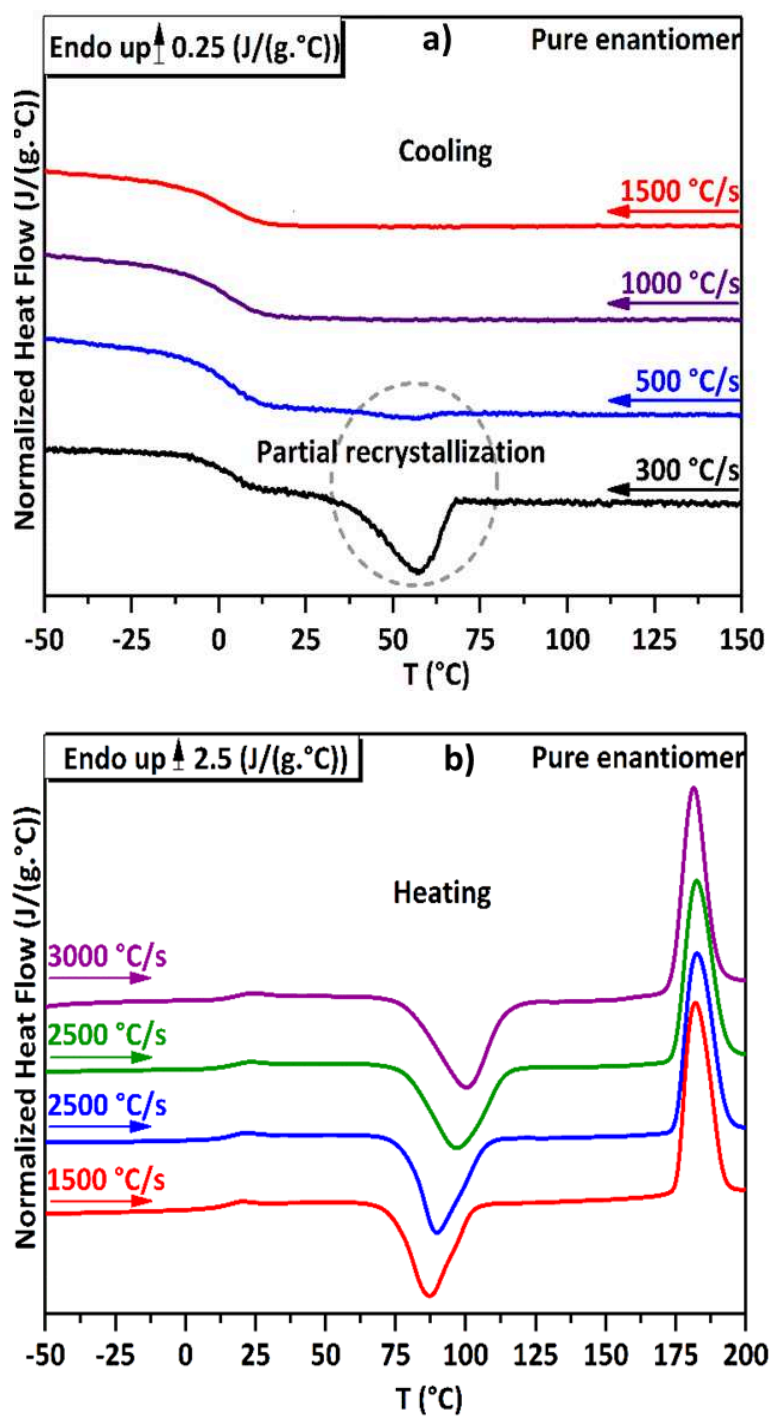


Figure 3: Thermal events of enantiopure 12H upon a) cooling and b) second heating at variable cooling and heating rates.

b) Maxima of nucleation and growth rates of pure enantiomer

The thermodynamic understanding of this fast crystallization tendency, passes through the localization of both nucleation and crystal growth temperature domains. In order to determine the temperature region where nucleation and growth maxima are located, a cyclic heat-cool protocol and annealing step at various temperatures well below and above T_g (from -50°C to 80°C) was applied. This thermal protocol consisted in cooling the melted sample at 1500°C/s down to an annealing temperature. The sample was kept for 30min at the annealing temperature and heated at 3000°C/s up to 210°C . As depicted in figure 4, no thermal event occurred upon heating when the annealing step was achieved from 70°C and beyond. For isotherms performed in the range -10°C to 60°C , crystallization took place during the isotherm and upon heating, melting occurred at the pure enantiomer melting point. Annealing performed at -50°C and -30°C led to an overshoot peak at the glass transition region upon heating. Cold crystallization was evidenced in the range 75°C to 130°C and melting at 173°C (enantiopure melting point). The nuclei formed at lower temperatures during the annealing and heating steps inevitably undergoes crystallization in the range 75°C to 130°C . The crystal growth rate is apparently very high in this temperature domain. But the localization of the temperature region where nucleation rate is at his maximum is not obvious in this case. Whatever the annealing temperature (from $T_g - 66^{\circ}\text{C}$ to $T_g + 44^{\circ}\text{C}$), complete crystallization occurred during annealing or heating. Consequently the melting enthalpies obtained were almost similar. Indeed, nucleation takes place well below T_g up to $T_g + 44^{\circ}\text{C}$. These results and their implications are discussed in section II.3.

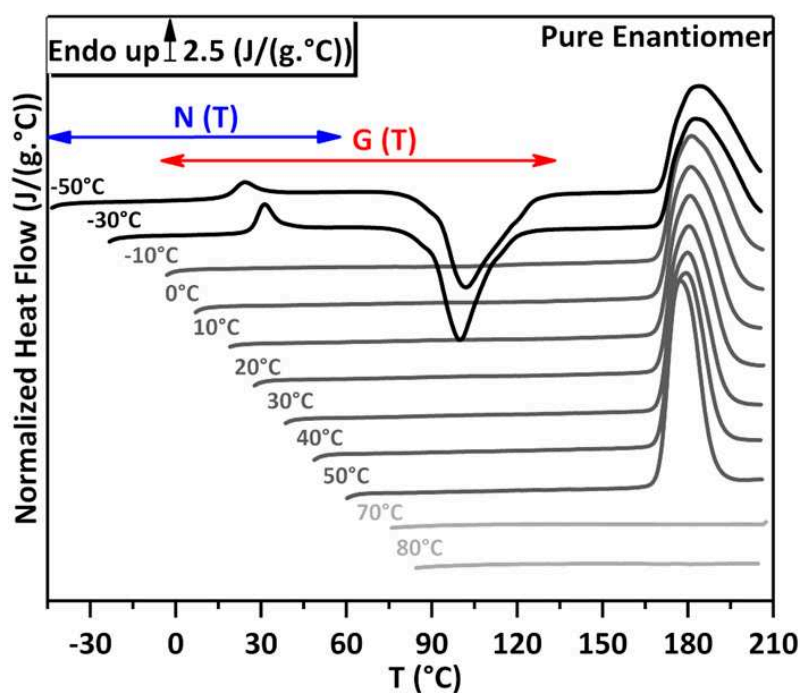


Figure 4: FSC scans of pure enantiomer recorded upon heating at 3000 °C/s after the melt was cooled at different isothermal temperatures T_a (from -50 °C to 80 °C) and annealed for 30 min. $N(T)$ and $G(T)$ refers as the nucleation growth temperature region respectively

4- Scalemic Composition ($0 \leq ee < 100\%$)

a) Amorphization vs Crystallization: case of scalemic 12H

In this section all the analyses were carried out with samples coming from the racemic batch. As depicted in the previous chapter, the sampling limitations imposed by FSC sampling method prevented to analyze a real racemic sample but only a scalemic (intermediate) composition close to the racemic one. Figures 5a and 5b present the thermal signature of such 12H sample upon melt cooling and heating from the amorphous state respectively. Full vitrification of the melt was achieved upon cooling (even at 300 °C/s). $T_{g \text{ (onset)}} = 16 \pm 2^\circ\text{C}$ was determined from cooling measurements. Upon heating, cold crystallization appears (figure 5b) and the shape of the peak is highly heating rate dependent. The exothermic crystallization peak was broadened and shifted towards higher temperatures as the heating rate increased. Furthermore, the crystallization enthalpy decreased as the heating rate increased. For heating rates lower than 3000 °C/s, the melting event was characterized as complex peak resulting

4- Scalemic Composition ($0 \leq ee < 100\%$)

from the overlapping of two successive endotherms. The first peak has an onset temperature around 130°C , and the onset temperature of the second peak could be extrapolated to 135°C . At 3000°C/s , only one endothermal peak was recorded with an onset temperature around 135°C .

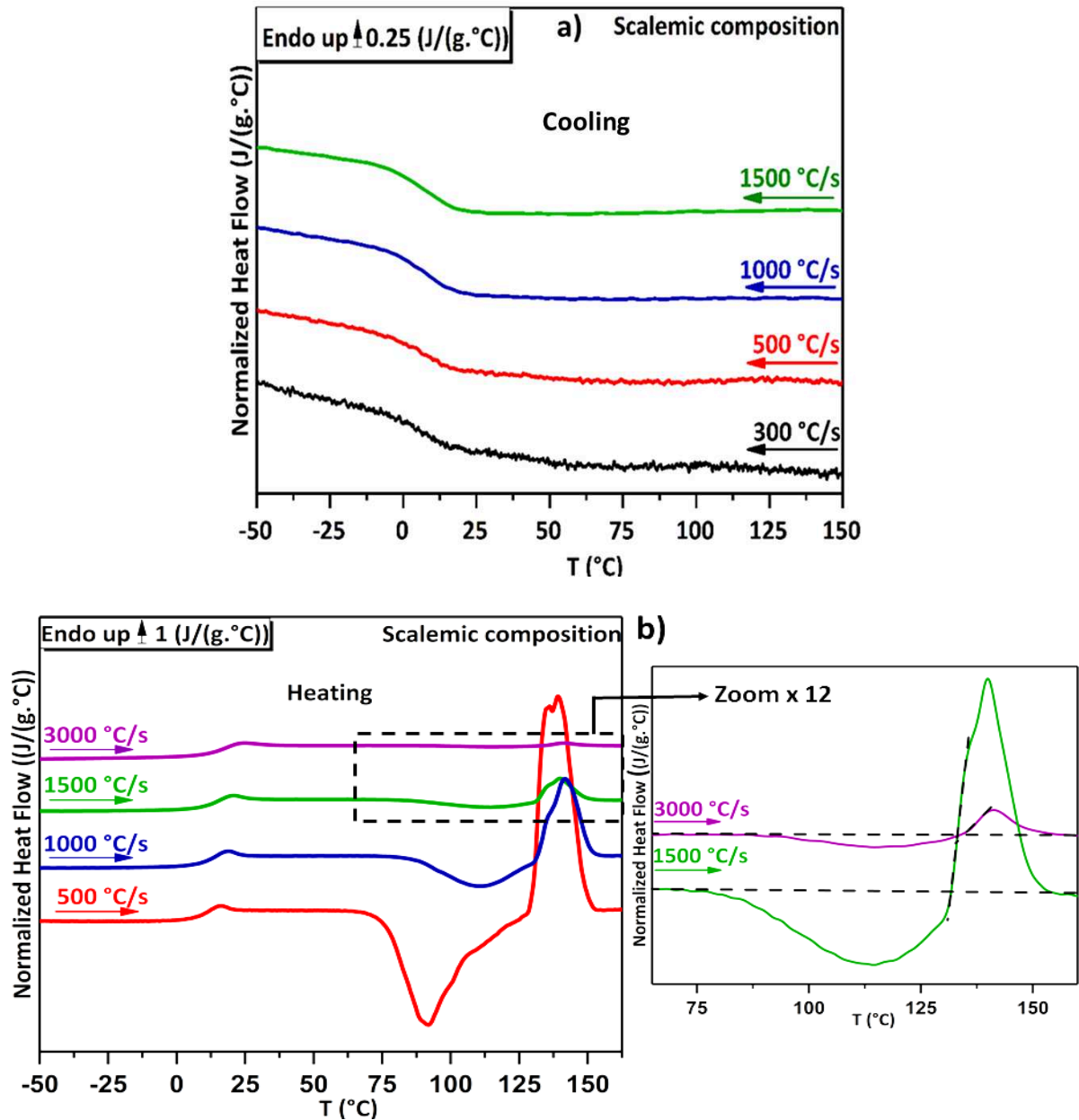


Figure 5: a) Thermal events upon cooling and b) upon heating for the sample at a scalemic composition

One may think that the presence of successive endothermic peak may be due to a slight difference in the melting point of both enantiomers. But regarding figure 6 no such difference of the melting temperature can be mentioned.

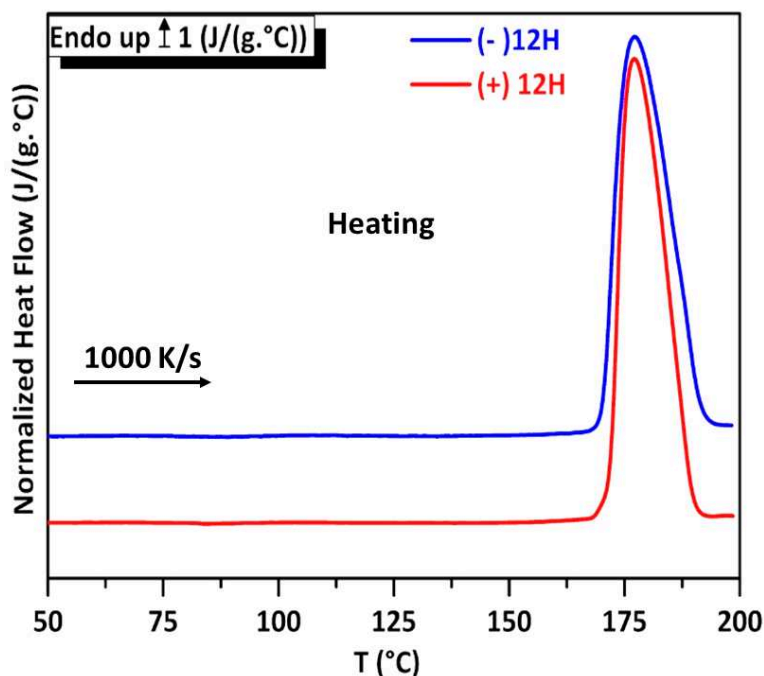


Figure 6: FSC melting curves of both 12H enantiomers

b) Maxima of nucleation and growth rates: scalemic 12H

As in the case of pure enantiomer, the identification of the temperature region where nucleation and crystal growth maxima are located was launch for the scalemic sample. The same cyclic melting-quenching to different annealing temperatures was applied for the same annealing time. This thermal protocol consisted in quenching at 1500 °C/s the melted sample at various annealing temperatures ranging from -50°C to 90°C. The annealing step was launch for 30 min and the sample reheated at 3000 °C/s up to 175°C. Figure 7 presents the heating curves after the annealing process. No thermal event was mentioned when the sample was held at $T_a \geq 70^\circ\text{C}$, consequently no crystallization occurred during the annealing or the quenching-heating steps. When the annealing temperature T_a was in between 10°C and 50°C, the sample fully recrystallized during the annealing period and a single endothermic peak was evidenced at 128°C. Heating the annealed sample at 0°C, led to a well-defined exothermic peak from 60°C to 110°C followed by melting at 128°C with the same melting enthalpy as for

4- Scalemic Composition ($0 \leq ee < 100\%$)

the previous annealing temperatures. Nucleation occurs from $T_g - 16^\circ\text{C}$ up to $T_g + 34^\circ\text{C}$ and crystal growth velocity is specially high from 60°C up to 110°C .

For annealing between -50°C and -10°C , recrystallization was always evidenced in the range 90°C to 125°C during the heating step. The recrystallized samples melt at 133°C and the enthalpy of crystallization same as the melting enthalpy increase as the annealing temperature increases. As the isothermal temperature increases from -50°C up to -10°C , the number of nuclei formed during the annealing step increases. Therefore the maximum of nucleation rate is approximatively located at $T_g - 26^\circ\text{C}$. At the glass transition region an overshoot peak is mentioned synonym of an aging effect.

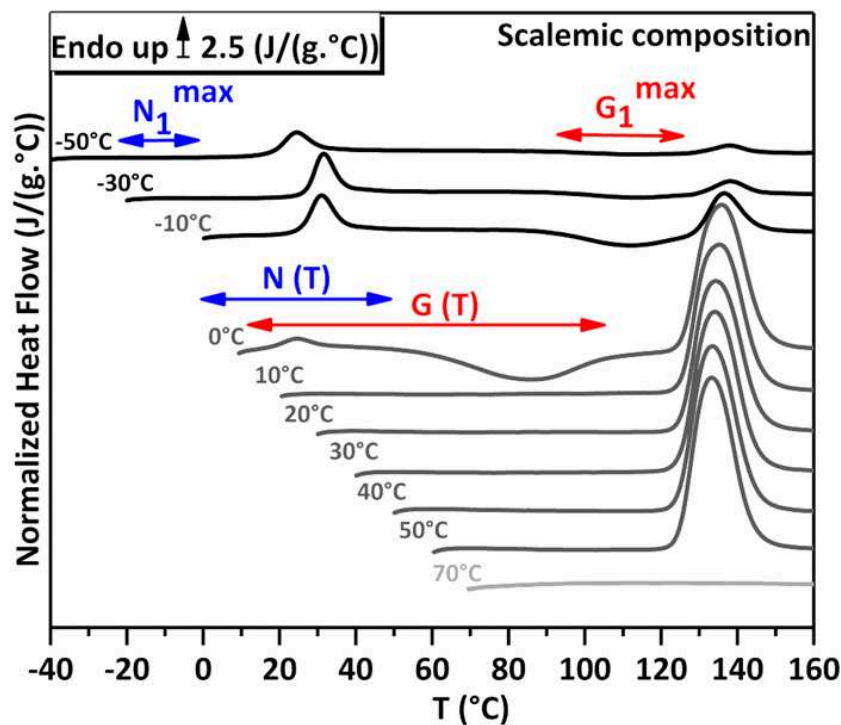


Figure 7: FSC curves of scalemic 12H recorded upon heating at 3000°C/s after the melt was cooled at different isothermal temperatures T_a (from -50°C to 70°C) and annealed for 30 min. $N(T)$ and $G(T)$ refers as the nucleation growth temperature region respectively

c) Thermal lag verification and sampling limitations

Thermal lag effects: As detailed in the introduction of section I.2, the thermal lag effects have to be considered regarding the sample size; more precisely its thickness. In order to evaluate at which extent thermal lag effects may impact the calorimetric signature, analyses were carried out with different samples of variable masses (from 19 ng up to 120 ng) taken from the same racemic batch. The samples presented identical thermal signatures at the glass transition region and the same T_g values at a constant heating rate. As illustrated in figure 8, only the kinetical character of the glass transition was observed (a shift of 1 to 2°C) when the heating rate was increased from 500 °C/s to 1000 °C/s or 1500 °C/s. Thus, the thermal lag effect on T_g can be considered as negligible for these experiments.

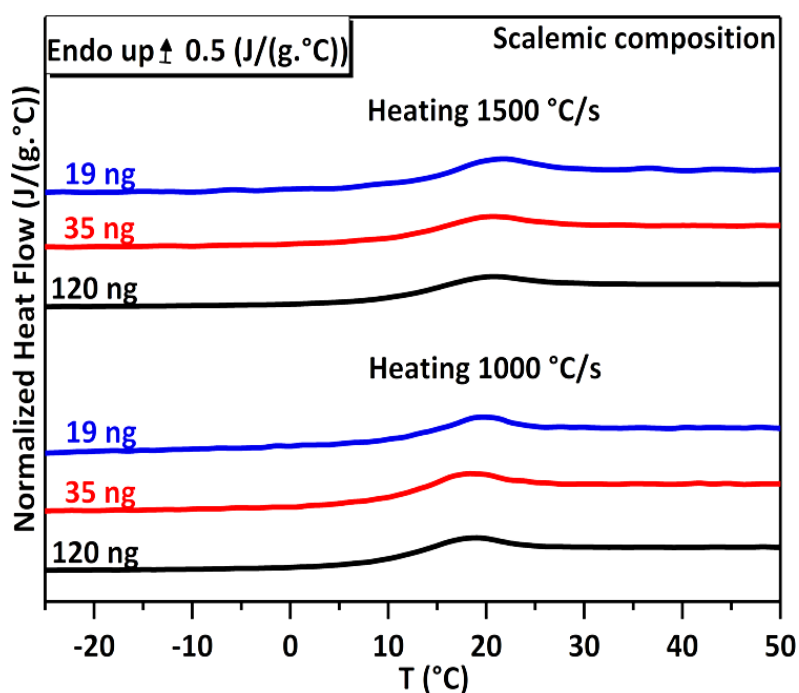


Figure 8: Glass transition signature at 1000 °C/s and 1500 °C/s for three samples (scalemic composition) with increasing masses.

FSC Sampling limitations: Generally the variation of the enantiomeric composition leads to different thermal signatures upon heating. In order to illustrate the difficulty of sampling reproducibility (enantiomeric composition, sample mass or sample thickness), analyses were carried out for seven samples prepared from the racemic batch. The thermal treatment consisted in quenching the melt at 1000 °C/s to ensure vitrification and then heating the glassy materials at 500 °C/s. The sample mass lied between 19 ng to 120 ng and the thermal behaviors upon heating are summarized in figure 9. The thermal events, at higher temperature strongly depend on the samples. Independently of the sample mass, three distinct thermal behaviors can be observed. Samples (1), (3) and (6) exhibited a similar thermal signature: a crystallization process followed by a triple endothermic peak. The crystallization process was well separated from the first endothermic peak. The enthalpy of the third endothermic event (arrow peak) increased as the sample mass increased. Samples (4) and (5) presented no thermal events apart from the glass transition signature. And finally, samples (2) and (7) presented a crystallization process followed by a double endothermic peak but the end of the crystallization peak was immediately followed by the endothermic processes. Due to steric hindrance effects, the required time for molecules of one enantiomer in the supercooled liquid to regain their crystalline configurations will be increased as the sample contains the two opposite enantiomers. Independently from the fact that pure enantiomer has a poor GFA compared to the scalemic composition, the temperature region where crystallization takes place, was shifted towards higher temperatures with the counter-enantiomer for the same scanning rate. Considering that this shift of temperature increases when the ee decreases, a classification of the samples of figure 9 may be established based on their behaviors upon re-heating: $ee = 0\% \leq ee$ samples ((4), (5)) < ee samples ((2), (7)) < ee samples ((1), (3), and (6)).

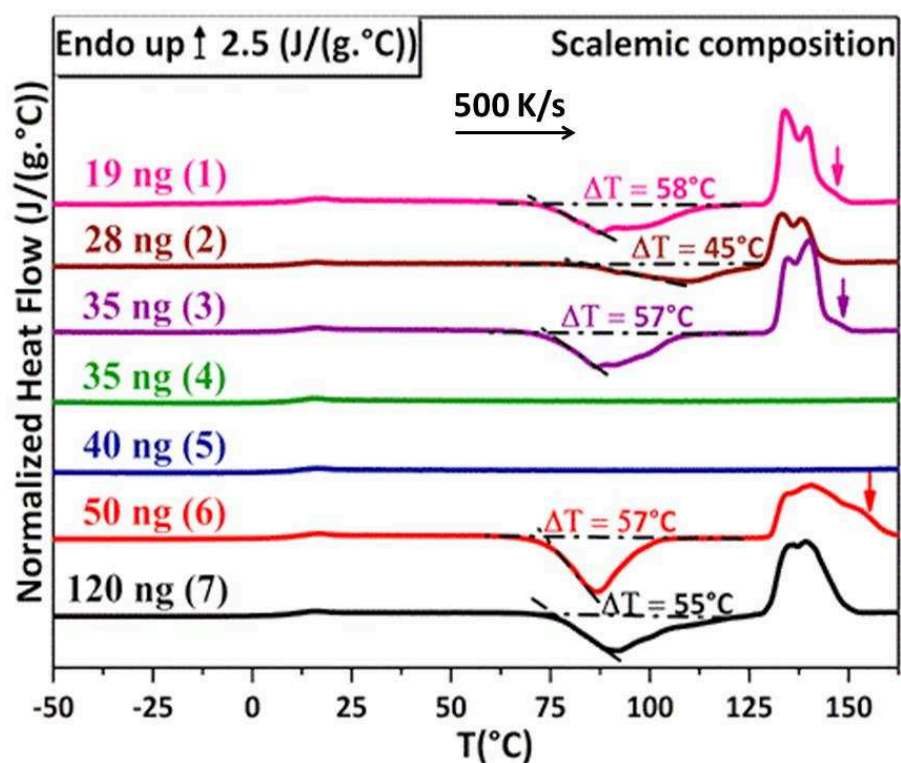
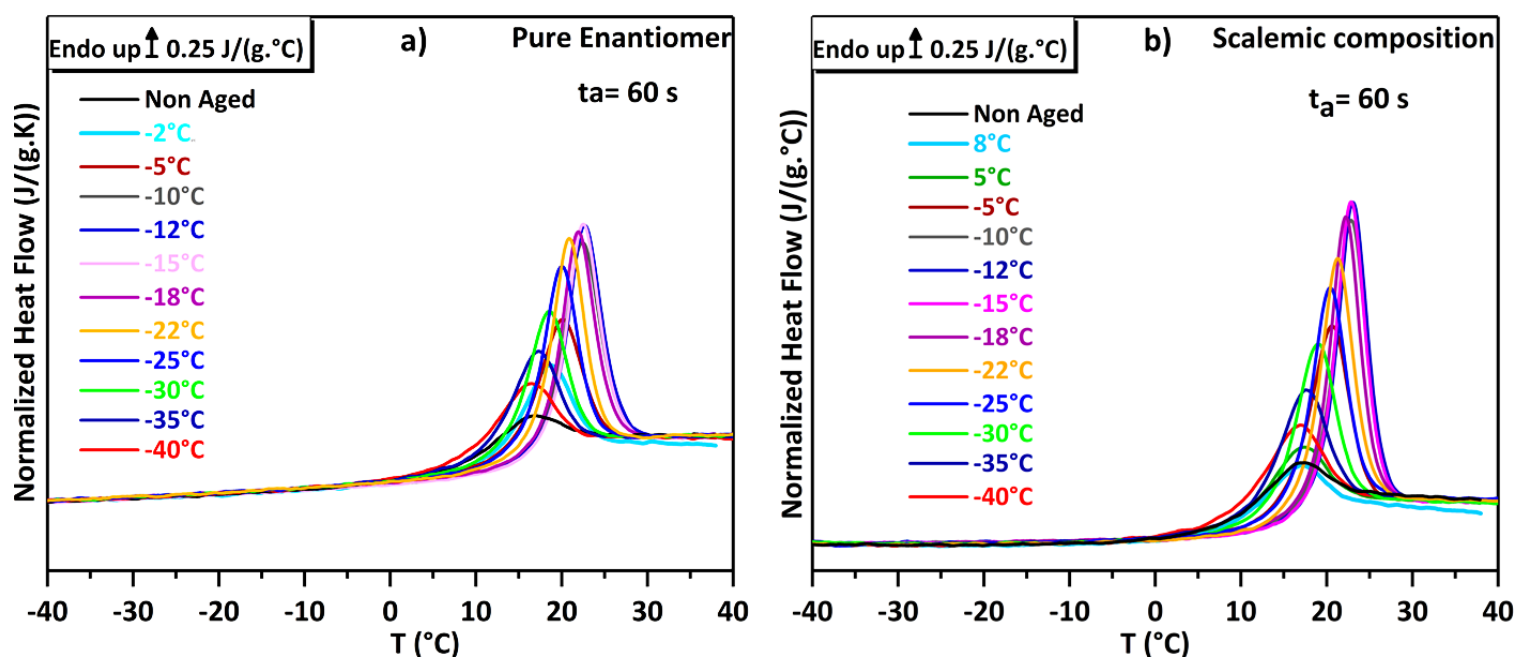


Figure 9: Heating curves from the amorphous state at 500 °C/s for seven samples coming from the racemic batch. ΔT represents the temperature between the onset of the crystallization peak and the onset of the first endothermic event. The arrow peak (third endothermic event) indicates samples with larger ee.

5- Physical Aging and Crystallization Propensity

A systematic study of physical aging phenomenon was launched for pure enantiomer and scalemic composition. The melted sample was cooled down to -70°C at 1000°C/s and heated 30°C above T_g in order to record the unaged glass signal. The sample was then cooled at different aging temperatures T_a (from -40°C to 5°C) and aged for 60 s. Before the final heating step at 1000°C/s up to 45°C , the sample is previously cooled down to -70°C . Figure 10 (a) and b)) present the final heating curves after 60 s of ageing at various temperatures for pure enantiomer and scalemic 12H respectively. Depending on the annealing temperature, a more or less intense overshoot peak occurs at the glass transition region. This behavior is due to the enthalpy recovery phenomenon and is classically observed for different glass formers [8–11] [12–14]. Figure 10 c) depicts the excess enthalpy evolution as function of T_a . Both samples presented a bell shape enthalpy recovery curve with the same maximum at $T_g - 28^{\circ}\text{C}$ for an ageing time of 60s. A significant drop of the heat capacity is observed in the case of pure enantiomer when the ageing is performed for 60 s at temperature higher than $T_g - 21^{\circ}\text{C}$. The heat capacity drop in the case of the scalemic composition occurred when T_a was higher than $T_g - 11^{\circ}\text{C}$ for the same ageing time. The drop of heat capacity in the supercooled liquid state suggests the early stages of crystallization occurrence.



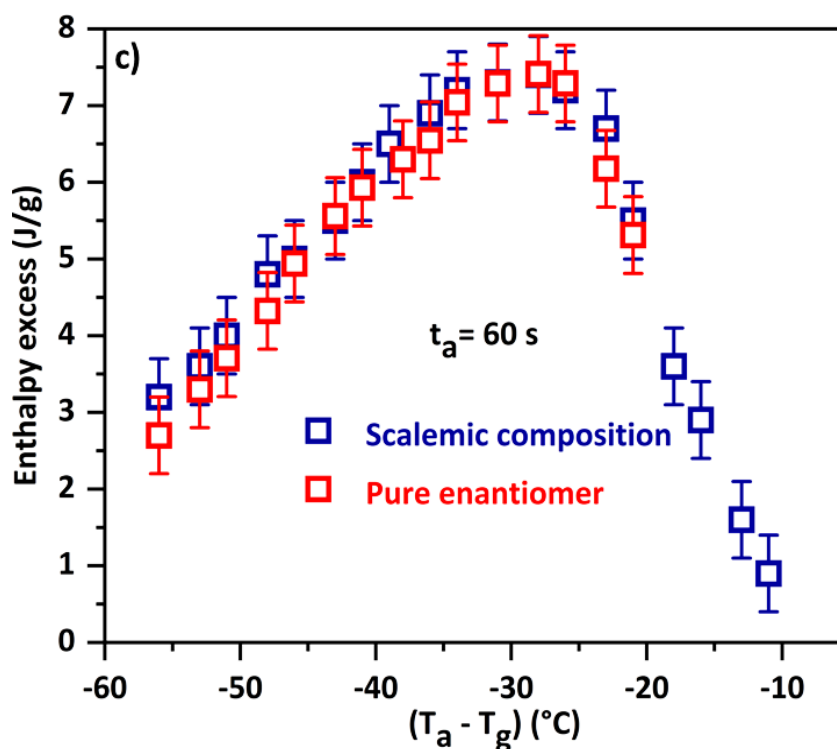


Figure 10: a, b) FSC heating scans at 1000 °C/s as a function of aging temperature for an aging time 60s after cooling at 1000 °C/s for pure enantiomer and scalemic 12H respectively. c) Evolution of the enthalpy excess value as function of the difference ($T_a - T_g$).

Moreover, for two selected aging temperatures ($T_g - 36^\circ\text{C}$ and $T_g - 26^\circ\text{C}$), aging was performed for various aging time t_a , from 1s up to 14440s and 1s up to 900s respectively and according to the same thermal protocol. Enantiopure 12H crystallizes for the two selected aging temperatures after short aging time (see figure 11). Figure 11 a) and b) depict the heat flow evolution of pure enantiomer as a function of temperature for several aging time at $T_a = -20^\circ\text{C}$ and -10°C . For the two aging temperatures, the heat capacity vanishes in the supercooled liquid state after an aging time of 600s and 120s for $T_a = -20^\circ\text{C}$ and -10°C respectively.

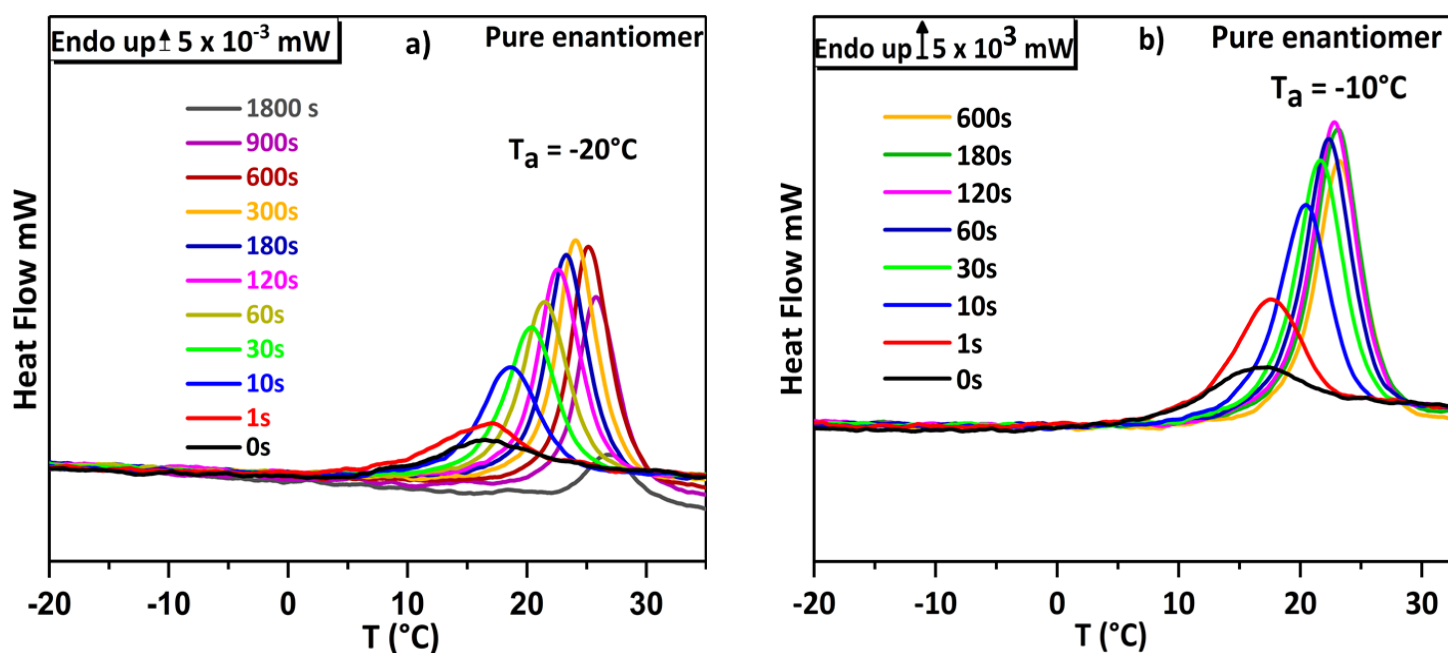


Figure 11: a, b) FSC heating scans of enantiopure 12H at 1000 °C/s as function of aging time for $T_a = T_g - 36 = -20^\circ\text{C}$ and $T_a = T_g - 26 = -10^\circ\text{C}$ respectively after cooling at 1000 °C/s

This behavior is a synonym of the presence of a crystallized fraction in the amorphous sample. One can envisage that upon the heating step of the aged glass in order to record the aging thermal signature, the sample entered a temperature region where crystallization is highly probable. Consequently, enantiopure 12H is not a suitable compound for aging characterization even at these high scanning rates due to its high crystallization propensity. Moreover complete crystallization of enantiopure 12H in the glassy state was evidenced at -20°C . The melted sample was cooled down to -20°C at 1000 °C/s, and aged at this temperature (36°C below T_g) for 4 hours then cooled down to -70°C . The sample was finally re-heated at 1000 °C/s in order to record the thermal signature of the aged material (figure 12). Upon heating, only the melting peak was evidenced. Thus, pure enantiomer fully crystallized during the aging process. Ones more, these results highlight the high crystallization propensity of enantiopure 12H in a large temperature range well below T_g ($T_g - 36^\circ\text{C}$) and above.

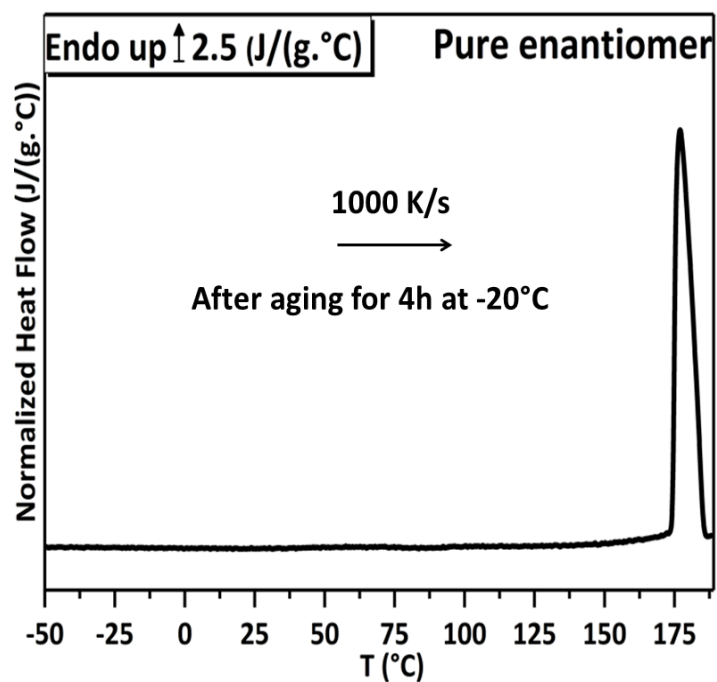


Figure 12: FSC heating curves of pure enantiomer at 1000 °C/s composition after aging the amorphous samples for 4h at T_g - 36°C.

On the contrary as illustrated in figure 13 a) in the case of scalemic 12H, the enthalpy relaxation at the glass transition region increases as the aging time increases up to a constant signal for longer aging time. The overshoot peak increases and reaches saturation intensity rapidly for T_g – 26°C than T_g – 36°C. But at T_g – 36°C the overshoot area attained higher intensities.

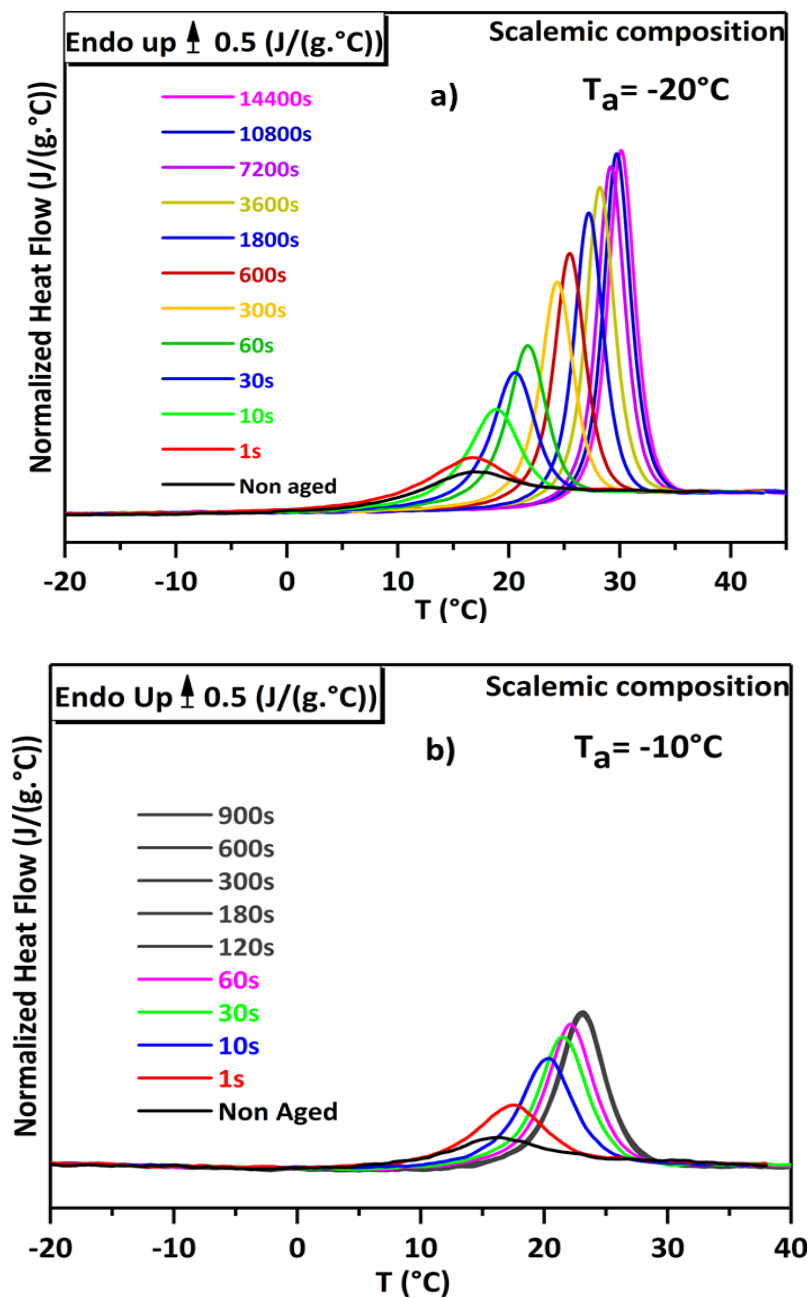


Figure 13 a, b) FSC heating scans of scalemic 12H at 1000 °C/s as function of aging time for $T_a = -20^\circ\text{C}$ and -10°C respectively after cooling at 1000 °C/s.

The out of equilibrium nature of the glassy state implies a slow evolution of the glass towards the metastable supercooled liquid state. Therefore, one can ask if the supercooled liquid equilibrium is reached when the saturation overshoot peak is obtained for the two aging temperatures. To answer this question, two methods are usually proposed. The first method consists of comparing the excess enthalpy at the supposed equilibrium and the value needed

to reach the supercooled liquid state ($\Delta H_{\infty} = \Delta C_p (T_g - T_a)$). The second method consists of calculating the fictive temperature T_f as a function of the aging time. T_f is defined as the actual temperature for the same compound in the equilibrium, metastable, supercooled state whose structure is expected to be similar to that of the non-equilibrium compound [15]. At the supercooled liquid equilibrium the T_f value is equal to the aging temperature. The calculation of ΔC_p only by FSC is problematic because of the uncertainty linked to the rough determination of the sample mass. Consequently in this analysis we chose to evaluate equilibrium by determining the T_f evolution as function of the aging time. The T_f is calculated from the heating curves using the “equal area rule” [16]. In Figure 14 the difference ($T_f - T_a$) is plotted as function of the aging time for the two aging temperatures. The fictive temperature value reaches the aging temperature after 120 s and 10800 s for $T_a = T_g - 26^{\circ}\text{C}$ and $T_a = T_g - 36^{\circ}\text{C}$ respectively. Consequently the supercooled liquid state is reached for the two aging temperatures.

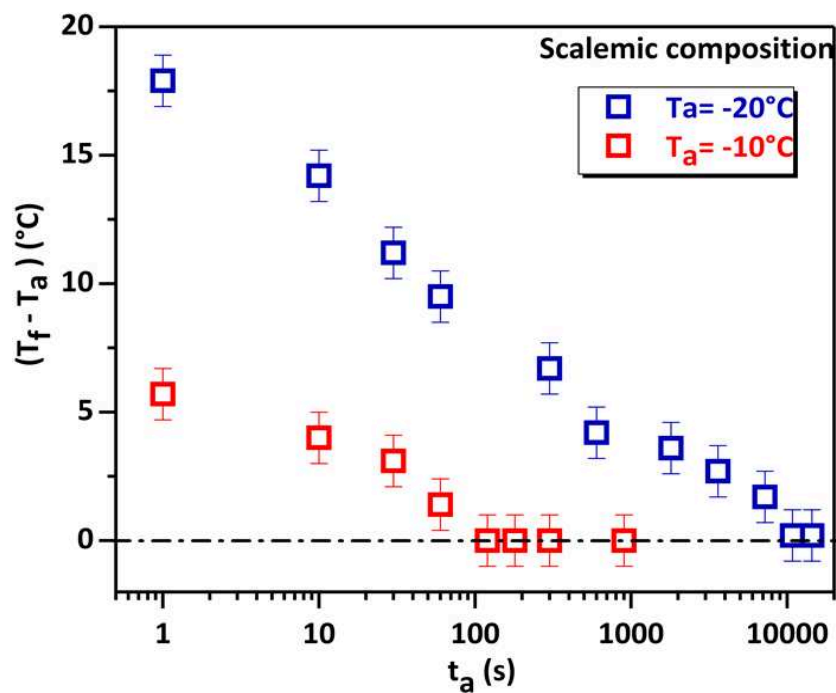


Figure 14: Evolution of the difference ($T_f - T_a$) as function of aging time.

II- Discussion

1- High Crystallization Propensity of 12H

As illustrated by DSC and FSC results, 12H exhibits a high crystallization propensity. This is a common feature shared by numerous small organic compounds. Due to their small size and relatively planar shape, the packing of such molecules in the crystalline configuration is mostly favored. It is well established that compounds with high molecular weight are difficult to crystallize compared to systems with low molecular weight [17]. Moreover, the propensity to form a glass can be affected by the number of aromatic rings, number of electronegative atoms, presence of flexible and rotating branches, intermolecular and intramolecular connections [18–20]. Furthermore, it was observed that liquids composed of symmetric molecules crystallize more easily than liquids made of asymmetric molecules. The case of meta and para xylene is commonly presented as an obvious example [3]. The meta-xylene liquid can undergo cooling and vitrifies, whereas for para-xylene isomer crystallization takes place in the same cooling conditions [21]. The tendency to crystallize (or to vitrify reversibly) can be related to numerous parameters: dynamics (viscosity or molecular mobility), thermodynamics (the driven force of crystallization) [22,23], kinetics and structural (the complexity to rebuild the bond networks between molecules after melting) [22]. None of these different parameters can be neglected when it comes to fully understand the GFA (Glass Forming Ability) of a compound or its crystallization propensity.

Based on the presence or absence of crystallization upon a cyclic heat-cool-heat protocol, Baird and coworkers proposed a classification system established on a set of 51 molecular compounds [17]. The set of molecules is classified into class I (class I (A), class I (B)), class II, and class III as a function of their GFA. From this classification, 12H (whatever the ee) could be considered as a class I (A) molecular compound, which means it would inevitably undergo crystallization upon moderate cooling (around 20 °C/min) or melt quenching in liquid N₂. As 12H system, class I molecules are usually of low molecular weight and present simple molecular structures with few flexible and rotating bonds [17]. The structural resolution of enantiopure 12H has been reported previously by S. Beilles and co-authors [24] and highlighted the presence of infinite H-bond chains along b-axis. These strong molecular ribbons (two H-bonds per molecule involving N1, O2 and N3, see figure 15) are held together

by means of van der Waals contacts [24], [25]. Moreover, the most probable flexible group (5-ethyl) is not implicated in the H-bond chain building. The crystallographic features of 12H match correctly with the previous ideas proposed by Baird *et al* [45].

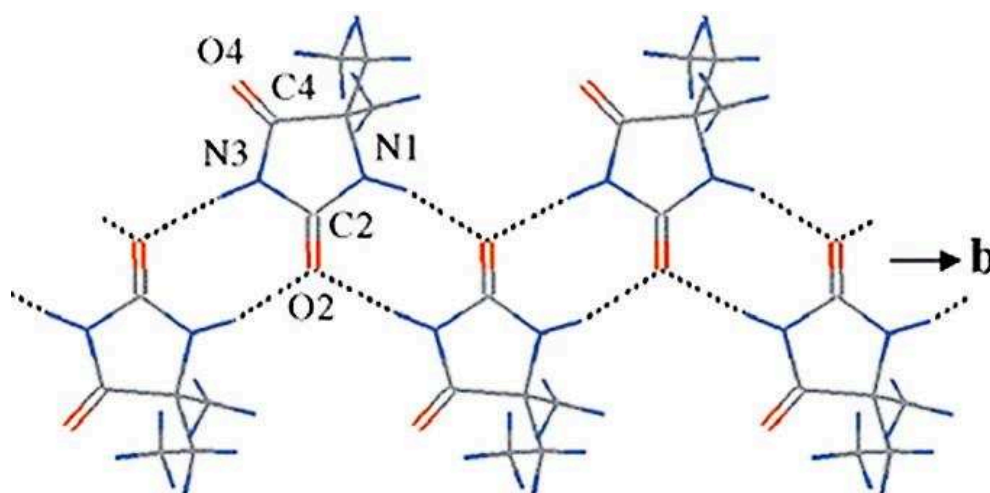


*Figure 15: Projection of the crystal structure of 12H along a-axis showing molecular ribbons running along the b-axis from C. Gervais *et al*. [25]*

2- Thermal Lag and Glass Transition Temperature vs ee

As presented far above, the sample thickness was always $< 10 \mu\text{m}$ in all experiments. Furthermore, in the same experimental conditions, T_g value remained constant when increasing the sample mass from 19 ng to 120 ng. For these reasons, the thermal lag effects on T_g were neglected. Independently of the enantiomeric composition, $T_{g(\text{onset})} = 16 \pm 2 \text{ }^\circ\text{C}$. Indeed, both enantiomers present the same scalar properties such as T_m , ΔH_m , T_g and ΔC_p . As discussed in chapter 1 in the Framework of Gordon Taylor law, T_g is independent from the enantiomeric composition [26]. Many experimental confirmations have been reported in literature: limonene [27], diprophylline [28] or ibuprofen [29]. Independently from the chiral specie (a conglomerate system in the present case), T_g value is not impacted by the asymmetric property of chirality.

3- Impact of Enantiomeric Composition on GFA and Crystallization Propensity in the Glassy State

FSC results suggested that 500 °C/s was not fast enough to completely skip the crystallization process in the case of enantiopure 12H. From DSC data upon cooling, one can assess that the degree of supercooling of pure enantiomer was higher than that of racemic mixture but still, this parameter cannot explain why upon cooling the pure enantiomer presented a poor GFA compared to racemic mixture. Considering that crystallization conjugates nucleation and crystal growth stages (that are temperature dependent processes), there is a temperature range at which the rate of crystallization is maximum. Consequently, nucleation and crystal growth temperature dependency curves overlap in that region. The Nucleation rate N ($\text{m}^{-3}\text{s}^{-1}$) and crystal growth G (m s^{-1}) were high enough to produce supercritical nuclei and aggregation of the molecules (growth) respectively in such way that 500 °C/s was not fast enough to completely inhibit the crystallization of enantiopure 12H. By contrast, for the intermediate/racemic compositions, crystallization was not evidenced upon cooling neither at 500 °C/s nor 300 °C/s. This fact highlights the role played by the counter enantiomer in the GFA of this conglomerate forming system. For numerous set of organic compounds (e.g. alkylamide derived from trans-1, 2-bis (amino) cyclohexane, diprophylline), racemic mixture has a much higher propensity to crystallize compared to the enantiomeric counterpart [28,30]. It is important to notice that the racemic mixtures studied in the mentioned works crystallize as racemic compounds (i.e. both enantiomers crystallize in the same crystal lattice) like more than 90% of racemic species [30]. By contrast, racemic 12H is a conglomerate forming system (around 5% of racemic mixtures). In our case the counter enantiomer acts like an impurity (of the same chemical nature) which delays or inhibits the crystallization process. Consequently, at intermediate enantiomeric compositions, 12H will have a higher GFA when compared to that of the pure enantiomer. If this counter-enantiomer effect is assumed in the whole composition domain of the binary system, GFA should then increase as the composition approaches the racemic mixture (ee decreases). From a structural point of view both systems are identical, the implication of the counter enantiomer could then be analyzed from a thermodynamic angle. The presence of the counter enantiomer modifies the molecular environment of the melt, which results in a modification of the thermodynamic and kinetics properties related to crystallization.

Similar observations may be considered when heating the amorphous glasses. Indeed, due to steric hindrance effects, the required time for molecules of one enantiomer in the supercooled liquid to regain their crystalline configurations will be increased as the sample contains the two opposite enantiomers. Independently from the fact that pure enantiomer has a poor GFA compared to the scalemic composition, the temperature region where crystallization takes place was shifted towards higher temperatures with the counter-enantiomer for the same scanning rate. Furthermore, nucleation and crystal growth domains of pure enantiomer overlap in a large temperature interval of about 70°C (from -10°C to 60°C), while at the scalemic composition, the two processes can either be well separated or overlap in a temperature region of about 40°C (from 10°C to 50°C) accordingly to the equilibrium reached after recrystallization. This is consistent with the higher GFA of the scalemic sample compared to that of the pure enantiomer.

Pure enantiomer was proven to crystallize after short aging time at $T_g - 36^\circ\text{C}$ or $T_g - 26^\circ\text{C}$. Even at this temperature range, where the structural bulk relaxation process is considered as frozen and only localized movements are expressed, enantiopure 12H had enough molecular mobility to regain the crystalline state. Moreover, the fact that nucleation and growth processes merge at low temperatures ($T_g - 26^\circ\text{C}$) strongly increases the probability for crystallization to occur well below T_g .

Nevertheless fast crystallization in the glassy state has been reported in literature for many molecular systems such as indomethacin [31], nifedipine [32], griseofulvin [33], and ortho-terphenyl [34,35]. This rapid crystallization process below T_g is usually attributed to the flimsy nature of the generated glassy material, which can easily promote crack formation [35,36]. Cracks can originate from deep quenching of the liquid for glass formation purposes [34,37]. Fractures induce free surface that favored heterogeneous nucleation, consequently the activation barrier of nucleation, the interfacial energy and driving force of crystallization are lowered and rapid crystallization can therefore be facilitated at lower temperature (below T_g), [36–38]. One important phenomenon that has also to be taken into account is the surface mobility that can help to amplify the process. It is well established that for many glassy molecular compounds the diffusion mechanism at the surface are higher than in the bulk for about 6 decades in magnitudes [33–35,39]. Such cracks formation effects generating heterogeneous nucleation can be envisaged in enantiopure 12H.

4- Impact of chirality upon physical aging

By contrast to pure enantiomer behavior, the sample close to the racemic composition (scalemic sample) did not crystallize during the aging process at the two aging temperatures. During the aging process, scalemic sample evolves irreversibly towards the metastable equilibrium state.

The equilibrium state (crystalline state) reached by enantiopure 12H after the annealing process is therefore physically different from the expected state (supercooled liquid state) reached by the scalemic sample. This evidenced the potential role played by chirality during the evolution from an out of equilibrium state towards equilibrium (stable or metastable) in such binary eutectic systems without detectable partial solid solution. The Scalemic sample aged at $T_g - 26^\circ\text{C}$ and $T_g - 36^\circ\text{C}$ reaches the metastable liquid state after 120s and 10800s. Furthermore the enthalpy excess values are very intense almost 1.3 kJ/mol for $T_a = -10^\circ\text{C}$ and 1.8 kJ/mol for $T_a = -20^\circ\text{C}$. This behavior is quite surprising considering that at this temperature range molecular mobility is very low. Recent studies on amorphous polymeric systems have reported accelerated return towards equilibrium and high magnitude values of the overshoot peak during the aging process [40–43]. These effects are mostly due to the high cooling rate facilities provided by FSC and sample size. The initial glass formed upon high cooling rate possesses high enthalpy value and greater free volume compared to an amorphous glass formed by conventional DSC cooling rate facilities. High free volume is here required for an accelerated return towards the metastable equilibrium, and high cooling rate provides this free volume during the early stages of glass formation.

5- Possible Metastable Equilibria

The access to 12H amorphous states (only feasible by FSC) offered also new routes to isolate unknown crystalline phases. Indeed, annealing from $T_g - 66^\circ\text{C}$ to $T_g - 26^\circ\text{C}$ and $T_g - 16^\circ\text{C}$ to $T_g + 44^\circ\text{C}$ promoted the nucleation of two different crystalline forms with a melting point at $133^\circ\text{C} \pm 1^\circ\text{C}$ and $128^\circ\text{C} \pm 1^\circ\text{C}$ respectively. These equilibria obtained were not reported in the binary phase diagram between both enantiomers. Consequently, crystallization from the amorphous and supercooled liquid states may have revealed the existence of possible polymorphism, metastable racemic compound or metastable equilibria between the two enantiomers and this highlights the benefits of accessing to fleeting amorphous states by novel techniques such as FSC. The following schematic diagram suggesting a metastable racemic compound can be proposed.

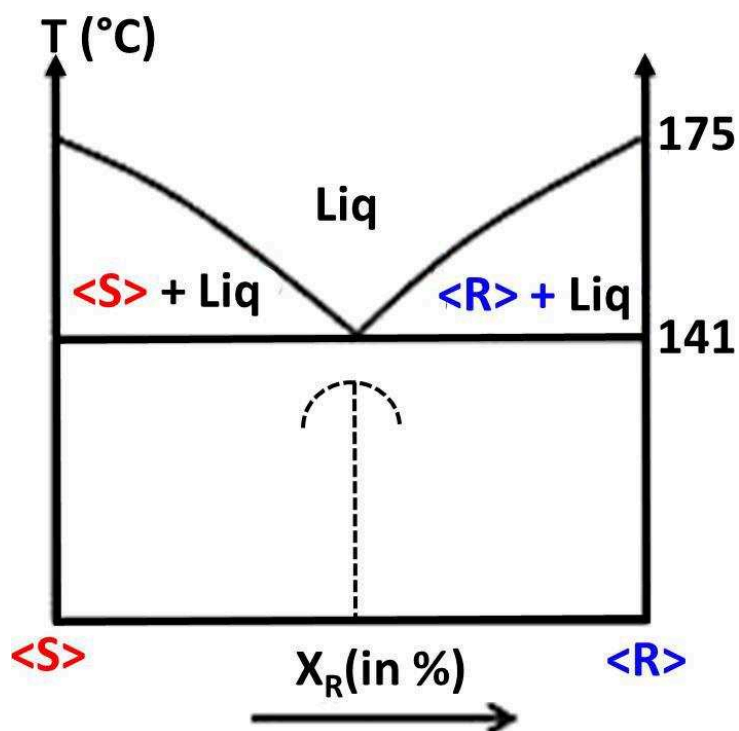


Figure 16: Binary phase diagram of 12H enantiomers, suggesting a possible metastable racemic compound.

III - Conclusions

The investigation of the glassy state of 5-ethyl-5-methyl hydantoin (or 12H, a chiral API which is a poor glass former) was successfully performed by FSC analyses. For the first time, the glassy state of 12H was reached, and its T_g value was determined: $T_{g \text{ (onset)}} = 16 \pm 2 \text{ }^\circ\text{C}$ (cooling 1000 $^\circ\text{C/s}$) regardless its enantiomeric composition.

Besides, this study revealed drastic limitations in the sampling procedure of FSC device. Indeed, when dealing with physical mixtures, the overall composition could not be reproducibly maintained on the chip sensor. Other preparations or sampling routes (such as multiple dilutions of saturated solutions and evaporation of a droplet directly on the chip) should be envisaged to ensure defined compositions.

In the case of 12H, GFA was proven to be independent from the cooling rate (degree of undercooling, $\Delta T = T_m - T$). The poor GFA of 12H is related to the poor separation of the nucleation and crystal growth events in both pure enantiomer and scalemic composition. Both phenomena overlap in more than 80 $^\circ\text{C}$ ($-20 \leq T \leq 60^\circ\text{C}$) in the case of pure enantiomer and 40 $^\circ\text{C}$ ($10^\circ\text{C} \leq T \leq 50^\circ\text{C}$) for the scalemic composition. Nevertheless, FSC analyses highlighted that chirality clearly impacts GFA. Inversely from the behavior usually observed for racemic compounds, upon cooling, the pure enantiomer presented a higher crystallization propensity compared to the intermediate / scalemic composition. Therefore, samples containing both enantiomers could be easily vitrified compared to pure enantiomers. Upon heating, the counter-enantiomer acted like an impurity that delayed or inhibited recrystallization from the glassy state. In addition, the stability of the glasses was investigated by an aging process. For the same annealing conditions the initial glasses formed evolves toward different equilibria. Annealing promotes a strong nucleation behavior in both samples and either crystallization or highly intense overshoot peak. When glassy pure enantiomer crystallizes during the annealing step, amorphous scalemic 12H evolves towards the metastable liquid equilibrium. In order to explain this fast crystallization behavior, a possible explanation involving cracks formation in the trigger of heterogeneous nucleation and fast surface crystallization was proposed. Thus, this fast crystallization behavior makes the investigation of the molecular mobility of the amorphous state of 12H by BDS ambiguous and simply impossible.

Furthermore, different putative metastable equilibria at 130°C and 135°C previously unknown from the binary phase diagram between both enantiomers have been highlighted. In particular, a metastable racemic compound may have recrystallized from the amorphous state but accurate tools such Second Harmonic Generation microscopy (to assess or not the centrosymmetry) would be required to confirm this hypothesis.

In the next chapter we will focus on the case of Nac-MBA, another conglomerate forming system by evaluating its GFA, the recrystallization behavior from the amorphous state, the kinetic of return towards equilibrium upon physical aging and the molecular mobility as a function of the ee.

References

- [1] B. Atawa, N. Couvrat, G. Coquerel, E. Dargent, A. Saiter, Impact of chirality on the Glass Forming Ability and the crystallization from the amorphous state of 5-ethyl-5-methylhydantoin, a chiral poor glass former, *Int. J. Pharm.* 540 (2018) 11–21. doi:10.1016/j.ijpharm.2018.01.050.
- [2] E. Ndzié, P. Cardinael, M.N. Petit, G. Coquerel, Enantiomeric resolution of (+/-)-5-ethyl-5-methylhydantoin by means of preferential nucleation, *Enantiomer.* 4 (1999) 97–+.
- [3] D. Turnbull, Under what conditions can a glass be formed?, *Contemp. Phys.* 10 (1969) 473–488. doi:10.1080/00107516908204405.
- [4] P.G. Debenedetti, *Metastable Liquids: Concepts and Principles*, Princeton University Press, 1996.
- [5] P.G. Debenedetti, F.H. Stillinger, Supercooled liquids and the glass transition, *Nature.* 410 (2001) 259–267. doi:10.1038/35065704.
- [6] J.E.K. Schawe, S. Pogatscher, Material Characterization by Fast Scanning Calorimetry: Practice and Applications, in: C. Schick, V. Mathot (Eds.), *Fast Scanning Calorim.*, Springer International Publishing, 2016: pp. 3–80. doi:10.1007/978-3-319-31329-0_1.
- [7] J.E.K. Schawe, Measurement of the thermal glass transition of polystyrene in a cooling rate range of more than six decades, *Thermochim. Acta.* 603 (2015) 128–134. doi:10.1016/j.tca.2014.05.025.
- [8] D. Cangialosi, V.M. Boucher, A. Alegría, J. Colmenero, Physical aging in polymers and polymer nanocomposites: recent results and open questions, *Soft Matter.* 9 (2013) 8619–8630. doi:10.1039/C3SM51077H.
- [9] A.J. Kovacs, R.A. Stratton, J.D. Ferry, DYNAMIC MECHANICAL PROPERTIES OF POLYVINYL ACETATE IN SHEAR IN THE GLASS TRANSITION TEMPERATURE RANGE, *J. Phys. Chem.* 67 (1963) 152–161. doi:10.1021/j100795a037.

- [10] A. Kozdras, R. Golovchak, O. Shpotyuk, S. Szymura, A. Saiter, J.-M. Saiter, Light-assisted physical aging in chalcogenide glasses: Dependence on the wavelength of incident photons, *J. Mater. Res.* 26 (2011) 2420–2427. doi:10.1557/jmr.2011.264.
- [11] M. Yoshioka, B.C. Hancock, G. Zografi, Crystallization of indomethacin from the amorphous state below and above its glass transition temperature, *J. Pharm. Sci.* 83 (1994) 1700–1705. doi:10.1002/jps.2600831211.
- [12] L. Gunawan, G.P. Johari, R.M. Shanker, Structural Relaxation of Acetaminophen Glass, *Pharm. Res.* 23 (2006) 967–979. doi:10.1007/s11095-006-9898-0.
- [13] B.C. Hancock, S.L. Shamblin, G. Zografi, Molecular Mobility of Amorphous Pharmaceutical Solids Below Their Glass Transition Temperatures, *Pharm. Res.* 12 (1995) 799–806. doi:10.1023/A:1016292416526.
- [14] R. Surana, A. Pyne, R. Suryanarayanan, Effect of Aging on the Physical Properties of Amorphous Trehalose, *Pharm. Res.* 21 (2004) 867–874. doi:10.1023/B:PHAM.0000026441.77567.75.
- [15] M. Descamps, J.-F. Willart, Some Facets of Molecular Disorder in Crystalline and Amorphous Pharmaceuticals, in: rc Descamps (Ed.), *Disord. Pharm. Mater.*, Wiley-VCH Verlag GmbH & Co. KGaA, 2016: pp. 1–56. doi:10.1002/9783527652693.ch1.
- [16] C.T. Moynihan, P.B. Macedo, C.J. Montrose, C.J. Montrose, P.K. Gupta, M.A. DeBolt, J.F. Dill, B.E. Dom, P.W. Drake, A.J. Easteal, P.B. Elterman, R.P. Moeller, H. Sasabe, J.A. Wilder, Structural Relaxation in Vitreous Materials*, *Ann. N. Y. Acad. Sci.* 279 (1976) 15–35. doi:10.1111/j.1749-6632.1976.tb39688.x.
- [17] J.A. Baird, B. Van Eerdenbrugh, L.S. Taylor, A classification system to assess the crystallization tendency of organic molecules from undercooled melts, *J. Pharm. Sci.* 99 (2010) 3787–3806. doi:10.1002/jps.22197.
- [18] T. Miyazaki, S. Yoshioka, Y. Aso, T. Kawanishi, Crystallization rate of amorphous nifedipine analogues unrelated to the glass transition temperature, *Int. J. Pharm.* 336 (2007) 191–195. doi:10.1016/j.ijpharm.2006.11.052.

- [19] K. Kawakami, T. Harada, Y. Yoshihashi, E. Yonemochi, K. Terada, H. Moriyama, Correlation between Glass-Forming Ability and Fragility of Pharmaceutical Compounds, *J. Phys. Chem. B.* 119 (2015) 4873–4880. doi:10.1021/jp509646z.
- [20] S. Baghel, H. Cathcart, W. Redington, N.J. O'Reilly, An investigation into the crystallization tendency/kinetics of amorphous active pharmaceutical ingredients: A case study with dipyrindamole and cinnarizine, *Eur. J. Pharm. Biopharm.* 104 (2016) 59–71. doi:10.1016/j.ejpb.2016.04.017.
- [21] C. Alba, L.E. Busse, D.J. List, C.A. Angell, Thermodynamic aspects of the vitrification of toluene, and xylene isomers, and the fragility of liquid hydrocarbons, *J. Chem. Phys.* 92 (1990) 617–624. doi:10.1063/1.458411.
- [22] J.A. Baird, D. Santiago-Quinonez, C. Rinaldi, L.S. Taylor, Role of Viscosity in Influencing the Glass-Forming Ability of Organic Molecules from the Undercooled Melt State, *Pharm. Res.* 29 (2012) 271–284. doi:10.1007/s11095-011-0540-4.
- [23] J. Gerges, F. Affouard, Predictive Calculation of the Crystallization Tendency of Model Pharmaceuticals in the Supercooled State from Molecular Dynamics Simulations, *J. Phys. Chem. B.* 119 (2015) 10768–10783. doi:10.1021/acs.jpcc.5b05557.
- [24] S. Beilles, P. Cardinael, E. Ndzié, S. Petit, G. Coquerel, Preferential crystallisation and comparative crystal growth study between pure enantiomer and racemic mixture of a chiral molecule: 5-ethyl-5-methylhydantoin, *Chem. Eng. Sci.* 56 (2001) 2281–2294. doi:10.1016/S0009-2509(00)00442-5.
- [25] C. Gervais, S. Beilles, P. Cardinaël, S. Petit, G. Coquerel, Oscillating Crystallization in Solution between (+)- and (-)-5-Ethyl-5-methylhydantoin under the Influence of Stirring, *J. Phys. Chem. B.* 106 (2002) 646–652. doi:10.1021/jp012622s.
- [26] Coquerel Gerard, Tamura Rui, “Enantiomeric Disorder” Pharmaceutically Oriented, *Disord. Pharm. Mater.* (2016). doi:10.1002/9783527652693.ch5.
- [27] H.E. Gallis, J.C. van Miltenburg, H.A.J. Oonk, Polymorphism of mixtures of enantiomers: A thermodynamic study of mixtures of D- and L-limonene, *Phys. Chem. Chem. Phys.* 2 (2000) 5619–5623. doi:10.1039/B005603K.

- [28] Q. Viel, C. Brandel, Y. Cartigny, M.E.S. Eusébio, J. Canotilho, V. Dupray, E. Dargent, G. Coquerel, S. Petit, Crystallization from the Amorphous State of a Pharmaceutical Compound: Impact of Chirality and Chemical Purity, *Cryst. Growth Des.* 17 (2017) 337–346. doi:10.1021/acs.cgd.6b01566.
- [29] T.H. Kim, T. Shibata, S. Kojima, D.-M. Shin, Y.-H. Hwang, J.-H. Ko, Comparison of thermal and elastic properties of glassy racemic and enantiomeric ibuprofen studied by Brillouin light scattering and modulated differential scanning calorimetry, *Curr. Appl. Phys.* 14 (2014) 965–969. doi:10.1016/j.cap.2014.05.001.
- [30] G. Coquerel, R. Tamura, “Enantiomeric Disorder” Pharmaceutically Oriented, in: *rc Descamps (Ed.), Disord. Pharm. Mater.*, Wiley-VCH Verlag GmbH & Co. KGaA, 2016: pp. 135–160. doi:10.1002/9783527652693.ch5.
- [31] T. Wu, L. Yu, Surface Crystallization of Indomethacin Below T_g, *Pharm. Res.* 23 (2006) 2350–2355. doi:10.1007/s11095-006-9023-4.
- [32] Surface-Enhanced Crystallization of Amorphous Nifedipine - Molecular Pharmaceutics (ACS Publications), (n.d.). <http://pubs.acs.org/doi/abs/10.1021/mp8000638> (accessed July 4, 2017).
- [33] L. Zhu, J. Jona, K. Nagapudi, T. Wu, Fast Surface Crystallization of Amorphous Griseofulvin Below T_g, *Pharm. Res.* 27 (2010) 1558–1567. doi:10.1007/s11095-010-0140-8.
- [34] C.T. Powell, H. Xi, Y. Sun, E. Gunn, Y. Chen, M.D. Ediger, L. Yu, Fast Crystal Growth in o-Terphenyl Glasses: A Possible Role for Fracture and Surface Mobility, *J. Phys. Chem. B.* 119 (2015) 10124–10130. doi:10.1021/acs.jpcc.5b05389.
- [35] L. Yu, Surface mobility of molecular glasses and its importance in physical stability, *Adv. Drug Deliv. Rev.* 100 (2016) 3–9. doi:10.1016/j.addr.2016.01.005.
- [36] M. Descamps, E. Dudognon, Crystallization from the amorphous state: nucleation-growth decoupling, polymorphism interplay, and the role of interfaces, *J. Pharm. Sci.* 103 (2014) 2615–2628. doi:10.1002/jps.24016.

- [37] J.F. Willart, E. Dudognon, A. Mahieu, M. Eddleston, W. Jones, M. Descamps, The role of cracks in the crystal nucleation process of amorphous griseofulvin, *Eur. Phys. J. Spec. Top.* 226 (2017) 837–847. doi:10.1140/epjst/e2016-60358-y.
- [38] V. Legrand, M. Descamps, C. Alba-Simionesco, Glass-forming meta-toluidine: A thermal and structural analysis of its crystalline polymorphism and devitrification, *Thermochim. Acta.* 307 (1997) 77–83. doi:10.1016/S0040-6031(97)00271-2.
- [39] S. Capaccioli, K.L. Ngai, M. Paluch, D. Prevosto, Mechanism of fast surface self-diffusion of an organic glass, *Phys. Rev. E Stat. Nonlin. Soft Matter Phys.* 86 (2012) 051503. doi:10.1103/PhysRevE.86.051503.
- [40] Y.P. Koh, S. Gao, S.L. Simon, Structural recovery of a single polystyrene thin film using Flash DSC at low aging temperatures, *Polymer.* 96 (2016) 182–187. doi:10.1016/j.polymer.2016.04.047.
- [41] Y.P. Koh, L. Grassia, S.L. Simon, Structural recovery of a single polystyrene thin film using nanocalorimetry to extend the aging time and temperature range, *Thermochim. Acta.* 603 (2015) 135–141. doi:10.1016/j.tca.2014.08.025.
- [42] X. Monnier, A. Saiter, E. Dargent, Physical aging in PLA through standard DSC and fast scanning calorimetry investigations, *Thermochim. Acta.* 648 (2017) 13–22. doi:10.1016/j.tca.2016.12.006.
- [43] S.L. Simon, Y.P. Koh, The Glass Transition and Structural Recovery Using Flash DSC, in: *Fast Scanning Calorim.*, Springer, Cham, 2016: pp. 433–459. doi:10.1007/978-3-319-31329-0_14.

CHAPTER IV:

CHIRALITY EFFECTS ON AMORPHOUS N-ACETYL-A-METHYLBENZYLAMINE

The present chapter focuses on the thermal characterization of amorphous Nac-MBA at various enantiomeric excess. As already developed in the case of the 12H, the GFA or the crystallization propensity and the kinetic of enthalpy relaxation as a function of the enantiomeric excess are investigated in the case of Nac-MBA. A particular interest is attached to the establishment of the binary phase diagram obtained from recrystallization of amorphous Nac-MBA and the physical aging process at variable temperature (down to 21°C below T_g) as a function of the ee at variable aging times. In order to achieve this purpose, the study combines different experimental techniques such as DSC, MT-DSC, and FSC.

Part of this chapter has been published in materials, letters (Vol **228** (2018) page 141-144) and entitled “Chirality Impact on Physical Aging: a New and Original case of a Small Organic Molecule” [1].

I- Heterogeneous equilibria and vitrification

1- Thermal and structural characterizations of both pure enantiomer and racemic Nac-MBA upon heating

The calorimetric characterization of Nac-MBA was performed by DSC, MT-DSC and FSC. Here we detail some DSC results obtained at different ee. When heated at 10 °C/min, both pure enantiomer and racemic mixture illustrated different thermal signatures. In the case of pure enantiomer, the endothermic event is associated to the melting process at T_m (R or S) = 100°C, with a melting enthalpy, $\Delta H_m = (20.1 \pm 0.3) \text{ kJ.mol}^{-1}$ and $\Delta S_m = 0.054 \text{ kJ.mol}^{-1}.\text{K}^{-1}$ the corresponding melting entropy. For the racemic mixture, three endothermic phenomena appear. The first endothermic peak at $67 \pm 1 \text{ °C}$ does not appear on the heating scan of the enantiomer, showing that this phenomenon is different from a polymorphic transition of enantiomers. Druot *et al.* [2] associated this process to the reversible and stable three-phase equilibrium (eutectoid type) conglomerate-racemate: $\langle R \rangle + \langle S \rangle \leftrightarrow \langle RS \rangle$. In this work, the eutectoid invariant appears circa 3°C above the eutectoid temperature mentioned by Druot and coworkers [2]. Additionally, the small endothermic peak is directly followed by a low magnitude exothermic event suggesting a crystallization process. The last phenomenon that occurs at $75 \text{ °C} \pm 2 \text{ °C}$ is associated to the melting of the racemic compound with a melting enthalpy $\Delta H_m = (16.3 \pm 0.8) \text{ kJ.mol}^{-1}$ ($\Delta S_m = 0.047 \text{ kJ.mol}^{-1}.\text{K}^{-1}$). These results suggest that there

is a transformation of the stable conglomerate towards the racemic compound, engaging at least two intermediate processes (melting of the residual conglomerate and recrystallization towards the racemic compound). This hypothesis is consistent with the fact that, due to the poor diffusion rate in solids, the eutectoid transition is not complete and the remaining proportion of R and S enantiomers melts as soon as the metastable melting temperature of the conglomerate is reached (See figure 1). Since no additional phase transformation such as polymorphism occurs in the case of pure enantiomer, all hypotheses engaging a polymorphic transformation between both enantiomers will not be discussed.

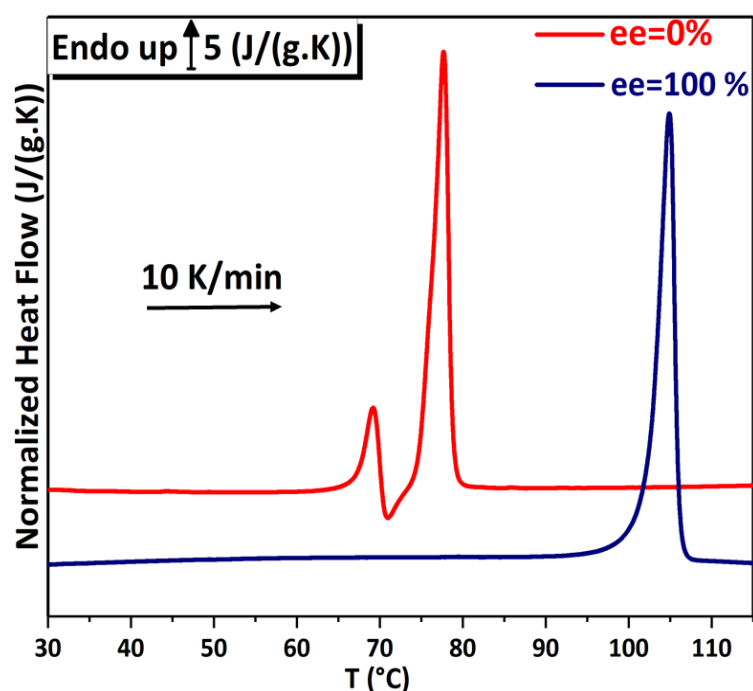


Figure 1: DSC Heating scans of pure enantiomer and racemic mixture at 10 K/min

Thus, upon heating of the stable conglomerate, there is a progressive transformation of the conglomerate towards the racemic compound (but not complete). As soon as the melting temperature of the conglomerate is reached, all the residual R and S enantiomers that have not undergone the eutectoid transition melt and recrystallize as a racemic compound. TR-XRD experiments were performed in order to follow the temperature evolution of the conglomerate (see figure 2). As temperature increases ($T > 20^{\circ}\text{C}$), there is a progressive appearance of characteristic peaks associated to the racemic compound and conversely some characteristic peaks related to the conglomerate disappear. Consequently the conglomerate

evolves gradually towards the racemic compound as temperature increases. These results are in adequacy with those obtained by Druot and coworkers [2].

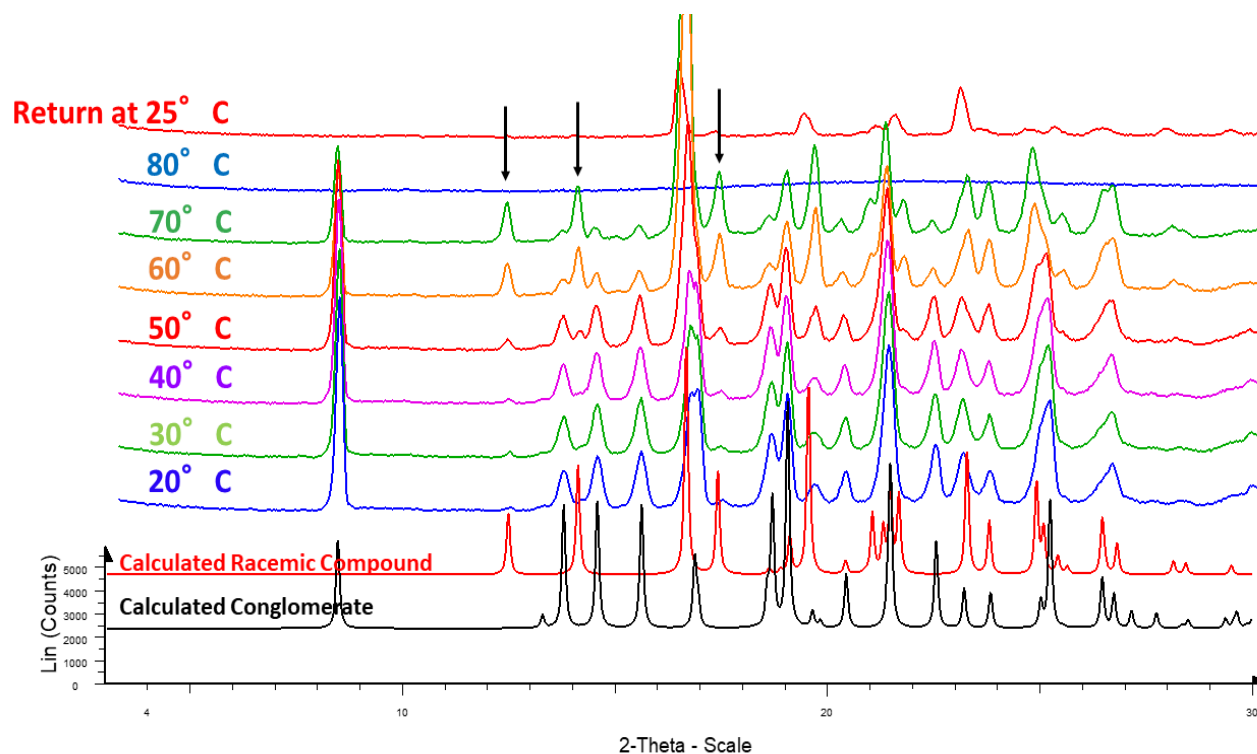


Figure 2: TR-XRD of the stable conglomerate showing a progressive evolution of the conglomerate towards the racemic compound upon heating. The black arrows point out the characteristic peaks of the racemic compound.

2- Vitrification and GFA of Nac-MBA versus ee: A kinetic competition

Both pure enantiomer and racemic mixture can undergo vitrification upon melt cooling. Therefore they possess typically different GFA. While vitrification of racemic Nac-MBA occurs at cooling rate higher or equal to 5 K/min (With a $T_g = -32^\circ\text{C}$), crystallization occurs in the case of the pure enantiomer even at 200 K/min. Such difference in the GFA between the pure enantiomer and the racemic composition has already been mentioned in the case of 12H. From our knowledge this is the second system that behaves similarly. The common feature between both systems is that they crystallize as stable conglomerate. The main explanation of this behavior remains kinetic. In fact, crystallization occurs only when the molecules of the liquid phase (disorder) reorganize in a certain way that they can build the long range order of

the crystal. This reorganization seems disturbed and delayed by the presence of the counter enantiomer.

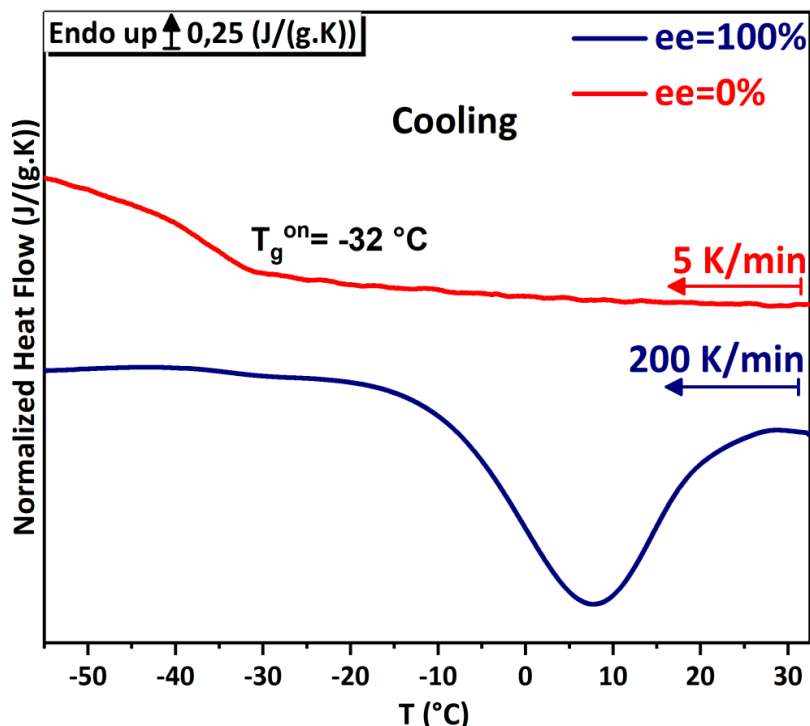


Figure 3: Thermal behavior upon cooling of both pure enantiomer and racemic mixture

In order, to build a crystalline phase that respect either the conglomerate or the racemic compound structure, each enantiomer must be surrounded by the right neighbors. Crystallization appears if this condition is fulfilled, and may be time consuming depending on the ee. In the case of a pure enantiomer, all neighbor molecules are of the same chirality, therefore, crystallization may occurred more rapidly than in a mixture of opposite enantiomers.

Figure 4 illustrates the behavior upon cooling at 10 K/min of different samples at various ee. While in the case of the racemic mixture, no crystallization occurs, samples at higher ee undergo partial or complete crystallization. Additionally, the crystallization peak increases as the ee increases, and is shifted towards lower temperatures as the ee decreases. These results suggest that, higher cooling rate than 10 K/min are required to vitrify the samples with an ee > 0%, and the cooling rate needed to inhibit crystallization increases as the ee increases. Therefore one can consider that the GFA is function of the enantiomeric composition and

increases with decreasing ee. In this case racemic Nac-MBA can be considered as a good glass former compared to the pure enantiomer.

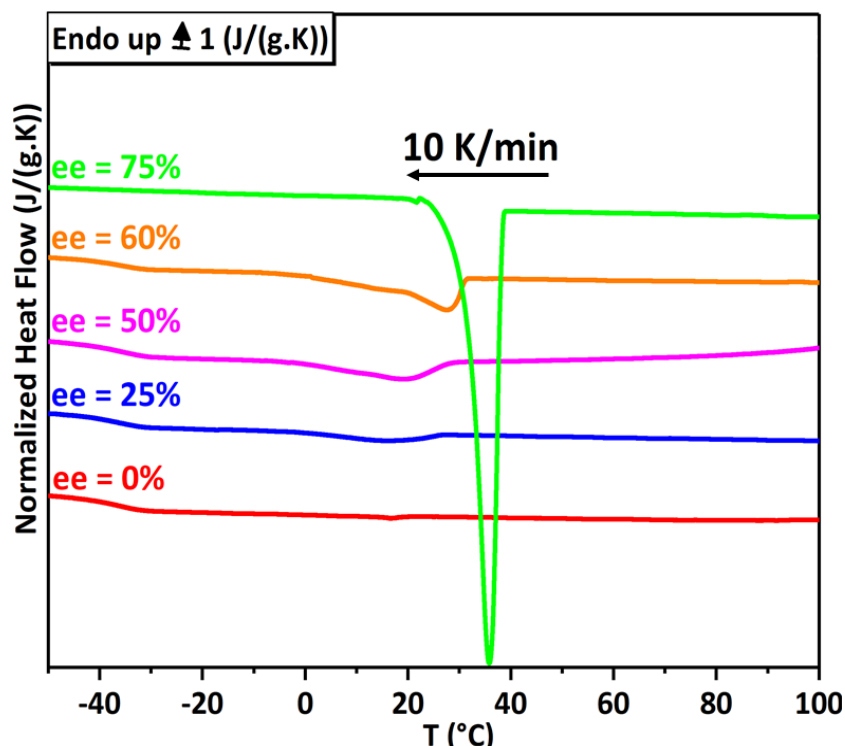


Figure 4: Thermal behavior upon cooling at 10 K/min for several ee

3- Thermal behavior upon heating from the amorphous state

In order to vitrify the system, appropriate cooling rate was provided regarding the enantiomeric composition. For $ee < 80\%$ a cooling rate of 100 K/min was applied, and for $ee > 80\%$ cooling rate higher than 250 K/min have to be considered to inhibit crystallization. After the cooling step, the amorphous sample was then heated at 10 K/min. Figure 5 presents the thermal signal upon heating at 10 K/min of the amorphous sample at different ee. Upon heating, at least three thermal events were evidenced. The glass transition appears at $T_g^{mid} = -33^\circ\text{C} \pm 1^\circ\text{C}$ independently of the enantiomeric composition. At higher temperature cold crystallization occurs depending on the enantiomeric composition; the crystallization temperature is shifted towards higher temperature with the decrease of the ee. The crystallization exothermal peak is followed by an endothermal event associated to the metastable eutectic invariant $T_E = 74^\circ\text{C} \pm 2^\circ\text{C}$ (the onset temperature is independent of the ee)

of the racemic compound. The last endothermic peak is associated to the liquidus phenomenon (The peak temperature is considered as the liquidus temperature).

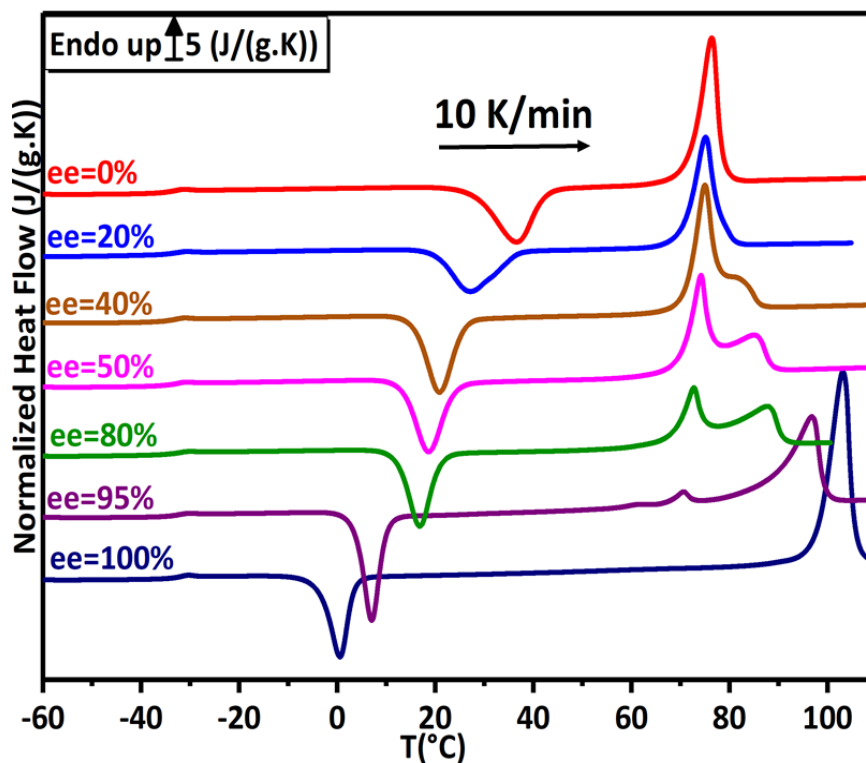


Figure 5: Heating at 10 K/min from amorphous state of samples at several ee

Upon recrystallization from the amorphous state, no eutectoid invariant was observed, only the metastable eutectic invariant associated to the melting of the racemic compound was evidenced. Thus, the recrystallization from the amorphous state led to the appearance of the metastable racemic compound. All the thermal events are rationalized in the metastable phase diagram illustrated in figure 6.

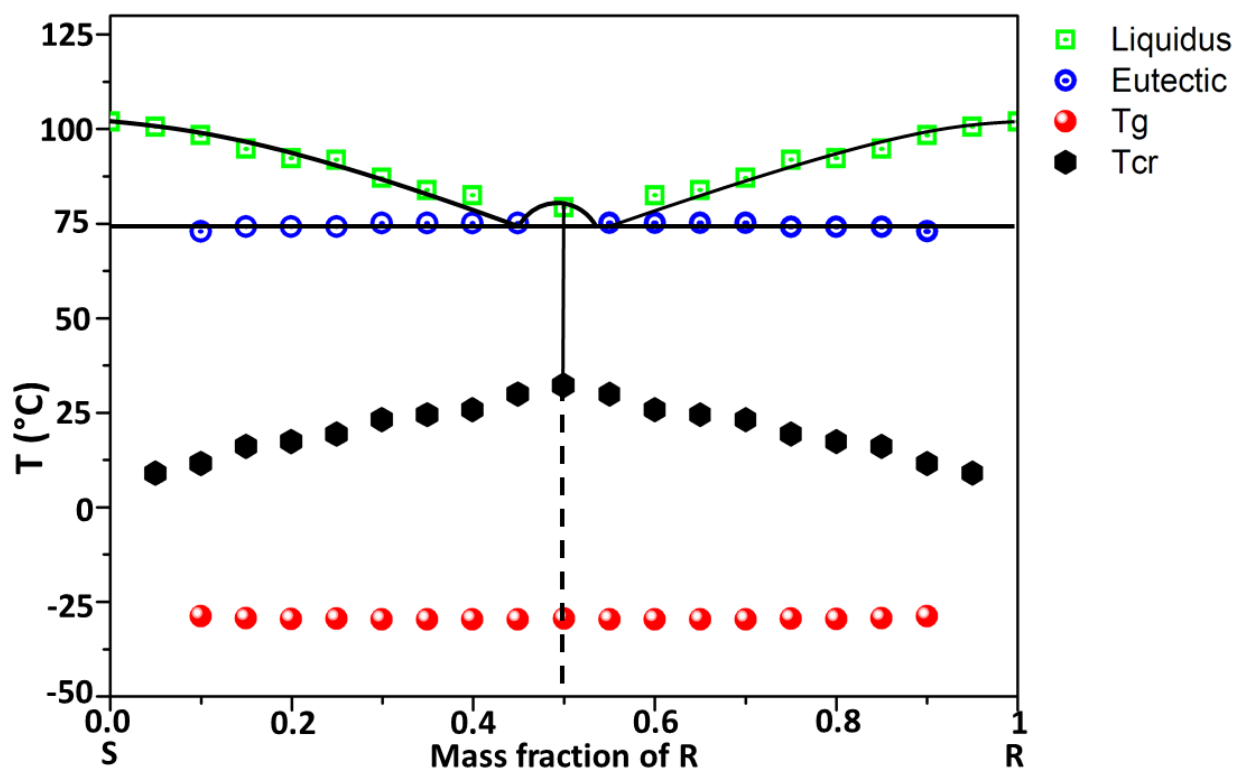


Figure 6: Metastable binary phase diagram between the two chiral antipodes, established from heating the glassy states. T_g and T_{cr} are the glass transition temperature and the onset of crystallization

These hypotheses are consistent with the TR-XRD diffractogram measurement performed upon heating of the glassy material. Racemic Nac-MBA was melted and quenched in liquid nitrogen. The diffractogram was registered from $-20\text{ }^{\circ}\text{C}$ up to $80\text{ }^{\circ}\text{C}$ by step of $10\text{ }^{\circ}\text{C}$. Figure 7 depicts the thermal behavior of the amorphous sample upon heating. At $-20\text{ }^{\circ}\text{C}$ and $-10\text{ }^{\circ}\text{C}$, only the amorphous halo was evidenced, suggesting that vitrification was successfully achieved upon quenching. The initial amorphous sample recrystallizes between $0\text{ }^{\circ}\text{C}$ and $10\text{ }^{\circ}\text{C}$ towards the racemic compound. No appearances of characteristic peaks corresponding to the conglomerate were evidenced. Consequently, amorphous Nac-MBA recrystallizes as a racemic compound.

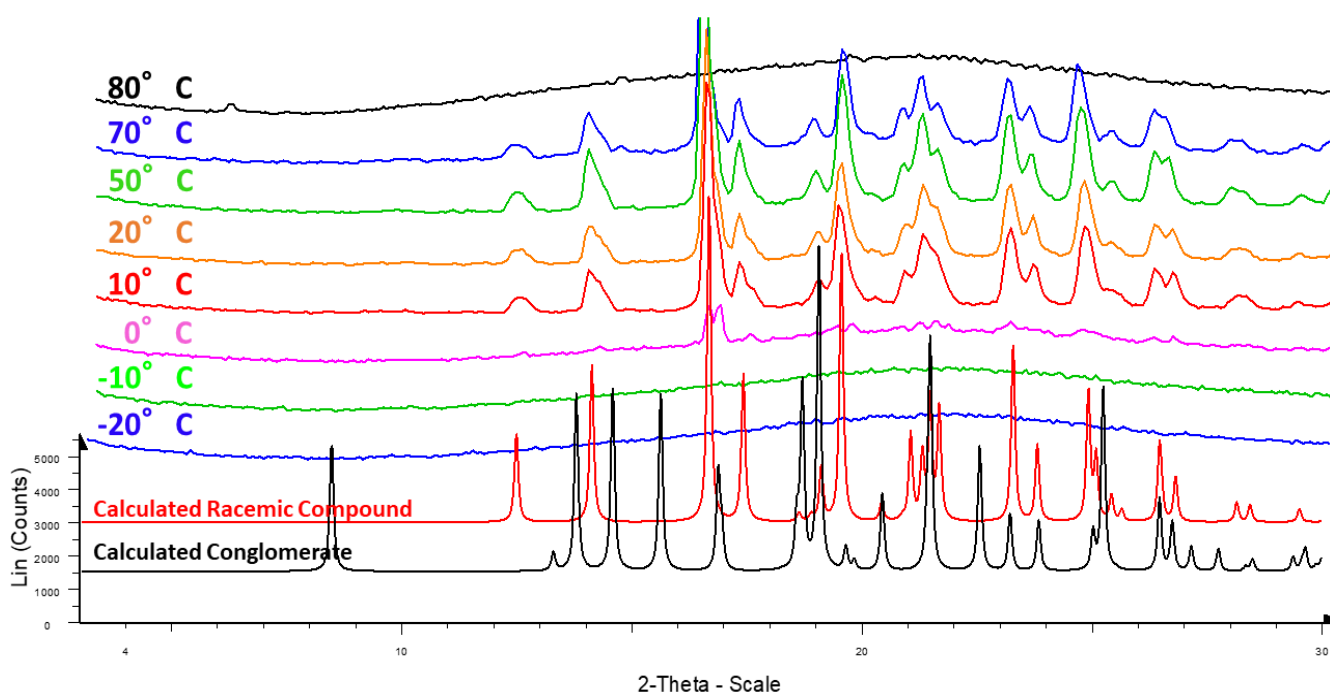


Figure 7: TR-XRD of the amorphous sample recrystallizing as a racemic compound upon heating.

Independently of the cooling rate, the melted sample always recrystallized as a racemic compound. This observation is in line with Oswald's steps rule, but may nevertheless seem contradictory regarding the weakly crystallogenic tendency of the racemic mixture. Even though the counter enantiomer acts as a configurational impurity during the cooling of the liquid, the possibility of forming centrosymmetric pairs (racemic compound) is nevertheless favored when the system is in conditions allowing crystallization. Nevertheless, this behavior seems accurate with the high occurrence of racemic compounds (95%) compared to conglomerate systems (5%).

4- High cooling rate and size effects from FSC measurements

In order to evaluate the high cooling rate and size effects on the eutectoid invariant, succinct FSC measurements were performed from crystals of the conglomerate and the racemic compound. Figure 8 illustrates the heating scan of conglomerate and racemic compound at 1000 K/s. The sample masses were estimated to be lower than 20 ng. Upon heating, the conglomerate presented a broad endothermic peak with an onset at $T_m = 68^\circ\text{C}$ associated to the melting of the conglomerate. The racemic compound presented a single endothermic

peak at $T_m=77^\circ\text{C}$ related to the melting phenomenon. Consequently, no obvious transition from the conglomerate towards the racemic occurred. The thermal fluctuation imposed to the conglomerate is fast enough in such a way that the kinetic of the solid – solid transition cannot follow and only the melting of the conglomerate was evidenced. For the case of the racemic compound, only the expected melting peak was observed.

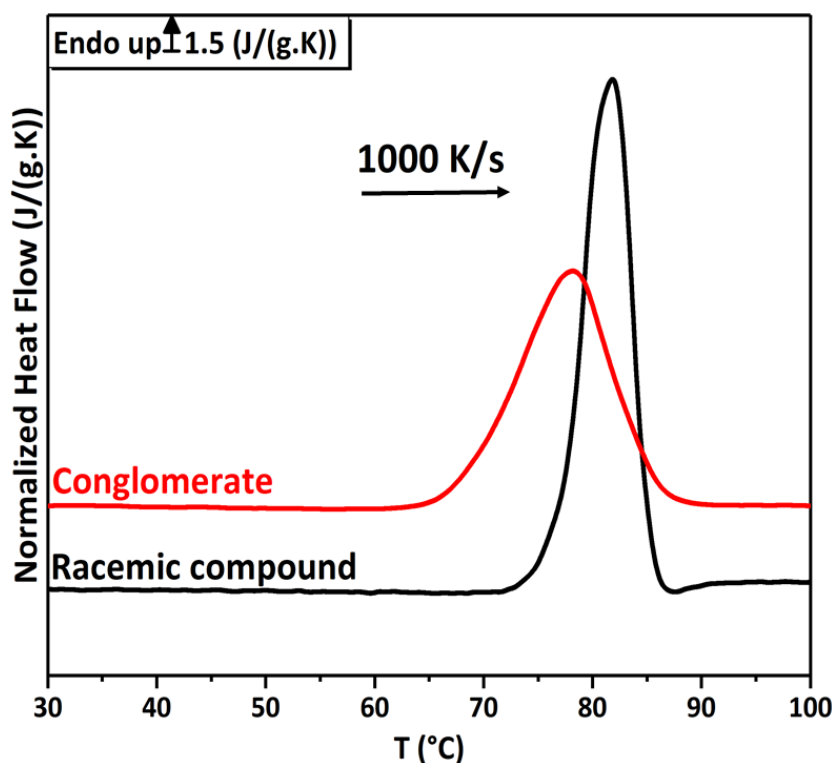


Figure 8: Heating scans at 1000 K/s of both conglomerate and racemic compound crystals

Both samples vitrified upon cooling at 1000 K/s. Therefore upon heating at 1000 K/s or 500 K/s the samples did not recrystallize. An isothermal step (for 2h) was then performed in the range -15°C up to 5°C by step of 5°C , and followed by heating at 1000 K/s. The thermal behaviors are independent from the fact that the sample was cold directly from the melt to the annealing temperatures or heated from the glassy state to the isothermal temperature. Upon heating, both samples presented the same thermal signature depending on the annealing temperature. For clarity and simplicity reasons we present results obtained only for the conglomerate (figure 9). When the annealing was performed at -10°C and -15°C , a single well defined endothermic peak appears at circa 67°C (the probable melting temperature of

the conglomerate). When the annealing was performed from -5 °C to 0 °C a double endothermic peak occurred. The onset of the first peak is identical to that of the conglomerate.

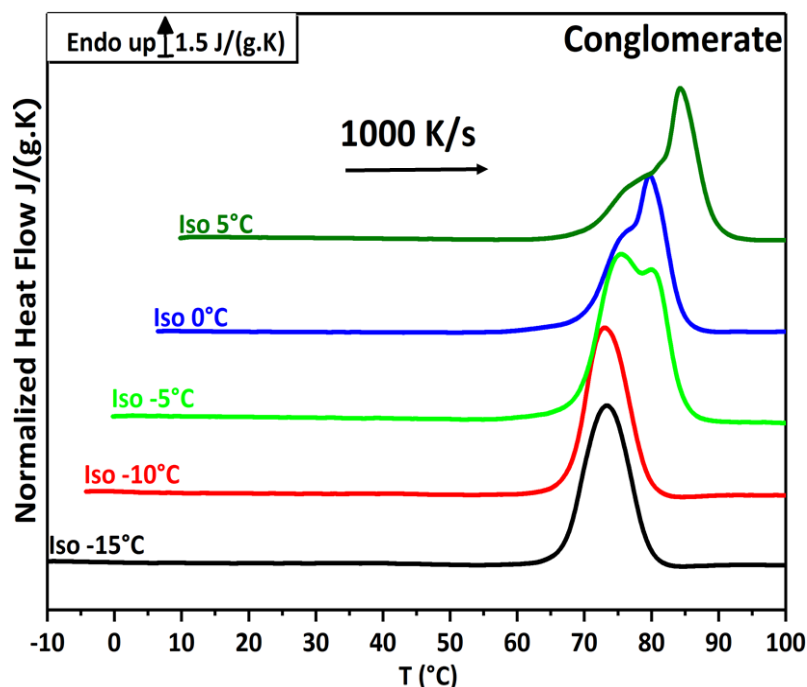


Figure 9: Thermal signature upon heating at 1000 K/s after an annealing step at several temperatures ranging from -15°C up to 5°C by step of 5°C

Several attempts to isolate these two thermal events by isothermal steps at higher temperatures turn out into failure, since the sample always skipped from the chip during the isothermal step and crystallizes out of the heating area. Nevertheless, it seems that between -5 °C to 0 °C additionally to the conglomerate, at least one solid phase crystallizes concomitantly with the conglomerate. Such behavior was not evidenced for the pure enantiomer. Moreover from DSC experiments, racemic compound was always preponderant upon crystallization from the melt or from the glassy state. This result suggests that the sample size and the kinetic of thermal fluctuation can highly impact the stability of enantiomeric systems. The hypothesis proposed by Druot and coworkers [2,3] on the existence of a metastable eutectic associated to the melting of the conglomerate is here reinforced. However a complete characterization of this metastable equilibrium requires XRD measurement.

II- Amorphous Nac-MBA and physical Aging

In this section we present some results of physical aging on amorphous Nac-MBA, for different aging temperatures, at several ee.

1- Thermal and kinetic properties of amorphous Nac-MBA

Amorphous Nac-MBA was obtained at various ee by melt cooling at 70 K/min. This cooling permitted to amorphize all the analyzed samples ($0 \leq ee \leq 75\%$). The samples were then submitted to a heat only temperature modulation protocol with a heating rate of 2K/min, modulation amplitude of ± 0.318 °C and a period of 60 s. Figure 10 depicts the glass transition signature upon heating at several ee. The glass transition temperature measured at the onset is $T_g^{on} = -32.5$ °C and independent of ee. The heat capacity jump at T_g , $\Delta C_p = 0.45 \pm 0.01$ (J/(g.K)) for $ee \leq 60\%$ and decreases slightly to $\Delta C_p = 0.42 \pm 0.01$ (J/(g.K)) for $ee = 75\%$.

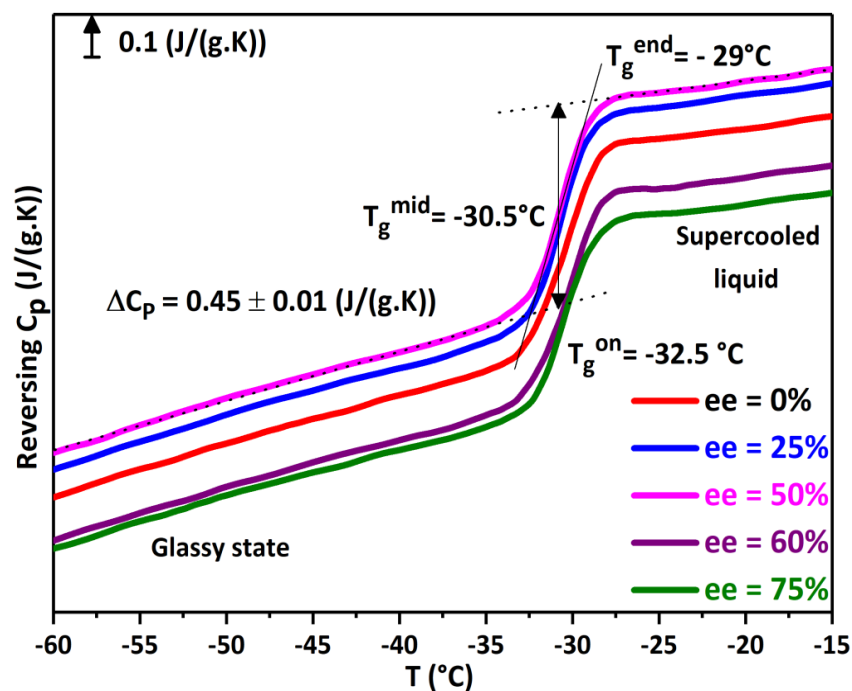


Figure 10: Reversing specific heat capacity as a function of temperature at a heating rate of 2 K/min, oscillation amplitude of ± 0.318 °C and a period of 60 s for several ee.

This slight difference may indicate that at this ee, Nac-MBA may possess less degree of freedom (lower configurational entropy) considering the greater crystallization propensity compared to lower ee. However no crystallization exothermic event was observed during cooling.

The kinetic behavior of the glass transition was clearly observed by combining DSC and FSC measurements. DSC analysis was performed at the same heating and cooling rate of 0.17 K/s with 5mg of a sample at an ee = 0%. In the case of FSC, the analyses were carried at two scanning rates (heating and cooling rates are identical) 1000 K/s and 1500 K/s with a sample at a scalemic composition. Therefore, since T_g is constant at variable ee, it makes sense to compare the T_g evolution as a function of the scanning rates using samples that are not at the same compositions. As illustrated in figure 11, the calorimetric glass transition signature is completely shifted towards higher temperatures for almost 20°C as the scanning rate increases for about four order of magnitude (from 0.17 K/s to 1500 K/s). This observation is consistent with the kinetic character of the glass transition, the higher the cooling rate, the higher the T_g value.

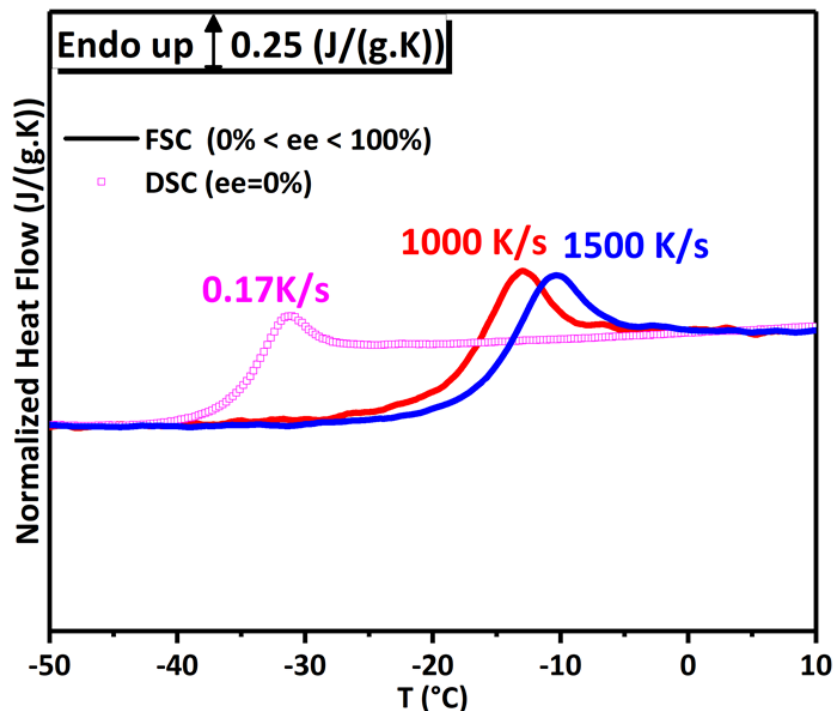


Figure 11: Kinetic behavior of the glass transition observed by DSC and FSC analyses for the same cooling and heating rates ranging from 0.17 K/s up to 1500 K/s

The small overshoot peak observed at the glass transition region is due to small aging effects that are related to the applied thermal protocol (before the final heating, a short isothermal step at low temperature is applied in order to stabilize the heat flow).

The knowledge of the T_g value is of primary importance when it comes to evaluate the kinetic of physical aging. In this work we consider the fictive temperature of the unaged glass as the reference T_g value. Since the glass transition appears over a certain temperature range, it is necessary to know exactly at what temperature enthalpy relaxation may occur during physical aging for a defined scanning rate. Another procedure consisted in performing an aging step at the vicinity of the glass transition region. If the amorphous sample is annealed below T_g , an additional overshoot peak is evidenced upon heating compared to the heating curve of the unaged glass. Therefore the heating curve of a glass annealed at exactly T_g or higher than T_g presents the same thermal signal as the unaged glass when heated from the glassy state. Figure 12 illustrates the heating curves (at 1500 K/s) of an amorphous sample (enantiomer), annealed in the vicinity of T_g (by increment of 1°C) for 5 s. For $T \leq -17^\circ\text{C}$ a small overshoot peak occurs upon heating and increases with decreasing aging temperature. But when $T \geq -16^\circ\text{C}$ the curves perfectly superimposed with the unaged scan.

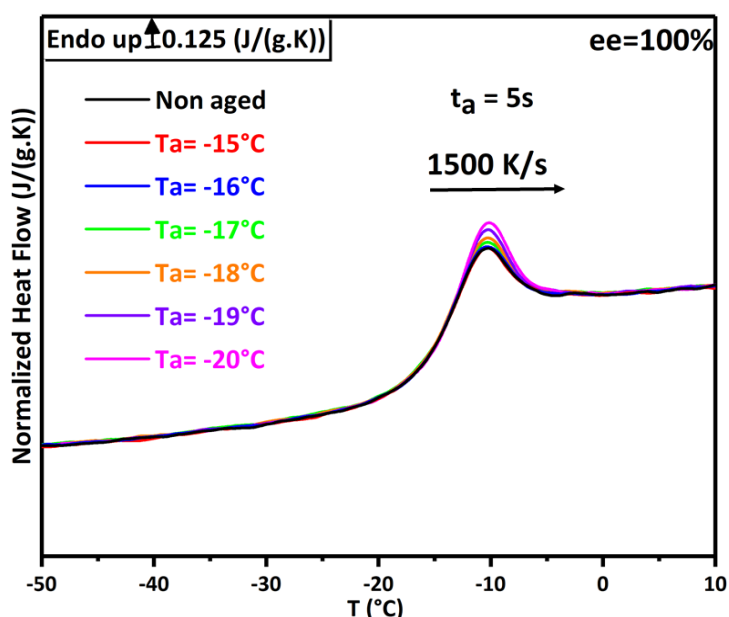
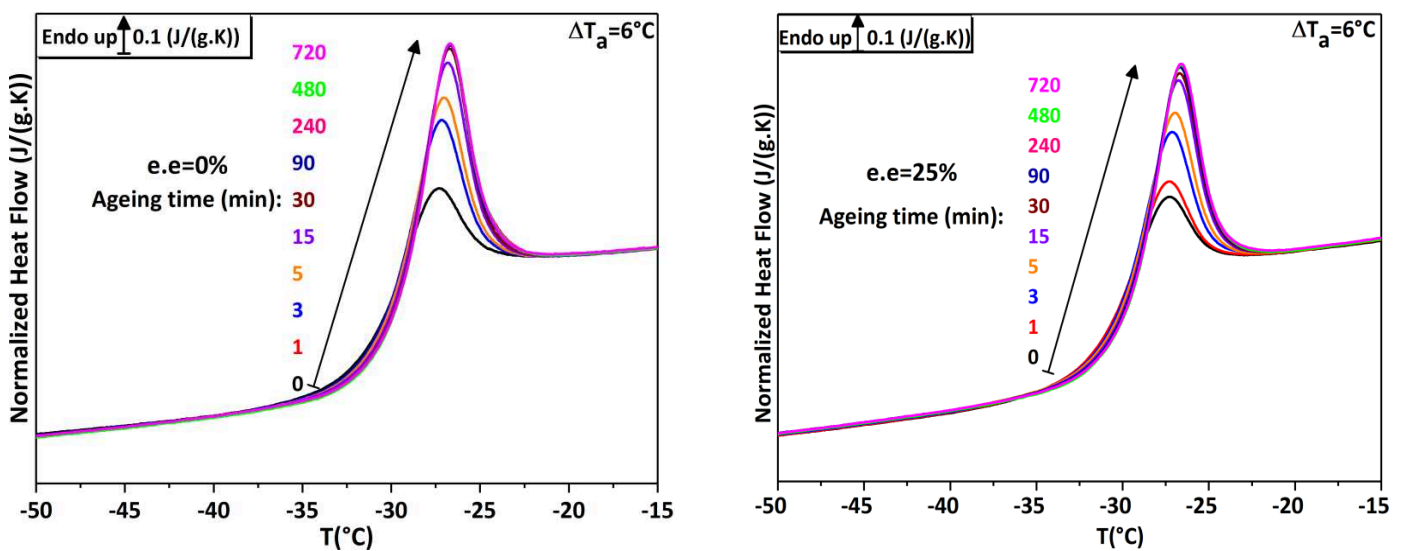


Figure 12: FSC heating scans at 1500 K/s of amorphous enantiomer (ee=100%) annealed at variable temperatures in the vicinity of T_g for 5s.

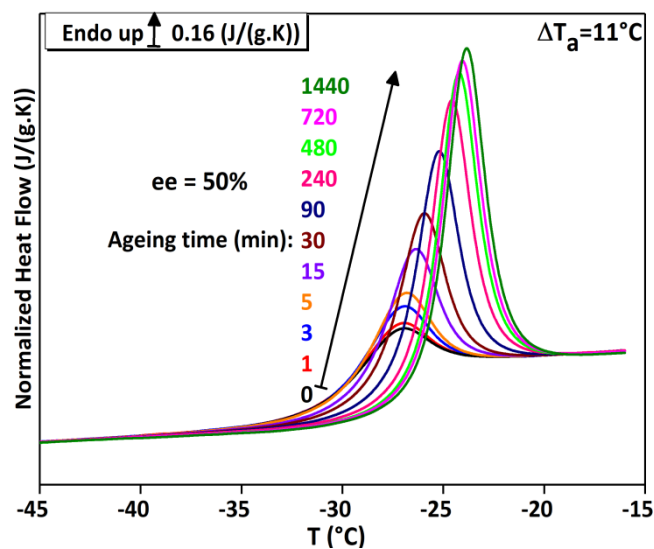
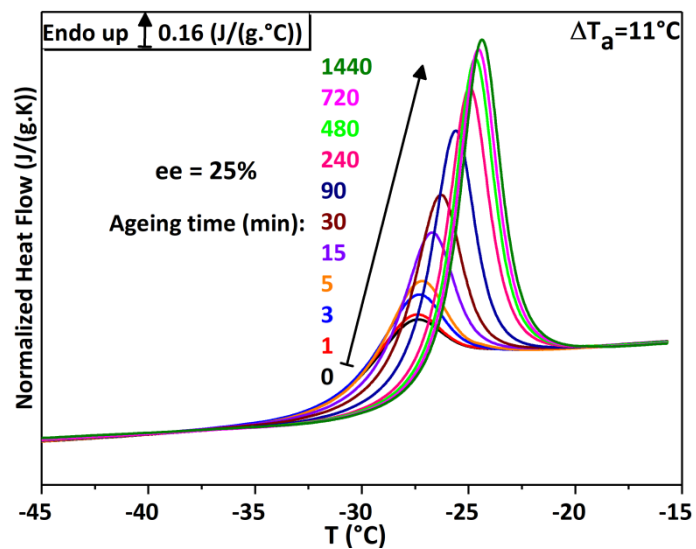
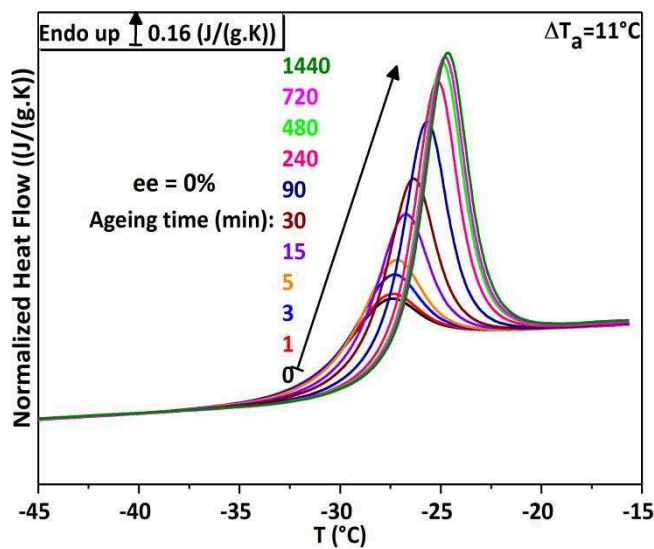
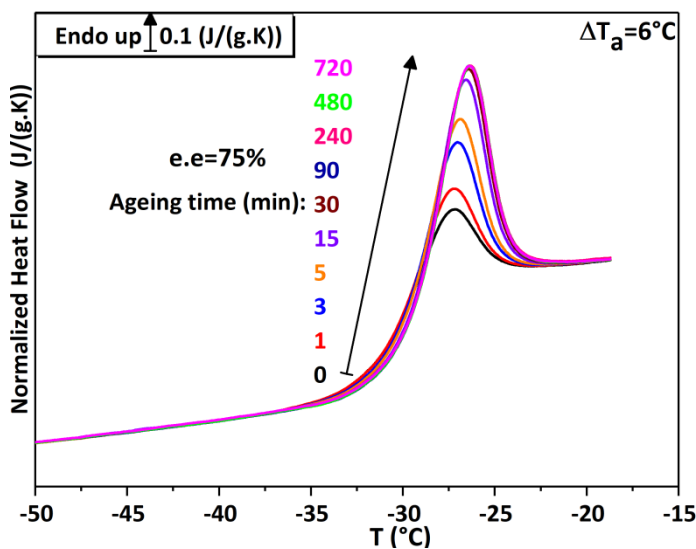
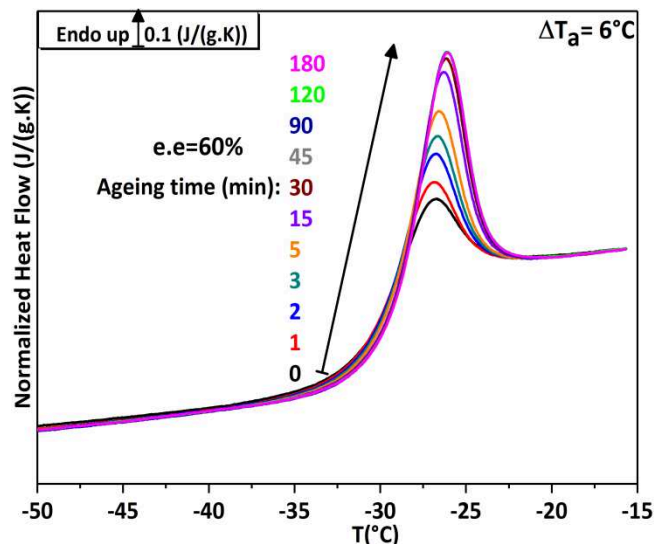
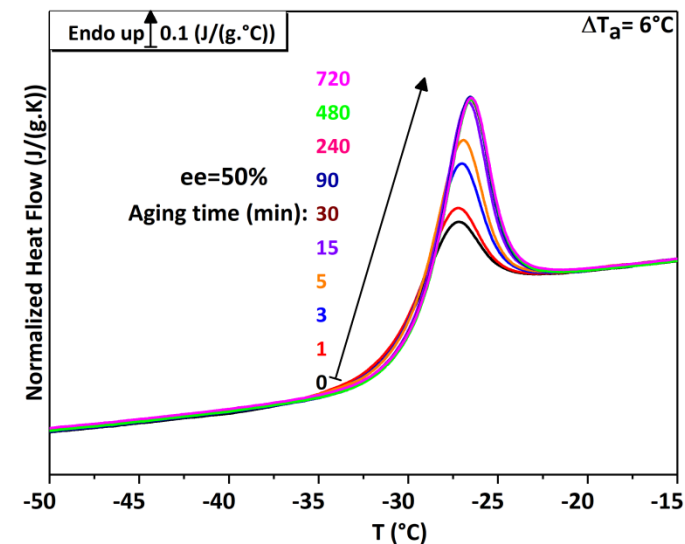
This result suggests that at $T \leq -17^\circ\text{C}$ the sample is already in the glassy state and consequently enthalpy relaxation can take place upon annealing. Conversely, at $T \geq -16^\circ\text{C}$ the sample is either exactly at the intersection of the glass region and the supercooled liquid or in the supercooled liquid state. Thus one can consider that $T_g = -16^\circ\text{C} \pm 1^\circ\text{C}$. This value is approximately the same as the fictive temperature found for the unaged glass (at 1500 K/s).

DSC Measurements: Aging was performed 6 °C and 11°C below $T_g = -32^\circ\text{C} \pm 1^\circ\text{C}$ for different aging durations t_a (from 1 to 720 min) after a rejuvenation cycle (sample heated above T_g and cooled down to T_a at 20 K/min). After the isothermal aging, the sample is cooled below T_a , i.e. -70°C , at 20 K/min, and heated at the same rate above T_g , in regards to record the aged glass signal. The same cycle is repeated to record the unaged glass signal.

Figure 13 depicts the thermal signature upon heating at 20 K/min of the aged glasses at different e_e . For a defined aging temperature T_a and independently of the e_e , similar overshoot peaks appear in all the analyzed samples. As expected, the overshoot peak superimposed to the heat capacity step at T_g , with an increasing amplitude and shift towards higher temperatures when the aging duration increasing from 0 up to 720 min (for $\Delta T_a=6^\circ\text{C}$) or from 0 up to 1440 min (for $\Delta T_a=11^\circ\text{C}$). Additionally, for long aging times, the overshoot peak signal becomes constant and perfectly superimposed with longer t_a . Moreover, the magnitude of the overshoot peak increases for lower aging temperatures and longer aging time are required to reach a constant overshoot peak. For $T_a = T_g - 6^\circ\text{C}$ and $T_a = T_g - 11^\circ\text{C}$ the saturation is reached after almost 30 min (independently of the e_e) and 1440 min respectively.



II- Amorphous Nac-MBA and Physical Aging



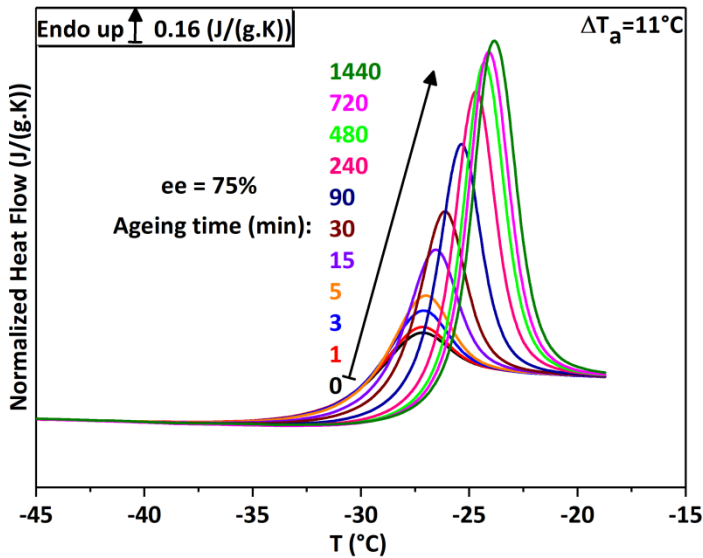


Figure 13: Normalized heat flow curves recorded after physical aging during heating ramps (20 K/min) as a function of ee%. $\Delta T_a = (T_g - T_a) = 6^\circ\text{C}$ and 11°C with $T_g = -32 \pm 1^\circ\text{C}$

FSC Measurements: As explained in chapter 2 section II. C) It is not easy to perfectly master the ee value (when $ee \neq 100\%$) during sample preparation for FSC experiments. In all this section two compositions will be considered, a pure enantiomer ($ee=100\%$) and a scalemic composition ($0\% \leq ee < 100\%$). Aging was performed 6°C , 11°C , 16°C and 21°C below T_g ($T_g = -22^\circ\text{C} \pm 0.5^\circ\text{C}$ at 1000°C/s) for different aging durations t_a (0.01 s to 14400s) after a rejuvenation cycle (sample heated above T_g and cooled at 1000°C/s down to T_a). After the isothermal aging, the sample is cooled below T_a , i.e. -70°C , at 1000°C/s , and heated at 1000°C/s above T_g to record the aged glass signal. The same cycle is repeated to record the unaged glass signal.

Figure 14 shows FSC curves obtained after in-situ aging performed at $T_a = -28^\circ\text{C} = T_g - 6^\circ\text{C}$ and $T_a = -38^\circ\text{C} = T_g - 16^\circ\text{C}$. As aging duration increases, the endothermic peaks superimposed to heat capacity step at T_g are shifted towards high temperatures with an increasing magnitude as expected.

We may note that the glass transition zone shifting in comparison to DSC experiments is classically observed from FSC experiments due to the very high heating rate used. This kinetical behavior have already been discussed in the previous section.

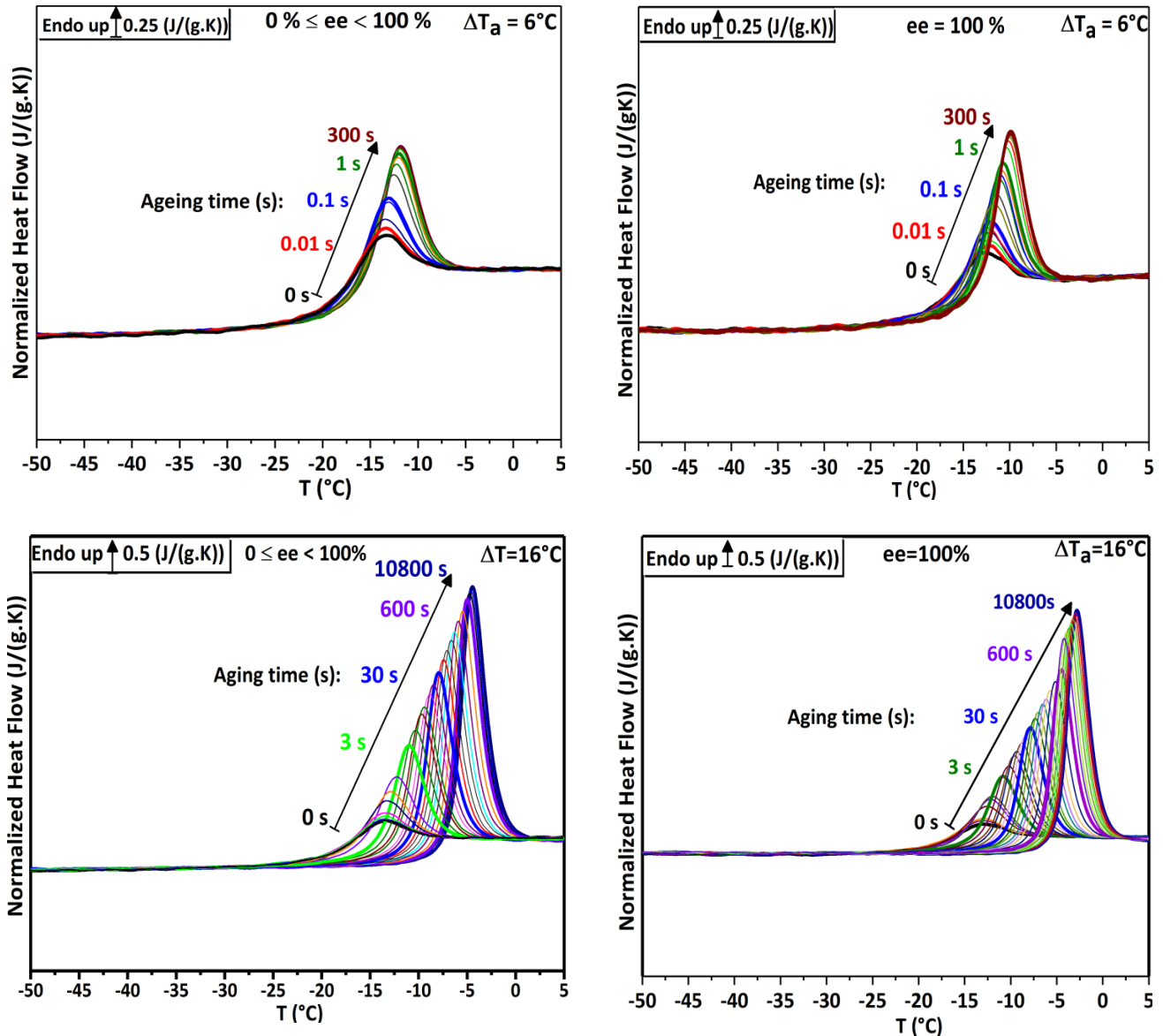


Figure 14: Normalized heat flow curves recorded after physical aging during heating ramps as a function of ee%. $\Delta T_a = (T_g - T_a) = 6^\circ\text{C}$ and 16°C with $T_g = -22 \pm 0.5^\circ\text{C}$

The shift of the overshoot peak to higher temperatures as t_a increases is due to the fact that enthalpy recovers the supercooled metastable liquid value upon heating only at the temperature where molecular mobility is high enough to allow this. As the aging temperature T_a decreases, molecular mobility drastically decreases, but if sufficient aging times t_a are provided, the initial glass will slowly evolve towards the metastable supercooled liquid by lowering its enthalpy. Thus high magnitude enthalpy recoveries are expected upon heating. For T_a near T_g (e.g. $T_a = T_g - 6^\circ\text{C}$) the glass reaches a certain equilibrium after short aging time and the difference of enthalpy between the unaged glass and the metastable supercooled

liquid is small. Thus, the overshoot peak will be of low magnitude. The fact that after long aging time the overshoot peak reaches a saturation value is not always synonym that the supercooled liquid metastable equilibrium have been reached. In order to verify if the enthalpy loss at the saturation value corresponds to the metastable equilibrium, the fictive temperature and the enthalpy recovery ΔT_a evolutions as a function of t_a are determined. Figure 15 depicts the fictive temperature evolution as a function of t_a at different ee for three aging temperatures (6°C and 11°C and 16°C below T_g) obtained either from DSC or FSC measurements.

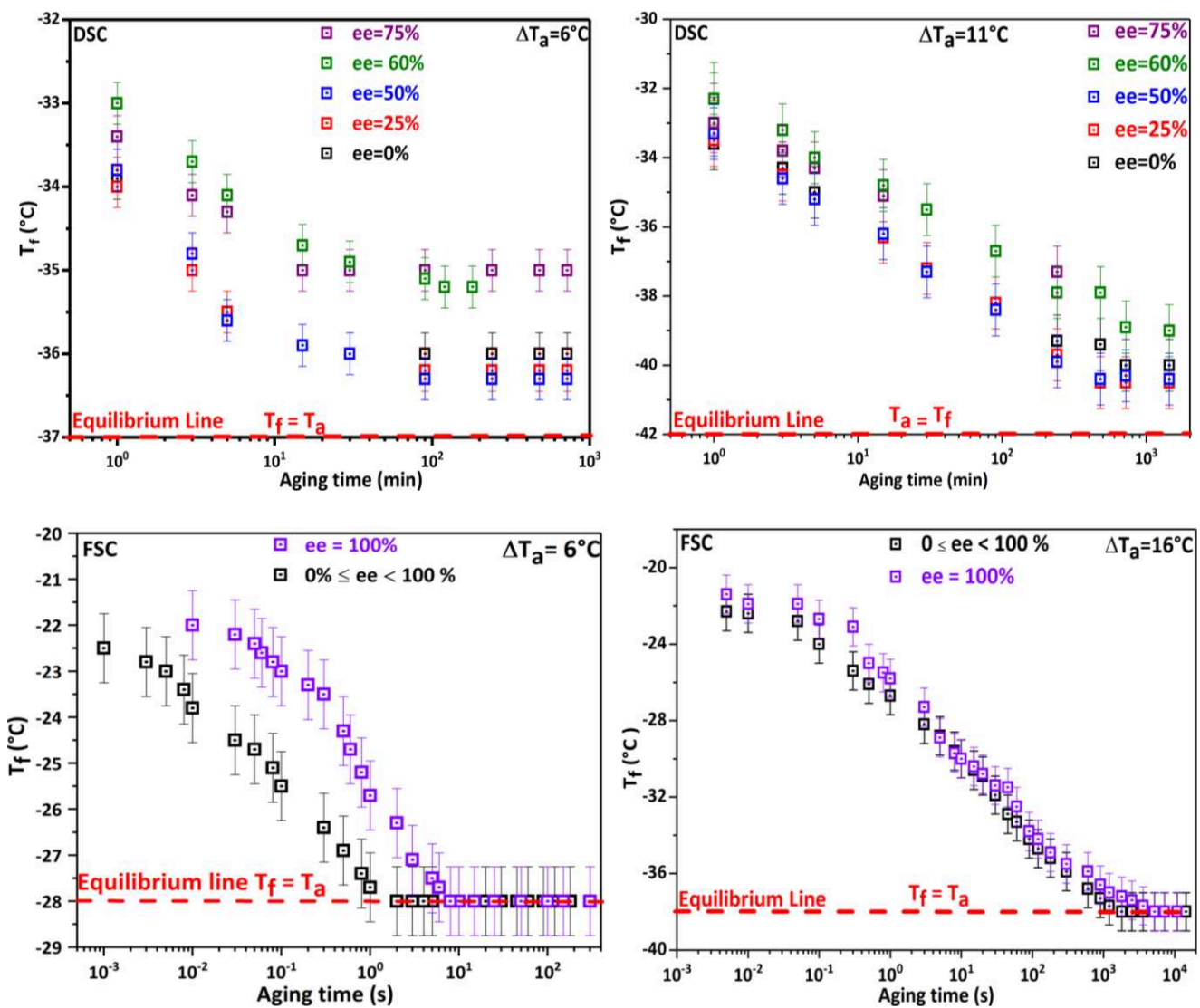


Figure 15: FSC and DSC experiments. Time evolution of the fictive temperature in function of several ee at $\Delta T_a = 6^\circ\text{C}$, 11°C and 16°C .

The main information provided by the DSC measurements are the following:

- i) As the aging time increases, the fictive temperature smoothly evolves towards lower temperatures and reaches a constant value. This is classically observed during physical aging phenomenon.
- ii) For all the analyzed ee, T_f at long aging time is always higher than T_a . Therefore, the supercooled liquid metastable equilibrium is not achieved. The aged samples can be considered at an intermediate state with an enthalpy higher than the enthalpy of the supercooled liquid extrapolated at T_a . Such behavior is conventionally observed from conventional DSC, the metastable equilibrium is rarely attainable from aging of amorphous glass generated by melt quenching [5–10]. It was also reported by Andreozzi and coworkers that the extrapolated liquid line is not reached at equilibrium for a high molecular weight PMMA because of the chain entanglement and topological constraints [9]. However Cangialosi and coworkers [11] found for a setgroup of polystyrene and polycarbonate that the metastable liquid equilibrium is reached through a double-step enthalpy recovery after very long aging time (almost 1 year).
- iii) For samples with an ee > 50%, T_f (at long aging time) is far from the equilibrium value compared to ee ≤ 50% since T_f value (at long aging time) is higher for ee > 50% than ee ≤ 50%. This behavior is observed for the two aging temperatures but well pronounced for aging achieved near T_g . Since the propensity to crystallize is important for high ee, such samples may exhibit high nucleation tendencies upon ageing compared to the lower ee. Moreover, near T_g this nucleation tendency can be much more pronounced compared to lower T_a . Thus long aging performed near T_g can highly promote a strong nucleation behavior. Even though crystallization may not occur during the aging protocol, nucleation can create slight density differences when comparing the different ee.

From FSC results the following discussion can be written:

- i) As the aging time increases, T_f decreases and reaches a constant value equal to the aging temperature independently of ee and T_a . This result suggests that the supercooled liquid metastable equilibrium has been attained contrary to DSC

measurements. More surprisingly is the time scale needed to reach the equilibrium in FSC measurements; the kinetic of aging is accelerated. One to eight seconds and 1000 s to 4000 s (function of ee) are required to reach equilibrium for $\Delta T_a=6^\circ\text{C}$, and $\Delta T_a=16^\circ\text{C}$ respectively. It is well established that the high cooling rate facilities provided by FSC can generate amorphous glass with high enthalpy and high free volume leading to accelerated enthalpy recovery processes [12–14].

- ii) The time required to reach the equilibrium is highly dependent of the ee even though the equilibrium is the same. For both aging temperatures, amorphous pure enantiomer requires more time to regain the equilibrium than the scalemic sample. The ee dependency of the aging kinetic is highly pronounced for aging near T_g . This may suggest additional constraint effects such as strong nucleation (below T_g) upon aging that can delay the return towards equilibrium in the case of pure enantiomer compared to the scalemic composition. Since equilibrium is reached independently of the ee, the enthalpy loss needed to reach equilibrium is not a function of the ee.

Since from DSC experiments the metastable equilibrium is not reached for all the investigated T_a , the enthalpy recovery must be lower than what is obtained from FSC measurements for the same T_a . Figure 15 illustrates the difference between the theoretical enthalpy loss at the equilibrium and the experimental enthalpy recovery as a function of t_a , at $\Delta T_a=6^\circ\text{C}$ obtained from DSC and FSC. From DSC experiments, the enthalpy recovery reached at the saturation value is less than half of the required loss needed to reach equilibrium.

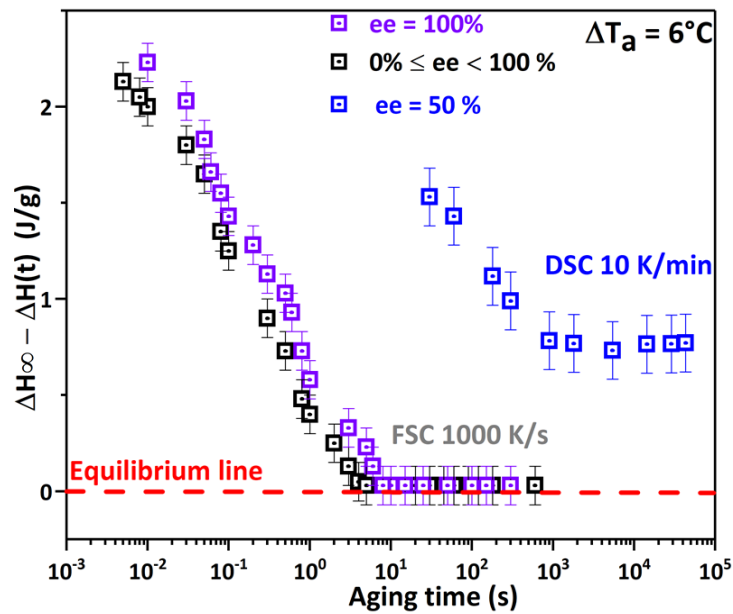


Figure 16: DSC and FSC time evolution of the difference between ΔH_{∞} and ΔH_t for the aged samples in function of ee at $\Delta T_a = 6^{\circ}\text{C}$

These results highlight the advantage of the FSC for structural recovery studies, which is the extended time and the high cooling rate allowing measurements to be made at times as short as 0.01 s [12] and the cooling rate as high as 1000 K/s. Such facilities permit to evaluate the time scale of structural relaxation at very short t_a for which DSC is insensitive. Furthermore regarding the accelerated physical aging process, lower aging temperatures can be investigated. Therefore compared to DSC is highly time save.

III- Conclusions

In this chapter, the amorphous state of Nac-MBA was investigated at various enantiomeric compositions. Upon heating, the stable conglomerate slowly evolves towards the racemic compound through at least two thermal events, an incomplete solid-solid transition (conglomerate to racemic compound), the melt of the conglomerate and recrystallization of the racemic compound. When high scanning rate is provided (1000 K/s) the transition from the conglomerate toward the racemic compound is suppressed and only the melting of the conglomerate is observed.

It is clear that the enantiomeric composition strongly influence the GFA. As the ee increases the GFA decreases. Therefore Racemic Nac-MBA can be considered as a good glass former compared to pure enantiomer. In this case, the counter enantiomer acts like a chemical impurity of same nature as the opposite enantiomer that may delay or inhibit crystallization upon cooling. Such behavior was previously observed in the case of another conglomerate system, 12H. Conversely, upon heating the amorphous glass recrystallizes as a racemic compound (same as 95% of chiral species). The recrystallization of the racemic compound does not require at all passing through the glassy state. By very slow cooling of the melt, the sample also recrystallized as the racemic compound. Therefore, from FSC analyses (<50 ng) the recrystallization from the amorphous glass or from the liquid state always led to the appearance of the conglomerate or a mixture of the conglomerate and an additional phase depending on the crystallization temperature. However structural characterizations are necessary to fully identify the additional phase.

The physical aging process of Nac-MBA was investigated by thermal analyses. Through FSC investigations, we have shown that the equilibrium state can be reached even if it seemed not possible from DSC investigations. Furthermore, as far as we know, this is the first study highlighting that: i) the enthalpy loss needed to reach the equilibrium for a chiral amorphous glass is independent from the enantiomeric excess (ee), whereas ii) the velocity to reach this equilibrium is ee dependent. This last behavior may be related to a strong nucleation tendency upon aging for high enantiomeric composition.

References

- [1] B. Atawa, N. Couvrat, G. Coquerel, E. Dargent, A. Saiter, Chirality impact on physical ageing: An original case of a small organic molecule, *Mater. Lett.* 228 (2018) 141–144. doi:10.1016/j.matlet.2018.05.133.
- [2] S. Druot, M.N. Petit, S. Petit, G. Coquerel, N.B. Chanh, Experimental Data and Modelling of the Interactions in Solid State and in Solution between (R) and (S) N-Acetyl- α -Methylbenzylamine. Influence on Resolution by Preferential Crystallization, *Mol. Cryst. Liq. Cryst. Sci. Technol. Sect. Mol. Cryst. Liq. Cryst.* 275 (1996) 271–291. doi:10.1080/10587259608034081.
- [3] S. Druot Houllemare, Influence des interactions homo- et heterochirales lors du dedoublement par cristallisation preferentielle de deux derives de l'alpha-methylbenzylamine : le n-acetamide et le chloroacetate, thesis, Caen, 1999. <http://www.theses.fr/1999CAEN2029> (accessed September 24, 2018).
- [4] C.T. Moynihan, P.B. Macedo, C.J. Montrose, C.J. Montrose, P.K. Gupta, M.A. Debolt, J.F. Dill, B.E. Dom, P.W. Drake, A.J. Easteal, P.B. Elterman, R.P. Moeller, H. Sasabe, J.A. Wilder, Structural Relaxation in Vitreous Materials, *Ann. N. Y. Acad. Sci.* 279 (1976) 15–35. doi:10.1111/j.1749-6632.1976.tb39688.x.
- [5] M. Descamps, J.-F. Willart, Some Facets of Molecular Disorder in Crystalline and Amorphous Pharmaceuticals, in: *Disord. Pharm. Mater.*, Wiley-Blackwell, 2016: pp. 1–56. doi:10.1002/9783527652693.ch1.
- [6] B.C. Hancock, S.L. Shamblin, G. Zografi, Molecular Mobility of Amorphous Pharmaceutical Solids Below Their Glass Transition Temperatures, *Pharm. Res.* 12 (1995) 799–806. doi:10.1023/A:1016292416526.
- [7] S.L. Shamblin, G. Zografi, Enthalpy Relaxation in Binary Amorphous Mixtures Containing Sucrose, *Pharm. Res.* 15 (1998) 1828–1834. doi:10.1023/A:1011997721086.
- [8] H.Y. Zhao, Y.P. Koh, M. Pyda, S. Sen, S.L. Simon, The kinetics of the glass transition and physical aging in germanium selenide glasses, *J. Non-Cryst. Solids.* 368 (2013) 63–70. doi:10.1016/j.jnoncrysol.2013.02.025.
- [9] L. Andreozzi, M. Faetti, M. Giordano, D. Palazzuoli, F. Zulli, Enthalpy Relaxation in Polymers: A Comparison among Different Multiparameter Approaches Extending the TNM/AGV Model, *Macromolecules.* 36 (2003) 7379–7387. doi:10.1021/ma0347870.
- [10] G.B. McKenna, S.L. Simon, Chapter 2 - The glass transition: its measurement and underlying physics, in: S.Z.D. Cheng (Ed.), *Handb. Therm. Anal. Calorim.*, Elsevier Science B.V., 2002: pp. 49–109. doi:10.1016/S1573-4374(02)80005-X.
- [11] D. Cangialosi, V.M. Boucher, A. Alegría, J. Colmenero, Direct Evidence of Two Equilibration Mechanisms in Glassy Polymers, *Phys. Rev. Lett.* 111 (2013) 095701. doi:10.1103/PhysRevLett.111.095701.

References

- [12] Y.P. Koh, S. Gao, S.L. Simon, Structural recovery of a single polystyrene thin film using Flash DSC at low aging temperatures, *Polymer*. 96 (2016) 182–187. doi:10.1016/j.polymer.2016.04.047.
- [13] L. Grassia, Y.P. Koh, M. Rosa, S.L. Simon, Complete Set of Enthalpy Recovery Data Using Flash DSC: Experiment and Modeling, (2018). doi:10.1021/acs.macromol.7b02277.
- [14] X. Monnier, A. Saiter, E. Dargent, Physical aging in PLA through standard DSC and fast scanning calorimetry investigations, *Thermochim. Acta*. 648 (2017) 13–22. doi:10.1016/j.tca.2016.12.006.

CHAPTER V:

MOLECULAR MOBILITY OF AMORPHOUS N-ACETYL-A- METHYLBENZYLAMINE AND IMPACT OF CHIRALITY EVIDENCED BY DIELECTRIC RELAXATION SPECTROSCOPY AND MOLECULAR DYNAMIC SIMULATIONS

In this chapter we focused on the molecular mobility characterization of amorphous N-acetyl- α -methylbenzylamine (Nac-MBA) by Broadband Dielectric Spectroscopy (BDS) coupled to Fast Scanning Calorimetry (FSC) and Molecular Dynamic (MD) Simulations covering over 12 decades in the frequency range. An ee=50% has initially been investigated since enantiomerically pure systems possess in general poor glass forming ability as discussed in the previous chapters [1,2]. A great interest is carried out on the impact of chirality on the molecular mobility of the system. For this purpose the molecular mobility of Nac-MBA is investigated at several ee= 100%, ee=75%, and ee=0% in comparison with ee=50%. Parts of these results have been submitted for publication in journal of Physical Chemistry Chemical Physics.

I- Molecular mobility of Nac-MBA

A- Dielectric Relaxation Spectroscopy (DRS): Molecular Mobility Characterization of Nac-MBA (ee = 50%)

As highlighted in chapter IV, amorphous glass Nac-MBA (ee=50%) can be obtained by melt quenching. For dielectric analysis, the amorphous sample was prepared *ex-situ* to guarantee a sufficient cooling rate in order to avoid crystallization. Measurements of the complex permittivity $\epsilon^*(f)$ was performed isothermally in the range [153 K, 273 K] with a frequency scan from 0.1 Hz to 2 MHz for each selected temperature. In the range 1 MHz – 1 GHz measurements were performed by means of a coaxial line reflectometer. The prepared sample was connected to the end of the coaxial line, and then melted *in situ* and annealed for 5min at 383 K. Isothermal frequency scans were carried out from 383 K down to 283 K, by steps of 10 K.

1- Glassy State ($T < T_g$)

Figure 1 illustrates the frequency evolution of the dielectric loss ϵ'' in the glassy state. As depicted in figure 1, it is obvious that at least one secondary process takes place in the available frequency range. At the lowest temperature, a very broad and low magnitude process is displayed. Nevertheless, at this point we considered this phenomenon as a relaxation process labelled γ . As temperature increases γ relaxation is shifted towards higher

frequencies (mobility increases) and a second process designated as β relaxation and further β_{JG} appears at $T \geq 224$ K as a weak shoulder at lower frequencies than γ .

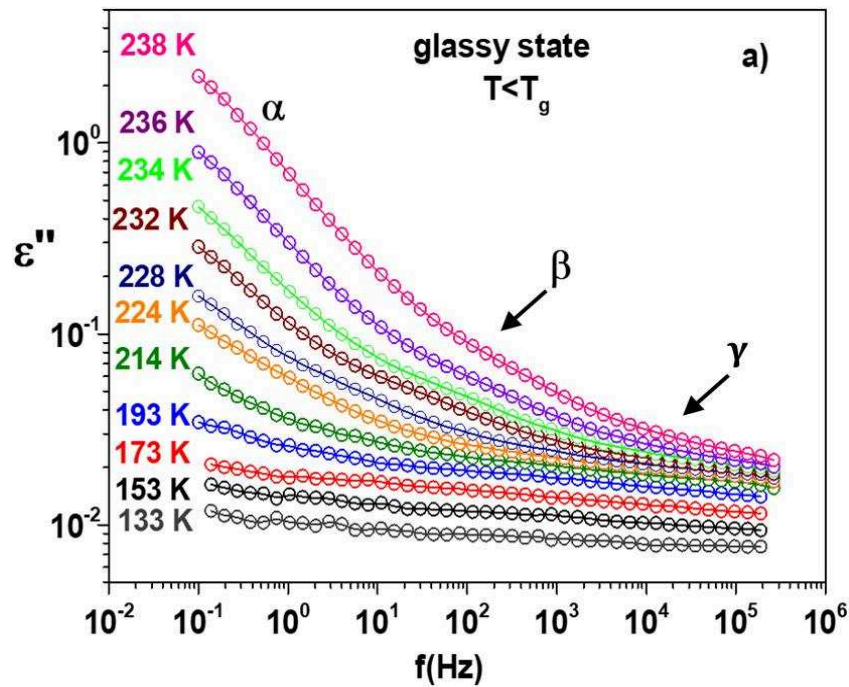


Figure 1: Temperature dependence behavior of dielectric loss ϵ'' in the glassy state (Below T_g) over 7 decades of frequency

2- Supercooled Liquid ($T > T_g$)

The evolution of the dielectric loss ϵ'' , the real permittivity ϵ' and its derivative ϵ''_{der} as a function of frequency in the supercooled liquid are shown in figure 2 a) b) and c) respectively. Measurements were performed from 241 K to 273 K with an increment of 1K. For sake of clarity, only features from 243 K to 263 K with a step of 2K are here presented. For temperatures higher than T_g , β process becomes broader while γ evolves out of the available frequency window and a very intense dielectric response (almost 90% of the dielectric strength) arises at lower frequency in the vicinity of the glass transition region. This process is designated as Debye process considering its pure exponential character. Molecular motions expressed by D process become faster as temperature increases. Furthermore, the intensity of D process suddenly decreases as temperature reaches 261 K as shown from the real dielectric permittivity profile (figure 2 b)). This behavior is related to the decrease of the amorphous fraction due to partial crystallization of the supercooled liquid. The magnitude of

all the processes vanishes and becomes zero upon complete crystallization. Moreover, conductivity arises at the low frequency window for temperature $T > 253$ K.

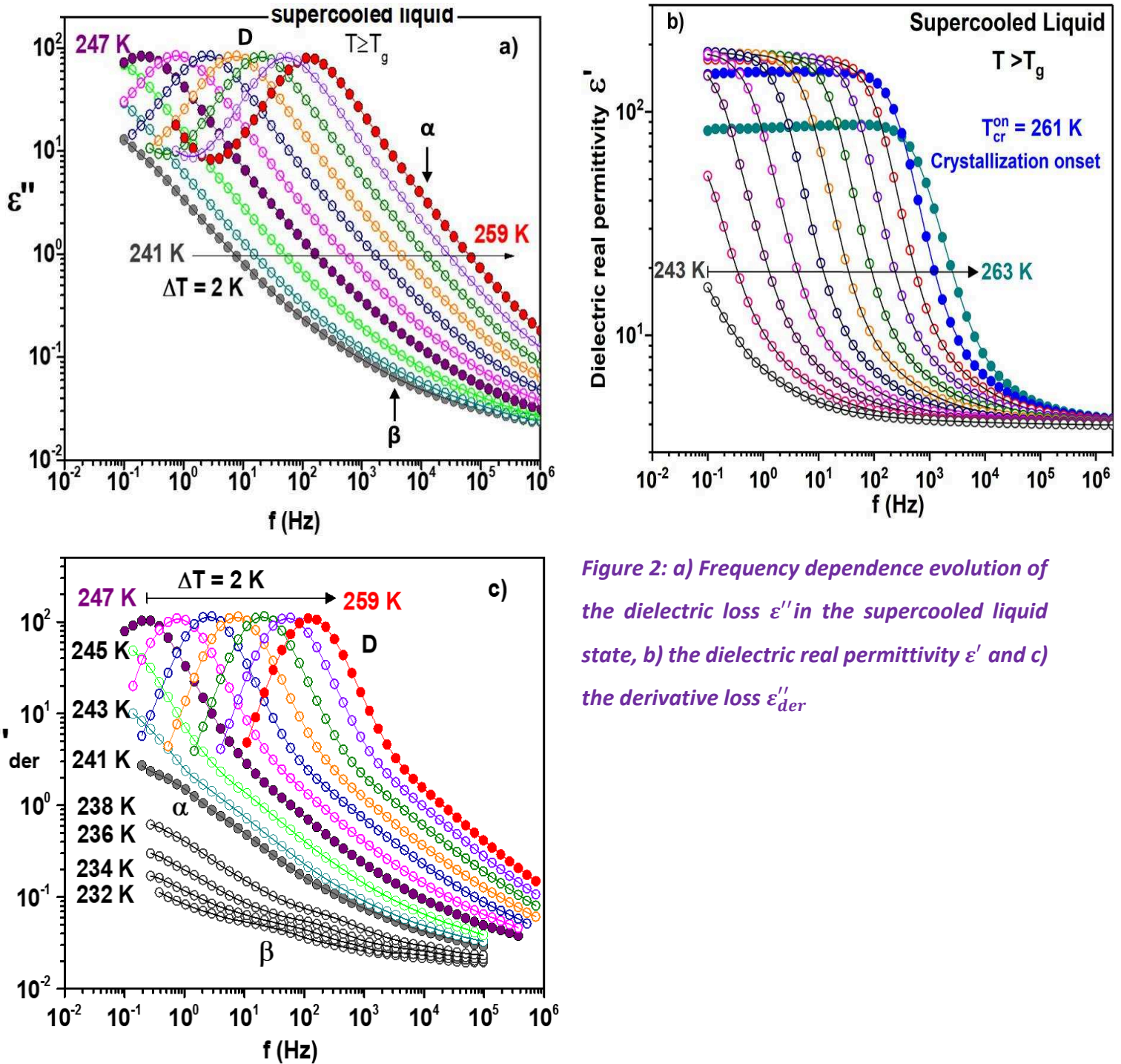


Figure 2: a) Frequency dependence evolution of the dielectric loss ϵ'' in the supercooled liquid state, b) the dielectric real permittivity ϵ' and c) the derivative loss ϵ''_{der}

The derivative method developed by Wübbenhorst and van Turnhout [3] helps to improve the frequency resolution of the α -process. The derivative is an alternative from the numerical Kramers-Kronig relation to obtain ϵ'' from the real permittivity ϵ' . The derivative loss ϵ''_{der} is given by [3]:

$$\varepsilon''_{der} = -\frac{\pi}{2} \frac{\partial \varepsilon'(f)}{\partial \ln(2\pi f)} \quad (1)$$

This method has the advantage to considerably improve the resolution of overlapping loss peaks and suppress ohmic conduction [3]. As illustrated in figure 2 c), additionally to D and β processes a third process namely α appears much more clearly from the derivative expression at intermediate frequency range between slower D process and faster β process. High frequency measurements (1 MHz – 1 GHz) were launched when cooling the liquid from 383 K – 283 K with regards to access the molecular motions at higher temperatures. The dielectric profile at lower temperature (T<283 K) could not be probed for reasons of crystallization appearance. Figure 3 shows the high frequency evolution of the real dielectric permittivity and its derivative from 383 K – 283 K. At high temperatures, only the intense D process is mentioned, and persists in the entire analyzed temperature region. The less intense α relaxation emerges at T \leq 313 K as a shoulder in the highest frequency range.

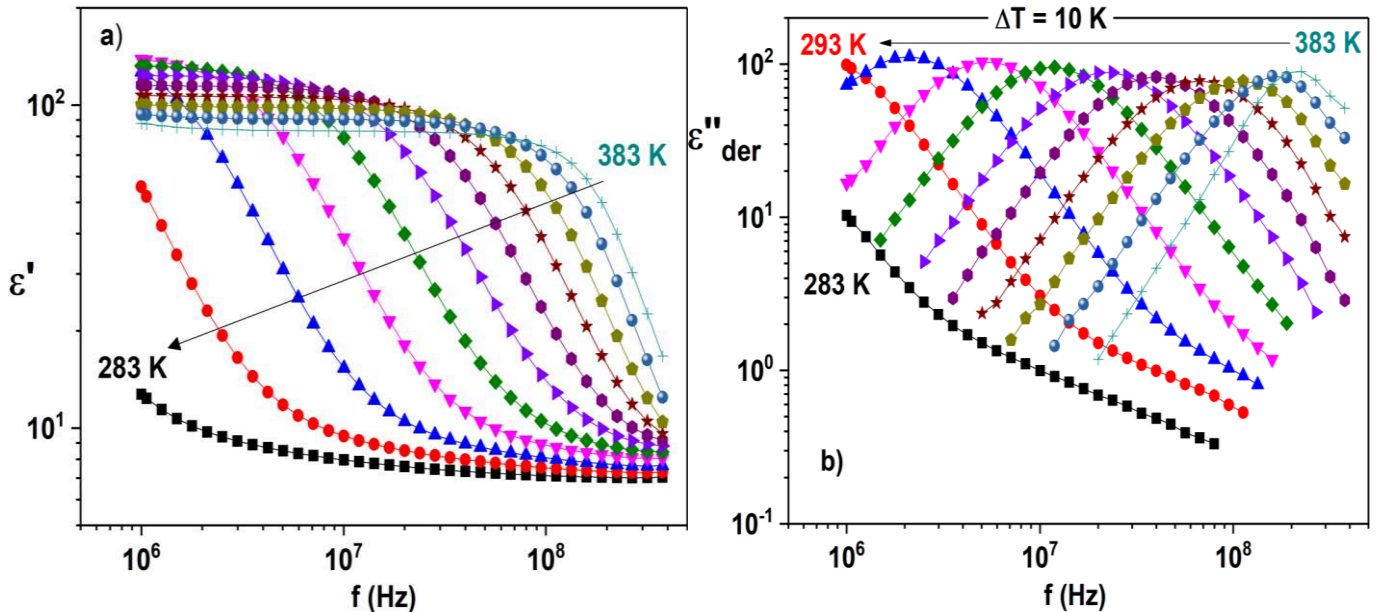
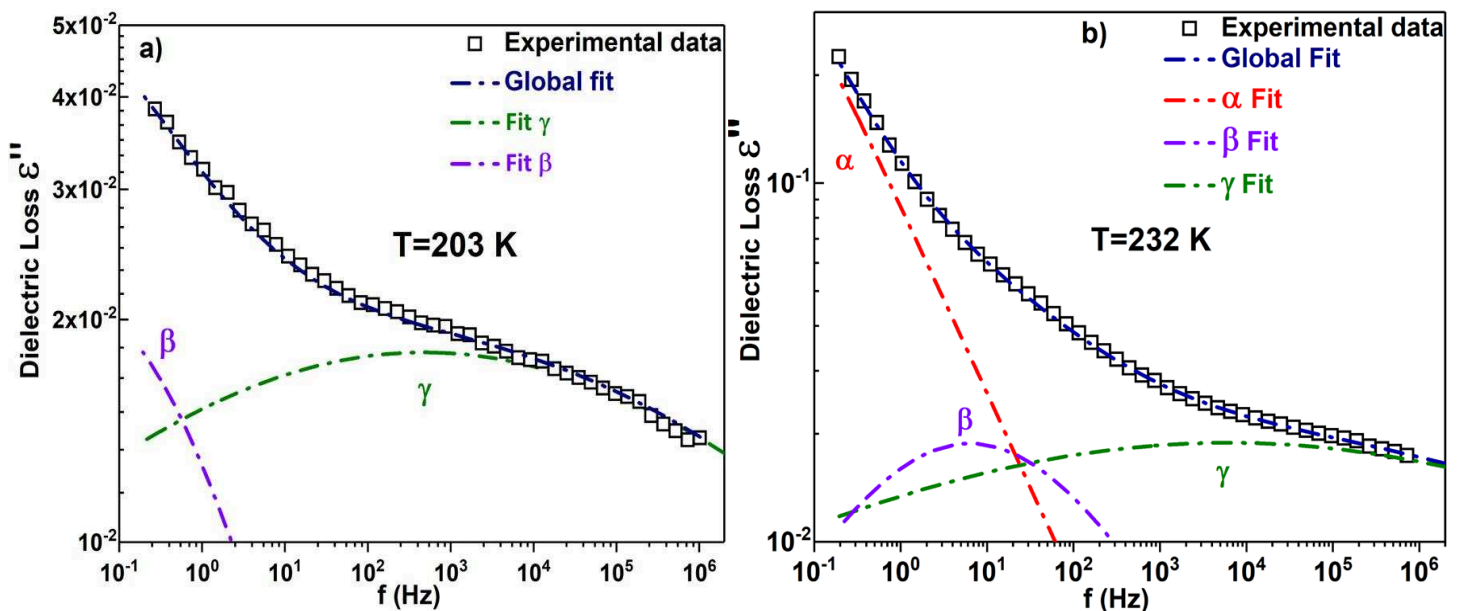


Figure 3: Frequency dependence of a) the real permittivity ε' and its b) derivative ε''_{der} in the high frequency region [1MHz – 1GHz] from 383 K up to 283 K

The Conductivity contribution and a sum of four HN functions were fitted to the dielectric experimental data. An illustrative example of the fitting procedure at 203 K, 232 K and 259 K is presented in figure 4. The fitting procedure permitted to derive information about the shape parameters, the dielectric strength and the relaxation time of the different processes. In the

present case such fitting procedure is somehow challenging and daring regarding poorly resolved or overlapping relaxation phenomena, and low magnitude processes. The latter parameters obtained from the fitting procedure are presented in the following:

Shape parameters: Both secondary γ , β contributions and structural α relaxation were fitted with a symmetrical Cole-Cole model function ($\beta_{HN} = 1$). In the case of secondary γ process the value $\alpha_{HN} = 0.14 \pm 0.01$ is obtained (see figure 4). This value corroborates with the broadness nature expressed by experimental features (see figures 1 and 4) and was kept constant in all the temperature region for which it was possible to follow γ trace in the available frequency region (from 153 K to 238 K). Concerning β relaxation, the broadness of the spectra is less pronounced and $\alpha_{HN} = 0.45$. Therefore, no significant change of this value is mentioned with temperature evolution. Concerning the structural α relaxation, the shape of the dielectric loss presented no significant temperature dependence and the parameter $\alpha_{HN} = 0.59 \pm 0.01$ remains constant in the supercooled liquid domain ($T > 241$ K). D process presented an exponential behavior. Consequently it was fitted with a simple Debye model function ($\alpha_{HN} = 1, \beta_{HN} = 1$) for $T > 241$ K (see figure 4 c)).



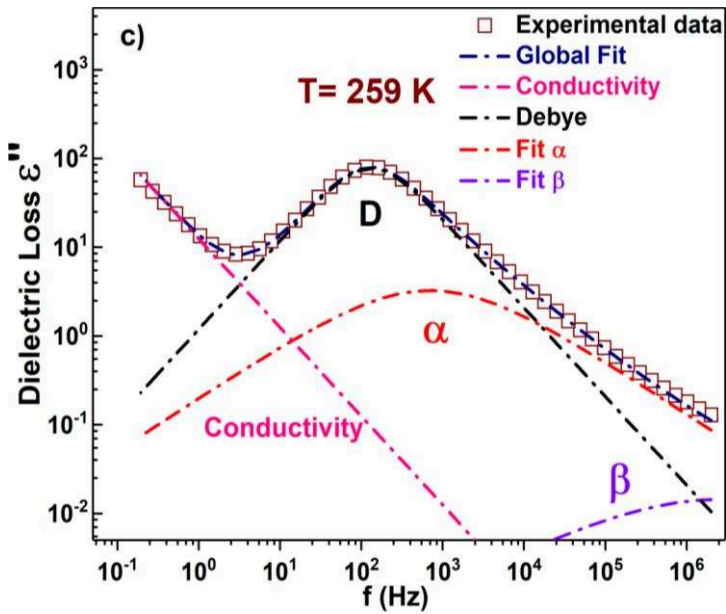


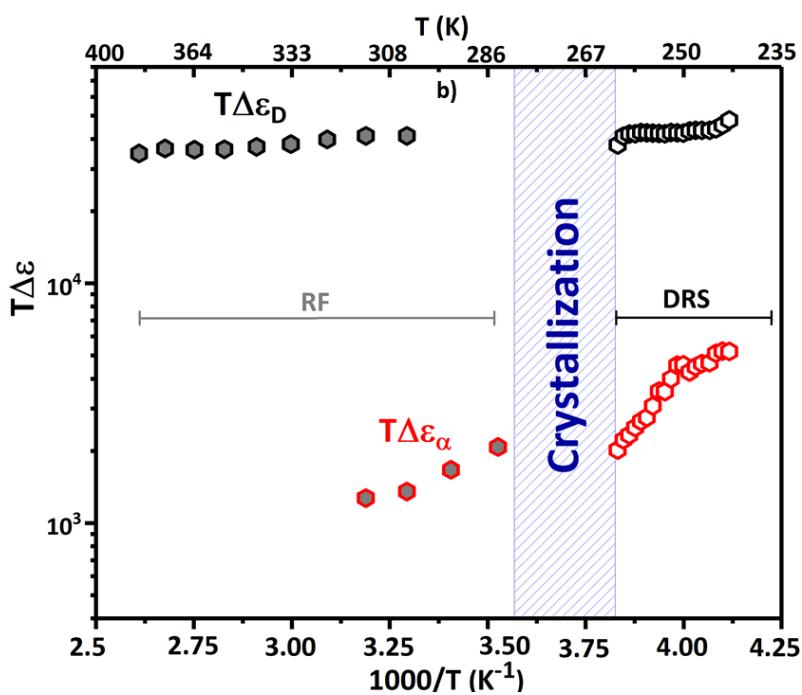
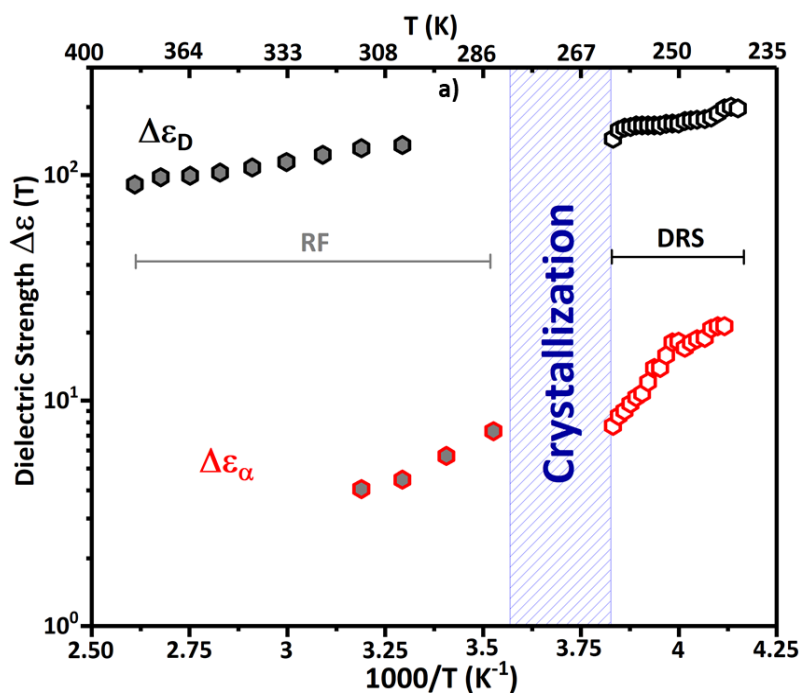
Figure 4: Fitting procedure of the dielectric loss peak in the glassy state (a) 203 K and b) 232 K and the supercooled liquid (c) 259 K. The dash-dot lines represent the fitting functions.

Dielectric strength: The dielectric strength is generally analyzed in the framework of the Onsager/Kirkwood/ Fröhlich formalism [4] which predicts:

$$\Delta\varepsilon = \frac{1}{3\varepsilon_0} G_K F \frac{\mu_0^2 N}{k_B T V} \quad (2)$$

where G_K is the Kirkwood correlation factor, $F \sim 1$ is the Onsager factor, μ_0 is the mean dipole moment of the moving unit in the vacuum, k_B is the Boltzmann constant, T is the temperature, and the ratio $\frac{N}{V}$ represents the density of dipole involved in the relaxation process. Figure 5 presents the temperature evolution of the dielectric strength of the four processes. The magnitude of the dielectric strength of D relaxation $\Delta\varepsilon_D$ represents almost 89% to 93% of the global dielectric intensity. This intensity seems constant near T_g and slowly decreases as temperature increases. Above 261 K, crystallization occurred and the dielectric strength vanishes completely (data not shown) due to a decrease of the number of relaxing units. It is of general thought that the pure exponential D process is linked to chain-like intermolecular associations induced by H-bonding not only in monohydroxy alcohol liquids [5–10], but also in pharmaceutical drugs such as acetaminophen [11] and N-mono-substituted amides [12–15]. It is likely to be same in the case of Nac-MBA. The latter H-bonding chain-like behavior can lead to the formation of a “giant dipole” with an effective moment μ_{eff} greater than that of an isolated molecule μ_0 . The reorientation motion of this effective dipole may be responsible of the D process. Excess permittivity of these strong Debye signals has been

rationalized on the basis of Kirkwood's model of dipole correlations [16], and will be discussed in more details in section II.



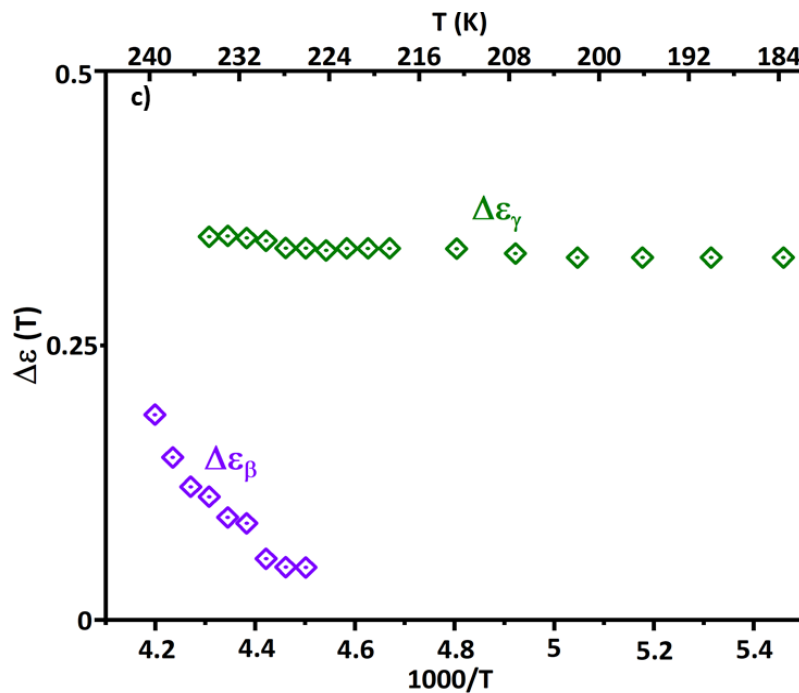


Figure 5: a) Temperature evolution of the dielectric strength and b) the product $T\Delta\epsilon$ for D and α processes. c) $\Delta\epsilon$ as a function $1000/T$ for β and γ processes.

As shown in figure 5 a) the dielectric strength of the structural relaxation $\Delta\epsilon_\alpha$ is largely smaller than $\Delta\epsilon_D$ but also drops as temperature increases. Same as $\Delta\epsilon_D$ temperature evolution, there is a stronger temperature dependence of $\Delta\epsilon_\alpha$ than that predicted from Eq 2. This behavior is generally observed for many amorphous polymers and glass forming liquids [52–56]. Figure 5 b) depicts the product $T\Delta\epsilon$ temperature dependence behavior of D and α processes. According to equation 2, $T\Delta\epsilon_\alpha$ should be temperature independent, however from figure 5 b), the product $T\Delta\epsilon_\alpha$ decreases with increasing temperature. This evolution may originates from an increasing cooperativity character related to the structural relaxation as temperature decreases resulting in a modification of the effective dipole moment [53,56,57]. This hypothesis is discussed in more details in the simulation part (section II) regarding the temperature dependence of the Kirkwood factor G_K which describes direct correlations between dipoles like associations.

The dielectric strength of the secondary β and γ relaxations are very low compared to α process. Figure 5 c) illustrates the temperature evolution of $\Delta\epsilon_\beta$ and $\Delta\epsilon_\gamma$. In both cases the dielectric strength slightly increases with temperature, thus they do not follow the temperature evolution predicted by equation 2. This feature seems to be conventional for many glass formers [53,54,57] and can be understood as the increase of the number of

fluctuating dipoles and/or the fluctuation angle of dipole vector with temperature since the temperature dependence of F and G_K factor seems difficult to envisaged below T_g [57].

Relaxation map: The temperature dependence of the relaxation time of the four processes is summed up in the relaxation map presented in Figure 6. This shows how complex and diverse can be the molecular motions in what seems to be at first glance a simple molecular glass former such as Nac-MBA. For sake of simplicity and clarity, the relaxation map will be analyzed from the glassy state towards the supercooled liquids.

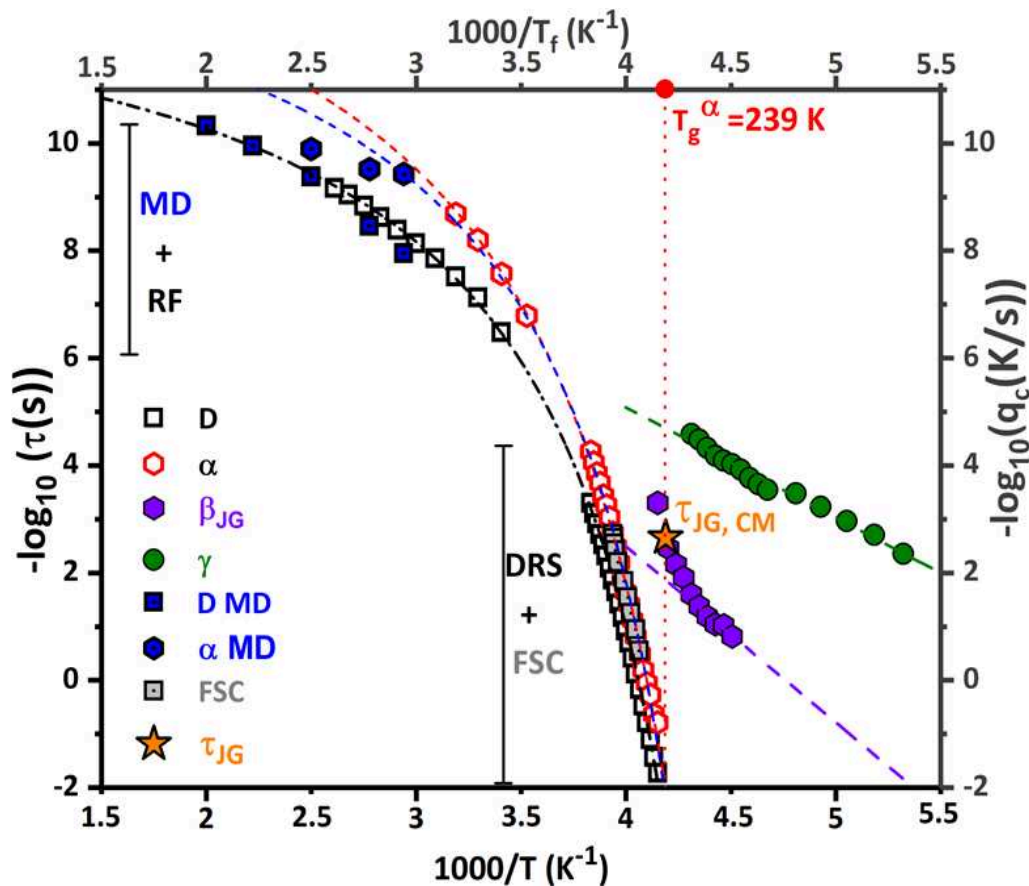


Figure 6: Relaxation map depicting the temperature evolution of the relaxation time τ for all the different processes from DRS and MD simulations (black layer) and cooling rate (dark gray layer) as a function of the inverse temperature determined from FSC. The data in blue were obtained from MD simulations and those in light gray from FSC. The orange star represents the JG relaxation time calculated at T_g from the Coupling Mode (equation 4). The dash-dot lines give the fit of the Arrhenius and VFTH equations to the corresponding data (same color as the data)

The evaluated parameters from the applied fits of the various processes are displayed in table 1.

Table 1: Fit parameters of the Arrhenius and VFTH functions used to describe the temperature evolution of the relaxation time of γ , β secondary motions and α , D processes respectively

$T < T_g$	E_a (kJ.mol ⁻¹)	τ_∞ (s)	
γ - process	39 ± 2	$(6.6 \pm 4.5) \times 10^{-14}$	
β -process	72 ± 8	$(5.37 \pm 5.36) \times 10^{-17}$	
$T > T_g$	B (K)	τ_∞ (s)	T_0 (K)
α -process VFTH (DRS)	1230 ± 57	$(3.0 \pm 1.2) \times 10^{-14}$	204.6 ± 1.4
VFTH (DRS + MD)	1090 ± 63	$(11 \pm 5) \times 10^{-14}$	208 ± 2
D- process VFTH	1074 ± 25	$(14 \pm 3) \times 10^{-13}$	207 ± 1

● Molecular mobility below T_g : γ and β relaxations

Two secondary relaxations are evidenced in the glassy state. As generally observed for localized motions, the relaxation time of both processes follows a linear temperature dependence of $\log \tau$ vs $1000/T$ well described by Arrhenius equation given by:

$$\tau(T) = \tau_\infty \exp\left(\frac{E_A}{RT}\right) \quad (3)$$

where τ_∞ is the pre exponential factor, E_A the barrier activation energy and R the ideal gas constant. The derived parameters from the fit are summarized in table 1. The barrier activation energy of γ process ($E_A^\gamma = (39.4 \pm 1.5) \text{ kJ/mol}$) is lower than that of β process ($E_A^\beta = (71.8 \pm 8) \text{ kJ/mol}$). In other words, γ relaxation may originate from small angular fluctuations of side groups of Nac-MBA molecules (such as N-acetyl group) which require less energy to move than a complete rotation of the molecule as a whole. Nevertheless the temperature evolution of τ_β strongly deviates from the Arrhenius behavior at the vicinity of T_g . This peculiar change of the temperature dependence of τ_β has been highlighted for many glass formers [18,19,23,24], and this relaxation is known as the β Johari-Goldstein (β_{JG}) process commonly analyzed in the framework of the Coupling Model [25] (CM). According to the CM, β_{JG} is considered as due to an independent or primitive motion (that implies the

rotation of the whole molecule) precursor of the cooperative structural α relaxation. The characteristic time of this primitive motion τ_0 is approximately the same as that of β_{JG} motion and correlated to τ_α through the following equation:

$$\tau_{JG}(T) \approx \tau_0(T) = t_c^n [\tau_\alpha(T)]^{1-n} \quad (4)$$

where n is the coupling parameter ($n = 1 - \beta_{KWW}$), t_c is the time characterizing the crossover from independent to cooperative fluctuations proven to be close to $t_c = 2 \times 10^{-12} s$ for molecular glass formers [26], τ_α is the relaxation time associated to the structural process. From experimental data it seems very difficult to estimate β_{KWW} value due to the poor frequency resolution of α relaxation dielectric spectrum. Though, a value $\beta_{KWW} = 0.66$ can be estimated from the empirical relation proposed by Alegria and coworkers [27] given by:

$$\beta_{KWW} \approx (\alpha_{HN} \beta_{HN})^{\frac{1}{1.23}} \quad (5)$$

where $\alpha_{HN} \sim 0.6$ and $\beta_{HN} = 1$ are the shape parameters of the structural relaxation obtained from the fitting procedure described in chapter 2. Therefore, taking into account the latter value in the CM at T_g where $\tau_\alpha = 100s$, the relaxation time $\tau_{JG}(T_g) = 2.22 \times 10^{-3} s$ is obtained. This value is in good agreement with the experimental data as shown in figure 6. At $T > T_g$, the broadness of β_{JG} process is much more pronounced and progressively this process get out of the investigated frequency range. Moreover, the most obvious manifestation of this secondary relaxation (a weak shoulder in the dielectric loss peak) takes place in a very narrow temperature range (almost 15 K). These difficulties increase the uncertainties for a direct confirmation of the β_{JG} nature of this slow secondary process. Therefore, empirical approaches such as the proposal of Ngai and Capaccioli [28] can be applied:

$$\frac{E_a}{RT_g} = 2.303 (2 - 13.7n - \log \tau_\infty) \quad (6)$$

The ratio $\frac{E_a}{RT_g} \sim 31.7$ while the second term of the equation $2.303 (2 - 13.7n - \log \tau_\infty) \sim 29.8$.

Both terms of equation 6 are approximately the same. One can consider that the empirical relation proposed by Ngai and Capaccioli [28] to verify the Johari-Goldstein nature of the secondary relaxation is verified.

- **Molecular mobility above T_g: α relaxation and D process**

The temperature dependence of the relaxation time τ_α is commonly described by the empirical VFTH equation given by:

$$\tau(T) = \tau_\infty \exp\left(\frac{B}{T-T_0}\right) \quad (7)$$

where τ_∞ , B and T_0 are the fit parameters summed up in table 1. The temperature T_0 is referred as the Vogel temperature and usually localized 50K to 70 K below T_g. In the case of Nac-MBA, the experimental data are fairly described by a single VFTH function. Furthermore when combining both DRS and MD simulations data the use of one VFTH fit function was satisfactory to describe the overall behavior even though the fit parameters may be slightly impacted. For example τ_∞ value changes from $(3.0 \pm 1.2) \times 10^{-14}$ s to $(11 \pm 5) \times 10^{-14}$ s and T_0 from 204.6 ± 1.4 K to 208 ± 2 K. Both τ_∞ values are acceptable since in the high temperature limit the dielectric relaxation time can be approximated to $\tau_\infty \sim 10^{-14} - 10^{-13}$ s. Moreover T_0 values are much more near T_g than what is generally observed. Such tendency may suggest a pronounced deviation from the Arrhenius behavior of the relaxation time temperature dependence as observed in fragile liquid. This may give an indication on the fragile or strong character of Nac-MBA.

The dielectric glass transition temperature $T_g^{\text{DRS}} = 238.9 \pm 0.4$ K is obtained by extrapolating the VFTH fit to the relaxation time $\tau = 100$ s. This value is 2K lower than the calorimetric T_g obtained from MTDSC experiment and presented in chapter IV. Often the difference between the calorimetric and the dielectric (kinetic) T_g ($T_g^{\text{DSC}} - T_g^{\text{DRS}}$) increases with the fragility of the liquid [14,29]. For example $T_g^{\text{DSC}} - T_g^{\text{DRS}} \approx 3$ K for very fragile liquids such as neat decalin (m=147) [30]. Conversely this difference is lower than 1K for less fragile systems such as glycerol (m=57). Considering the fitting parameters reported in table 2 an average value of $m = 111 \pm 7$ is obtained, allowing considering Nac-MBA as a fragile glass former. This fragile character is consistent with the previous assumption considering the 2K difference between the calorimetric and dynamic T_g. Additionally this seems to corroborate the idea that fragile systems usually present strong crystallization tendency [31].

Remark: Cooling rate dependence of the fictive temperature

The structural relaxation can also be described in terms of the change in the fictive temperature at variable cooling rates [32]. Figure 7 depicts the temperature evolution of the normalized heat flow after several cooling with a rate ranging from 5 K/s to 1500 K/s. An endothermic relaxation peak is observed at the glass transition region and shifts towards higher temperature with decreasing cooling rate as classically observed in literature [32,34,35]. Furthermore the magnitude of the latter peak increases with decreasing cooling rate. When $q_c = q_h = 1500 \text{ K/s}$, T_g is shifted toward higher temperatures for more than 10 K compared to DSC results. This shift is the expression of the kinetical character of the glass transition phenomenon and is always observed for such kind of thermal protocol [36].

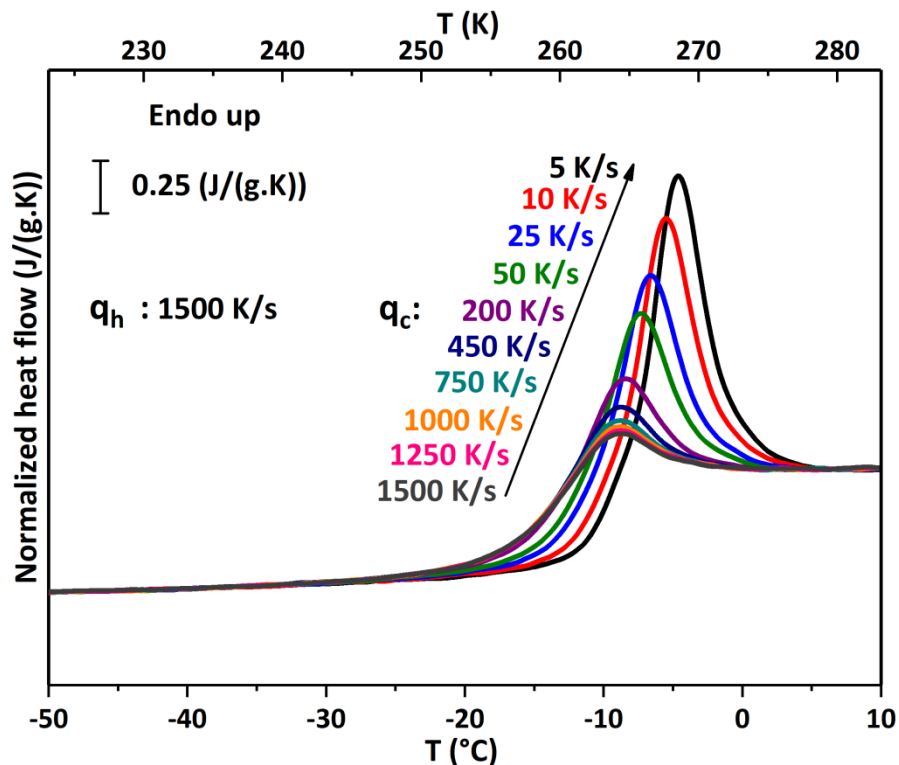


Figure 7: FSC heating curves of Nac-MBA obtained at $q_h = 1500 \text{ K/s}$ after cooling from the supercooled liquid state down to the glassy state at q_c ranging from 5 K/s to 1500 K/s

The cooling rate dependency of the T_f can be described accurately by a VFTH equation as it is the case for the temperature dependence of the structural relaxation time. The empirical approach proposed by Frenkel-Kobeko-Reiner (FKR) [37] illustrates the link between the cooling rate q_c and the relaxation time τ expressed as follow:

$$q_c \tau = C \quad (8)$$

where C is a shift factor usually assume to be a constant [32,38]. Consequently it should be considered that:

$$\log(q_c) = -\log(\tau) + \log(C) \quad (9)$$

This proposal is generally used to combine DSC and/or FSC data with features of the dynamic glass transition from heat or dielectric spectroscopy [32,38–41].

In the present case T_f calculation was performed accordingly from the equal area rule method [42]. The superposition of both cooling rate and relaxation time temperature dependence are reported in figure 6. As depicted in the relaxation map, the evolution of the cooling rate q_c as a function of T_f perfectly mimics the temperature dependence of the structural relaxation time. Therefore, as proposed from the FKR relation, a vertical shift factor $\log C = 0.67 \pm 0.12$ or $C = (4.7 \pm 1.3)$ K was necessary in order to superimpose both behaviors. Thus, the determination of the calorimetric T_g cooling rate dependency is consistent with the dynamic evolution of the structural relaxation time.

The temperature dependence of D process relaxation time τ_D follows the VFTH equation in the supercooled liquid state. The fit parameters presented in table 1 highlighted obvious similarities with α process. The non-Arrhenius temperature dependence of τ_α is highly correlated with non-Debye dynamics. However the Debye process is not liable to any dispersion of the relaxation time. Consequently, D process can not originate from the same microscopic phenomena as α process [58,59]. Nevertheless, the observe similarities between both relaxations could possibly mean that D process may be controlled or governed by α relaxation [54]. As displayed in figure 6, the relaxation time τ_D is at least 1 order of magnitude slower than τ_α even though the dielectric T_g^D of D process obtained from $\tau_D = 100$ s is just 2K higher than the calorimetric T_g . The temperature T_g^D here refers as the temperature were the relaxation time is equal to 100s rather than to any glass transition temperature since the Debye process do not possess a calorimetric signature. The decoupling between both D and α

processes is well illustrated in figure 8 where the temperature dependence of $\log_{10}(\tau_D/\tau_\alpha)$ is plotted.

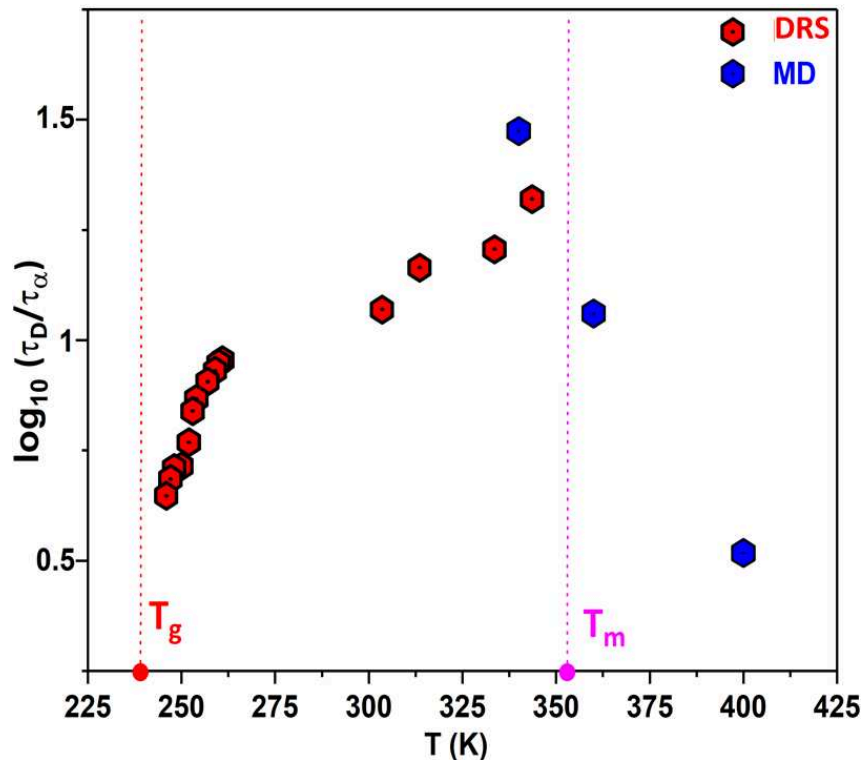


Figure 8: Temperature evolution of the logarithmic time scale decoupling ratio $\log_{10}(\tau_D/\tau_\alpha)$ plotted from DRS and MD data

The decoupling of D and α time scales is highly impacted by temperature. At the vicinity of T_g the time scales of both processes are separated for almost half a decade. As temperature increases, the difference of D and α time scales strongly increases and reaches a maximum value near the melting temperature T_m ($\log_{10}(\tau_D/\tau_\alpha) \sim 1.4$). However MD simulation results evidenced a well pronounced drop of the temperature evolution of $\log_{10}(\tau_D/\tau_\alpha)$ as soon as the melting point is reached. In the liquid state, the difference of the time scales among both processes is circa half a decade as similarly observed near T_g . The content and essence of these results are discussed in the framework of Hydrogen bond (HB) aggregate formation and depicted in the next section. Moreover the microscopic origin of D process and its implications in the dielectric response of Nac-MBA system are probed by MD simulation and presented in the following.

B- MD simulations investigations

The MD simulations results here presented were performed by Professor Frédéric Affouard in the framework of a collaboration between UMET, SMS and GPM laboratories. The following simulations were performed only in the case of Nac-MBA system at an ee=50%.

1- Static dipolar properties

The individual dipole moment of a given molecule at time t is calculated from the classical expression $\vec{\mu}(t) = \sum_{\alpha=1}^{N_a} q_{\alpha} \vec{r}_{\alpha}(t)$ where q_{α} and $\vec{r}_{\alpha}(t)$ are respectively the fixed charge localized on atom α and its position at time t , and $N_a = 25$ is the number of atoms in the considered Nac-MBA molecules $C_{10}H_{13}NO$. Fixed charges are directly taken from the ab-initio calculation. In the present investigation, the average dipole moment $\langle \mu \rangle$ of Nac-MBA molecules computed from MD is found to be about 3.93 +/- 0.01 Debye in the liquid state, and does not significantly vary with temperature. The symbol $\langle \rangle$ indicates an average on both time and molecules. It could be noted that this value is close to the value 3.74 Debye directly obtained from the ab-initio calculations of a single molecule in the gas phase. These results thus show that the polarity of the Nac-MBA remains quite constant.

Dipolar correlations are well described by the so-called Kirkwood correlation factor G_K given by the following equation [4]

$$G_K = 1 + (N - 1) \langle \vec{\mu}_i \cdot \vec{\mu}_j \rangle / \langle \mu^2 \rangle \quad (10)$$

where $\vec{\mu}_i$ is the dipole moment of the molecule i , $\langle \mu^2 \rangle$ the average dipole moment, and $\langle \vec{\mu}_i \cdot \vec{\mu}_j \rangle$ indicates an average over distinct pairs of molecules ($i \neq j$). The Kirkwood correlation factor accounts for the orientational correlation of neighboring dipoles. Parallel and antiparallel dipoles orientation lead to $G_K > 1$ and $G_K < 1$, respectively. If orientations of individual dipoles are completely random, one finds $G_K = 1$. The Kirkwood correlation factor G_K was calculated at different temperatures from Eq. 10 and it is shown in figure 9. The Kirkwood correlation factor monotonically increases from about 1.6 at $T = 500$ K to about 2.6 at $T = 340$ K.

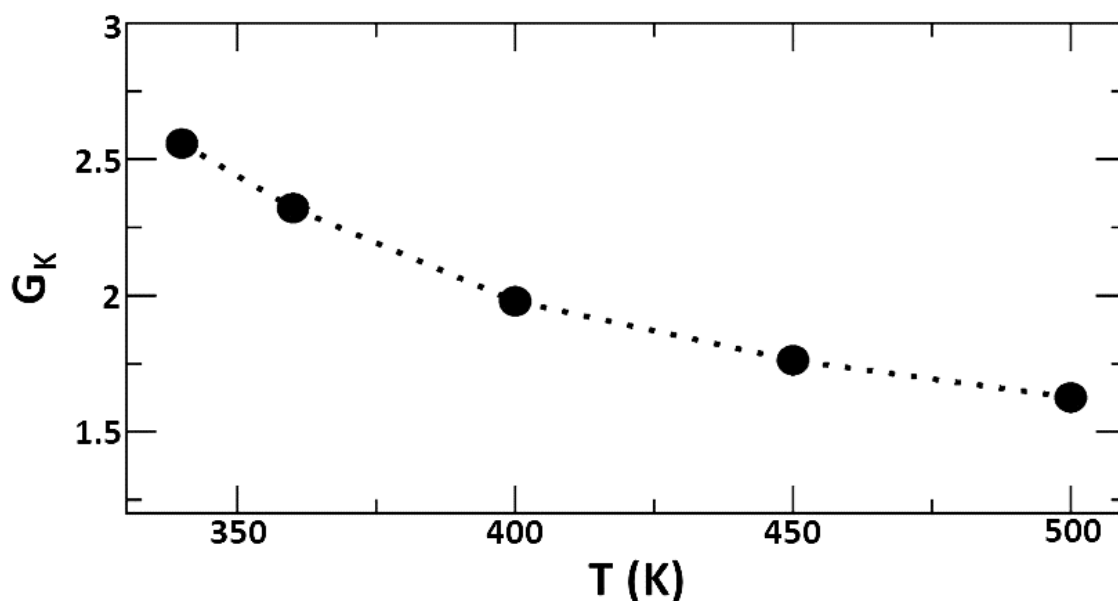


Figure 9: Temperature evolution of the Kirkwood correlation factor G_K of Nac-MBA determined from MD simulations

A factor G_K greater than 1 is often found in monohydroxy alcohols [60–63] and secondary amides [58,64] for which values may range from 3 up to 4. It is interpreted as the capability of the liquids to form HB associating structures as linear chain showing HB aggregates with parallel dipoles orientation. This type of HB associations has been often detected from the present MD investigations from snapshots of instantaneous configuration of the system, and will be discussed below. An example of an $n = 6$ molecule HB aggregate is displayed in figure 10. It should be also noted that the G_K values increase with decreasing temperature suggesting an increasingly parallel correlation of dipoles which can be seen as a precursor of the crystalline structure that may ultimately formed as observed many times in HB molecular liquids [54,65]. The crystalline structure of Nac-MBA suggests that the strongest intermolecular link is a HB between $N - H \cdots O$ atoms with $d(N - O) = 2.87 \text{ \AA}$, $d(H \cdots O) = 2.10 \text{ \AA}$; $(N - H \cdots O) = 171.8 \text{ deg}$. The structure reveals infinite syndiotactic linear chains of H-bonded molecules alternately parallel to $\langle 110 \rangle$ and $\langle 1\bar{1}0 \rangle$ in successive (004) slices. More details about the crystalline structure can be found in the work of Druot *et al* [66].

The high dielectric intensity values may emanate from the linear nature of the H-bonding chains and linked to the number of molecules involved in these intermolecular associations. The latter hypothesis is consistent with the main feature of the crystalline structure (being the steric accessibility of the NH group leading to the presence of infinite linear H-bond chains of

molecules between $N - H \cdots O$ atoms) [67]. Though in the liquid or supercooled liquid state this infinite intermolecular associations cannot be envisaged (lack of long range order), it is very likely that as temperature fluctuation increases the number of molecules implicated in these associations diminishes. Consequently, the intensity of D process may decrease as temperature increases as predicts by Onsager/Kirkwood/Fröhlich theory. Same as for D process the temperature dependence of $\Delta\varepsilon_\alpha$ is dominated by the temperature behavior of G_K .

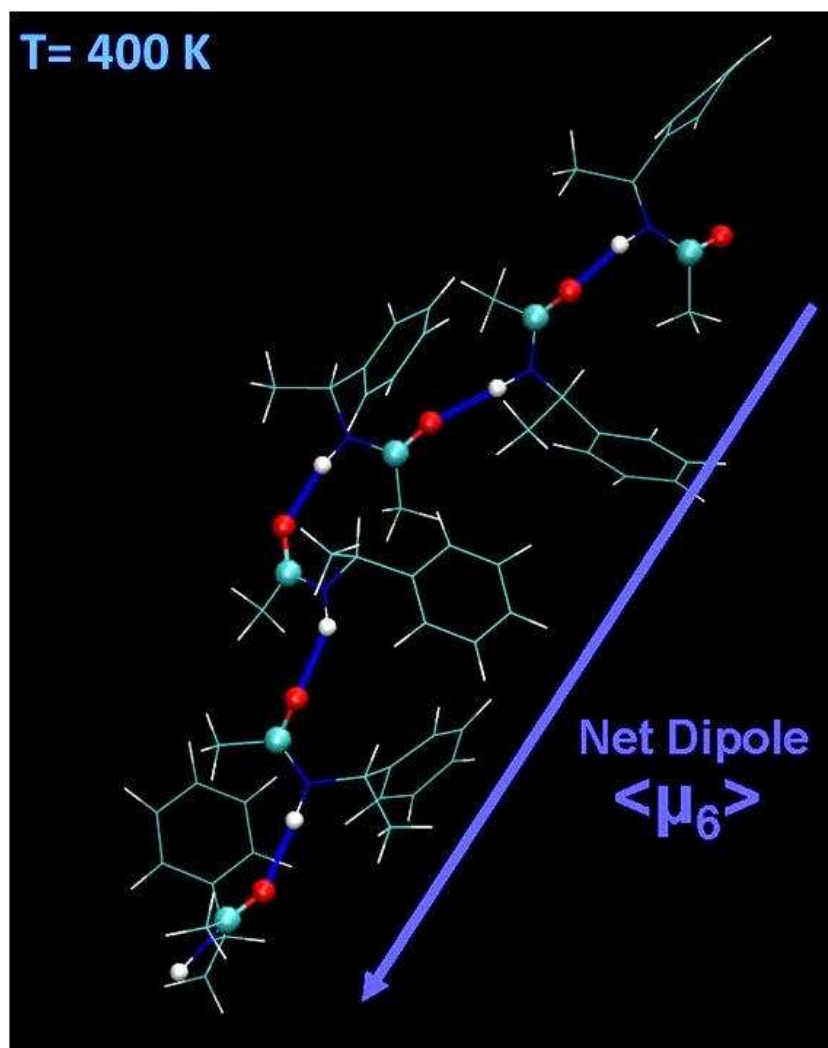


Figure 10: Snapshot extracted from an MD simulation run at $T = 400$ K showing an HB aggregate composed of $n = 6$ Nac-MBA molecules. This HB aggregate possesses a linear shape and the net dipole $\langle \mu_6 \rangle$ of this aggregate is also schematically represented. Intermolecular HB are displayed as bold line

2- Dynamical dipolar properties

Molecular mobility can be probed from the time dependence of the total electric dipole moment $\vec{M}(t)$ at time t [68]. The total electric dipole moment is defined as $\vec{M}(t) = \sum_{i=1}^N \vec{\mu}_i(t)$ where $\vec{\mu}_i(t)$ is the individual dipole moment of the molecule i at time t and $N = 64$ the total number of molecules. In a first approximation, the complex frequency dependent permittivity $\varepsilon^*(f) = \varepsilon'(f) - i \cdot \varepsilon''(f)$ measured experimentally by DRS is actually proportional to the Fourier transform of the time-dependent correlation function $\Phi_M(t) = \langle \vec{M}(t) \cdot \vec{M}(0) \rangle$ of the total dipole moment [54]. This function allows probing the collective dynamics of Nac-MBA dipoles and has been calculated at different temperatures (see figure 11). The long time behavior of the $\Phi_M(t)$ functions is dominated by a single exponential decay which can be well fitted with $\sim \exp[-t/\tau_D^{(MD)}]$, where $\tau_D^{(MD)}$ is the characteristic time associated with this long time decay. This behavior is well in line with the D process observed by DRS. The single exponential law allowed us to reproduce the evolution of $\Phi_M(t)$ almost over the whole investigated time domain except at relatively short times ($10 < t < 100$ ps) where an additional fast relaxational process is present (see figure 11). This fast process possesses a very low intensity and a reliable characterization is difficult from the present MD data. It has thus just been taken into account considering an additional law $\sim \exp\left[-\left(t/\tau_{fast}^{(MD)}\right)^{\beta_{fast}^{(MD)}}\right]$ in order to reproduce the behavior of the $\Phi_M(t)$ function over the complete investigated time range. $\beta_{fast}^{(MD)} \approx 0.82$ is found to provide a reasonable adjustment in the fitting procedures.

The characteristic times $\tau_D^{(MD)}$ and $\tau_{fast}^{(MD)}$ obtained at different temperatures have been represented in Figure 6 for comparison with the DRS experimental data. It clearly shows that the characteristic times determined from MD simulations are in very fair agreement respectively with the relaxation times of the D and α processes obtained from DRS experiments. Both processes are separated by about one to two decades in time and closely follow each other's in the investigated temperature domain very much like the behavior observed in monohydroxy alcohols and secondary amides. While comparing the temperature evolution of the logarithmic time scales decoupling ratio $\log_{10}(\tau_D/\tau_\alpha)$ near the liquid state it appears that the ratio (τ_D/τ_α) approaches 1 as temperature increases and exceeds the

melting point. This suggests that at very high temperature, the relaxation times of both processes are equal. At such elevated temperature the formation of HB aggregates with large clusters size is inconsistent since the most probable situation remains a cluster made of an isolated molecule.

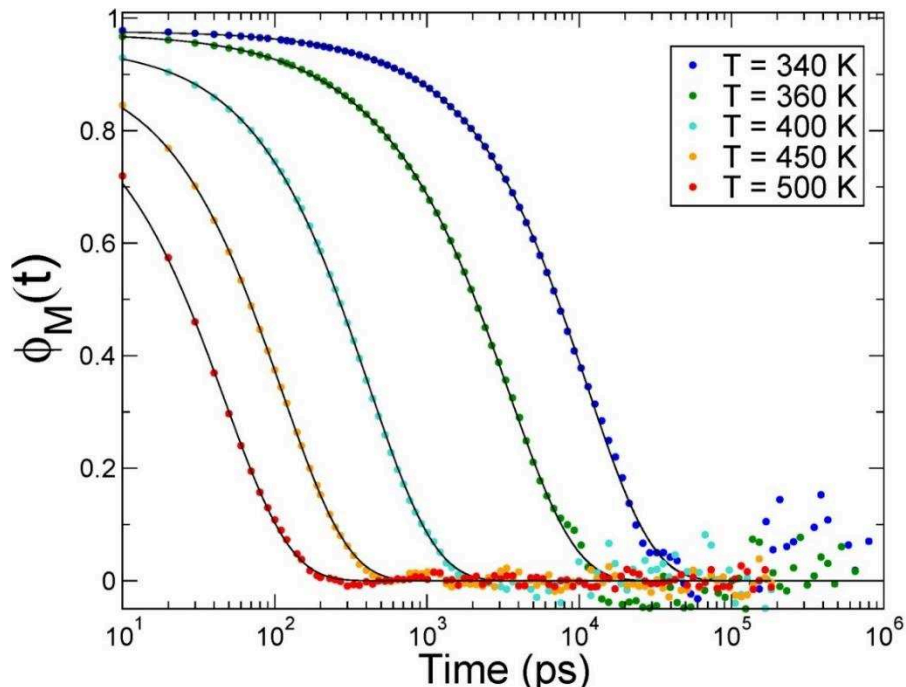


Figure 11: Time-dependent of the total dipole correlation function $\Phi_M(t) = \langle \vec{M}(t) \cdot \vec{M}(0) \rangle$ for Nac-MBA represented at different temperatures $T = 340, 360, 400, 450,$ and 500 K. The solid lines indicate a fit with the function $\Phi_M(t) = A_D^{(MD)} \exp[-t/\tau_D^{(MD)}] + A_{fast}^{(MD)} \exp\left[-\left(t/\tau_{fast}^{(MD)}\right)^{\beta_{fast}^{(MD)}}\right]$ where the index “D” and “fast” refer to the long time single exponential decay (D process) and to the fast relaxational process ($10 < t < 100$ ps) respectively (see text)

3- Hydrogen bonding structures

HB statistics allow determining the population of different HB associating structures and probing the structure of the investigated liquid with the aim to clarify experimental and numerical dipolar properties. The investigated molecule Nac-MBA possesses both a —NH and C=O group from which they may form intermolecular HBs (see figure 10). In the present study, two Nac-MBA molecules are considered to be H-bonded if i) the nitrogen-oxygen distance is less than 3.4 \AA and ii) the (O···H-N) angle is larger than 150 deg . This criterion is classically used in MD simulations and allows including more deformed and weaker HBs in statistics [69].

The fraction P_n of a HB aggregates composed of n Nac-MBA molecules detected on average during the MD simulation is displayed in figure 12 at the highest $T = 500$ K and the lowest $T = 340$ K investigated temperatures. A monotonic trend of the HB statistics is found from 500 K down to 340 K and data obtained at 450, 400 and 360 K are not shown for clarity. Figure 12 clearly shows that a large variety of HB aggregates are theoretically possible ranging from isolated molecule ($n = 1$) to very large aggregates made of $n = 20$ molecules. Additional even larger associated structures could be also transiently observed but their fraction remains really very small at all investigated temperatures. As expected from results obtained on dipolar correlations in the present study, the dominant intermolecular HB association originates from the formation of linear chain. As an example, a snapshot of an $n = 6$ HB aggregate is displayed in figure 10. Upon decreasing temperature, the fraction of isolated molecules ($n = 1$) and dimers ($n = 2$) progressively decreases. The population of trimers ($n = 3$) remains stable while the population of $n > 3$ aggregates increases. At the lowest investigated temperatures $T = 340$ K, associations as dimer ($n = 2$) and trimer ($n = 3$) are seen as the most probable structures. However, it may be speculated that the trend found in the investigated temperature range will continue somehow at lower temperatures at which larger structures $n > 3$ might become the most probable. It is confirmed by simply plotting the number of molecule n corresponding to the maximum of P_n as a function of temperature (data not shown). This evolution shows a monotonic increase of n upon decreasing temperature. Additional MD simulations are clearly required that unfortunately extends beyond the scope of this study due to the difficulty to equilibrate liquid states at temperatures below $T = 340$ K from MD because of the slow dynamics of the dominant D process (see below).

In addition to the population P_n of a given HB aggregate of size n , the average total dipolar moment $\langle \mu_n \rangle$ for this aggregate may also be computed (see figure 12). The evolution of $\langle \mu_n \rangle$ as a function of n clearly shows that $\langle \mu_n \rangle$ increases with n , which is well in line with the linear nature of the HB aggregates (see snapshot on figure 10) and the Kirkwood correlation factor $G_K > 1$ (see figure 9). Cyclic aggregates would cause $\langle \mu_n \rangle$ to decrease or even to go to zero. Interestingly, it may be also mentioned that the evolution of $\langle \mu_n \rangle$ is quite temperature-independent. All $\langle \mu_n \rangle$ data at $T = 340$ and 500 K overlap onto the same curve as well as $T = 360, 400$ and 450 K data (data not shown). It suggests that the same types of association may potentially form at all temperature whose the exact conformation – linear

chain above all – does not change very much with temperature. From both P_n and $\langle \mu_n \rangle$, it is also possible to calculate the product $P_n \cdot \langle \mu_n \rangle$ which provides an estimation of the “dipolar weight” of an aggregate made of n molecules. At $T = 340$ K, although the population of aggregates made of $n = 4, 5$ or 6 molecules is weaker than $n = 2$ or 3 , they could contribute to a larger extent to the dipolar response since they possess a total higher dipole moment.

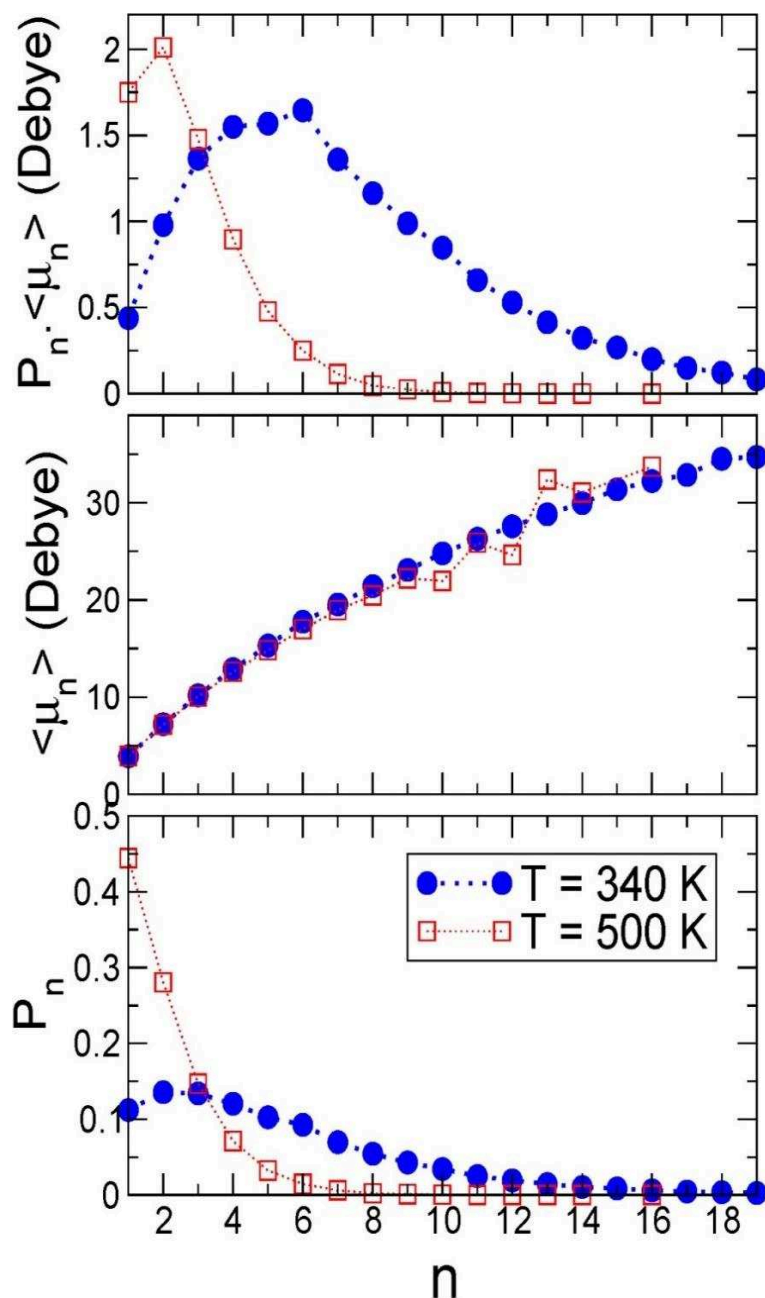


Figure 12: Evolution of the population P_n (bottom), the average net dipole $\langle \mu_n \rangle$ (middle) and the product $P_n \cdot \mu_n$ (top) for HB aggregate made of n Nac-MBA molecules at $T = 340$ and 500 K

II- Impact of chirality

In order to evaluate the impact of chirality on the molecular mobility of amorphous Nac-MBA, several ee ranging from ee = 0% up to ee = 100% were investigated by DRS. However, since the ee strongly impacts the crystallization propensity, it was not possible to register the molecular mobility in all the temperature range as performed for ee=50%. Figure 13 illustrates the isochronal temperature evolution of the real dielectric permittivity at different ee for a selected frequency $f = 11$ Hz.

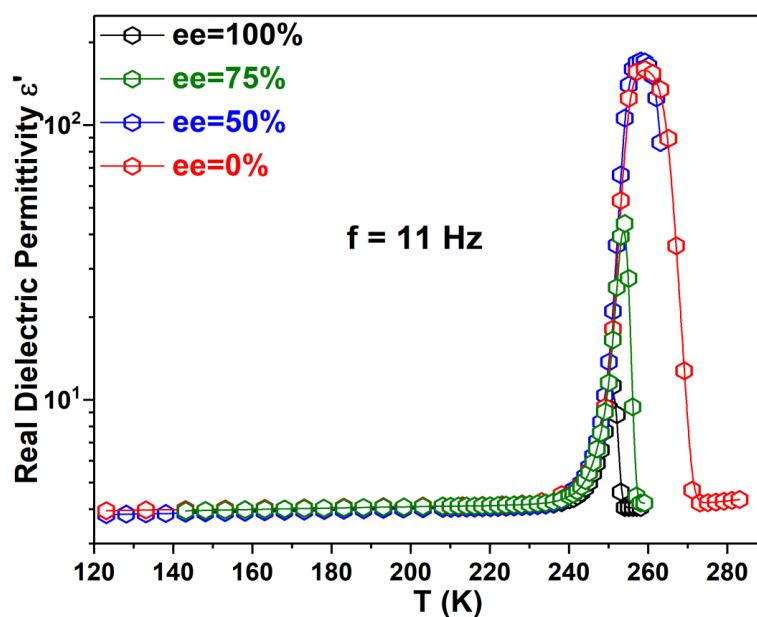


Figure 13: Temperature evolution of the real dielectric permittivity at several ee at $f=11$ Hz

The drop of the dielectric permittivity is strongly ee dependent. The real dielectric permittivity ϵ' drops at $T > 251$ K and $T > 254$ K for ee= 100% and ee= 75% respectively. For ee= 50%, and ee= 0% ϵ' drops at $T > 260$ K. This behavior is synonym of the occurrence of crystallization upon heating. These results are consistent with the fact that high ee possesses high crystallization propensity. For simplicity and clarity reasons, we do not detail the dielectric response of each ee separately but we combined on the same figure the behavior of all the analyzed ee at suitable selected temperatures or frequencies.

A- Chirality effects on the molecular mobility below T_g

Figure 14 depicts the frequency evolution of the dielectric loss at several ee below T_g . Independently of the ee, two secondary processes appear. The slow secondary β_{JG} occurs at lower frequency or higher temperature and the secondary γ process is localized at higher frequencies (kHz region) or lower temperature region. The dielectric loss peak of all the samples seems similar even though they do not superimposed perfectly. This may suggest very subtle differences function of the ee. The nature of both processes has been discussed in the previous section for ee= 50%. It is ambiguous to imagine that the ee intrinsically can modify the microscopic origin of these secondary processes since both enantiomers possess identical flexible branches and molecular unit of opposite chirality. Therefore, considering the influence of the ee on the crystallization tendency, it can happen that the time scales of both processes and the shape parameters describing the dielectric function may be influenced indirectly by the ee.

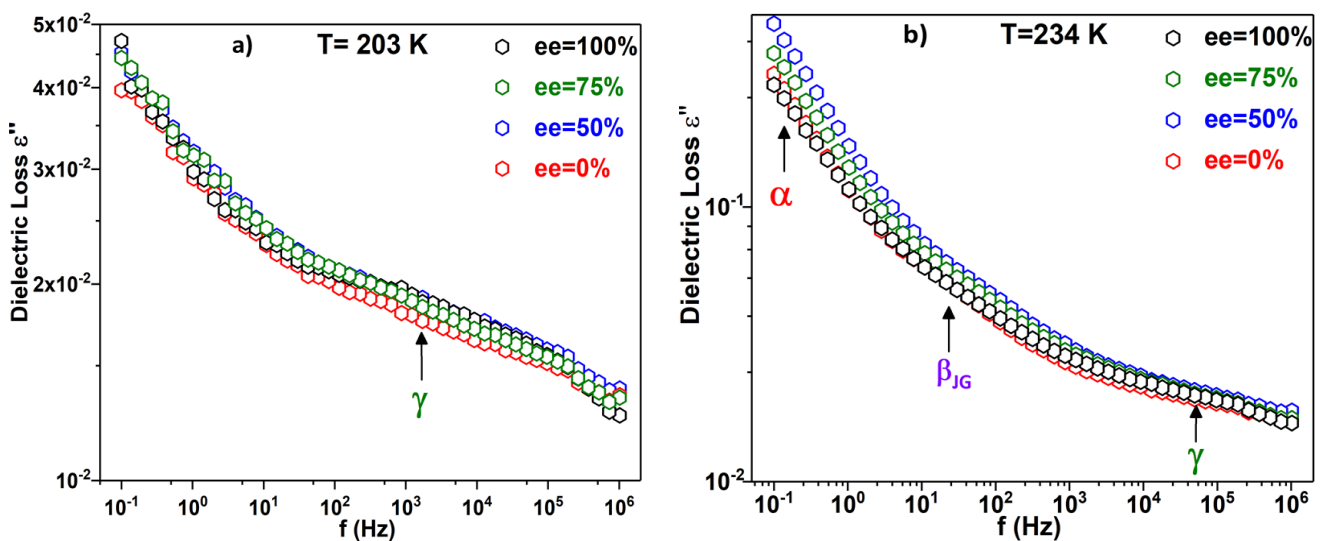


Figure 14: Frequency evolution of the dielectric loss at various ee in the glassy state

a) T = 203 K, b) T = 234 K.

B- Chirality Effects on the Molecular Mobility above T_g

The frequency evolution of the dielectric loss peak at several temperatures in the supercooled liquid (247 K and 313 K) and liquid states (363 K) are reported (for different ee) in figure 15. The very intense and slow single exponential Debye response localized at the lowest frequency range overlaps with the structural relaxation α . The secondary β_{JG} process becomes broader and evolves out of the available frequency range as temperature increases. The different samples (ee= 100%, ee= 75% and ee= 0%) illustrated identical relaxation processes as those reported for ee=50%. Thus, the relaxational landscape seems not to be impacted by chirality in the case of Nac-MBA. However, all the processes do not superimposed perfectly at variable ee. This may suggest slight differences on the value of the shape parameters, the dielectric strength or the relaxation time.

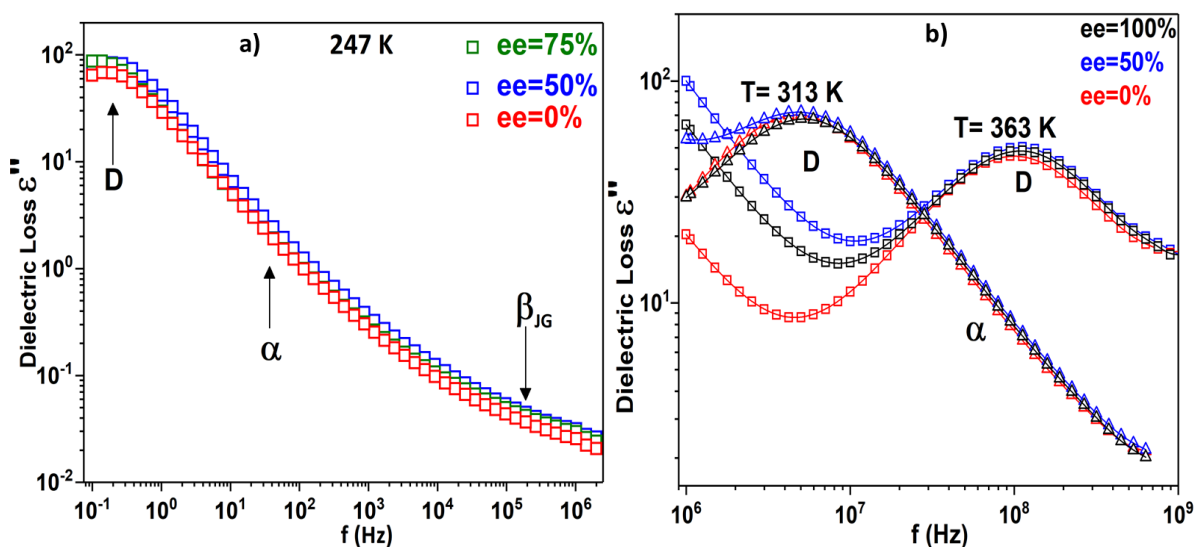


Figure 15: Isothermal frequency evolution of the dielectric loss in the supercooled liquid state for several ee and temperatures a) 247 K, b) 313 K and 363 K

In order to subtract the essential information about these relaxation processes (relaxation time, shape parameters, dielectric strength) the isothermal dielectric loss peak was fitted with a sum of Havriliak- Negami equations and a conductivity contribution when necessary. The shape parameters are sum-up in table 2.

Table2: Shape parameters of the four processes for different ee

	ee = 0%		ee = 50%		ee = 75%		ee = 100%	
	α_{HN}	β_{HN}	α_{HN}	β_{HN}	α_{HN}	β_{HN}	α_{HN}	β_{HN}
D	0.96	1	0.95 - 1	1	0.95 - 1	1	0.95 - 1	1
α	0.6	1	0.58 - 0.6	1	0.6	1	0.6	1
β_{JG}	0.4 - 0.5	1	0.38 - 0.45	1	0.42 - 0.45	1	0.4 - 0.45	1
γ	0.11 - 0.15	1	0.14	1	0.14	1	0.14	1

Globally the symmetric and asymmetric broadening of the loss peak are typically the same and independent of the enantiomeric composition.

Figure 16 illustrates the temperature evolution of the dielectric strength of each process at the investigated ee. As depicted in figure 16 a) the dielectric strength of both secondary processes follow the same behavior as described for ee=50%. The dielectric strength increases with increasing temperature. The increase of $\Delta\varepsilon$ is well pronounced for β_{JG} process compared to γ . The subtle differences of $\Delta\varepsilon$ as function of the ee are not significant enough to conclude about any impact of chirality on the dielectric response of secondary processes. These differences may originate from several experimental or data treatment difficulties: the exact repeatability of the ex-situ sample preparation and the ambiguous fitting procedure of very low magnitude processes. This may give an explanation on the fact that $\Delta\varepsilon_{\beta_{JG}}$ seems lower for ee=0% compared to other compositions.

Figure 16 b) illustrates the temperature evolution of the dielectric strength of α process obtained from DRS (low temperature range) and reflectometry (high temperature range) at ee=0% and ee=50%. Analysis at higher ee could not be conclusive since rapid crystallization occurs for higher enantiomeric compositions. At the T_g higher temperature limit, $\Delta\varepsilon_{\alpha}$ at ee=50% is higher than that of the racemic composition, this difference continuously vanishes and reaches zero in the liquid as evidenced by reflectometry measurements. The same behavior is depicted for D process (see figure 16 c) and d)). Moreover in the liquid state the D relaxation dielectric strength at ee=100% is similar to that of ee=50% and ee=0%. Thus the dielectric strength of D and α processes is ee dependent in the supercooled liquid state, but this dependence vanishes at the vicinity of the melting temperature.

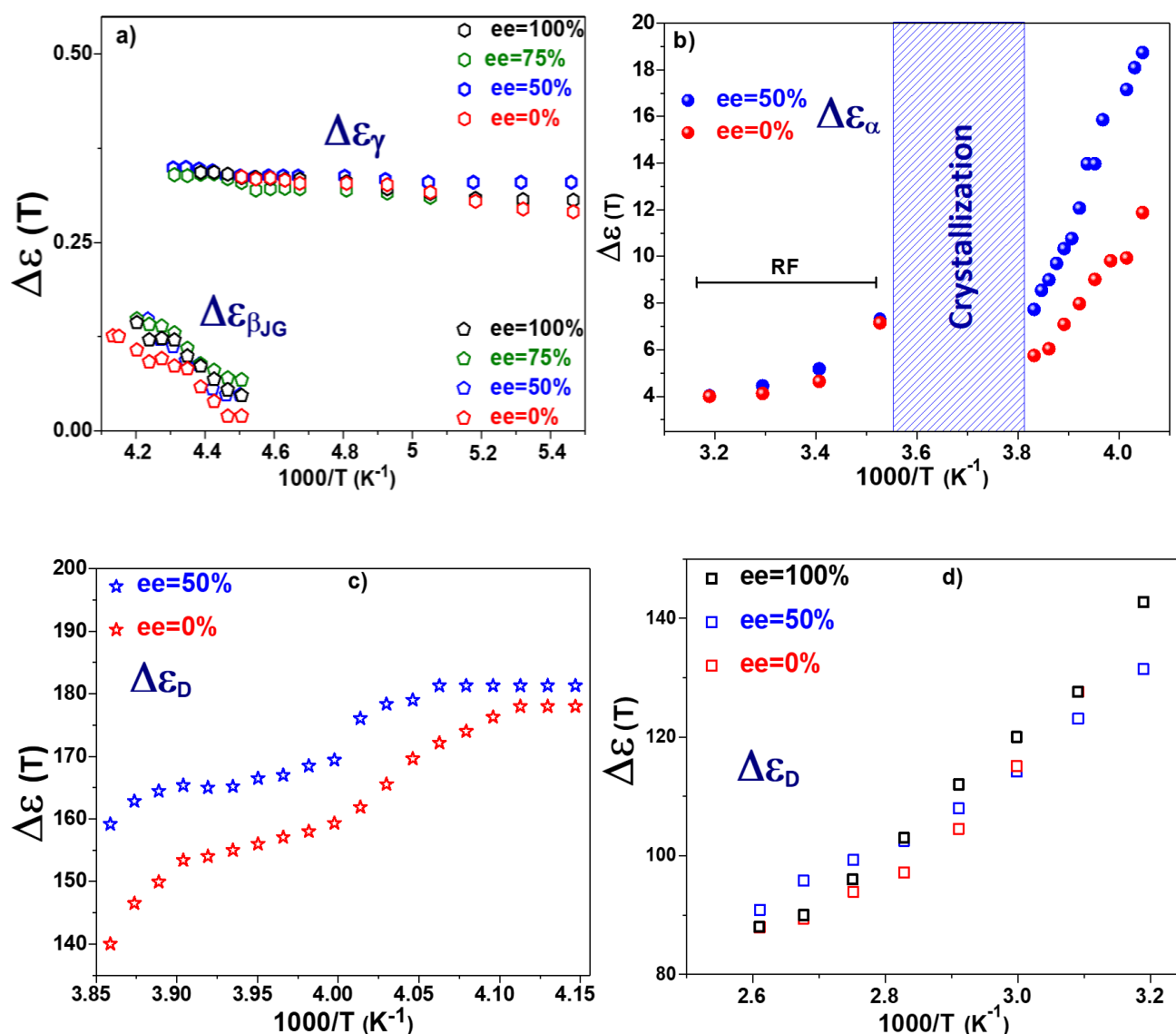


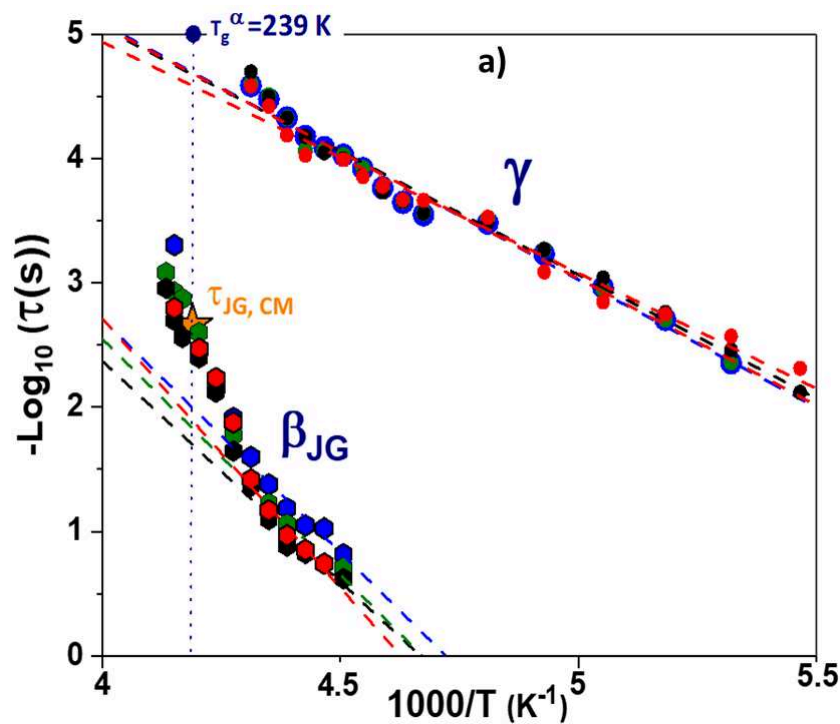
Figure 16: temperature dependence of the dielectric strength at several ee of a) the two secondary γ and β_{JG} processes b) α process c) D process in the low temperature region and d) D process in the high temperature region

This behavior can be understood in the framework of the temperature dependence of G_K and the formation homo chiral isotactic or atactic linear molecular chains of HB aggregates. In the previous section it was clear that the temperature evolution of the dielectric response of D and α relaxations is strongly linked to G_K . In fact as temperature increases and overpasses the supercooled liquid state, the correlation between neighboring molecules strongly decreases and G_K progressively approaches unity. Therefore, at high temperature (near the melting point) very few molecules are engaged in the formation of an HB aggregates (for example

clusters of 2 molecules). Therefore, one may speculate that independently of the tacticity of the chains, the dipolar response is identical considering variable ee. When temperature decreases, the number of molecules implicated in the formation of these linear HB molecular chains increases. Since the dielectric intensity is a witness of this additional effect of HB aggregates made of high cluster number, logically the response is of high magnitude. Therefore the tacticity of the chain or simply chirality may impact the dielectric response of the chains. For reminder when ee=100%, the sample (crystalline) is made of infinite homo chiral isotactic HB molecular chains. However as the counter enantiomer comes into play, the sample is made of alternated homochiral HB molecular chains. In the amorphous such alternated homochiral HB chains is ambiguous to imagine regarding the disorder character. For the case of ee=100%, the aggregates are formed with clusters of the same chirality. When the ee decreases, the aggregates can be formed of clusters with opposite chirality. The most polar group (N-acetyl), donor and acceptor of HB is directly connected to the asymmetric carbon, consequently the dipolar moment vectors of the two enantiomers are opposite by sign. Consequently there is no reason why for large cluster number the dielectric intensity should be identical at variable ee since the concentration of each enantiomer changes. From our results it seems that high ee made of great number of one enantiomer favors higher dielectric intensity compared to equimolar contains of the two opposites enantiomers.

C- Relaxation Map

The temperature dependence of all the four processes is plotted in the relaxation map illustrated in figure 17. For sake of clarity the relaxation map is displayed into two figures reporting the temperature dependency of secondary processes relaxation time, and D and α relaxation time respectively. Independently of the ee the temperature evolution of $\tau_{\beta_{JG}}$ and τ_{γ} followed an Arrhenius behavior (see figure 17 a)) as already reported for e=50%. Both τ_{α} and τ_D processes presents a VFTH temperature dependency (see figure 17b)). No general trend of the relaxation rates evolution regarding the ee has been identified. This may suggest that the relaxation rates of secondary processes are not directly impact by chirality itself. This assumption is also valid for D and α processes since their relaxation time superimposed for all the analyzed ee (see figure 17 c)).



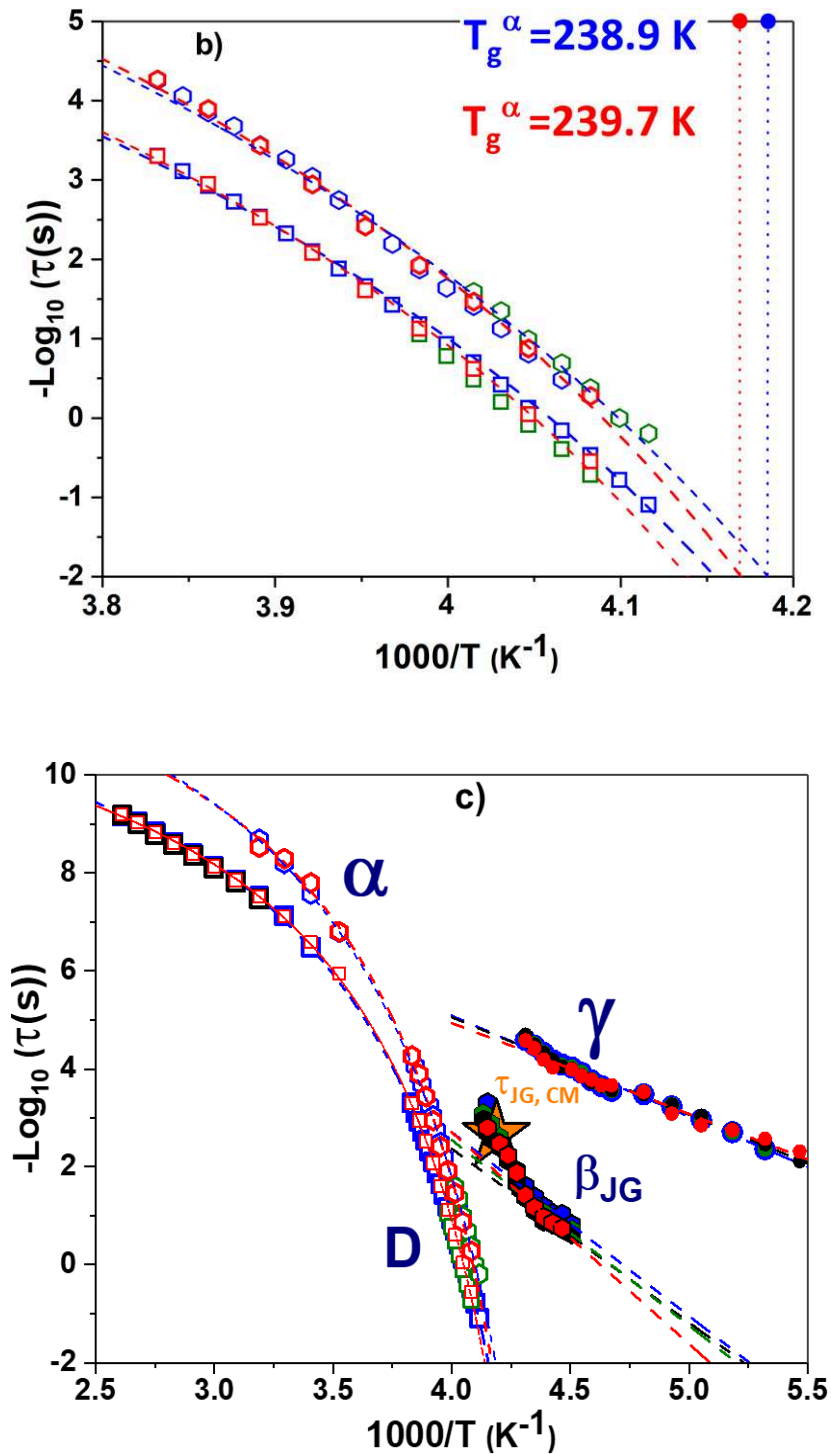


Figure 17: Temperature dependency of the relaxation time of the four processes at different ee . Each color is attributed to an ee , black for $ee=100\%$, green for $ee=75\%$, blue for $ee=50\%$ and red for $ee=0$ the orange star represents the JG relaxation time calculated at T_g from the Coupling Model. The dash-dot lines give the fit of the Arrhenius and VFTH equations to the corresponding data (same color as the data)

The fitting parameters of the four processes are displayed in table 3.

Table 3: Fit parameters of the Arrhenius and VFTH functions used to describe the temperature evolution of the relaxation time of γ , β secondary motions and α , D processes at several ee.

$T < T_g$	E_a (kJ.mol ⁻¹)	τ_∞ (s)	
γ - process	38 ± 2	(1.4 ± 1.0) × 10⁻¹³	
β -process	70 ± 10	(2.38 ± 2.37) × 10⁻¹⁵	
γ - process	39 ± 2	(9 ± 7) × 10⁻¹⁴	
β -process	73 ± 8	(5.48 ± 5.47) × 10⁻¹⁷	
γ - process	39 ± 2	(7 ± 5) × 10⁻¹⁴	
β -process	72 ± 8	(5.37 ± 5.36) × 10⁻¹⁷	
γ - process	36 ± 2	(6 ± 4) × 10⁻¹³	
β -process	83 ± 9	(6.71 ± 6.70) × 10⁻¹⁹	
$T > T_g$	B (K)	τ_∞ (s)	T_0 (K)
α -process VFTH	1230 ± 56	(3 ± 1) × 10⁻¹⁴	205 ± 1
D- process VFTH	1074 ± 25	(14 ± 3) × 10⁻¹³	207 ± 1
α -process VFTH	1081 ± 23	(9 ± 6) × 10⁻¹⁴	209 ± 2
D- process VFTH	957 ± 95	(27 ± 3) × 10⁻¹³	211.0 ± 0.7

The fitting parameters indicate similar secondary γ - process with an activation energy ranging from 34 kJ/mol up to 41 kJ/mol. Moreover the high temperature limit of the relaxation time τ_∞ is approximately the same at all the analyzed. Therefore, secondary γ - process originates from the same microscopic origin independently of chirality.

As mentioned in the case of ee=50%, secondary β process is of β_{JG} type. This consideration remains valid for other enantiomeric compositions. The activation energy of β_{JG} process when ee=0% seems to deviate from the average value presented at other ee. Furthermore, τ_∞ values are typically higher than the value usually obtained in glass forming liquid (approximety $10^{-14} - 10^{-13}$). This situation may be inherent to the fitting procedure and not inevitably to the sample itself, since the fitting is conducted with very few data for this specific process.

The fitting parameters of both D and α processes as function of ee suggest similar dynamics with very subtle differences. In the case of α process the Vogel temperature T_0 increases for approximately 4.4 K when changing the composition from ee=50% to ee=0%. This difference is nearly the same for D-process (4K). Additionally the dynamic T_g is not perfectly the same regarding the two compositions. The difference T_g (ee=0%) - T_g (ee=50%) = 0.8 K is very small but not negligible. These results may suggest that the relaxation rate at ee=50% seems very slightly faster than that of ee=0%. However a general trend regarding the ee can not be drawn since at higher ee a strong crystallization behavior disturbed the measurements.

The calculated fragility of both samples are in the same range, $m = 119 \pm 10$ for ee=0% and $m = 108 \pm 5$ for ee=50%. This result allow to classify Nac-MBA as a fragile system independently of it enantiomeric composition.

III - Conclusions

Molecular mobility investigations in amorphous Nac-MBA system was achieved by combining experimental and simulation tools such as DRS, FSC and MD simulations covering over 12 decades in the frequency window. A special interest was attached on the investigation of the molecular mobility at variable enantiomeric compositions. This system revealed a complex relaxational landscape independently of the ee, going from fast and weak secondary γ process, to single exponential high magnitude and slow D process. In between these two extreme motions, one evidenced a slow secondary β relaxation presenting some similar characteristics with the genuine β_{JG} motion. Moreover, its characteristic time at T_g is in good agreement with that predicted from the CM model. Besides, at lower frequency the structural relaxation appears concomitantly with a D process. Due to very intense D motion the visualization and localization of α relaxation seems fastidious. Somehow, the derivative method applied on experimental ε' permitted improving the frequency resolution of α process.

The relaxation time of both secondary processes exhibited Arrhenius temperature dependence. Considering the low activation energy and weak dielectric intensity of γ process, with an average value of 38 kJ/mol it may probably originates from the fluctuations of polar side groups of Nac-MBA (such as the N-acetyl group). Taking into account that secondary β is of β_{JG} type, this process could emanates from the motion of the molecule as a whole as generally speculated from the coupling model [70].

The characteristic time of the glass transition dynamic τ_α follows a single VFTH temperature evolution and matches with high temperature values derived from MD simulations. The evaluated dielectric $T_g = 239.0 \pm 0.8$ K matches with the calorimetric $T_g = 240.65 \pm 0.50$ K. Additionally, the temperature dependence (fictive temperature) of the cooling rate performed by FSC mimics with an excellent agreement the temperature evolution of the structural relaxation time. The deviation from the Arrhenius behavior at T_g measured by the fragility index $m = 111 \pm 8$ revealed that amorphous Nac-MBA can be classified as a fragile glass forming liquid. The relaxation time of the highly intense D process that appears at lower frequencies in comparison with the structural relaxation is well described by a VFTH law and the fit parameters show some similarities with that of α relaxation. This may be an indication

of the fact that the dynamic of D process may be controlled by α relaxation. D process contributes almost for 90% in the global dielectric polarization. MD simulations allowed to evidence in the liquid state the existence of linear chain of HB aggregates with parallel dipole orientation confirmed by $G_K > 1$ (the same behavior is reported for monohydroxy alcohols and secondary amides). As temperature decreases, G_K increases, suggesting that the molecule population involved in the H-bonded aggregates will increase and precursor of the future crystalline structure. The temperature evolution of G_K controls that of the dielectric strength of D process. Furthermore the high dielectric response of D process is related to the formation of an effective "super-dipole" generated by linear HB chains involving dimers, trimers, tetramers and so on (which can persist even in the vicinity of the liquid state). Moreover, the linear chain like nature of the liquid structure is confirmed by an increase of the average total dipolar moment $\langle \mu_n \rangle$ with increasing aggregates size n . Therefore $\langle \mu_n \rangle$ is found to be temperature independent implying that identical linear chain associations could probably formed at all temperatures. Additionally at a given temperature, high size aggregates largely contribute to the dielectric response since they possess the higher dipolar moment even though small size aggregates could be more probable.

Globally, the results presented here reinforce and confirmed the idea that the main exponential dielectric response in amorphous NAC-MBA, originates from the HB aggregate associations as it is the case for some subgroups of H-bonded liquid such as secondary amides and monohydroxy alcohols. Regarding the dielectric strength, the activation energy, the relaxation time, and shape parameters, the secondary processes appear nearly identical at variable ee. The most spectacular evidence of chirality impact is found in the expression of the dielectric strength of both Debye and α relaxations. Even though in the liquid state, all the mentioned parameters are identical for ee=0% and ee=50% (same for ee=100%). It appears that in the supercooled liquid state and near to T_g , the dielectric strength of the two processes seems to be ee dependent. As temperature increases and reaches the vicinity of the melting point, the correlation between neighboring molecules decreases and the number of clusters implicated in the HB aggregate formation strongly drops independently on the ee. As temperature decreases G_K increases and the number of clusters implicated in the linear HB molecular chains increases. Linear homo chiral HB molecular chains strongly favor high magnitude dielectric response compared to hetero chiral HB molecular chains since the side

III- Conclusions

polar group responsible of the formation of HB aggregates is directly connected to the stereogenic center and opposite enantiomers present opposite dielectric moment.

References

- [1] B. Atawa, N. Couvrat, G. Coquerel, E. Dargent, A. Saiter, Impact of chirality on the Glass Forming Ability and the crystallization from the amorphous state of 5-ethyl-5-methylhydantoin, a chiral poor glass former, *Int. J. Pharm.* 540 (2018) 11–21. doi:10.1016/j.ijpharm.2018.01.050.
- [2] B. Atawa, N. Couvrat, G. Coquerel, E. Dargent, A. Saiter, Chirality impact on physical ageing: An original case of a small organic molecule, *Mater. Lett.* 228 (2018) 141–144. doi:10.1016/j.matlet.2018.05.133.
- [3] M. Wübbenhorst, J. van Turnhout, Analysis of complex dielectric spectra. I. One-dimensional derivative techniques and three-dimensional modelling, *J. Non-Cryst. Solids.* 305 (2002) 40–49. doi:10.1016/S0022-3093(02)01086-4.
- [4] C.J.F. Böttcher, CHAPTER I - ELECTRIC DIPOLES AND MULTIPOLES, in: *Theory Electr. Polariz.* Second Ed., Elsevier, Amsterdam, 1973: pp. 9–58. doi:10.1016/B978-0-444-41019-1.50007-9.
- [5] W. Dannhauser, Dielectric Study of Intermolecular Association in Isomeric Octyl Alcohols, *J. Chem. Phys.* 48 (1968) 1911–1917. doi:10.1063/1.1668989.
- [6] F. Stickel, E.W. Fischer, R. Richert, Dynamics of glass-forming liquids. II. Detailed comparison of dielectric relaxation, dc-conductivity, and viscosity data, *J. Chem. Phys.* 104 (1996) 2043–2055. doi:10.1063/1.470961.
- [7] C. Hansen, F. Stickel, T. Berger, R. Richert, E.W. Fischer, Dynamics of glass-forming liquids. III. Comparing the dielectric α - and β -relaxation of 1-propanol and o-terphenyl, *J. Chem. Phys.* 107 (1997) 1086–1093. doi:10.1063/1.474456.
- [8] O.E. Kalinovskaya, J.K. Vij, The exponential dielectric relaxation dynamics in a secondary alcohol's supercooled liquid and glassy states, *J. Chem. Phys.* 112 (2000) 3262–3266. doi:10.1063/1.480909.
- [9] D. Fragiadakis, C.M. Roland, R. Casalini, Insights on the origin of the Debye process in monoalcohols from dielectric spectroscopy under extreme pressure conditions, *J. Chem. Phys.* 132 (2010) 144505. doi:10.1063/1.3374820.
- [10] G. Power, M. Nagaraj, J.K. Vij, G.P. Johari, Debye process and dielectric state of an alcohol in a nonpolar solvent, *J. Chem. Phys.* 134 (2011) 044525. doi:10.1063/1.3543713.
- [11] H.-J. Kwon, T.H. Kim, J.-H. Ko, Y.-H. Hwang, Relaxation phenomena in supercooled liquid and glassy acetaminophen studied by dielectric, photon correlation and Brillouin light scattering spectroscopies, *Chem. Phys. Lett.* 556 (2013) 117–121. doi:10.1016/j.cplett.2012.11.072.
- [12] S.J. Bass, W.I. Nathan, R.M. Meighan, R.H. Cole, Dielectric Properties of Alkyl Amides. II. Liquid Dielectric Constant and Loss, *J. Phys. Chem.* 68 (1964) 509–515. doi:10.1021/j100785a011.
- [13] R.G. Wassink, P. Bordewijk, Dielectric relaxation of some amides in carbon tetrachloride, *Adv. Mol. Relax. Interact. Process.* 13 (1978) 299–308. doi:10.1016/0378-4487(78)80051-X.
- [14] L.-M. Wang, R. Richert, Identification of dielectric and structural relaxations in glass-forming secondary amides, *J. Chem. Phys.* 123 (2005) 054516.

- [15] C. Gainaru, S. Bauer, E. Vynokur, H. Wittkamp, W. Hiller, R. Richert, R. Böhmer, Dynamics in Supercooled Secondary Amide Mixtures: Dielectric and Hydrogen Bond Specific Spectroscopies, *J. Phys. Chem. B.* 119 (2015) 15769–15779. doi:10.1021/acs.jpcc.5b10034.
- [16] L.-M. Wang, R. Richert, Dynamics of glass-forming liquids. IX. Structural versus dielectric relaxation in monohydroxy alcohols, *J. Chem. Phys.* 121 (2004) 11170–11176. doi:10.1063/1.1811072.
- [17] F. Kremer, A. Schönhals, The Scaling of the Dynamics of Glasses and Supercooled Liquids, in: *Broadband Dielectr. Spectrosc.*, Springer, Berlin, Heidelberg, 2003: pp. 99–129. doi:10.1007/978-3-642-56120-7_4.
- [18] A.C. Rodrigues, M.T. Viciosa, F. Danède, F. Affouard, N.T. Correia, Molecular Mobility of Amorphous S-Flurbiprofen: A Dielectric Relaxation Spectroscopy Approach, *Mol. Pharm.* 11 (2014) 112–130. doi:10.1021/mp4002188.
- [19] A.R. Brás, J.P. Noronha, A.M.M. Antunes, M.M. Cardoso, A. Schönhals, F. Affouard, M. Dionísio, N.T. Correia, Molecular Motions in Amorphous Ibuprofen As Studied by Broadband Dielectric Spectroscopy, *J. Phys. Chem. B.* 112 (2008) 11087–11099. doi:10.1021/jp8040428.
- [20] A. Bourdet, A. Esposito, S. Thiyagarajan, L. Delbreilh, F. Affouard, R.J.I. Knoop, E. Dargent, Molecular Mobility in Amorphous Biobased Poly(ethylene 2,5-furandicarboxylate) and Poly(ethylene 2,4-furandicarboxylate), *Macromolecules.* 51 (2018) 1937–1945. doi:10.1021/acs.macromol.8b00108.
- [21] B. Rijal, L. Delbreilh, A. Saiter, Dynamic Heterogeneity and Cooperative Length Scale at Dynamic Glass Transition in Glass Forming Liquids, *Macromolecules.* 48 (2015) 8219–8231. doi:10.1021/acs.macromol.5b01152.
- [22] A. Schönhals, Molecular Dynamics in Polymer Model Systems, in: *Broadband Dielectr. Spectrosc.*, Springer, Berlin, Heidelberg, 2003: pp. 225–293. doi:10.1007/978-3-642-56120-7_7.
- [23] K. Adrjanowicz, Z. Wojnarowska, P. Włodarczyk, K. Kaminski, M. Paluch, J. Mazgalski, Molecular mobility in liquid and glassy states of Telmisartan (TEL) studied by Broadband Dielectric Spectroscopy, *Eur. J. Pharm. Sci.* 38 (2009) 395–404. doi:10.1016/j.ejps.2009.09.009.
- [24] M. Paluch, C.M. Roland, S. Pawlus, J. Ziolo, K.L. Ngai, Does the Arrhenius Temperature Dependence of the Johari-Goldstein Relaxation Persist above T_g ?, *Phys. Rev. Lett.* 91 (2003) 115701. doi:10.1103/PhysRevLett.91.115701.
- [25] K.L. Ngai, An extended coupling model description of the evolution of dynamics with time in supercooled liquids and ionic conductors, *J. Phys. Condens. Matter.* 15 (2003) S1107. doi:10.1088/0953-8984/15/11/332.
- [26] K.L. Ngai, M. Paluch, Classification of secondary relaxation in glass-formers based on dynamic properties, *J. Chem. Phys.* 120 (2003) 857–873. doi:10.1063/1.1630295.
- [27] F. Alvarez, A. Alegría, J. Colmenero, Interconnection between frequency-domain Havriliak-Negami and time-domain Kohlrausch-Williams-Watts relaxation functions, *Phys. Rev. B.* 47 (1993) 125–130. doi:10.1103/PhysRevB.47.125.

References

- [28] K.L. Ngai, S. Capaccioli, Relation between the activation energy of the Johari-Goldstein β relaxation and T_g of glass formers, *Phys. Rev. E.* 69 (2004) 031501. doi:10.1103/PhysRevE.69.031501.
- [29] L.-M. Wang, V. Velikov, C.A. Angell, Direct determination of kinetic fragility indices of glassforming liquids by differential scanning calorimetry: Kinetic versus thermodynamic fragilities, *J. Chem. Phys.* 117 (2002) 10184–10192. doi:10.1063/1.1517607.
- [30] K. Duvvuri, R. Richert, Dynamics of glass-forming liquids. VI. Dielectric relaxation study of neat decahydro-naphthalene, *J. Chem. Phys.* 117 (2002) 4414–4418. doi:10.1063/1.1497158.
- [31] S. Baghel, H. Cathcart, W. Redington, N.J. O’Reilly, An investigation into the crystallization tendency/kinetics of amorphous active pharmaceutical ingredients: A case study with dipyridamole and cinnarizine, *Eur. J. Pharm. Biopharm.* 104 (2016) 59–71. doi:10.1016/j.ejpb.2016.04.017.
- [32] A. Dhotel, B. Rijal, L. Delbreilh, E. Dargent, A. Saiter, Combining Flash DSC, DSC and broadband dielectric spectroscopy to determine fragility, *J. Therm. Anal. Calorim.* 121 (2015) 453–461. doi:10.1007/s10973-015-4650-9.
- [33] A.Q. Tool, C.G. Eicitlin, Variations Caused in the Heating Curves of Glass by Heat Treatment1, *J. Am. Ceram. Soc.* 14 (n.d.) 276–308. doi:10.1111/j.1151-2916.1931.tb16602.x.
- [34] A. Saiter, C. Devallencourt, J.M. Saiter, J. Grenet, Thermodynamically “strong” and kinetically “fragile” polymeric glass exemplified by melamine formaldehyde resins, *Eur. Polym. J.* 37 (2001) 1083–1090. doi:10.1016/S0014-3057(00)00242-1.
- [35] A. Saiter, M. Hess, N.A. D’Souza, J.M. Saiter, Entropy and fragility in vitreous polymers, *Polymer.* 43 (2002) 7497–7504. doi:10.1016/S0032-3861(02)00631-6.
- [36] Y.P. Koh, S. Gao, S.L. Simon, Structural recovery of a single polystyrene thin film using Flash DSC at low aging temperatures, *Polymer.* 96 (2016) 182–187. doi:10.1016/j.polymer.2016.04.047.
- [37] J.E.K. Schawe, Vitrification in a wide cooling rate range: The relations between cooling rate, relaxation time, transition width, and fragility, *J. Chem. Phys.* 141 (2014) 184905. doi:10.1063/1.4900961.
- [38] J.E.K. Schawe, Measurement of the thermal glass transition of polystyrene in a cooling rate range of more than six decades, *Thermochim. Acta.* 603 (2015) 128–134. doi:10.1016/j.tca.2014.05.025.
- [39] A. Hensel, J. Dobbartin, J.E.K. Schawe, A. Boller, C. Schick, Temperature modulated calorimetry and dielectric spectroscopy in the glass transition region of polymers, *J. Therm. Anal.* 46 (1996) 935–954. doi:10.1007/BF01983612.
- [40] A. Hensel, C. Schick, Relation between freezing-in due to linear cooling and the dynamic glass transition temperature by temperature-modulated DSC, *J. Non-Cryst. Solids.* 235–237 (1998) 510–516. doi:10.1016/S0022-3093(98)00607-3.
- [41] S. Weyer, A. Hensel, J. Korus, E. Donth, C. Schick, Broad band heat capacity spectroscopy in the glass-transition region of polystyrene, *Thermochim. Acta.* 304–305 (1997) 251–255. doi:10.1016/S0040-6031(97)00286-4.

- [42] C.T. Moynihan, P.B. Macedo, C.J. Montrose, P.K. Gupta, M.A. DeBolt, J.F. Dill, B.E. Dom, P.W. Drake, A.J. Easteal, P.B. Elterman, R.P. Moeller, H. Sasabe, J.A. Wilder, Structural Relaxation in Vitreous Materials*, *Ann. N. Y. Acad. Sci.* 279 (n.d.) 15–35. doi:10.1111/j.1749-6632.1976.tb39688.x.
- [43] U. Kaatze, R. Behrends, R. Pottel, Hydrogen network fluctuations and dielectric spectrometry of liquids, *J. Non-Cryst. Solids.* 305 (2002) 19–28. doi:10.1016/S0022-3093(02)01084-0.
- [44] S.S.N. Murthy, M. Tyagi, Experimental study of the high frequency relaxation process in monohydroxy alcohols, *J. Chem. Phys.* 117 (2002) 3837–3847. doi:10.1063/1.1494428.
- [45] S. Pal, B. Bagchi, S. Balasubramanian, Hydration Layer of a Cationic Micelle, C10TAB: Structure, Rigidity, Slow Reorientation, Hydrogen Bond Lifetime, and Solvation Dynamics, *J. Phys. Chem. B.* 109 (2005) 12879–12890. doi:10.1021/jp0510793.
- [46] P. Derollez, A. Hédoux, Y. Guinet, F. Danède, L. Paccou, Structure determination of the crystalline phase of n-butanol by powder X-ray diffraction and study of intermolecular associations by Raman spectroscopy, *Acta Crystallogr. Sect. B Struct. Sci. Cryst. Eng. Mater.* 69 (2013) 195–202. doi:10.1107/S2052519213004843.
- [47] S. Druot, M.N. Petit, S. Petit, G. Coquerel, N.B. Chanh, Experimental Data and Modelling of the Interactions in Solid State and in Solution between (R) and (S) N-Acetyl- α - Methylbenzylamine. Influence on Resolution by Preferential Crystallization, *Mol. Cryst. Liq. Cryst. Sci. Technol. Sect. Mol. Cryst. Liq. Cryst.* 275 (1996) 271–291. doi:10.1080/10587259608034081.
- [48] S. Druot Houlemare, Influence des interactions homo- et heterochirales lors du dedoublement par cristallisation preferentielle de deux derives de l'alpha-methylbenzylamine : le n-acetamide et le chloroacetate, Caen, 1999. <http://www.theses.fr/1999CAEN2029> (accessed March 7, 2018).
- [49] F. Affouard, N.T. Correia, Debye Process in Ibuprofen Glass-Forming Liquid: Insights from Molecular Dynamics Simulation, *J. Phys. Chem. B.* 114 (2010) 11397–11402. doi:10.1021/jp1046358.
- [50] A. Lerbret, P. Bordat, F. Affouard, M. Descamps, F. Migliardo, How Homogeneous Are the Trehalose, Maltose, and Sucrose Water Solutions? An Insight from Molecular Dynamics Simulations, *J. Phys. Chem. B.* 109 (2005) 11046–11057. doi:10.1021/jp0468657.

CONCLUSIONS AND PROSPECTS

The aim of this thesis was to investigate the influence of chirality on the amorphous state of chiral molecular compounds forming stable conglomerates. For this purpose, two model systems were studied: 5-ethyl-5-methylhydantoin (12H) and N-acetyl- α -methylbenzylamine (Nac-MBA). Thermal (DSC, FSC, TMDSC), structural (TRXRD) and dielectric characterizations (DRS, and MD simulations) were combined to deeply characterize those systems.

An evaluation of the GFA or the crystallization propensity, the viability of the amorphous state, the kinetic of enthalpy recovery upon physical aging and the recrystallization behavior from the amorphous state were investigated for the two model systems at variable enantiomeric compositions. In addition to the thermal and structural characterization of glassy Nac-MBA the determination of the relaxational landscape as a function of the ee was achieved.

From these investigations, the following conclusions emerge:

C1) The GFA is highly influenced by chirality. For both investigated systems, the GFA increases with decreasing ee. Therefore, the pure enantiomer possess significantly high crystallization propensity compared to racemic mixtures. A kinetical explanation was proposed to illustrate this feature. At racemic composition, in order to build a crystalline phase in respect with either the conglomerate or the racemic compound structure, each enantiomer must be surrounded by the right neighbors. Crystallization appears if this condition is satisfied, but may be time consuming depending on the ee. In the case of a pure enantiomer, all neighbor molecules are of the same chirality, therefore, each enantiomer is surrounded by the "right neighbor". In such situation, crystallization may occur more rapidly in enantiomerically pure sample than in a mixture of opposite enantiomers, where neighboring molecules are not necessarily of the same chirality. The probability of a molecule to be positioned with the right neighbor thus decreases as the sample contain the same amount of the two enantiomers (the inverse situation is generally observed in racemic compounds). Additionally, the thermodynamic parameters related to crystallization can significantly differ between pure enantiomer and samples presenting low ee. In the case of 12H, the calorimetric determination of the temperature domain of maximum nucleation and growth rates depicts the fact that, the temperature difference between both regions is narrow for pure enantiomer compared to a scalemic composition. Thus, pure enantiomer possesses poor GFA compared

to a scalemic composition in the studied conglomerate systems. This is, so far, the opposite behaviour as that observed for stable racemic compound forming systems.

C2) The viability of the glassy state upon physical aging would (implicitly) be impacted by chirality. In fact, samples with high ee value presented a strong nucleation behavior over a wide temperature range, going from the supercooled liquid state to the vicinity of T_g and well below. After long aging time, the nuclei overpassed their critical size and crystallization may occur. This situation was evidenced from FSC analysis in the case of the pure enantiomer. For example in the case of 12H, an initial glass of pure enantiomer formed by melt quenching at 1000 K/s completely crystallizes 36°C below T_g just after 4h hours of storage. Conversely, at lower ee, the aged sample evolves towards the metastable liquid equilibrium and the crystallization would be delayed.

C3) High cooling rates accelerate the kinetics of enthalpy recovery due to the higher level of enthalpy induced (or free volume) in the glass initially formed. From FSC analysis (at 1000 K/s), the metastable equilibrium was reached for short aging time (1s was necessary to reach equilibrium for $\Delta T_a = 6^\circ\text{C}$ and 1000s for $\Delta T_a = 16^\circ\text{C}$) while in DSC analysis (20 K/min), after long aging time (almost half a day), an intermediate state with higher enthalpy was achieved for the same aging temperature.

C4) The kinetics of structural enthalpy recovery seems to be indirectly impacted by the ee. Glassy pure enantiomer requires more time to reach equilibrium than that of a scalemic composition. This behavior is not related to any difference in the time scale of secondary processes expressed in the glassy state at variable ee. It may be due to constraints effects mostly resulting from a pronounced nucleation behavior in the glass state of high ee.

C5) FSC is an interesting calorimetric tool which can help to track highly metastable phases, bypassed kinetic processes or phase transition such crystallization or solid-solid transition. However this technique has to be coupled to structural characterization methods in order to fully understand the mechanism engaged.

C6) The relaxational landscape of amorphous Nac-MBA revealed a high magnitude and slow Debye relaxation (almost 90% of the global polarization and slower than the structural process) similarly than that observed in monohydroxy alcohols and N-monosubstituted amides. This process would originate from the formation and reorganization of transient linear HB molecular chains. The temperature dependency of the calculated correlation factor between neighboring dipoles G_k suggested an increasing parallel correlation of dipoles which can be seen as a precursor of the future crystalline structure that may ultimately formed as temperature decreases. Regarding the crystalline structure resulting from the amorphous state, one may ask if these HB aggregates are made only of homo chiral clusters. Such possibility seems less plausible regarding the disordered character of the glassy state and the transient nature of formation and disruption of this HB aggregates. Nevertheless, regarding the crystalline structures, a Debye behavior can be predicted.

C7) From the analyzed case, it seems that, the relaxational landscape of amorphous Nac-MBA is ee independent. Furthermore, the time scale of all the processes (D , α , β_{JG} , γ) and the evolution of their temperature dependency are approximatively identical. Therefore, no significant difference in the dynamical T_g , the fragility index m , the shape parameters is mentioned at variable ee. Since for all the analyzed compositions the time scale of all the relaxational processes were estimated identical, while the crystallization behavior differs significantly from one composition to another, it seems that molecular mobility would not be a key parameter in the crystallization behavior of Nac-MBA.

C8) The dielectric strength of both secondary processes seems constant with the ee variation. The main expression of chirality in amorphous Nac-MBA is evidenced in the signature of the dielectric strength of both D and α processes. In fact, the time scale of both processes merges at the vicinity of the liquid state suggesting that at very high temperature, the probability of forming HB aggregates with large cluster number considerably diminishes; consequently, isolated molecules largely contribute in the dielectric response. For this reason, the dielectric intensity of Debye and α processes are constant at variable ee. Conversely, when temperature decreases larger linear HB aggregates are formed. Since the two enantiomers possess opposite dipole moment vector, it is consistent that, for large HB aggregates, the dielectric intensity differs depending on the ee. In pure enantiomer, the linear HB aggregates

are built from homo chiral molecular units. When the sample contains the two opposite enantiomers, homo chiral and hetero chiral linear HB aggregates are possibly formed. The probability to formed hetero chiral HB aggregates increases with decreasing ee. It seems that hetero chiral HB aggregates form low magnitude effective dipole compared to homo chiral linear HB aggregates. Thus, the intensity of dielectric response is a function of the initial ee.

From this study many questions are still pending and we do not claim to predict a general behavior of the amorphous state of conglomerate forming systems based on the two model compounds, even if though strong similarities were evidenced. Nevertheless, some prospects can be envisaged:

P1) FSC presents thus inherent limitations to investigate physical mixtures such as (in our case) a conglomerate composed by a 50/50 ratio of crystals of both enantiomers. Indeed, the sampling method proposed by the manufacturer is not adequate for such investigations as it remains difficult to maintain a fixed composition even when started from a micronized powder. New sampling methods (multiple dilutions for example) should be envisaged to investigate those systems or any physical mixture by FSC to ensure robust and reproducible results.

P2) In order to improve the viability of the amorphous state of highly crystallogenic enantiomers, the formation of amorphous molecular alloys should be envisaged by mixing the enantiomers with excipients exhibiting high T_g values such as trehalose, maltose, glucose, *etc.* This situation could permit to extract the molecular mobility of amorphous enantiopure 12H for example.

P3) Since the main impact of chirality in the amorphous state is expressed in the capability of the liquid to build linear HB aggregates, it may be interesting to understand if these linear HB chains are preferentially homo chiral or hetero chiral at variable compositions. Molecular dynamic simulation can be an interesting path to shed light on these interrogations.

P4) High pressure measurements can be envisaged since the Debye response under pressure application is still matter of debate in the dielectric spectroscopy community. Moreover, pressure application can inhibit crystallization of poor glass former. Therefore, the

molecular mobility of highly crystallogenic compositions can be investigated. Additionally: the relaxational behavior, the time scale of different processes and different parameters describing the relaxational landscape, and the crystallization behavior can be investigated under high pressure application.

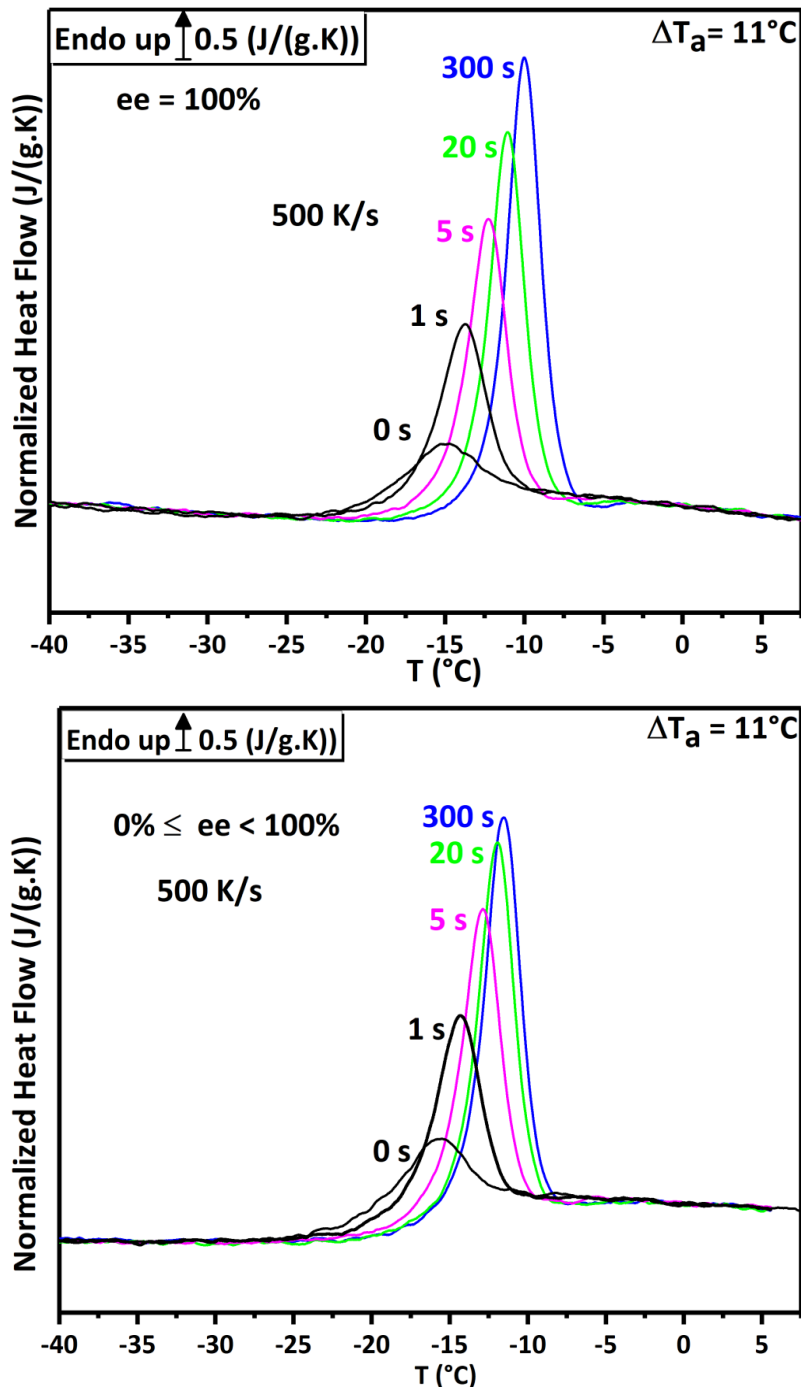
P5) It may be also interesting to probe the chirality impact (molecular mobility, GFA, crystallization behavior, physical aging) in systems forming stable racemic compounds and presenting the same capability of forming linear HB aggregates (and thus Debye processes) in order to compare their behavior with Nac-MBA.

P6) The study must be made on a subgroup of linear HB forming liquid with a Debye signature to determine the putative existence of a general behavior and to extend it to other chiral compounds presenting several asymmetric centers.

ANNEXES

A1- Ambiguous Aging behavior at lower Scanning Rate in Nac-MBA system

When changing the cooling and heating rates from 1000 K/s to 500 K/s and considering the identical aging procedure, an intriguing behavior appears upon enthalpy recovery after a certain aging time. Figure 16 depicts the normalized heat flow as a function of temperature for three aging time at scanning rate of 500 K/s.



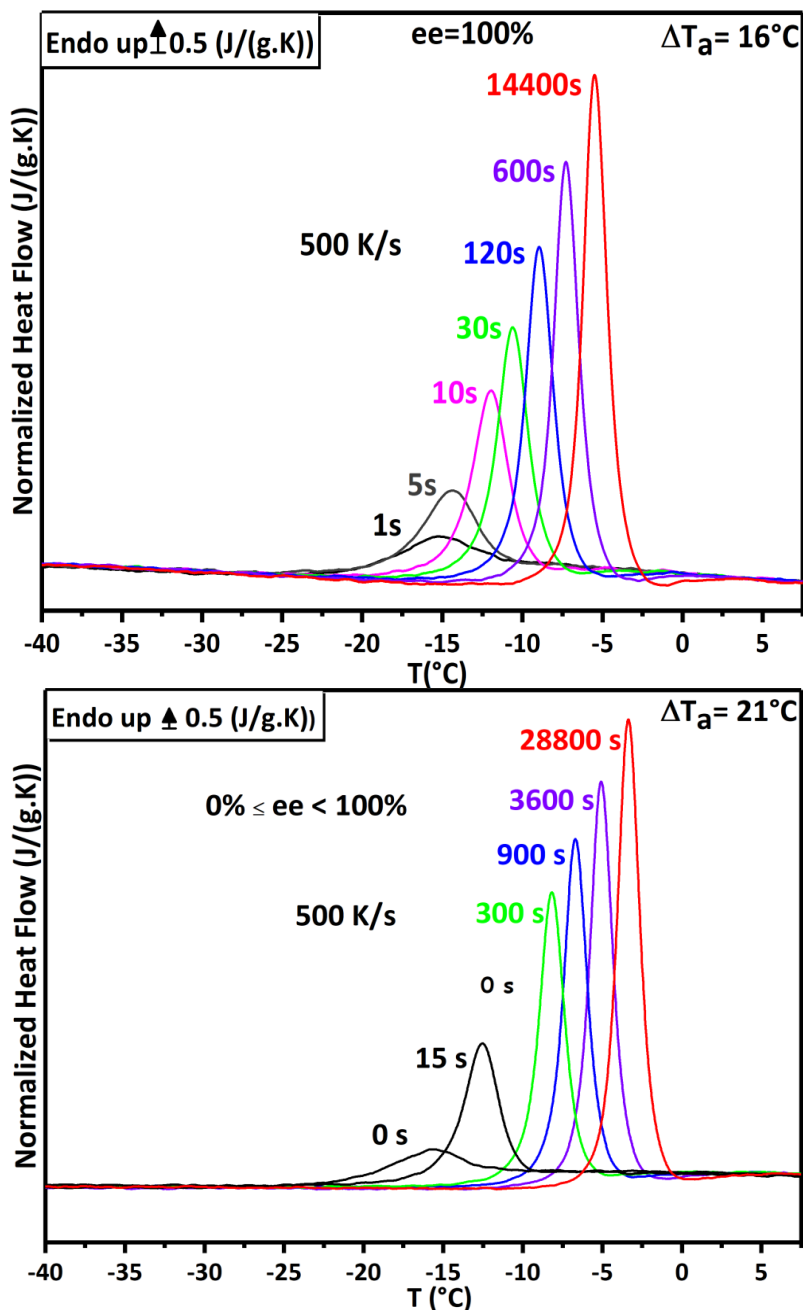


Figure A1: Normalized heat flow curves recorded after physical aging during heating ramps at 500 K/s as a function of $ee\%$. $\Delta T_a = (T_g - T_a) = 11^\circ\text{C}$, 16°C and 21°C with $T_g = -22 \pm 0.5^\circ\text{C}$

Upon heating at 500 K/s, enthalpy recovery overshoot peak is directly followed by an ambiguous low magnitude exothermal event occurs. This process is different from a crystallization event, since no drop of ΔC_p occurs for higher aging time. Additionally, the intensity of the exothermal peak seems to increase with increasing aging time and becomes constant as the overshoot peak stopped to evolve. This behavior appears for both analyzed

composition but regarding its small magnitude; no ee dependency can be drawn. Moreover, such behavior was not evidenced for very short aging time, neither at 1000 K/s nor 1500 K/s. Consequently, this phenomenon is a combined effect of the aging process and the scanning rate which has to be low enough to visualize such thermal response. As depicted in figure 16, this exothermal event has no influence on the return towards equilibrium. The fictive temperature is equal to the aging temperature for long aging time and the kinetic of aging delay for high enantiomeric concentration. Therefore, the origin of this intriguing exothermal event is still unknown since, to our knowledge, such behaviors have never been reported in literature.

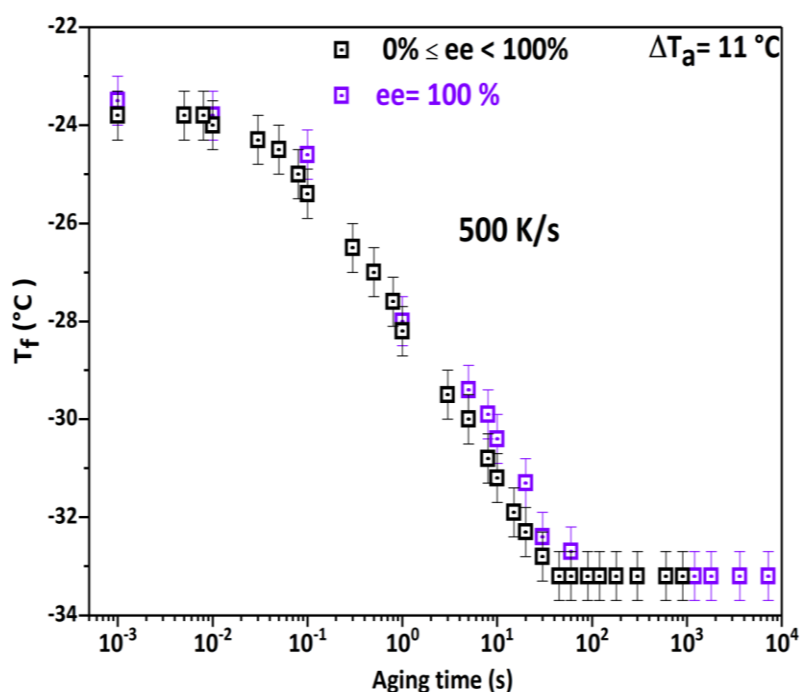


Figure A2: Time evolution of the fictive temperature at 500 K/s in function of two ee at $\Delta T_a = 11^\circ\text{C}$



Impact of chirality on the Glass Forming Ability and the crystallization from the amorphous state of 5-ethyl-5-methylhydantoin, a chiral poor glass former

Bienvenu Atawa^{a,b}, Nicolas Couvrat^{b,*}, Gérard Coquerel^b, Eric Dargent^a, Allisson Saiter^{a,*}

^a Normandie Univ, UNIROUEN Normandie, UMR CNRS 6634, Groupe de Physique des Matériaux, F76801 Saint Etienne du Rouvray, France

^b Normandie Univ, UNIROUEN Normandie, EA3233, Science et Méthodes Séparatives, F76821 Mont Saint Aignan, France

ARTICLE INFO

Chemical compounds studied in this article:

5-Ethyl-5-methylhydantoin (PubChem CID: 82,162)

Keywords:

Fast Scanning Calorimetry
Glass Forming Ability
Chirality
Glassy state
Physical ageing

ABSTRACT

The investigation of the glassy state of 5-ethyl-5-methylhydantoin (*i.e.* 12H, a chiral Active Pharmaceutical Ingredient) was attempted by Differential Scanning Calorimetry (DSC) and Fast Scanning Calorimetry (FSC). This compound exhibits a high crystallization propensity for every enantiomeric composition. Nevertheless, glassy states of pure enantiomer or mixtures between enantiomers were successfully reached by FSC at cooling rates of: 1000 °C/s and 300 °C/s respectively, even though limitations on the sampling reproducibility were evidenced due to FSC sample size. The Glass Forming Ability (GFA) was proven to increase with the counter-enantiomer content. From the glassy state, pure enantiomer displayed a more pronounced crystallogenic character (with a crystallization occurring 36 °C below T_g during ageing) than that of the mixture between enantiomers. Ageing of amorphous 12H promotes a strong nucleation behavior in both samples but enantiopure 12H crystallizes upon ageing while scalemic 12H evolves towards the metastable equilibrium. Finally, potential new phase equilibria (previously not reported) in the enantiomeric phase diagram could have been highlighted by FSC by recrystallization from the amorphous state.

1. Introduction

Active Pharmaceutical Ingredients (APIs) are mostly formulated in the crystalline state for obvious reasons of stability, chemical and structural purities (Variankaval *et al.*, 2008). But regarding the Bio-pharmaceutical Classification System (BCS), not less than 90% of the commercialized APIs are poorly water soluble and consequently have poor bioavailability (Amidon *et al.*, 1995). This fact is a critical issue for pharmaceutical industries. Many techniques are therefore proposed to enhance the bioavailability of APIs. Among them, the formulation of the APIs in the amorphous state is one of the most promising routes to enhance their bioavailabilities (Bhugra and Pikal, 2008; Hancock and Parks, 2000). Numerous operations may lead to amorphous compounds (Nagapudi and Jona, 2008; Vasconcelos *et al.*, 2016): melt quenching, freeze and spray drying (Rey, 2016), high energy milling (Descamps *et al.*, 2007; Schammé *et al.*, 2016; Willart and Descamps, 2008), fast dehydration (Willart *et al.*, 2002). If the targeted molecule is thermally stable at the liquid state, melt quenching remains one of the most

common and easiest way to obtain pure amorphous material. Upon cooling, a liquid can either crystallize or remains liquid below the melting temperature. At a certain temperature, the super-cooled liquid falls in an out-of-equilibrium state (namely the glassy state) characterized by the glass transition temperature (T_g). At this temperature, the heat capacity, C_p of the super-cooled liquid decreases abruptly to a value slightly higher than that of the crystal (Descamps and Willart, 2016). This phenomenon has a kinetical character and is not a thermodynamic phase transition. Indeed, the higher the cooling rate, the higher the T_g value (Saiter *et al.*, 2007). A shift of 3–5 °C can be observed as the cooling rate changes by one order of magnitude (Descamps and Willart, 2016).

T_g is considered as a reference temperature for the viability of an amorphous state and is intrinsic to the compound. Accordingly, its value can give some ideas about the storage temperature of an amorphous API. It also plays an important role during the phase transformation of a molecular compound submitted to mechanical or thermal solicitations such as milling. Indeed, applying the milling above or

Abbreviations: API, Active Pharmaceutical Ingredient; GFA, Glass Forming Ability; FSC, Fast Scanning Calorimetry; DSC, Differential Scanning Calorimetry; BCS, BioPharmaceutical Classification System; ee, Enantiomeric Excess; AS3PC, Auto-Seeded Programmed Polythermic Preferential Crystallization

* Corresponding authors.

E-mail addresses: bienvenu.atawa@etu.univ-rouen.fr (B. Atawa), nicolas.couvrat@univ-rouen.fr (N. Couvrat), gerard.coquerel@univ-rouen.fr (G. Coquerel), eric.dargent@univ-rouen.fr (E. Dargent), allisson.saiter@univ-rouen.fr (A. Saiter).

<https://doi.org/10.1016/j.ijpharm.2018.01.050>

Received 18 September 2017; Received in revised form 24 January 2018; Accepted 25 January 2018

Available online 31 January 2018

0378-5173/ © 2018 Elsevier B.V. All rights reserved.

below T_g can respectively lead either to other molecular ordered phases (*i.e.* polymorphs) or to pure or partial amorphous materials (Descamps et al., 2007), (Schammé et al., 2016). Furthermore, the importance of T_g determination is well established for industrial drying processes such as freeze drying or spray drying. A porous amorphous solid, obtained by freeze drying may easily collapse or shrink if the storage temperature is above T_g (Bhandari and Howes, 1999). For all the above reasons, the determination of T_g is of a primary importance for pharmaceutical applications.

Differential scanning calorimetry (DSC) is one of the most conventional techniques used to evaluate T_g value for a given cooling or heating rate. T_g characterization is sometimes problematic for some molecular compounds: the glass transition region may overlap with different thermal events such as crystallization (Yu et al., 1998) or structural enthalpy recovery, the heat capacity jump at the glass transition region can be of very small magnitude (Yu, 2001). Theoretically, crystallization can be avoided if sufficient cooling rate is provided (Debenedetti, 1996; Debenedetti and Stillinger, 2001; Turnbull, 1969). However, numerous molecular compounds exhibit a very high propensity to crystallize upon melt cooling, and standard DSC is limited in cooling rate ability (usually, an accurately cooling rate up to 50 °C/min). An alternative was proposed by High Performance DSC's (HPer) which improved the cooling maximum of more than 1 decade. The first HPer DSC was developed by Perkin Elmer and carries out scans up to 750 °C/min ("LAB SYS-DSC 8500-N5340501," n.d.). But still at these high cooling rates, it remains possible for some systems to regain the crystalline configuration. One of the most recent tools developed by Mettler Toledo is the Flash DSC (Fast Scanning Calorimetry or FSC hereafter) device based on a calorimeter chip (Mathot et al., 2011; van Herwaarden et al., 2011; Zhuravlev and Schick, 2010a,b) which can accurately provide very high cooling rates (up to 4000 °C/s) in a wide range of temperature and therefore could permit to avoid re-crystallization of most highly crystallogenic systems. Furthermore, this technique has largely proven its worth in the investigation of disordered polymeric and metallic systems (Cangialosi et al., 2016; Dhotel et al., 2015; Gao et al., 2016; Monnier et al., 2017b,a; Schick and Androsch, 2016; Simon et al., 2016; Simon and Koh, 2016). Therefore, up to our knowledge, few studies are reported in the case of small organic molecular compounds (Corvis et al., 2015a,b; Kawakami et al., 2012; Magoń et al., 2015; Schammé et al., 2017; Shamim et al., 2015).

The present work focuses on the case of 5-ethyl-5methyl-hydantoin (12H hereafter). This hydantoin derivative (Fig. 1a) is used for its antibacterial and antifungal properties (Beilles et al., 2001) and is chiral. The racemic mixture (*i.e.* enantiomeric excess or ee = 0%) crystallizes as a stable conglomerate (Beilles et al., 2001; Ndzié et al., 1999), which is an eutectic mixture (50/50 composition) between both enantiomers (ee = 100%) with a simple eutectic melting as illustrated in Fig. 1b. 12H exhibits a very high tendency to crystallize for both pure enantiomer and racemic composition, in such way that the amorphous state may not be obtained with conventional methods. This study aims thus at isolating amorphous states of enantiopure and racemic 12H, to

determine their physical differences in terms of Glass Forming Ability (GFA) and crystallization propensity, and by extension to predict chirality implications on the glassy state of conglomerate forming systems.

2. Materials and methods

2.1. Materials

Racemic mixture of 12H was supplied by ABCR GmbH. The pure enantiomer was obtained by means of Auto-Seeded Programmed Polythermic Preferential Crystallization method (AS3PC) and performed by Beilles and co-workers (Beilles et al., 2001). The melting temperatures measured in this work were T_m (R or S) = 173 ± 2 °C for the pure enantiomer and T_m (RS) = 140 ± 2 °C for the racemic composition, in accordance with the literature data (Ndzié et al., 1999). The melting enthalpies were ΔH_m = 21 ± 1 kJ/mol and ΔH_m = 18 ± 1 kJ/mol for the pure enantiomer and racemic composition respectively.

2.2. Methods

2.2.1. DSC

The DSC experiments were launched with a Perkin Elmer 8500. This power controlled DSC is made of two independent identical small furnaces, one for the sample material and one for the reference. Cooling was ensured by a refrigerated cooling system (IntraCooler II, using a dual stage heat exchanger with the lowest puck temperature at -96 °C), allowing a cooling down to -70 °C. The baseline was calibrated in the range [-70 °C; 200 °C] at 10 °C/min (the same heating rate for all the experiments), the calibrations in temperature and enthalpy were achieved using indium and benzophenone as reference materials. Measurements were done under a nitrogen gas flow of 20 mL/min and the sample mass was about 5 mg. All the samples were submitted to a heat-cool-heat cyclic protocol at 10 °C/min for the heating and a cooling of 50 °C/min.

2.2.2. FSC

The measurements were performed with a power compensation twin-chip namely Flash DSC 1 (FSC) from Mettler-Toledo. The chip consists of two membranes (0.5 mm of diameter), one for the sample and the other one as the reference. There are 16 thermocouples (8 to control the temperature on the sample side and 8 to control the temperature on the reference side), symmetrically arranged around the sample and reference areas ensured temperature measurements (Mathot et al., 2011). Conditioning and correction of the chip were performed according to the manufacturer and prior to measurements. The cooling was ensured down to -70 °C by an intracooler model Huber TC100. The Huber TC100 is a dual step cooling device that can ensure the cooling of the sensor down to -95 °C. The sample was submitted to a nitrogen purge gas flow at a rate of 20 mL/min and placed on the sample chip area by the mean of an optical microscope and a long fiber for sample positioning.

Preparation of the sample: a first chip was used for the pure enantiomer and a second for the samples taken from the racemic batch. As detailed above, racemic 12H batch is composed by a 50/50 mixture of pure enantiomer crystals and so far, no racemic compound was characterized for this molecule. Therefore, despite a pre-milling (manually) of the powder to ensure homogenization, the experimental constraints on the sample size did not permit to isolate an equimolar proportion between enantiomers during the sampling from the racemic batch. Thus, the sampling from the racemic batch always led to samples at scalemic compositions (*i.e.* ee is different from 0% or 100%) and only the thermal signature of the samples could give an approximation of their enantiomeric compositions (please refer to [supplementary information](#) for further details about sample composition variations).

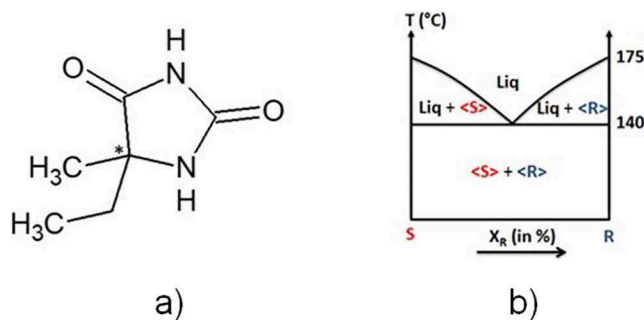


Fig. 1. (a) Developed Formulae of racemic 12H, (b) Binary phase diagram between 12H enantiomers.

Measurements: A first pre-melting step is launched to ensure a good thermal contact between the sample and the sensor. In this study, the samples were submitted to a heat-cool-heat cyclic protocol. The cooling and heating rates chosen were in the range [300–3000 °C/s]. The sample mass can be estimated by using an equivalence DSC–FSC based on the thermal properties of the liquid or the glassy state linked to the sample mass. These properties can be either the melting enthalpy or the heat capacity jump at the glass transition region (Schawe and Pogatscher, 2016). In this work, the sample mass used for FSC analyses was determined using Eq. (1):

$$m(\text{FSC}) = \frac{\Delta H_m(\text{FSC})}{\Delta H_m(\text{DSC})} \times m(\text{DSC}) \quad (1)$$

where ΔH_m represents the area of the melting pic normalized by the cooling rate and m the sample mass.

2.2.3. Thermal lag considerations

In FSC analyses, the sample is directly deposited on the chip and is heated from the bottom part in contact with the chip. Hence, there could be a thermal gradient dependent from sample thermal conductivity and size (Schawe and Pogatscher, 2016). Dynamic and static temperature gradients linked to the sample size and the high scanning rate during FSC experiments are reported in literature (Schawe, 2015). The dynamic thermal lag at the glass transition is corrected by averaging T_g values on cooling and on heating. This dynamic thermal lag can be neglected for small organic compounds if three conditions are fulfilled: i) a good thermal contact is ensured between the sample and the sensor, ii) the sample thickness is lower than 10 μm and iii) the heating rate is low enough (circa 1000 °C/s) (Schawe and Pogatscher, 2016). The static thermal gradient is essentially due to the temperature difference between the furnace and its immediate environment. This effect is mostly impacted by the sample thickness. As reported in the case of polystyrene (Schawe, 2015), the static thermal lag becomes obvious when the thickness of the sample is > 10 μm . Thickness calculation was purchased based on simple geometric considerations. We assume that the samples are 3D cylindrical objects with different geometrical bases. The sample volume can be determined knowing the density of the crystal lattice ($d = 1.28 \text{ g/cm}^3$) and the sample mass. Consequently knowing the area occupied by the sample on the chip, one can determine its thickness. A universal EPI-illuminator optical microscope equipped with a digital sight system camera from Nikon Corporation was used in reflection mode to observe the sample shape. Fig. 2 depicts images of four samples of different masses (from 19 to 120 ng) noted (a), (b), (c), (d) and Table 1 summarizes the sample geometrical characteristics.

In this study, all sample thicknesses were estimated below 10 μm and thermal lag effects were then considered as negligible (up to 120 ng of sample mass and a heating rate of 1500 °C/s).

3. Results

3.1. DSC

Fig. 3 displays the thermal behavior of both pure enantiomer and racemic mixture upon heating and cooling (at 10 °C/min and 50 °C/min respectively). Upon heating, only a single thermal event corresponding to the melting of each compound is mentioned. Upon cooling, recrystallization was not inhibited despite the applied cooling rate. These observations support the highly crystallogenic character of this molecule. Other attempts to vitrify the liquid by applying higher cooling rates in the range [100–250] °C/min resulted in failure (data not shown here). Another possibility remained quenching directly (manually) the melt of both samples in liquid nitrogen. Nevertheless, this possibility was quickly put aside. Actually, during the quenching, an extremely fast crystal growth occurred leaving no chance for vitrification.

Considering that the glass formation probability increases when fast

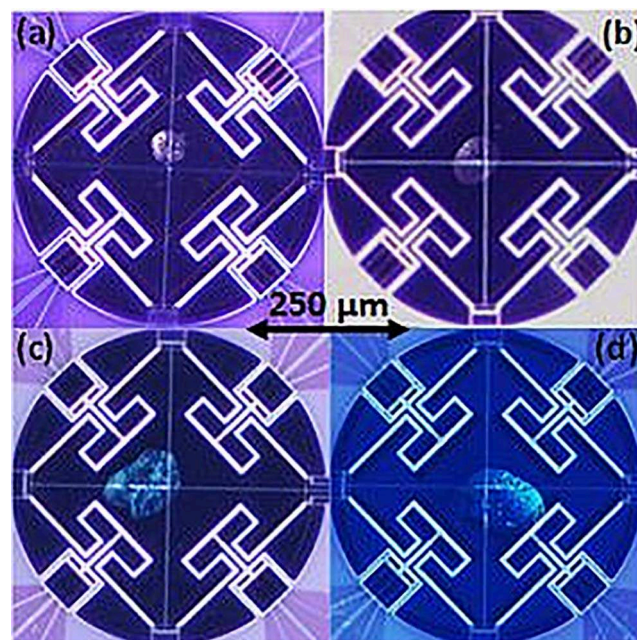


Fig. 2. Pre-molten samples with different geometric parameters.

Table 1
Geometrical characteristics of samples (a), (b), (c) and (d).

Sample mass (ng)	Volume 10^1 (μm^3)	Surface (μm^2)	Thickness (μm)
(a) 19	1484	2294	6.5
(b) 35	2734	3853	7.0
(c) 50	3906	8482	4.6
(d) 120	9375	10,993	8.5

cooling is provided (Debenedetti, 1996; Debenedetti and Stillinger, 2001; Turnbull, 1969), vitrification and crystallization propensities of 12H were apprehended by FSC.

3.2. Pure enantiomer by FSC

Fig. 4 illustrates the thermal signature of pure enantiomer upon cooling and the second heating by FSC. First, the recorded melting temperature was consistent with the value obtained by classical DSC (175 °C). Thus, cooling rates higher than 500 °C/s were required to inhibit recrystallization and fully amorphize enantiopure 12H. The thermal signature of the glass transition was well illustrated by an endothermal step jump of the heat flow at T_g . The latter was measured on cooling and no obvious cooling rate dependency was noticed: $T_g(\text{onset}) = 16 \pm 2$ °C. Nevertheless, at cooling rates of 300 °C/s and 500 °C/s, partial crystallization was evidenced. Cold crystallization remained unavoidable when the compound was heated from the amorphous state, even at 3000 °C/s. Cold crystallization was always followed by an endothermal peak corresponding to the melting of enantiopure 12H.

In order to determine the temperature region where nucleation and growth maxima are located, a cyclic heat-cool protocol and annealing step at various temperatures well below and above T_g (from -50 °C to 80 °C) was applied. This thermal protocol consisted in cooling the melted sample at 1500 °C/s to an annealing temperature. The sample was kept for 30 min at the annealing temperature and heated at 3000 °C/s up to 210 °C. As depicted in Fig. 5, no thermal event occurred upon heating when the annealing step was achieved from 70 °C and beyond. For isotherms performed in the range -10 °C to 60 °C, crystallization took place during the isotherm and upon heating, melting occurred at the pure enantiomer melting point. Annealing performed at -50 °C and -30 °C led to an overshoot peak at the glass transition

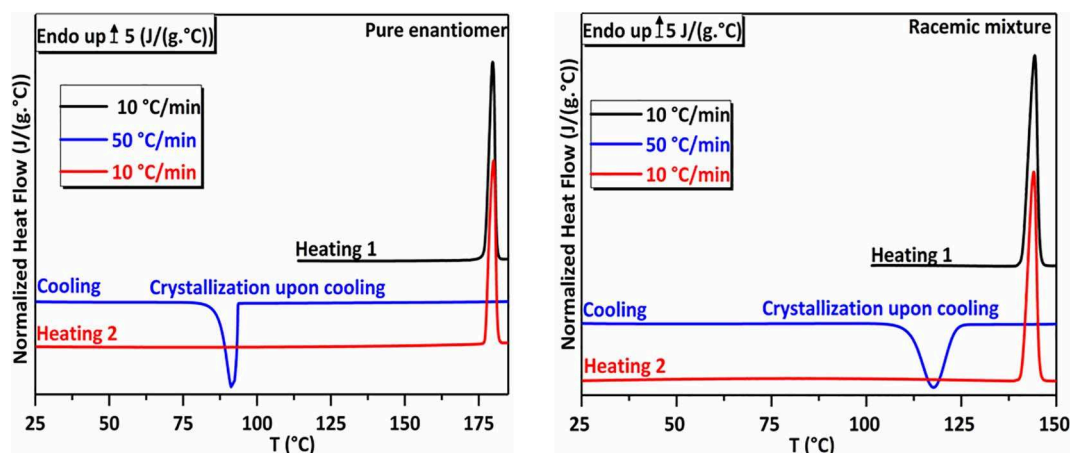


Fig. 3. Heating and cooling curves of pure enantiomer (left part) and racemic mixture (right part) in classical DSC.

region upon heating. Crystallization was evidenced in the range 75 °C up to 130 °C and melting at 173 °C (enantiopure melting point). The nuclei formed at lower temperatures during the annealing and heating steps inevitably undergoes crystallization in the range 75 °C up to 130 °C. The crystal growth rate $G(T)$ is apparently very high in this temperature domain. But the localization of the temperature region where nucleation rate $N(T)$ is at its maximum is not obvious in this case. Whatever the annealing temperature (from $T_g - 66$ °C up to $T_g + 44$ °C), complete crystallization occurred during annealing or heating. Consequently the melting enthalpies obtained were almost similar. Indeed, nucleation takes place well below T_g up to $T_g + 44$ °C. These results and their implications are discussed in Section 4.3.

3.3. Scalemic composition by FSC

Analyses were then carried out with samples coming from the racemic batch. As depicted in 2.3 section, the sampling limitations imposed by FSC prevented to analyze a real racemic sample but only a scalemic (intermediate) composition close to the racemic one. Fig. 6a and 6b present the thermal signature of such 12H sample upon melt cooling and heating from the amorphous state respectively. Full vitrification of the melt was achieved upon cooling (even at 300 °C/s). $T_{g(onsset)} = 16 \pm 2$ °C was determined from cooling measurements. Upon heating, cold crystallization appears (Fig. 6b) and the shape of the peak is highly heating rate dependent. The exothermic crystallization peak was broadened and shifted towards higher temperatures as the heating rate increased. Furthermore, the crystallization enthalpy decreased as

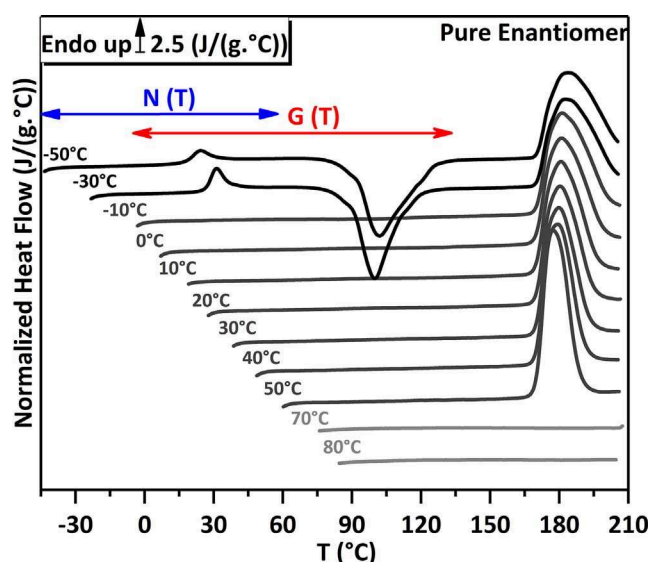


Fig. 5. FSC scans of pure enantiomer recorded upon heating at 3000 °C/s after the melt cooled at different isothermal temperatures T_a (from -50 °C up to 80 °C) and annealed for 30 min. $N(T)$ and $G(T)$ refers to nucleation and growth temperature region respectively.

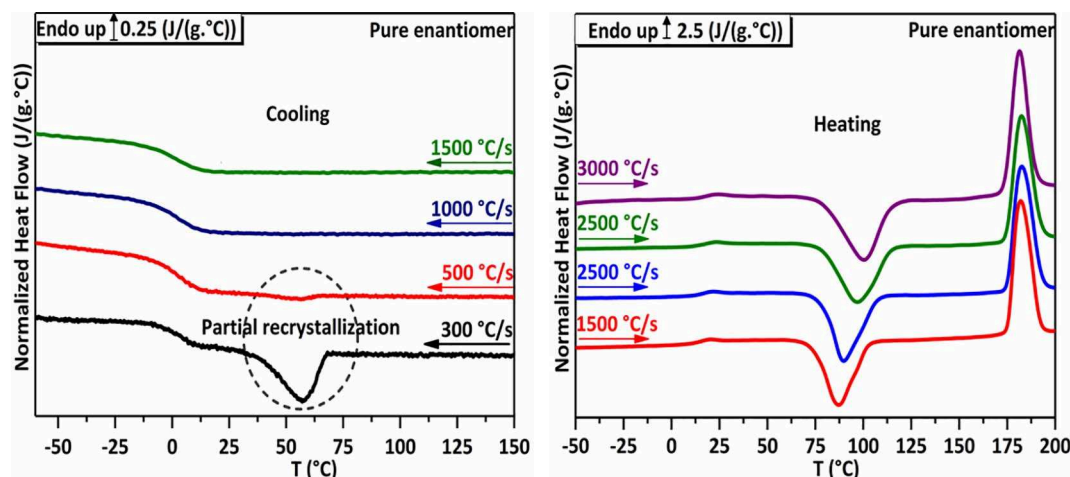


Fig. 4. Thermal events of enantiopure 12H upon cooling (left part) and second heating (right part) at variable cooling and heating rates.

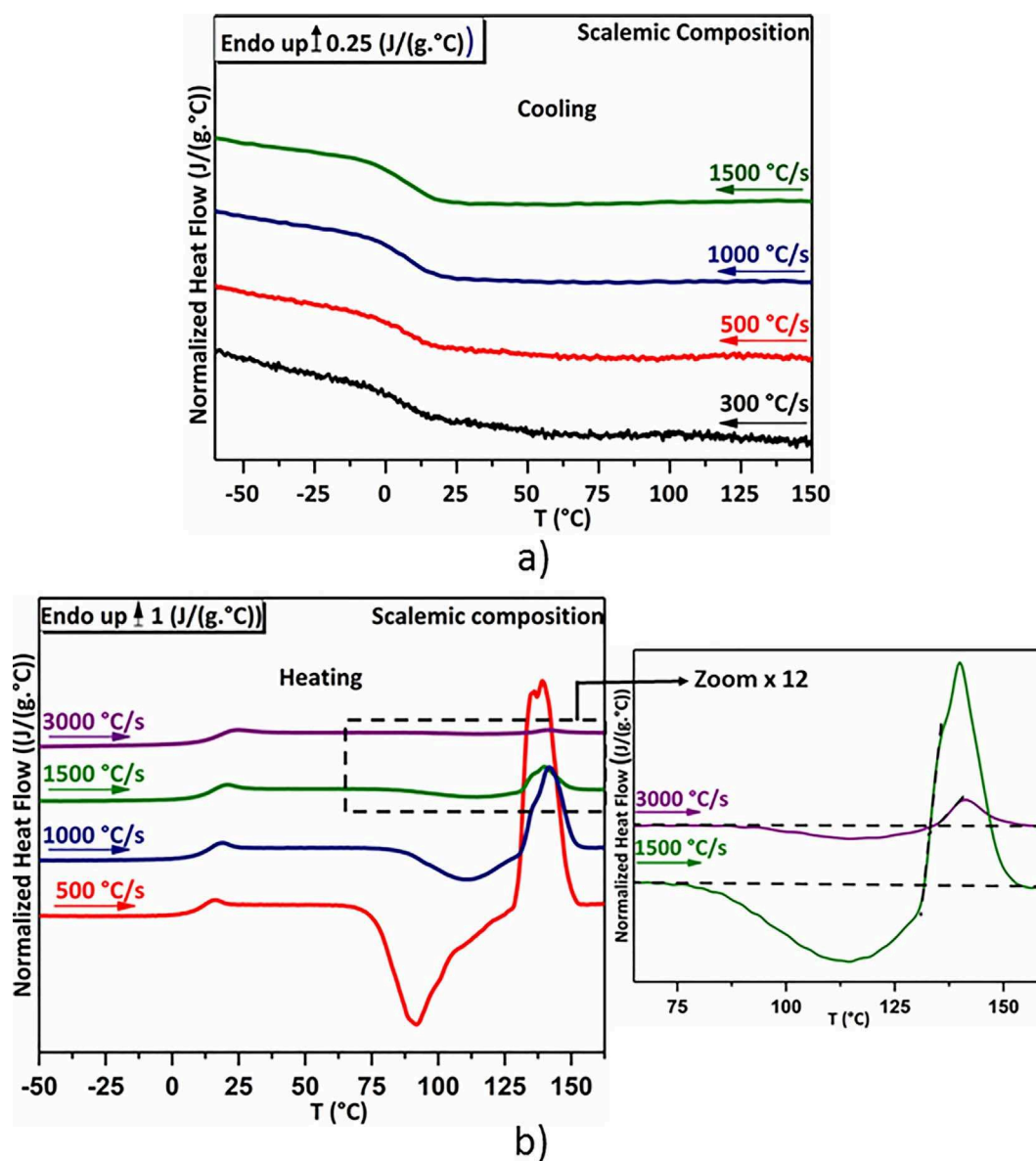


Fig. 6. (a) Thermal events upon cooling and (b) upon heating for the sample at a scalemic composition.

the heating rate increased. For heating rates lower than 3000 °C/s, the melting event was characterized as complex peak resulting from the overlapping of two successive endotherms. The first peak has an onset temperature around 130 °C and the onset temperature of the second peak could be extrapolated to 135 °C. At 3000 °C/s, only one endothermic peak was recorded with an onset temperature around 135 °C.

As in the case of pure enantiomer, the identification of the temperature region where nucleation and crystal growth maxima are located was launch for the scalemic sample. The same cyclic melting-quenching to different annealing temperatures was applied for the same annealing time. This thermal protocol consisted in quenching at 1500 °C/s the melted sample at various annealing temperatures ranging from -50 °C up to 90 °C. The annealing step was launch for 30 min and the sample reheated at 3000 °C/s up to 175 °C. Fig. 7 presents the heating curves after the annealing process. No thermal event was mentioned when the sample was hold at $T_a \geq 70$ °C therefore no crystallization occurred during the annealing or the quenching-heating steps.

When 10 °C $\leq T_a \leq 50$ °C, the sample fully recrystallized during the annealing period and a single endothermic peak was evidenced at 128 °C. Heating the annealed sample at 0 °C, led to a well-defined

exothermic peak from 60 °C to 110 °C followed by melting at 128 °C with the same melting enthalpy as for the previous annealing temperatures. Nucleation occurs from $T_g - 16$ °C up to $T_g + 34$ °C and $G(T)$ is especially high from 60 °C up to 110 °C.

When -50 °C $\leq T_a \leq -10$ °C, recrystallization was always evidenced in the range 90 °C up to 125 °C during the heating step. Accordingly, the maximum of growth rate G_1^{\max} is localized in this temperature region. The recrystallized samples melt at 133 °C and the crystallization enthalpy (as the melting enthalpy) increases as the annealing temperature increases. As the isothermal temperature increases from -50 °C up to -10 °C the number of nuclei formed during the annealing step increases. Therefore the maximum of nucleation rate N_1^{\max} is approximately located at $T_g - 26$ °C. At the glass transition region an overshoot peak is mentioned synonym of an ageing effect.

Analyses were carried out with different samples of variable masses taken from the same racemic batch. The samples presented identical thermal signatures in the glass transition region and the same T_g values at a constant heating rate. As illustrated in Fig. 8, only the kinetical character of the glass transition was observed (a shift of 1 to 2 °C) when the heating rate was increased from 500 °C/s up to 1000 °C/s or 1500 °C/s.

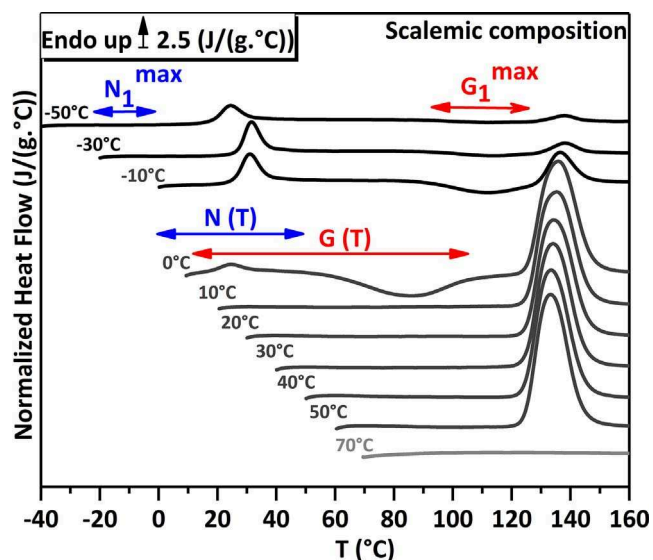


Fig. 7. FSC curves of scalemic 12H recorded upon heating at 3000 °C/s after the melt was cooled at different isothermal temperatures T_a (from -50 °C to 70 °C) and annealed for 30 min. $N(T)$ and $G(T)$ refers to the temperature region where nucleation and growth take place respectively. N_1^{\max} and G_1^{\max} refers to the temperature region where the rate of nucleation and crystal growth are at their maxima.

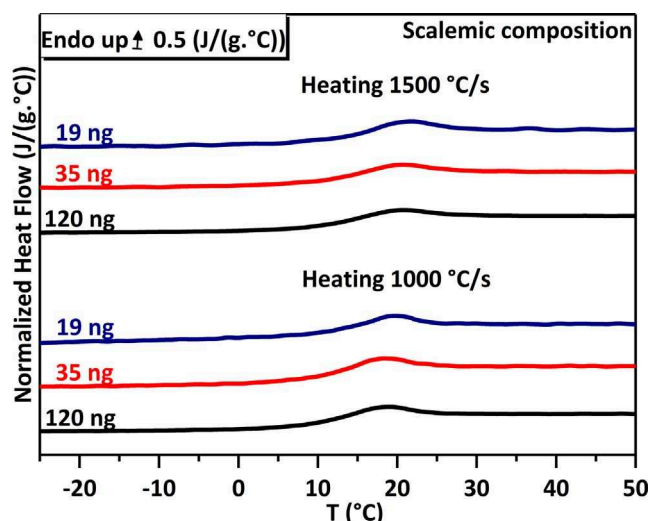


Fig. 8. Glass transition signature at 1000 °C/s and 1500 °C/s for three samples with increasing masses.

As depicted in 2.2.3 section, the thermal lag effect on T_g was considered as negligible for these experiments.

3.4. Physical ageing and crystallization propensity

A systematic study of physical ageing process was launched for pure enantiomer and scalemic composition. The melted sample was cooled down to -70 °C at 1000 °C/s and heated 30 °C above T_g in order to record the unaged glass signal. The sample was then cooled down to T_a (from -40 °C up to 5 °C) and aged for 60 s (before the final heating step at 1000 °C/s up to 45 °C, the sample is previously cooled down to -70 °C). Fig. 9 (a and b) presents the final heating curves after the ageing procedure for pure enantiomer and scalemic 12H respectively. Depending on the annealing temperature, a more or less intense overshoot peak occurs at the glass transition region. This behavior is due to the irreversible enthalpy recovery phenomenon and is classically observed for different glass formers (Cangialosi et al., 2013; Kovacs et al., 1963; Kozdras et al., 2011; Yoshioka et al., 1994) (Gunawan et al.,

2006; Hancock et al., 1995; Surana et al., 2004). Fig. 9 c depicts the enthalpy excess evolution as function of T_a . All the samples presented a bell shape enthalpy recovery curve with the same maximum at $T_g - 28$ °C for an ageing time of 60 s.

A significant drop of the heat capacity is observed in the case of pure enantiomer when the ageing is performed for 60 s at temperature higher than $T_g - 21$ °C. The heat capacity drop in the case of the scalemic composition occurred when T_a was higher than $T_g - 11$ °C for the same ageing time. This drop of heat capacity in the supercooled liquid point out the early stages of the crystallization.

Moreover, for two selected ageing temperatures ($T_g - 36$ °C and $T_g - 26$ °C), ageing was performed for various ageing times t_a , from 1 s up to 14,440 s and 1 s up to 900 s respectively and according to the same thermal protocol. Enantiopure 12H crystallizes for the two ageing temperatures after short ageing time (see Supplementary Information: Glassy pure enantiomer). In contrary as illustrated in Fig. 10a) in the case of scalemic 12H, the enthalpy relaxation at the glass transition region increases as the ageing time increases up to a constant signal for longer ageing time. The overshoot peak increases with ageing time and reaches a constant magnitude more rapidly for $T_g - 26$ °C than for $T_g - 36$ °C. However at $T_g - 36$ °C the overshoot area attained higher intensities. The out of equilibrium nature of the glassy state implies a slow evolution of the glass towards the metastable supercooled liquid state. Therefore, one can ask if the supercooled liquid equilibrium is reached when the saturation overshoot peak is obtained for the two ageing temperatures. To answer this question, two methods are usually proposed. The first method consists in comparing the excess of enthalpy at the supposed equilibrium and the value needed to reach the supercooled liquid state ($\Delta H_\infty = \Delta C_p (T_a - T_g)$). The second method consists in calculating the fictive temperature T_f as function of the ageing time. T_f is defined as the actual temperature for the same compound in the equilibrium, metastable, supercooled state whose structure is expected to be similar to that of the non-equilibrium compound (Descamps and Willart, 2016). At the supercooled liquid equilibrium, the T_f value is equal to the ageing temperature. The calculation of ΔC_p only by FSC is problematic because of the uncertainty linked to the rough determination of the sample mass. Consequently in this analysis we chose to determine T_f evolution as function of the ageing time. The T_f is calculated from the heating curves using the “equal area rule” (Moynihan et al., 1976) method written here in terms of the heat flow:

$$\int_{T_f}^{T \gg T_g} (\dot{Q}_l - \dot{Q}_g) dT = \int_{T \ll T_g}^{T \gg T_g} (\dot{Q} - \dot{Q}_g) dT \quad (2)$$

where \dot{Q}_l and \dot{Q}_g are the liquid and glassy heat flow lines and \dot{Q} is the sample heat flow.

In Fig. 10c) the difference ($T_f - T_a$) is plotted as a function of the ageing time for the two ageing temperatures. The fictive temperature value reaches the ageing temperature after 120 s and 10,800 s for $T_a = T_g - 26$ °C and $T_a = T_g - 36$ °C respectively. Thus the supercooled liquid state is reached for the two ageing temperatures.

4. Discussion

4.1. High crystallization propensity of 12H

As illustrated by DSC and FSC results, 12H exhibits a high crystallization propensity. This is a common feature shared by numerous small organic compounds (Baird et al., 2010). Due to their small size and relatively planar shape, the packing of such molecules in the crystalline configuration is mostly favored. It is well established that compounds with high molecular weight are difficult to crystallize compared to systems with low molecular weight (Baird et al., 2010). Moreover, the propensity to form a glass can be affected by the number of aromatic rings, number of electronegative atoms, presence of flexible and rotating branches, intermolecular and intramolecular connections (Baghel et al., 2016; Kawakami et al., 2015; Miyazaki et al., 2007).

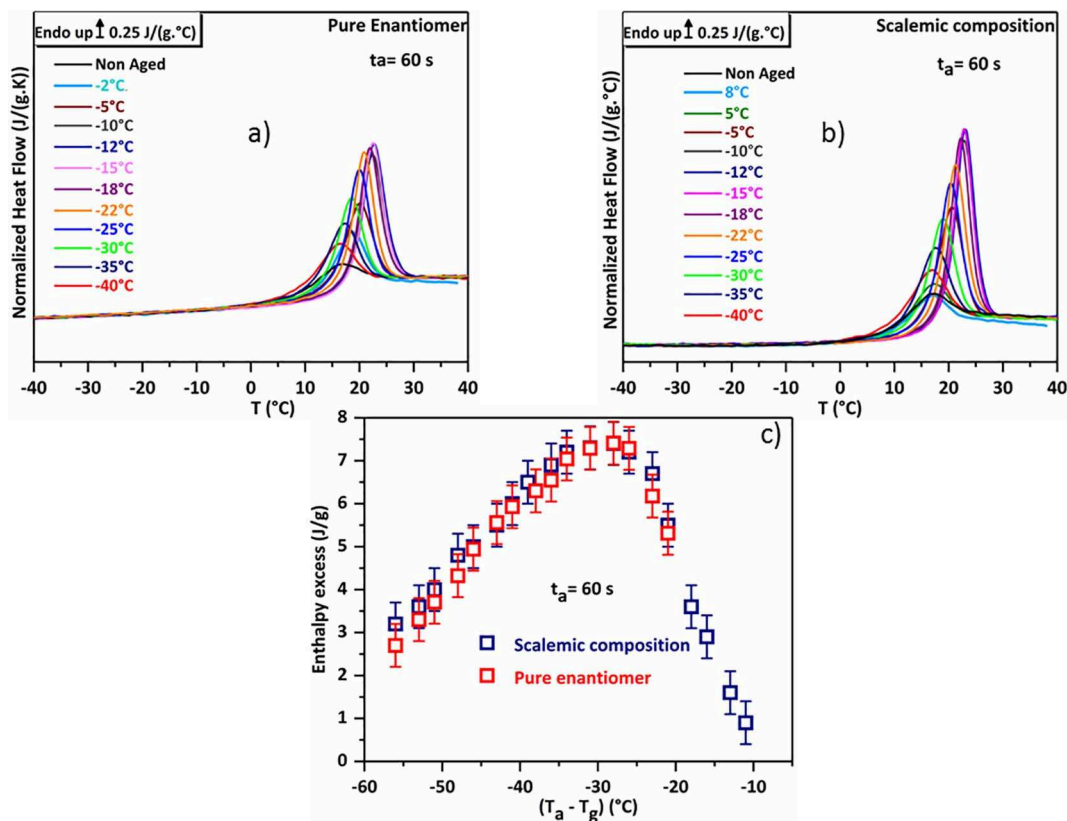


Fig. 9. (a, b) FSC heating scans at 1000 °C/s as a function of ageing temperatures for an ageing time of 60 s after cooling at 1000 °C/s for pure enantiomer and scalemic 12H respectively c) Evolution of the enthalpy excess value as a function of the difference $(T_a - T_g)$.

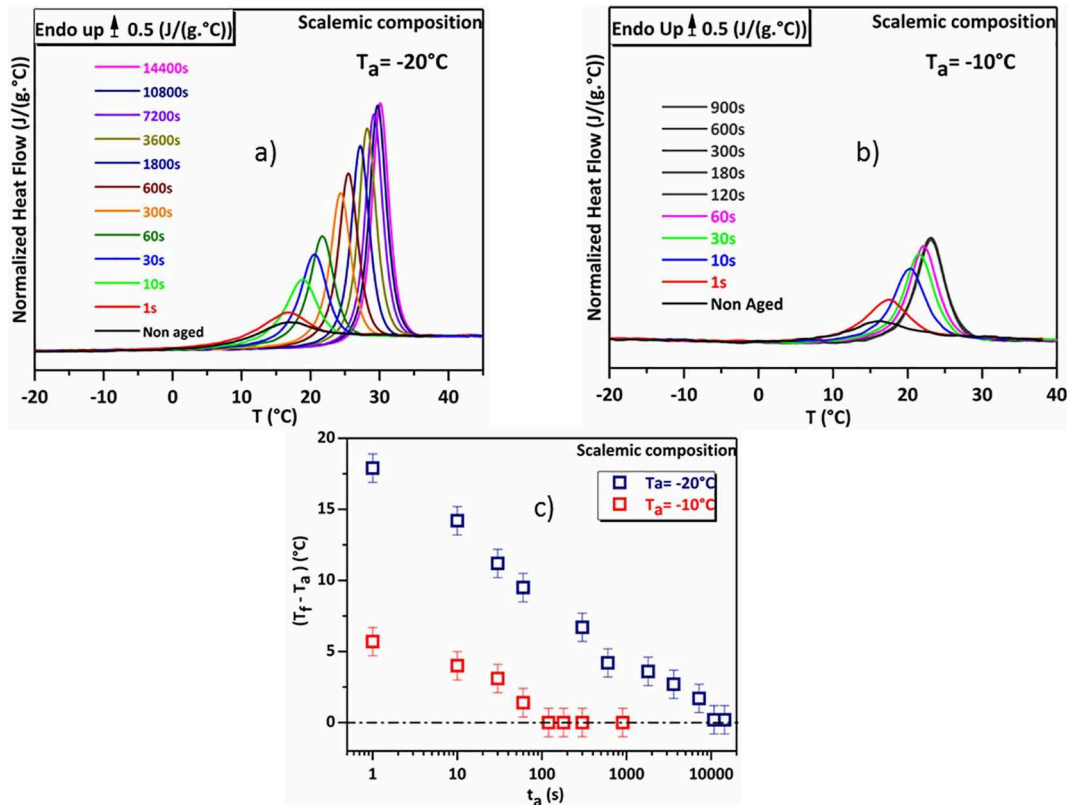


Fig. 10. (a, b) FSC heating scans of scalemic 12H at 1000 °C/s as a function of ageing time for $T_a = -20$ °C and -10 °C respectively after cooling at 1000 °C/s c) Evolution of the difference $(T_f - T_a)$ as a function of ageing time t_a .

Furthermore, it was observed that liquids composed of symmetric molecules crystallize more easily than liquids made of asymmetric molecules. The case of meta and para xylene is commonly presented as an obvious example (Turnbull, 1969). The meta-xylene liquid can undergo cooling and vitrify, whereas for para-xylene isomer crystallization takes place in the same cooling conditions (Alba et al., 1990). The tendency to crystallize (or to vitrify reversibly) can be related to numerous parameters: dynamics (viscosity or molecular mobility), thermodynamics (the driven force of crystallization) (Baird et al., 2012; Gerges and Affouard, 2015), kinetics and structural (the complexity to rebuild the bond networks between molecules after melting) (Baird et al., 2012). None of these different parameters can be neglected when it comes to fully understand the GFA of a compound or its crystallization propensity.

Based on the presence or absence of crystallization upon a cyclic heat-cool-heat protocol, Baird and coworkers proposed a classification system established on a set of 51 molecular compounds (Baird et al., 2010). The set of molecules is classified into class I (class I (A), class I (B)), class II, and class III as a function of their GFA. From this classification, 12H (whatever the ee) could be considered as a class I (A) molecular compound, which means it would inevitably undergo crystallization upon moderate cooling (around 20 °C/min) or melt quenching in liquid N₂. As 12H system, class I molecules are usually of low molecular weight and present simple molecular structures with few flexible and rotating bonds (Baird et al., 2010). The structural resolution of enantiopure 12H has been reported previously by S. Beilles and co-authors (Beilles et al., 2001) and highlighted the presence of infinite H-bond chains along b-axis. These strong molecular ribbons (two H-bonds per molecule involving N1, O2 and N3, see Fig. 11) are held together by means of van der Waals contacts (Beilles et al., 2001), (Gervais et al., 2002). Moreover, the most probable flexible group (5-ethyl) is not implicated in the H-bond chain building. The crystallographic features of 12H match correctly with the previous ideas proposed by Baird and coworkers (Baird et al. 2010).

4.2. Thermal lag and glass transition

As presented above, the sample thickness was always less than 10 μm in all experiments. Furthermore, in the same experimental conditions, T_g value remained constant when increasing the sample mass from 19 ng up to 120 ng. For these reasons, the thermal lag effects on T_g were neglected. Independently of the enantiomeric composition, T_{g (onset)} = 16 ± 2 °C. Indeed, both enantiomers present the same scalar properties such as T_m, ΔH_m, T_g and ΔC_p. From Gordon Taylor Law reported in Eq. (3):

$$T_g(x) = \frac{xT_{gS} + (1-x)KT_{gR}}{x + (1-x)K}, \quad \text{where } K = \frac{\Delta C_{pR}}{\Delta C_{pS}} = 1 \quad (3)$$

It was demonstrated that, $T_g(x) = T_{gS} = T_{gR} = T_{gRS}$ (Coquerel and Tamura, 2016). Many experimental confirmations have been reported

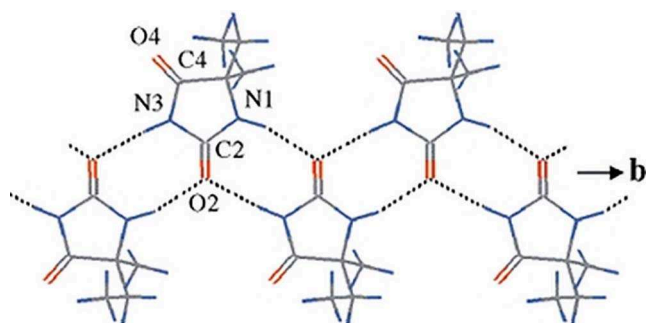


Fig. 11. Projection of the crystal structure of 12H along a-axis showing molecular ribbons running along the b-axis from C. Gervais et al. (2002).

in literature: limonene (Gallis et al., 2000), diprophylline (Viel et al., 2017) or ibuprofen (Kim et al., 2014). For the same cooling or heating conditions, T_g value was not impacted by the asymmetric property of chirality.

4.3. Impact of enantiomeric composition on GFA and crystallization propensity in the glassy state

FSC results suggested that 500 °C/s was not fast enough to completely skip the crystallization process in the case of enantiopure 12H. From DSC data upon cooling, one can assess that the degree of supercooling of pure enantiomer was higher than that of racemic mixture but still, this parameter cannot explain why upon cooling the pure enantiomer presented a poor GFA compared to racemic mixture. Considering that crystallization conjugates nucleation and crystal growth stages (that are temperature dependent processes), there is a temperature range at which the rate of crystallization is maximum. Consequently, nucleation and crystal growth temperature dependency curves overlap in that region. The Nucleation rate N (m⁻³s⁻¹) and crystal growth G (m s⁻¹) were high enough to produce supercritical nuclei and aggregation of the molecules (growth) respectively in such way that 500 °C/s was not fast enough to completely inhibit the crystallization of enantiopure 12H. By contrast, for the intermediate/scalemic compositions, crystallization was not evidenced upon cooling neither at 500 °C/s nor 300 °C/s. This fact highlights the role played by the counter enantiomer in the GFA of this conglomerate forming system. For numerous set of organic compounds (e.g. alkylamide derived from trans-1,2-bis(amino)cyclohexane, diprophylline), racemic mixture has a much higher propensity to crystallize compared to the enantiomeric counterpart (Coquerel and Tamura, 2016; Viel et al., 2017). It is important to notice that the racemic mixtures studied in the mentioned works crystallize as racemic compounds (i.e. both enantiomers crystallize in the same crystal lattice) like more than 90% of racemic species (Coquerel and Tamura, 2016). By contrast, racemic 12H is a conglomerate forming system (around 5% of racemic mixtures). In our case the counter enantiomer acts like an impurity (of the same chemical nature) which delays or inhibits the crystallization process. Therefore, at intermediate enantiomeric compositions, 12H will have a higher GFA when compared to that of the pure enantiomer. If this counter-enantiomer effect is assumed in the whole composition domain of the binary system, GFA should then increase as the composition approaches the racemic mixture (ee decreases). From a structural point of view both systems are identical, the implication of the counter enantiomer could then be analyzed from a thermodynamic angle. The presence of the counter enantiomer modifies the molecular environment of the melt, which results in a modification of the thermodynamic and kinetics properties related to crystallization.

Similar observations may be considered when heating the amorphous glasses. Indeed, due to steric hindrance effects, the required time for molecules of one enantiomer in the supercooled liquid to regain their crystalline configurations will be increased as the sample contains the two opposite enantiomers. Independently from the fact that pure enantiomer has a poor GFA compared to the scalemic composition, the temperature region where crystallization takes place was shifted towards higher temperatures with the counter-enantiomer for the same scanning rate. Furthermore, nucleation and crystal growth domains of pure enantiomer overlap in a large temperature interval of about 70 °C (from -10 °C up to 60 °C) while at the scalemic composition, the two processes can either be well separated or overlap in a temperature region of about 40 °C (from 10 °C up to 50 °C) accordingly to the equilibrium reached after recrystallization. This is consistent with the higher GFA of the scalemic sample compared to that of the pure enantiomer.

Pure enantiomer was proven to crystallize after short ageing time at T_g - 36 °C or T_g - 26 °C (See Supplementary Information: Glassy pure enantiomer). Even at this temperature range, where the structural bulk relaxation process is considered as frozen and only localized

movements are expressed, enantiopure 12H had enough molecular mobility to regain the crystalline state. Moreover, the fact that nucleation and growth processes merge at low temperatures ($T_g - 26^\circ\text{C}$) increases the probability for crystallization to occur well below T_g .

Nevertheless fast crystallization in the glassy state have been reported in literature for many molecular systems such as indomethacin (Wu and Yu, 2006), nifedipine (Zhu et al., 2008), griseofulvin (Yu, 2001), and *ortho*-terphenyl (Powell et al., 2015; Yu, 2016). This rapid crystallization process below T_g is usually attributed to the flimsy nature of the generated glassy material, which can easily promote crack formation (Descamps and Dudognon, 2014; Yu, 2016). Cracks can originate from deep quenching of the liquid for glass formation purposes (Powell et al., 2015; Willart et al., 2017). Fractures induce free surface that favored heterogeneous nucleation, consequently the activation barrier of nucleation, the interfacial energy and driving force of crystallization are lowered and rapid crystallization can therefore be facilitated at lower temperature (below T_g), (Descamps and Dudognon, 2014; Legrand et al., 1997; Willart et al., 2017). One important phenomenon that has also to be taken into account is the surface mobility that can help to amplify the process. It is well established that for many glassy molecular compounds the diffusion mechanism at the surface are higher than in the bulk for about 6 decades in magnitudes (Capaccioli et al., 2012; Powell et al., 2015; Yu, 2016; Zhu et al., 2010). Such cracks formation effects generating heterogeneous nucleation can be envisaged in enantiopure 12H.

By contrast to pure enantiomer behavior, the sample close to the racemic composition (scalemic sample) did not crystallize during the ageing process at the two ageing temperatures. During the ageing process, scalemic sample evolves irreversibly towards the metastable equilibrium state. This evolution is induced by a progressive loss of free volume, enthalpy and entropy acquired during the initial step of glass formation. The intense overshoot peak registered originated from the recovery of the loosen properties upon heating. At temperature where molecular mobility is high enough, enthalpy recovery takes place (Descamps and Willart, 2016). For this reason, the temperature region where the structural relaxation appears is shifted towards higher temperature compared to an unaged glass. Enthalpy recovery depend on the pair (T_a , t_a). As T_a evolves towards lower temperatures (highly deviate from T_g), molecular mobility in the glassy state becomes slower but the enthalpy and time needed to reach the supercooled liquid metastable equilibrium are greater. Accordingly, when T_a is close to T_g , equilibrium can be reached for short ageing time and enthalpy recovery magnitude is low. Indeed, to reach equilibrium, short annealing is insufficient when T_a deviates far from T_g . Therefore, enthalpy recovery intensity can also be low.

The equilibrium state (crystalline state) reached by enantiopure 12H after the ageing process is therefore physically different from the expected state (supercooled liquid state) reached by the scalemic sample. This evidenced the potential role played by chirality during the evolution from an out of equilibrium state towards equilibrium (stable or metastable) in such binary eutectic systems without detectable partial solid solution. The Scalemic sample aged at $T_g - 26^\circ\text{C}$ and $T_g - 36^\circ\text{C}$ reaches the metastable liquid state after 120 s and 10,800 s. This is confirmed by the fact that T_a and T_f values are equal after 120 s and 10,800 s for $T_a = T_g - 26^\circ\text{C}$ and $T_a = T_g - 36^\circ\text{C}$ respectively. Furthermore the enthalpy excess values are very intense almost 9 J/g for $T_a = -10^\circ\text{C}$ and 12.5 J/g for $T_a = -20^\circ\text{C}$. This behavior is quite surprising considering that at this temperature range molecular mobility is very low and the metastable liquid state is rarely reached. Nevertheless, even after short ageing time (60 s) high enthalpy recovery values (7.5 J/g) are obtained for T_a around $T_g - 28^\circ\text{C}$. Strangely, at this temperature range a maximum of nucleation is reported for scalemic 12H. Ageing of amorphous 12H therefore simultaneously produces a strong nucleation behavior and an intriguing intense overshoot peak. The conjugation of these two previous events may bring to some relevant questions. One may ask about the critical nucleation size and the

nature of such nucleation process at these low temperatures. The critical nucleation size must be extremely small. Under these conditions the reversion of a large part of the nuclei formed well below T_g can be expected at low temperature upon reheating. This effective melting could contribute to the intriguing large endothermic relaxation peak. Nonetheless, recent studies on physical ageing through FSC on amorphous polymeric systems have reported accelerated return towards equilibrium and high magnitude values of the overshoot peak during the ageing process (Koh et al., 2015, 2016; Monnier et al., 2017b; Simon and Koh, 2016). These effects are mostly due to the high cooling rate facilities provided by FSC and sample size. The initial glass formed upon high cooling rate possesses high enthalpy value and greater free volume compared to an amorphous glass formed by conventional DSC cooling rate facilities. High free volume is here required for an accelerated return towards the metastable equilibrium and high cooling rate provides this free volume during the early stages of glass formation.

The access to 12H amorphous states (only feasible by FSC) offered also new routes to isolate unknown crystalline phases. Indeed, annealing from $T_g - 66^\circ\text{C}$ up to $T_g - 26^\circ\text{C}$ and $T_g - 16^\circ\text{C}$ up to $T_g + 44^\circ\text{C}$ promoted the nucleation of two different crystalline forms with a melting point at $133^\circ\text{C} \pm 1^\circ\text{C}$ and $128^\circ\text{C} \pm 1^\circ\text{C}$ respectively. These equilibria obtained were not reported in the binary phase diagram between both enantiomers. Consequently, crystallization from the amorphous and supercooled liquid states may have revealed the existence of possible polymorphism, metastable racemic compound or metastable equilibria between the two enantiomers and this highlights the benefits of accessing to fleeting amorphous states by novel techniques such as FSC.

5. Conclusions

The investigation of the glassy state of 5-ethyl-5-methylhydantoin was successfully performed by FSC analyses. For the first time, the glassy state of 12H was reached, and its T_g value was determined: $T_{g(\text{onset})} = 16 \pm 2^\circ\text{C}$ (cooling 1000°C/s) regardless its enantiomeric composition.

Besides, this study revealed drastic limitations in the sampling procedure of Flash DSC device. Indeed, when dealing with physical mixtures, the overall composition could not be reproducibly maintained on the chip sensor. Other preparations or sampling routes (such as multiple dilutions of saturated solutions and evaporation of a droplet directly on the chip) should be envisaged to ensure defined compositions.

In the case of 12H, GFA was proven to be independent from the degree of undercooling. The poor GFA of 12H is related to the poor separation of the nucleation and crystal growth events in both pure enantiomer and scalemic composition. Nevertheless, FSC analyses highlighted that chirality clearly impacts GFA. Inversely from the behavior usually observed for racemic compounds, upon cooling, the pure enantiomer presented a higher crystallization propensity compared to the intermediate/scalemic composition. Therefore, samples containing both enantiomers could be easily vitrified compared to pure enantiomers. Upon heating, the counter-enantiomer acted like an impurity that delayed or inhibited recrystallization from the glassy state. In addition, the stability of the glasses was investigated by an ageing process. For the same ageing conditions, the initial glass formed evolves toward different equilibria. Ageing promotes a strong nucleation behavior in every sample and either crystallization or highly intense overshoot peak. When glassy pure enantiomer crystallizes during the ageing step, amorphous scalemic 12H evolves towards the metastable liquid equilibrium. A possible explanation involving cracks formation in the trigger of heterogeneous nucleation and fast surface crystallization was proposed in the case of enantiopure 12H.

Furthermore, different putative metastable equilibria around 130°C and 135°C previously unknown from the binary phase diagram

between both enantiomers have been highlighted. In particular, a metastable racemic compound may have recrystallized from the amorphous state but accurate tools such Second Harmonic Generation microscopy (to assess or not the centrosymmetry) would be required to confirm this hypothesis.

This study confirmed the large benefits brought by FSC to investigate molecular amorphous states (even with highly crystallogenic molecules) but also the limitations of the technique to investigate properly phase diagrams and metastable equilibria. The direct coupling between FSC and “classical” experimental techniques such as Secondary-Harmonic generation imaging Microscopy, Polarized Optical Microscopy, Temperature Resolved X-ray Diffraction would be interesting to draw a comprehensive view of the different equilibria (stable and metastable) in this binary chiral system.

6. Author contributions

The manuscript was written through contributions of all authors. All authors have given approval to the final version of the manuscript.

7. Notes

The authors declare no competing financial interest.

Acknowledgements

The authors are grateful to FEDER and Region Normandie for the financial support of this work through the FEDER MACHI project.

Appendix A. Supplementary data

Supplementary data associated with this article can be found, in the online version, at <http://dx.doi.org/10.1016/j.ijpharm.2018.01.050>.

References

- Alba, C., Busse, L.E., List, D.J., Angell, C.A., 1990. Thermodynamic aspects of the vitrification of toluene, and xylene isomers, and the fragility of liquid hydrocarbons. *J. Chem. Phys.* 92, 617–624. <http://dx.doi.org/10.1063/1.458411>.
- Amidon, G.L., Lennernäs, H., Shah, V.P., Crison, J.R., 1995. A theoretical basis for a biopharmaceutical drug classification: the correlation of in vitro drug product dissolution and in vivo bioavailability. *Pharm. Res.* 12, 413–420. <http://dx.doi.org/10.1023/A:1016212804288>.
- Baghel, S., Cathcart, H., Redington, W., O'Reilly, N.J., 2016. An investigation into the crystallization tendency/kinetics of amorphous active pharmaceutical ingredients: a case study with dipyrindamole and cinnarizine. *Eur. J. Pharm. Biopharm.* 104, 59–71. <http://dx.doi.org/10.1016/j.ejpb.2016.04.017>.
- Baird, J.A., Santiago-Quinonez, D., Rinaldi, C., Taylor, L.S., 2012. Role of viscosity in influencing the glass-forming ability of organic molecules from the undercooled melt state. *Pharm. Res.* 29, 271–284. <http://dx.doi.org/10.1007/s11095-011-0540-4>.
- Baird, J.A., Van Eerdenbrugh, B., Taylor, L.S., 2010. A classification system to assess the crystallization tendency of organic molecules from undercooled melts. *J. Pharm. Sci.* 99, 3787–3806. <http://dx.doi.org/10.1002/jps.22197>.
- Beilles, S., Cardinael, P., Ndzíé, E., Petit, S., Coquerel, G., 2001. Preferential crystallisation and comparative crystal growth study between pure enantiomer and racemic mixture of a chiral molecule: 5-ethyl-5-methylhydantoin. *Chem. Eng. Sci. Ind. Crystallisation* 56, 2281–2294. [http://dx.doi.org/10.1016/S0009-2509\(00\)00442-5](http://dx.doi.org/10.1016/S0009-2509(00)00442-5).
- Bhandari, B.R., Howes, T., 1999. Implication of glass transition for the drying and stability of dried foods. *J. Food Eng.* 40, 71–79. [http://dx.doi.org/10.1016/S0260-8774\(99\)00039-4](http://dx.doi.org/10.1016/S0260-8774(99)00039-4).
- Bhugra, C., Pikal, M.J., 2008. Role of thermodynamic, molecular, and kinetic factors in crystallization from the amorphous state. *J. Pharm. Sci.* 97, 1329–1349. <http://dx.doi.org/10.1002/jps.21138>.
- Cangialosi, D., Alegría, A., Colmenero, J., 2016. Cooling rate dependent glass transition in thin polymer films and in bulk. In: *Fast Scanning Calorimetry*. Springer, Cham, pp. 403–431. https://doi.org/10.1007/978-3-319-31329-0_13.
- Cangialosi, D., Boucher, V.M., Alegría, A., Colmenero, J., 2013. Physical aging in polymers and polymer nanocomposites: recent results and open questions. *Soft Matter* 9, 8619–8630. <http://dx.doi.org/10.1039/C3SM51077H>.
- Capaccioli, S., Ngai, K.L., Paluch, M., Prevosto, D., 2012. Mechanism of fast surface self-diffusion of an organic glass. *Phys. Rev. E Stat. Nonlin. Soft Matter Phys.* 86, 051503. <http://dx.doi.org/10.1103/PhysRevE.86.051503>.
- Coquerel, G., Tamura, R., 2016. “enantiomeric disorder” pharmaceutically oriented. In: Descamps, rc (Ed.), *Disordered Pharmaceutical Materials*. Wiley-VCH Verlag GmbH & Co. KGaA, pp. 135–160. <https://doi.org/10.1002/9783527652693.ch5>.
- Corvis, Y., Wurm, A., Schick, C., Espeau, P., 2015a. Vitreous state characterization of pharmaceutical compounds degrading upon melting by using fast scanning calorimetry. *J. Phys. Chem. B* 119, 6848–6851. <http://dx.doi.org/10.1021/acs.jpcc.5b03041>.
- Corvis, Y., Wurm, A., Schick, C., Espeau, P., 2015b. New menthol polymorphs identified by flash scanning calorimetry. *CrystEngComm* 17, 5357–5359. <http://dx.doi.org/10.1039/C5CE00697J>.
- Debenedetti, P.G., 1996. *Metastable Liquids: Concepts and Principles*. Princeton University Press.
- Debenedetti, P.G., Stillinger, F.H., 2001. Supercooled liquids and the glass transition. *Nature* 410, 259–267. <http://dx.doi.org/10.1038/35065704>.
- Descamps, M., Dudognon, E., 2014. Crystallization from the amorphous state: nucleation-growth decoupling, polymorphism interplay, and the role of interfaces. *J. Pharm. Sci.* 103, 2615–2628. <http://dx.doi.org/10.1002/jps.24016>.
- Descamps, M., Willart, J.-F., 2016. Some facets of molecular disorder in crystalline and amorphous pharmaceuticals. In: Descamps, rc (Ed.), *Disordered Pharmaceutical Materials*. Wiley-VCH Verlag GmbH & Co. KGaA, pp. 1–56. <https://doi.org/10.1002/9783527652693.ch1>.
- Descamps, M., Willart, J.F., Dudognon, E., Caron, V., 2007. Transformation of pharmaceutical compounds upon milling and commilling: the role of Tg. *J. Pharm. Sci.* 96, 1398–1407. <http://dx.doi.org/10.1002/jps.20939>.
- Dhotel, A., Rijal, B., Delbreilh, L., Dargent, E., Saiter, A., 2015. Combining Flash DSC, DSC and broadband dielectric spectroscopy to determine fragility. *J. Therm. Anal. Calorim.* 121, 453–461. <http://dx.doi.org/10.1007/s10973-015-4650-9>.
- Gallis, H.E., van Miltenburg, J.C., Oonk, H.A.J., 2000. Polymorphism of mixtures of enantiomers: a thermodynamic study of mixtures of D- and L-limonene. *Phys. Chem. Chem. Phys.* 2, 5619–5623. <http://dx.doi.org/10.1039/B005603K>.
- Gao, Y., Zhao, B., Yang, B., Schick, C., 2016. Fast Scanning Calorimetry of Phase Transitions in Metals. In: *Fast Scanning Calorimetry*. Springer, Cham, pp. 691–721. https://doi.org/10.1007/978-3-319-31329-0_21.
- Gerges, J., Affouard, F., 2015. Predictive calculation of the crystallization tendency of model pharmaceuticals in the supercooled state from molecular dynamics simulations. *J. Phys. Chem. B* 119, 10768–10783. <http://dx.doi.org/10.1021/acs.jpcc.5b05557>.
- Gervais, C., Beilles, S., Cardinael, P., Petit, S., Coquerel, G., 2002. Oscillating crystallization in solution between (+)- and (–)-5-Ethyl-5-methylhydantoin under the influence of stirring. *J. Phys. Chem. B* 106, 646–652. <http://dx.doi.org/10.1021/jp012622s>.
- Gunawan, L., Johari, G.P., Shanker, R.M., 2006. Structural relaxation of acetaminophen glass. *Pharm. Res.* 23, 967–979. <http://dx.doi.org/10.1007/s11095-006-9898-0>.
- Hancock, B.C., Parks, M., 2000. What is the true solubility advantage for amorphous pharmaceuticals? *Pharm. Res.* 17, 397–404. <http://dx.doi.org/10.1023/A:1007516718048>.
- Hancock, B.C., Shamblin, S.L., Zografi, G., 1995. Molecular mobility of amorphous pharmaceutical solids below their glass transition temperatures. *Pharm. Res.* 12, 799–806. <http://dx.doi.org/10.1023/A:1016292416526>.
- Kawakami, K., Harada, T., Yoshihashi, Y., Yonemochi, E., Terada, K., Moriyama, H., 2015. Correlation between glass-forming ability and fragility of pharmaceutical compounds. *J. Phys. Chem. B* 119, 4873–4880. <http://dx.doi.org/10.1021/jp509646z>.
- Kawakami, K., Usui, T., Hattori, M., 2012. Understanding the glass-forming ability of active pharmaceutical ingredients for designing supersaturating dosage forms. *J. Pharm. Sci.* 101, 3239–3248. <http://dx.doi.org/10.1002/jps.23166>.
- Kim, T.H., Shibata, T., Kojima, S., Shin, D.-M., Hwang, Y.-H., Ko, J.-H., 2014. Comparison of thermal and elastic properties of glassy racemic and enantiomeric ibuprofen studied by Brillouin light scattering and modulated differential scanning calorimetry. *Curr. Appl. Phys.* 14, 965–969. <http://dx.doi.org/10.1016/j.cap.2014.05.001>.
- Koh, Y.P., Gao, S., Simon, S.L., 2016. Structural recovery of a single polystyrene thin film using Flash DSC at low aging temperatures. *Polymer* 96, 182–187. <http://dx.doi.org/10.1016/j.polymer.2016.04.047>.
- Koh, Y.P., Grassia, L., Simon, S.L., 2015. Structural recovery of a single polystyrene thin film using nanocalorimetry to extend the aging time and temperature range. *Thermochimica Acta Chip Calorimetry* 603, 135–141. <http://dx.doi.org/10.1016/j.tca.2014.08.025>.
- Kovacs, A.J., Stratton, R.A., Ferry, J.D., 1963. Dynamic mechanical properties of polyvinyl acetate in shear in the glass transition temperature range. *J. Phys. Chem.* 67, 152–161. <http://dx.doi.org/10.1021/j100795a037>.
- Kozdras, A., Golovchak, R., Shpotyuk, O., Szymura, S., Saiter, A., Saiter, J.-M., 2011. Light-assisted physical aging in chalcogenide glasses: dependence on the wavelength of incident photons. *J. Mater. Res.* 26, 2420–2427. <http://dx.doi.org/10.1557/jmr.2011.264>.
- LAB SYS-DSC 8500-N5340501 [WWW Document], n.d. PerkinElmer. URL <http://www.perkinelmer.com/product/dsc-8500-lab-system-n5340501> (accessed 7.6.17).
- Legrand, V., Descamps, M., Alba-Simionesco, C., 1997. Glass-forming meta-toluidine: a thermal and structural analysis of its crystalline polymorphism and devitrification. *Thermochim. Acta* 307, 77–83. [http://dx.doi.org/10.1016/S0040-6031\(97\)00271-2](http://dx.doi.org/10.1016/S0040-6031(97)00271-2).
- Magoni, A., Wurm, A., Schick, C., Pangloli, P., Zivanovic, S., Skotnicki, M., Pyda, M., 2015. Reprint of “Heat capacity and transition behavior of sucrose by standard, fast scanning and temperature-modulated calorimetry”. *Thermochimica Acta Chip Calorimetry* 603, 149–161. <http://dx.doi.org/10.1016/j.tca.2014.12.013>.
- Mathot, V., Pyda, M., Pijpers, T., Vanden Poel, G., van de Kerkhof, E., van Herwaarden, S., van Herwaarden, F., Leenaers, A., 2011. The Flash DSC 1, a power compensation twin-type, chip-based fast scanning calorimeter (FSC): first findings on polymers. *Thermochimica Acta Special Issue: Interplay between Nucleation, Crystallization, and the Glass Transition* 522, 36–45. <http://dx.doi.org/10.1016/j.tca.2011.02.031>.
- Miyazaki, T., Yoshioka, S., Aso, Y., Kawanishi, T., 2007. Crystallization rate of amorphous

- nifedipine analogues unrelated to the glass transition temperature. *Int. J. Pharm.* 336, 191–195. <http://dx.doi.org/10.1016/j.ijpharm.2006.11.052>.
- Monnier, X., Maigret, J.-E., Lourdin, D., Saiter, A., 2017a. Glass transition of anhydrous starch by fast scanning calorimetry. *Carbohydr. Polym.* 173, 77–83. <http://dx.doi.org/10.1016/j.carbpol.2017.05.042>.
- Monnier, X., Saiter, A., Dargent, E., 2017b. Physical aging in PLA through standard DSC and fast scanning calorimetry investigations. *Thermochim. Acta* 648, 13–22. <http://dx.doi.org/10.1016/j.tca.2016.12.006>.
- Monnier, X., Saiter, A., Dargent, E., 2017c. Vitriification of PLA by fast scanning calorimetry: towards unique glass above critical cooling rate? *Thermochim. Acta* 658, 47–54. <http://dx.doi.org/10.1016/j.tca.2017.10.019>.
- Moynihan, C.T., Macedo, P.B., Montrose, C.J., Montrose, C.J., Gupta, P.K., DeBolt, M.A., Dill, J.F., Dom, B.E., Drake, P.W., Eastale, A.J., Elterman, P.B., Moeller, R.P., Sasabe, H., Wilder, J.A., 1976. Structural relaxation in vitreous materials*. *Ann. N. Y. Acad. Sci.* 279, 15–35. <http://dx.doi.org/10.1111/j.1749-6632.1976.tb39688.x>.
- Nagapudi, K., Jona, J., 2008. Amorphous active pharmaceutical ingredients in preclinical studies: preparation, characterization, and formulation. *Curr. Bioact. Compd.* 4, 213–224. <http://dx.doi.org/10.2174/157340708786847852>.
- Ndzié, E., Cardinael, P., Petit, M.N., Coquerel, G., 1999. Enantiomeric resolution of (+/-)-5-ethyl-5-methylhydantoin by means of preferential nucleation. *Enantiomer* 4, 97–+.
- Powell, C.T., Xi, H., Sun, Y., Gunn, E., Chen, Y., Ediger, M.D., Yu, L., 2015. Fast crystal growth in o-terphenyl glasses: a possible role for fracture and surface mobility. *J. Phys. Chem. B* 119, 10124–10130. <http://dx.doi.org/10.1021/acs.jpcc.5b05389>.
- Rey, L., 2016. Freeze-drying/lyophilization of pharmaceutical and biological products, Third Edition. CRC Press.
- Saiter, A., Couderc, H., Grenet, J., 2007. Characterisation of structural relaxation phenomena in polymeric materials from thermal analysis investigations. *J. Therm. Anal. Calorim.* 88, 483–488. <http://dx.doi.org/10.1007/s10973-006-8117-x>.
- Schammé, B., Couvrat, N., Malpeli, P., Dudogon, E., Delbreilh, L., Dupray, V., Dargent, E., Coquerel, G., 2016. Transformation of an active pharmaceutical ingredient upon high-energy milling: a process-induced disorder in Biclptomol. *Int. J. Pharm.* 499, 67–73. <http://dx.doi.org/10.1016/j.ijpharm.2015.12.032>.
- Schammé, B., Monnier, X., Couvrat, N., Delbreilh, L., Dupray, V., Dargent, E., Coquerel, G., 2017. Insights on the physical state reached by an active pharmaceutical ingredient upon high-energy milling. *J. Phys. Chem. B* 121, 5142–5150. <http://dx.doi.org/10.1021/acs.jpcc.7b02247>.
- Schawe, J.E.K., 2015. Measurement of the thermal glass transition of polystyrene in a cooling rate range of more than six decades. *Thermochimica Acta, Chip Calorimetry* 603, 128–134. <http://dx.doi.org/10.1016/j.tca.2014.05.025>.
- Schawe, J.E.K., Pogatscher, S., 2016. Material Characterization by Fast Scanning Calorimetry: Practice and Applications. In: Schick, C., Mathot, V. (Eds.), *Fast Scanning Calorimetry*. Springer International Publishing, pp. 3–80. https://doi.org/10.1007/978-3-319-31329-0_1.
- Schick, C., Androsch, R., 2016. New insights into polymer crystallization by fast scanning chip calorimetry. In: *Fast Scanning Calorimetry*. Springer, Cham, pp. 463–535. https://doi.org/10.1007/978-3-319-31329-0_15.
- Shamim, N., Koh, Y.P., Simon, S.L., McKenna, G.B., 2015. The glass transition of trinitrotoluene (TNT) by flash DSC. *Thermochim. Acta* 620, 36–39. <http://dx.doi.org/10.1016/j.tca.2015.10.003>.
- Simon, C., Zhang, Y., Wilde, G., 2016. Nucleation kinetics analyses of deeply undercooled metallic liquids by fast scanning calorimetry. In: *Fast Scanning Calorimetry*. Springer, Cham, pp. 661–689. https://doi.org/10.1007/978-3-319-31329-0_20.
- Simon, S.L., Koh, Y.P., 2016. The glass transition and structural recovery using flash DSC. In: *Fast Scanning Calorimetry*. Springer, Cham, pp. 433–459. https://doi.org/10.1007/978-3-319-31329-0_14.
- Surana, R., Pyne, A., Suryanarayanan, R., 2004. Effect of aging on the physical properties of amorphous trehalose. *Pharm. Res.* 21, 867–874. <http://dx.doi.org/10.1023/B:PHAM.0000026441.77567.75>.
- Turnbull, D., 1969. Under what conditions can a glass be formed? *Contemp. Phys.* 10, 473–488. <http://dx.doi.org/10.1080/00107516908204405>.
- van Herwaarden, S., Iervolino, E., van Herwaarden, F., Wijffels, T., Leenaers, A., Mathot, V., 2011. Design, performance and analysis of thermal lag of the UFS1 twin-calorimeter chip for fast scanning calorimetry using the Mettler-Toledo Flash DSC 1. *Thermochimica Acta, Special Issue: Interplay between Nucleation, Crystallization, and the Glass Transition* 522, 46–52. <http://dx.doi.org/10.1016/j.tca.2011.05.025>.
- Variankaval, N., Cote, A.S., Doherty, M.F., 2008. From form to function: crystallization of active pharmaceutical ingredients. *AIChE J.* 54, 1682–1688. <http://dx.doi.org/10.1002/aic.11555>.
- Vasconcelos, T., Marques, S., das Neves, J., Sarmiento, B., 2016. Amorphous solid dispersions: rational selection of a manufacturing process. *Adv. Drug Deliv. Rev. Amorphous Pharmaceutical Solids* 100, 85–101. <http://dx.doi.org/10.1016/j.addr.2016.01.012>.
- Viel, Q., Brandel, C., Cartigny, Y., Eusébio, M.E.S., Canotilho, J., Dupray, V., Dargent, E., Coquerel, G., Petit, S., 2017. Crystallization from the amorphous state of a pharmaceutical compound: impact of chirality and chemical purity. *Cryst. Growth Des.* 17, 337–346. <http://dx.doi.org/10.1021/acs.cgd.6b01566>.
- Willart, J.F., De Gussemme, A., Hemon, S., Descamps, M., Leveiller, F., Rameau, A., 2002. Vitriification and polymorphism of trehalose induced by dehydration of trehalose dihydrate. *J. Phys. Chem. B* 106, 3365–3370. <http://dx.doi.org/10.1021/jp012836+>.
- Willart, J.F., Descamps, M., 2008. Solid state amorphization of pharmaceuticals. *Mol. Pharmaceutics* 5, 905–920. <http://dx.doi.org/10.1021/mp800092t>.
- Willart, J.F., Dudogon, E., Mahieu, A., Eddleston, M., Jones, W., Descamps, M., 2017. The role of cracks in the crystal nucleation process of amorphous griseofulvin. *Eur. Phys. J. Spec. Top.* 226, 837–847. <http://dx.doi.org/10.1140/epjst/e2016-60358-y>.
- Wu, T., Yu, L., 2006. Surface crystallization of indomethacin below Tg. *Pharm Res* 23, 2350–2355. <http://dx.doi.org/10.1007/s11095-006-9023-4>.
- Yoshioka, M., Hancock, B.C., Zografi, G., 1994. Crystallization of indomethacin from the amorphous state below and above its glass transition temperature. *J. Pharm. Sci.* 83, 1700–1705. <http://dx.doi.org/10.1002/jps.2600831211>.
- Yu, L., 2016. Surface mobility of molecular glasses and its importance in physical stability. *Adv. Drug Deliv. Rev. Amorphous Pharmaceutical Solids* 100, 3–9. <http://dx.doi.org/10.1016/j.addr.2016.01.005>.
- Yu, L., 2001. Amorphous pharmaceutical solids: preparation, characterization and stabilization. *Adv. Drug Deliv. Rev. Character. Solid State* 48, 27–42. [http://dx.doi.org/10.1016/S0169-409X\(01\)00098-9](http://dx.doi.org/10.1016/S0169-409X(01)00098-9).
- Yu, L., Mishra, D.S., Rigsbee, D.R., 1998. Determination of the glass properties of D-Mannitol using sorbitol as an impurity. *J. Pharm. Sci.* 87, 774–777. <http://dx.doi.org/10.1021/js970224o>.
- Zhu, L., Jona, J., Nagapudi, K., Wu, T., 2010. Fast surface crystallization of amorphous griseofulvin below Tg. *Pharm. Res.* 27, 1558–1567. <http://dx.doi.org/10.1007/s11095-010-0140-8>.
- Zhu, L., Wong, L., Yu, L., 2008. Surface-enhanced crystallization of amorphous nifedipine. *Mol. Pharmaceutics* 5, 921–926. <http://dx.doi.org/10.1021/mp8000638>.
- Zhuravlev, E., Schick, C., 2010a. Fast scanning power compensated differential scanning nano-calorimeter: 1. The device. *Thermochimica Acta* 505, 1–13. <http://dx.doi.org/10.1016/j.tca.2010.03.019>.
- Zhuravlev, E., Schick, C., 2010b. Fast scanning power compensated differential scanning nano-calorimeter: 2. Heat capacity analysis. *Thermochimica Acta* 505, 14–21. <http://dx.doi.org/10.1016/j.tca.2010.03.020>.



Chirality impact on physical ageing: An original case of a small organic molecule

Bienvenu Atawa^{a,b}, Nicolas Couvrat^b, Gérard Coquerel^b, Eric Dargent^a, Allisson Saiter^{a,*}

^a Normandie Univ, UNIROUEN Normandie, INSA Rouen, UMR CNRS 6634, Groupe de Physique des Matériaux, 76801 Saint Etienne du Rouvray, France

^b Normandie Univ, UNIROUEN Normandie, EA3233, Sciences et Méthodes Séparatives, 76821 Mont Saint Aignan, France

ARTICLE INFO

Article history:

Received 29 March 2018

Received in revised form 25 May 2018

Accepted 31 May 2018

Available online 1 June 2018

Keywords:

Organic compounds

Physical ageing

Differential scanning calorimetry

Fast scanning calorimetry

Chirality

ABSTRACT

The purpose of this paper is to investigate the structural relaxation of N-acetyl- α -methylbenzylamine (Nac-MBA), a chiral organic molecule, through the study of the glass transition temperature T_g and the well-known physical ageing, occurring at temperatures lower than T_g . The influence of the enantiomeric excess (ee) on the structural relaxation kinetics is highlighted through standard differential scanning calorimetry (DSC) and fast scanning calorimetry (FSC) investigations. This original work evidences that even if the enthalpy loss to reach equilibrium remains globally the same whatever the ee, the structural relaxation kinetics are clearly slowed down when ee is increased.

© 2018 Elsevier B.V. All rights reserved.

1. Introduction

The physical ageing is a well-known natural phenomenon occurring when a glass is maintained during a certain time below its glass transition temperature. The thermal signature of this physical phenomenon (corresponding to an endothermic peak) is more or less intensive, depending on the ageing duration t_a and on the gap between the glass transition temperature T_g and the temperature at which the glass is maintained T_a . Using physical ageing signature to reveal the thermal history and the thermal stability of a glass is a common procedure as proven by the recent literature on this topic [1–5]. Furthermore, knowing the physical ageing process is essential for predicting the time-dependent behavior of glassy systems, particularly if they are used under their glass transition temperature for a long time. One of the main relevant parameter related to the physical ageing is the enthalpy loss calculated by integrating the difference between the scans of aged and rejuvenated sample according to the following equation:

$$\Delta H(T_a, t_a) = \int_{T_1}^{T_2} [C_p^a(T) - C_p^r(T)] \cdot dT \quad (1)$$

in which $C_p^a(T)$ and $C_p^r(T)$ are the specific heat of aged and rejuvenated samples respectively, and T_1 and T_2 are arbitrary temperatures below and above T_g . Under the assumption that ther-

modynamic equilibrium is reached for an infinite aging time, the expected enthalpy loss ΔH_∞ extrapolated from the equilibrium melt depends on T_a , T_g and on the heat capacity step ΔC_p of the sample, according to the following relation:

$$\Delta H_\infty = \Delta C_p \cdot (T_g - T_a) \quad (2)$$

Reaching or not the equilibrium state after a very long ageing time duration is still matter of debate in the scientific community [6–11]. Andreozzi et al. [12] explained that the equilibrium state cannot be reached in the case of high molecular weight PMMA because of the chain entanglement. The influence of chain entanglement and steric hindrance on the enthalpy loss is also the hypothesis used in the entropic model proposed by J.L. Gomez Ribelles to explain that the equilibrium state cannot be reached [13]. However, using the fast scanning calorimetry (FSC) has proven the possibility to reach the equilibrium state in acceptable times on the experimental scale [14–17]. This phenomenon is clearly explained by the fact that FSC investigations accelerate the kinetics of physical aging.

The aim of this work is to investigate the structural relaxation of N-acetyl- α -methylbenzylamine (Nac-MBA), a chiral organic compound derivative from α -methylbenzylamine (a widely used chiral resolving agent for optical resolution [18]), through the study of T_g and the physical ageing process. In the specific case of the Nac-MBA, the enantiomeric excess (i.e. the absolute difference between the mole fractions of each enantiomer, noted ee) influence on the structural relaxation kinetics have been highlighted.

* Corresponding author.

E-mail address: allisson.saiter@univ-rouen.fr (A. Saiter).

2. Materials and methods

2.1 Materials

Optically pure and racemic Nac-MBA were synthesized by acetylation of α -methylbenzylamine purchased from Aldrich (99%) using either acetic anhydride or acetyl chloride (for more details see [supplementary information: Materials](#)). Samples of several ee were prepared by physical mixtures of both enantiomers. For example, an ee = 0% contains the same amount of both enantiomers (i.e. racemic), when an ee = 100% is enantiomerically pure.

2.2 Differential scanning calorimetry analysis

DSC experiments were launched with a Perkin Elmer 8500. Cooling was ensured by a refrigerated cooling system (IntraCooler II). The temperature and enthalpy calibrations were achieved using indium and benzophenone as reference materials. Measurements were performed with 5 mg of material under nitrogen gas flow. Ageing was performed 5 °C below T_g for different ageing duration t_a (from 1 to 720 min) after a rejuvenation cycle (sample heated above T_g and cooled down to T_a at 20 °C/min). After the isothermal ageing, the sample is cooled below T_a , i.e. -70 °C, at 20 °C/min, and heated at the same rate above T_g , in regards to record the aged glass signal. The same cycle is repeated to record the unaged glass signal.

2.3 Fast scanning calorimetric measurements

FSC analyses were performed using a power compensation twin-type chip-based fast scanning calorimeter Flash DSC 1

(Mettler Toledo) equipped with a Huber TC100 intra-cooler. The specific calibration procedure for this tool is detailed in ref [17]. The samples were placed on the sensitive area of a MultiSTAR UFS 1 MEMS chip sensor. A thin layer of silicone oil has been used, promoting adhesion of the sample onto the chip and improving thermal contact. Samples were continuously flushed with a gaseous nitrogen flow. Sample masses (few ten nanograms) were estimated by normalizing the heat capacity jump at T_g with the value obtained from classical DSC measurements. As well explained in ref [17] it is not easy to perfectly master the ee value during sample preparation for FSC experiments. Ageing was performed 6 °C below T_g for different ageing duration t_a (0.01 s–14400 s) after a rejuvenation cycle (sample heated above T_g and at 1000 °C/s down to T_a). After the isothermal ageing, the sample is cooled below T_a , i.e. -70 °C, at 1000 °C/s, and heated at 1000 °C/s above T_g to record the aged glass signal. The same cycle is repeated to record the unaged glass signal.

3. Results and discussion

Fig. 1 shows normalized heat flow curves recorded during heating ramps from DSC experiments. Expected behavior is obtained, i.e. an endothermic peak superimposed to the heat capacity step at T_g , with an increasing amplitude and shifting towards higher temperatures when the ageing duration increasing from 0 up to 720 min. Whatever the enantiomeric excess, the same behavior is observed.

Fig. 2 shows FSC curves obtained after in-situ ageing performed at $T_a = T_g - 6$ °C. As ageing duration increases, the endothermic peaks superimposed to heat capacity step at T_g are shifted towards

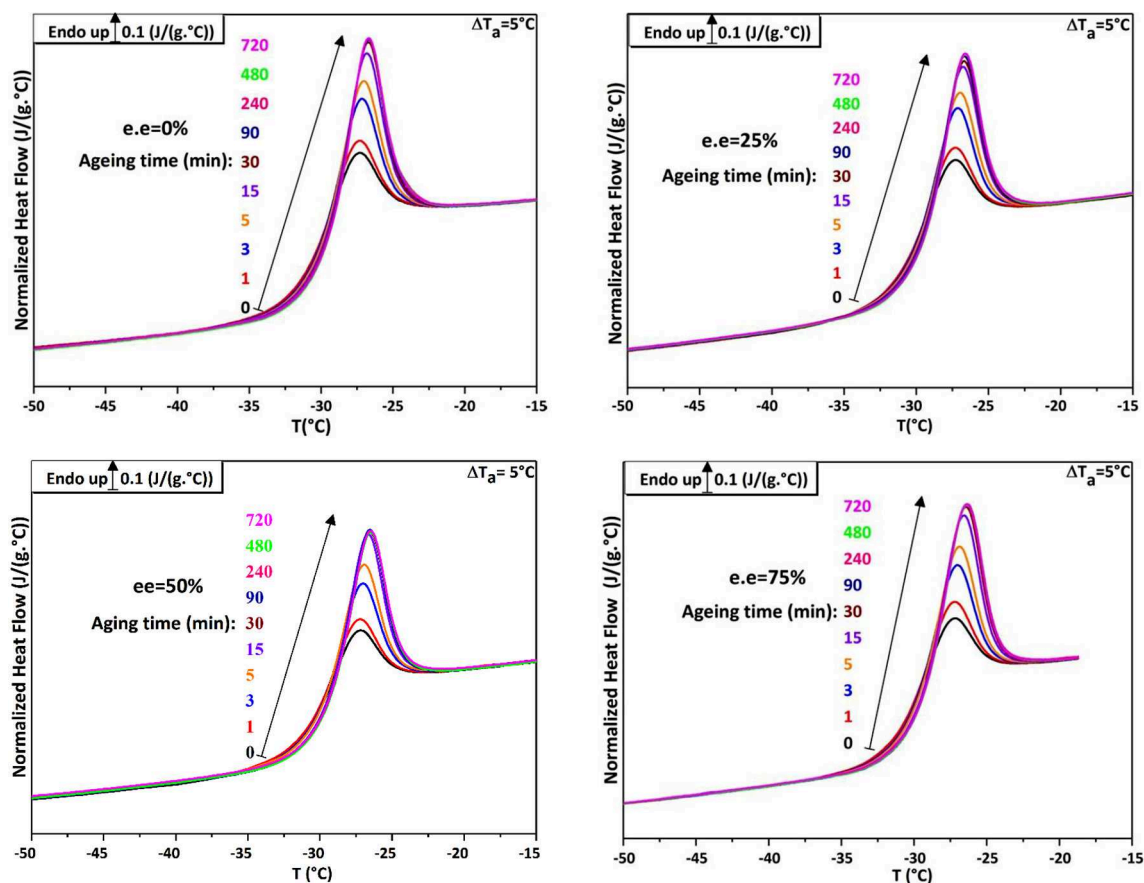


Fig. 1. DSC experiments: Normalized Heat Flow curves recorded during heating ramps after isothermal ageing as a function of ee%. $\Delta T_a = (T_g - T_a) = 5$ °C with $T_g = -32 \pm 0.5$ °C.

high temperatures with an increasing magnitude as expected. We may note that the glass transition zone shifting in comparison to DSC experiments is classically observed from FSC experiments due to the very high heating rate used.

Fig. 3 (top) gives the evolution of the difference between the ΔH_{∞} calculated from Eq. (2) and ΔH_t depending on the ageing duration calculated from Eq. (1). Concerning the reaching of equilibrium state, a clear difference is observed between the

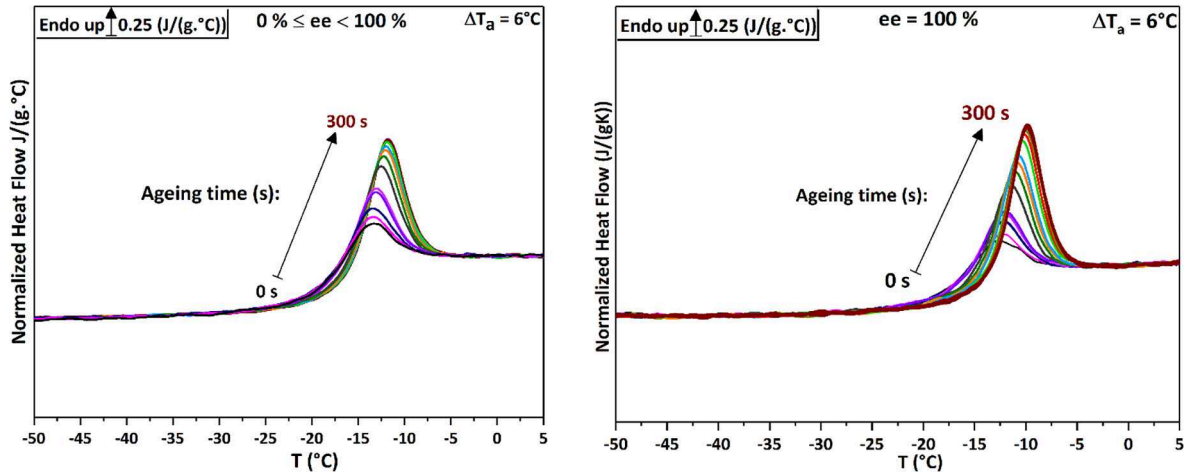


Fig. 2. FSC experiments: Normalized heat flow curves recorded after physical ageing during heating ramps as a function of ee. $\Delta T_a = (T_g - T_a) = 6^\circ\text{C}$ with $T_g = -22 \pm 0.5^\circ\text{C}$.

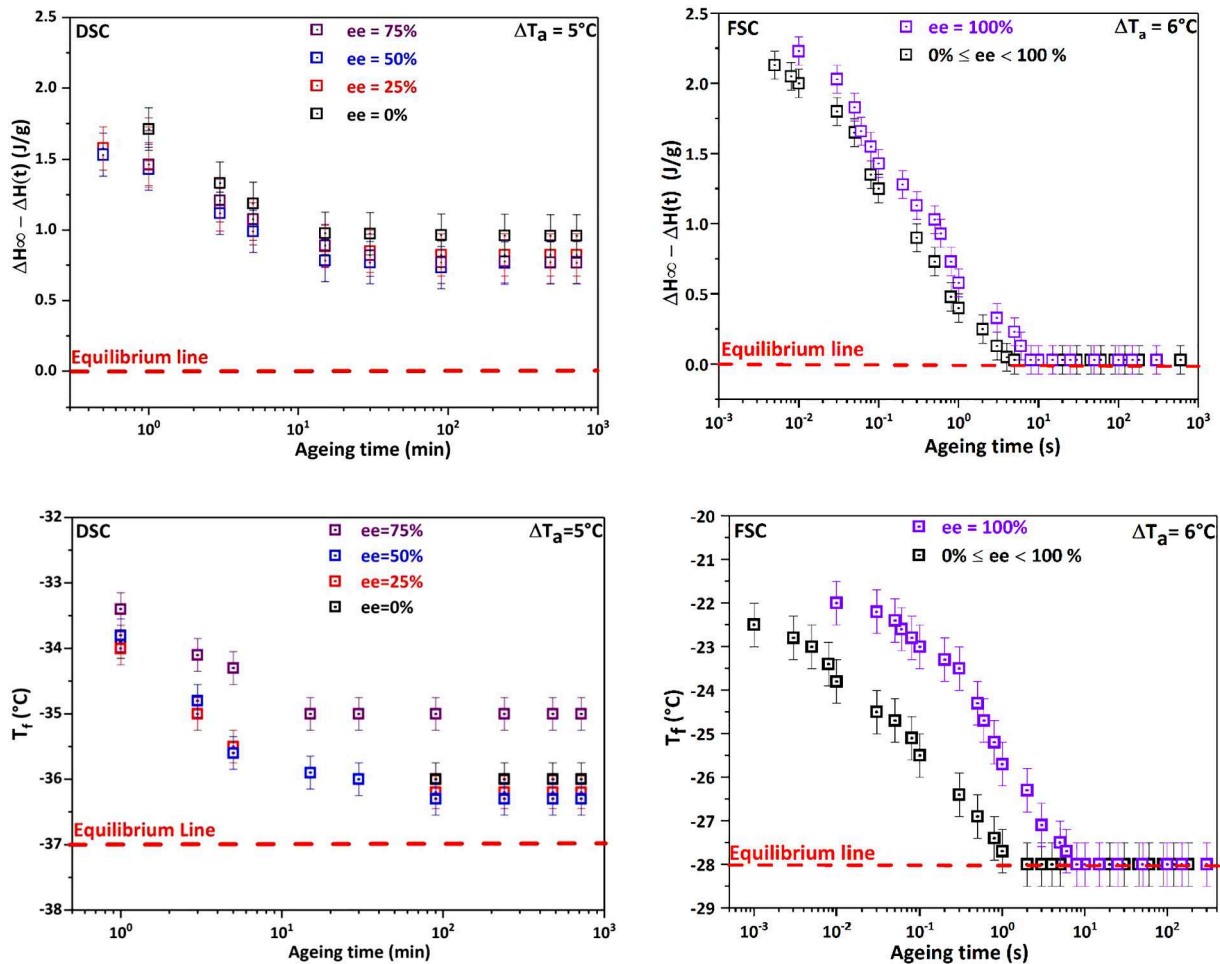


Fig. 3. FSC and DSC experiments. On the top: Time evolution of the difference between ΔH_{∞} and ΔH_t for the aged samples in function of ee. On the bottom: Time evolution of the fictive temperature in function of ee.

experiments performed by DSC (left) and those performed by FSC (right): as expected, FSC experiments allow reaching the equilibrium line as explained in literature [14–17]. Unfortunately, according to the error bars it is not possible to highlight a tendency concerning the ee influence on the enthalpy loss. Fig. 3 (bottom) shows the time evolution of the fictive temperature T_f in function of ee. The T_f concept has been introduced by Tool in 1931 and defines the temperature at which any properties, related to the structural relaxation, are at the equilibrium state [19,20]. T_f is calculated from the heating curves using the “equal area rule” method [20]. According to this concept, the equilibrium state is reached when T_f is equal to T_a . This allows us to confirm that FSC experiments are consistent since $T_f = -28\text{ °C} = T_g - 6\text{ °C}$ at the equilibrium state as shown in Fig. 3 (bottom – right). Concerning the influence of ee, we observe in Fig. 3 (bottom-right) that, for a same ageing duration t_a , the gap between T_f and the equilibrium line is greater for ee = 100% than for $0 < ee < 100\%$. Thus, the ee seems to slow down the structural relaxation kinetics during the physical ageing. Thus, we can conclude that the enthalpy loss needed to reach the equilibrium does not depend on ee (similar variations in terms of gap between ΔH_∞ and ΔH_t), but the velocity to reach this equilibrium is ee dependent.

4. Conclusion

The physical ageing process of N-acetyl- α -methylbenzylamine (Nac-MBA) was investigated by thermal analyses. Through FSC investigations, we have shown that the equilibrium state can be reached even if it seemed not possible from DSC investigations. Furthermore, as far as we know, this is the first study highlighting that: i) as expected (T_g and ΔC_p being ee independent) the enthalpy loss needed to reach the equilibrium for a chiral amorphous glass is independent from the enantiomeric excess (ee), whereas ii) the velocity to reach this equilibrium is ee dependent.

Acknowledgments

The authors are grateful to FEDER and Region Normandie for the financial support of this work through FEDER MACHI project.

Appendix A. Supplementary data

Supplementary data associated with this article can be found, in the online version, at <https://doi.org/10.1016/j.matlet.2018.05.133>.

References

- [1] J.-L. Adam, X. Zhang, *Chalcogenide Glasses: Preparation Properties and Applications*, Woodhead Publishing, 2014.
- [2] B.C. Hancock, S.L. Shamblyn, G. Zograf, *Pharm. Res.* 12 (1995) 799–806, <https://doi.org/10.1023/A:1016292416526>.
- [3] J.M. Hutchinson, P. Cortés, *Polym. Test.* 65 (2018) 480–490, <https://doi.org/10.1016/j.polymertesting.2017.12.024>.
- [4] C. Ma, W.J. Koros, *J. Membr. Sci.* 551 (2018) 214–221, <https://doi.org/10.1016/j.memsci.2018.01.049>.
- [5] A. Saiter, C. Devalencourt, J.M. Saiter, J. Grenet, *Eur. Polym. J.* 37 (2001) 1083–1090, [https://doi.org/10.1016/S0014-3057\(00\)00242-1](https://doi.org/10.1016/S0014-3057(00)00242-1).
- [6] L. Grassia, Y.P. Koh, M. Rosa, S.L. Simon, *Macromolecules* (2018), <https://doi.org/10.1021/acs.macromol.7b02277>.
- [7] Y.P. Koh, S. Gao, S.L. Simon, *Polymer*. 96 (2016) 182–187, <https://doi.org/10.1016/j.polymer.2016.04.047>.
- [8] H.Y. Zhao, Y.P. Koh, M. Pyda, S. Sen, S.L. Simon, *J. Non-Cryst. Solids* 368 (2013) 63–70, <https://doi.org/10.1016/j.jnoncrysol.2013.02.025>.
- [9] R. Golovchak, A. Kozdras, V. Balitska, O. Shpotyuk, *J. Phys. Condens. Matter.* 24 (2012), <https://doi.org/10.1088/0953-8984/24/50/505106> 505106.
- [10] J. Grenet, E. Bouthegourd, A. Esposito, A. Saiter, J.M. Saiter, *Philos. Mag.* 93 (2013) 2932–2946, <https://doi.org/10.1080/14786435.2013.793482>.
- [11] A. Saiter, M. Hess, N.A. D'Souza, J.M. Saiter, *Polymer* 43 (2002) 7497–7504, [https://doi.org/10.1016/S0032-3861\(02\)00631-6](https://doi.org/10.1016/S0032-3861(02)00631-6).
- [12] L. Andreozzi, M. Faetti, M. Giordano, D. Palazzuoli, F. Zulli, *Macromolecules* (2003), <https://doi.org/10.1021/ma0347870>.
- [13] M.S. Sánchez, Y. Touzé, A. Saiter, J.M. Saiter, J.L.G. Ribelles, *Colloid Polym. Sci.* 283 (2005) 711–720, <https://doi.org/10.1007/s00396-004-1207-z>.
- [14] R. Pilar, P. Honcová, G. Schulz, C. Schick, J. Málek, *Thermochim. Acta* 603 (2015) 142–148, <https://doi.org/10.1016/j.tca.2014.09.026>.
- [15] Y.P. Koh, L. Grassia, S.L. Simon, *Thermochim. Acta* 603 (2015) 135–141, <https://doi.org/10.1016/j.tca.2014.08.025>.
- [16] X. Monnier, A. Saiter, E. Dargent, *Thermochim. Acta* 648 (2017) 13–22, <https://doi.org/10.1016/j.tca.2016.12.006>.
- [17] B. Atawa, N. Couvrat, G. Coquerel, E. Dargent, A. Saiter, *Int. J. Pharm.* 540 (2018) 11–21, <https://doi.org/10.1016/j.ijpharm.2018.01.050>.
- [18] S. Druot, M.N. Petit, S. Petit, G. Coquerel, N.B. Chanh, *Mol. Cryst. Liq. Cryst. Sci. Technol. Sect. Mol. Cryst. Liq. Cryst.* 275 (1996) 271–291, <https://doi.org/10.1080/10587259608034081>.
- [19] I.M. Hodge, Adam-Gibbs, *J. Res. Natl. Inst. Stand. Technol.* 102 (1997) 195–205, <https://doi.org/10.6028/jres.102.015>.
- [20] C.T. Moynihan, P.B. Macedo, C.J. Montrose, C.J. Montrose, P.K. Gupta, M.A. Debolt, J.F. Dill, B.E. Dom, P.W. Drake, A.J. Easteal, P.B. Elterman, R.P. Moeller, H. Sasabe, J.A. Wilder, *Structural relaxation in vitreous materials*, *Ann. N.Y. Acad. Sci.* 279 (1976) 15–35, <https://doi.org/10.1111/j.1749-6632.1976.tb39688.x>.



Cite this: DOI: 10.1039/c8cp04880k

Molecular mobility of amorphous *N*-acetyl- α -methylbenzylamine and Debye relaxation evidenced by dielectric relaxation spectroscopy and molecular dynamics simulations†

 Bienvenu Atawa,^{ab} Natália T. Correia,^{id c} Nicolas Couvrat,^{id b} Frédéric Affouard,^{id *c} Gérard Coquerel,^b Eric Dargent,^{id a} and Allisson Saiter,^{id a}

The present work focusses on the molecular mobility characterization of amorphous *N*-acetyl- α -methylbenzylamine (Nac-MBA) by Broadband Dielectric Relaxation Spectroscopy (DRS) coupled with Fast Scanning Calorimetry (FSC) and Molecular Dynamics (MD) simulations covering over 12 decades in the frequency range. This study reveals another example of a secondary amide that shows a very intense Debye-like contribution (almost 90% of the global dielectric intensity) in addition to the structural α -relaxation and secondary Johari–Goldstein β -relaxation. The D- and α -relaxations are separated by about one decade (in frequency) and their relaxation times follow a near parallel temperature evolution (Vogel–Fulcher–Tammann–Hesse). The micro-structure of Nac-MBA has been investigated from MD simulations. It is shown that the intense Debye-like process emanates from the formation of linear intermolecular H-bonding aggregates (precursors of the crystalline structure) generating super-dipole moments.

 Received 31st July 2018,
Accepted 3rd December 2018

DOI: 10.1039/c8cp04880k

rsc.li/pccp

1. Introduction

Glass forming materials are omnipresent in our daily life and play an essential role in modern technology. Their physical understanding is still controversial and remains an unsolved problem of condensed matter physics.^{1,2} One of the most intriguing phenomena is the extraordinary increase of the structural relaxation time in the supercooled liquid state when approaching the glass transition temperature (T_g), the non-Debye character of the frequency or time domain response and the non-Arrhenius behavior of the temperature dependence.^{3–8} The dynamical behavior of glass-forming liquids and thus of their relaxational processes covers a wide range of time scales from local vibrations to highly cooperative motions as the temperature approaches T_g .⁹ When it comes to molecular mobility investigation of glass forming liquids or disordered systems exhibiting a permanent dipole moment, Dielectric Relaxation Spectroscopy (DRS) remains one of the most powerful and useful tools to achieve this goal.^{10–17}

Generally, for most glass forming liquids, the main process localized at the lowest frequency is recognized as the structural

relaxation process (α -relaxation) associated with the dynamics of the glass transition and molecular cooperative motions in an environment of a few nanometers.^{7,18–20} The frequency and temperature dependency of dielectric features of the α -relaxation present a non-Debye and non-Arrhenius character respectively. However, some glass formers display a slower dielectric relaxation than the α -process with a Debye-like behavior and a non-Arrhenius temperature dependency of the relaxation times.

The so-called D-process has been observed in many hydrogen-bonded liquids such as water,^{21,22} monohydroxy alcohols,^{9,23–28} secondary amides, *N*-mono-substituted amides,^{29–32} and pharmaceuticals.^{12,33–35}

Furthermore, for monohydroxy alcohols and secondary amides, the dielectric strength usually exceeds by several orders of magnitude the expected value predicted from the molecular dipole moment basis.^{23,29} Surprisingly, the D-process does not contribute to the calorimetric signature^{36,37} although it has a very intense dielectric response. Likewise, viewed from earlier shear mechanical spectroscopy experiments, no significant contribution to the mechanical shear signal was associated with the D-process. Since then, Gainaru *et al.*³⁸ evidenced by high resolution shear mechanical spectroscopy the mechanical signature of the D-process in two monohydroxy alcohols close to the glass transition region. Moreover, the rheological behavior is similar to what is observed for short chain polymers.³⁸ Nevertheless, the origin of the D-process has been a matter of

^a Normandie Univ, UNIROUEN, INSA Rouen, CNRS, GPM, 76000 Rouen, France

^b Normandie Univ, UNIROUEN, SMS, 76000 Rouen, France

^c Univ Lille, CNRS, UMR 8207, UMET, Unité Matériaux et Transformations, F59000 Villeneuve d'Ascq, France. E-mail: frederic.affouard@univ-lille.fr

† Electronic supplementary information (ESI) available. See DOI: 10.1039/c8cp04880k

discussion for many decades and still remains an unsolved puzzle in condensed matter physics.^{24,39–41} In H-bonded liquids, the D-process often originates from structural correlation between several dipoles.⁴² Numerous models have been proposed to explain the microscopic origin of the D-process in these systems: wait and switch models of dipole reorientation^{25,43,44} (breaking of H-bonds in a chain and formation of a new chain leading to end-to-end fluctuations of the dipole moment), dipole inversion by cooperative rotation of the OH-groups⁴⁵ and the self-restructuring transient-chain model, where molecules break off from or add to the ends of the chain promoting slow rotations of the effective dipoles of the chain.⁴⁶ So far, none of these models can give a universal account of the origin of the Debye behavior. Thus, a more fundamental and predictive model is still expected.⁴² Nevertheless, the postulated models figure out the important role played by H-bonds in the expression of the D-process.

In order to shed some light on the microscopic origin of the peculiar D-process, we have performed a thorough combined investigation of the physical properties of an H-bond (HB) glass forming liquid, *N*-acetyl- α -methylbenzylamine, C₁₀H₁₃NO (Fig. 1), by means of Dielectric Relaxation Spectroscopy (DRS), Temperature Modulated Differential Scanning Calorimetry (TMDSC), Fast Scanning Calorimetry (FSC), and Molecular Dynamics (MD) simulations. *N*-Acetyl- α -methylbenzylamine (Nac-MBA hereafter) is a chiral mono-substituted amide derivative from α -methylbenzylamine (a widely used chiral resolving agent for optical resolution procedures⁴⁷).

In this study the investigated Nac-MBA system (Fig. 1) is actually a mixture of 25% of the pure *R*(+) enantiomer with 75% of the counter *S*(-) enantiomer, since the optically pure enantiomers of Nac-MBA present an enhanced crystallization tendency (forthcoming paper).

2. Materials and methods

2.1 Synthesis of *R*(+) and *S*(-) Nac-MBA

Optically pure *R*(+) or *S*(-) Nac-MBA was obtained by acetylation of *R*(+) or *S*(-) α -methylbenzylamine purchased from Aldrich (99%) using acetyl chloride.^{48,49} The method (see ref. 50 for more details) consists of diluting the amine in dichloromethane and mixing the diluted solution with an aqueous solution of sodium

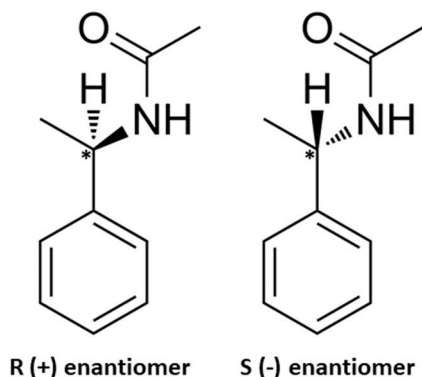


Fig. 1 Developed formula of Nac-MBA enantiomers.

carbonate initially prepared. A slight excess of diluted acetyl chloride in dichloromethane is slowly added to the previous solution. After stirring, the reaction mixture is decanted and the unreacted products are removed by successive washing with acid and basic aqueous solutions. The washed solution is dried with MgSO₄ and evaporated (yield almost 90%). The white solid obtained is doubly recrystallized from toluene or purified by column chromatography.⁵⁰

The mixture studied in the present work (25% *R*(+) plus 75% *S*(-)) corresponds to an enantiomeric excess, ee (*i.e.* the absolute difference between the mole fractions of each enantiomer), of 50%.

2.2 Temperature modulated differential scanning calorimetry (TMDSC)

TMDSC and conventional DSC analyses were carried out with a Q100 DSC from TA Instruments equipped with a refrigerated cooling system allowing cooling down to 203 K. All measurements were performed under a nitrogen gas flow of 50 mL min⁻¹. The baseline (empty cell) was calibrated at a chosen heating rate from 203 to 423 K. Temperature and enthalpy calibrations were achieved using indium and benzophenone as reference materials. An empty aluminum pan, identical to that used for the sample, was used as a reference. The specific heat capacity was calibrated using two sapphire discs as reference materials.

TMDSC experiments were carried out in the “heat only” modulation mode with (1) an oscillation amplitude of ± 0.318 K and oscillation period of 60 s, during heating at 2 K min⁻¹ and (2) an oscillation amplitude of ± 1 K and oscillation period of 60 s during heating at 0.5 K min⁻¹. The oscillation period refers to the time needed to complete one temperature modulation cycle.

The modulation scanning was performed on an initially amorphous sample obtained during previous cooling at 70 K min⁻¹ carried out in the conventional mode.

Sample preparation. In order to prepare the DSC samples with an enantiomeric excess of 50% of the *S*(-) enantiomer, 75 mg of *S*(-) Nac-MBA and 25 mg of *R*(+) Nac-MBA were manually ground in a mortar and 5 mg of this physical mixture was encapsulated in a *T*_{zero} aluminum pan. Each experiment was repeated at least twice using fresh samples.

2.3 Fast scanning calorimetry (FSC)

FSC measurements were conducted with a power compensation twin-chip, namely Flash DSC 1 (FSC) from Mettler-Toledo. Cooling was ensured down to 203 K by an intracooler model Huber TC100. Approximately 35 ng of sample was loaded onto the central position of a sensor chip using an optical microscope and a long fiber for sample positioning. The sample was submitted to a nitrogen purge gas flow at a rate of 20 mL min⁻¹. Successive conditioning and corrections of the chip sensor were performed according to the manufacturer and prior to measurements.⁵¹ As highlighted in previous work on FSC,⁵² it remains ambiguous to ensure an effective composition of ee = 50% even though the samples (dozens of ng) were taken from a 10 mg mixture of both enantiomers in such a way that the average ee = 50%. Here, we considered the ee as intermediate between enantiomerically pure and racemic compositions (*i.e.* scalemic).

The sample mass was estimated by comparing the amplitude of the heat capacity step at the glass transition with values obtained from classical DSC. A pre-melting step was performed to ensure a homogeneous distribution of the sample on the chip area. With regards to determining the cooling rate dependency of the fictive temperature T_f , a cyclic heat-cool thermal program was applied. This protocol consisted of quenching the liquid at different cooling rates from 1500 K s^{-1} down to 5 K s^{-1} followed by a heating scan at 1500 K s^{-1} . To ensure reproducibility, all measurements were performed at least twice.

2.4 Dielectric relaxation spectroscopy (DRS)

a. Low frequency range 0.1 Hz–1 MHz. Dielectric measurements were performed using high quality interdigitated gold plated electrodes, IE (BDS1410-20-150) purchased from Novocontrol GmbH. The electrode has round shape 20 mm diameter gold plated copper layers with $35 \mu\text{m}$ thickness and a comb structure for convenient sample attachment. The spacing between the comb fingers and their width are both $150 \mu\text{m}$. Prior to sample deposition, the electrode was calibrated by measuring its respective geometric (empty cell) capacity, C_0 , and substrate capacity, C_{su} , through measurement of a standard material with known permittivity (B-oil; Vacuubrand). As the substrate material of the IE has a low loss factor ($\tan \delta = 0.001$) and the substrate real part permittivity is approximately constant over frequency and temperature, the calibration procedure⁵³ can be simplified if the permittivity of the electrode substrate ϵ_{su}^* is approximated by a real constant ϵ_{su} . For a selected frequency, f (e.g. 10 kHz), the capacity of the empty electrode without sample material attached $C_e^*(f)$ and the capacity of the electrode with the calibration oil attached C_c^* (permittivity ϵ_s^*) are measured. The total capacity is determined considering that the upper and lower electrodes constitute two independent volumes generating two independent capacitors^{54,55} with a total capacity of:

$$C_m^* = C_0(\epsilon_s^*(f) + \epsilon_{\text{su}}(f)) \quad (1)$$

with

$$C_0 = \frac{C_c^*(f) - C_e^*(f)}{\epsilon_c^*(f)} \quad (2)$$

The complex frequency-dependent permittivity $\epsilon^*(f) = \epsilon'(f) - i\epsilon''(f)$ (where ϵ' = storage permittivity and ϵ'' = loss permittivity) was measured over the range 10^{-1} Hz – 2 MHz using an Alpha-A analyzer from Novocontrol Technologies GmbH. Sample preparation and amorphization steps were performed *ex situ*. Almost 150 mg of the crystalline powder was deposited on the IE then heated above the liquidus temperature at 383 K and annealed for 5 minutes to guarantee complete melting. The melt was then promptly quenched in liquid nitrogen in order to ensure total amorphization (according to previous work by some of us on the amorphization conditions of Nac-MBA).⁵⁰ Dielectric spectra were collected isothermally from 153 K up to 273 K with suitable consecutive steps: measurements were performed from 241 K to 273 K with an increment of 1 K; for $T < 241 \text{ K}$ an increment of 2 or 5 K was considered.

b. High frequency range 1 MHz–1 GHz. Measurements were performed in the range 1 MHz–1 GHz by means of a coaxial line reflectometer based on the impedance analyzer HP 4191 from Novocontrol Technologies GmbH. Preceding the measurements, two successive calibration steps were achieved: line and sample cell calibrations. Samples were prepared in a parallel plate geometry between two gold-plated electrodes of 10 mm diameter, separated by silica spacers of $50 \mu\text{m}$ thickness. The prepared sample cell was connected to the end of the coaxial line, then melted *in situ* and annealed for 5 minutes at 383 K. Isothermal frequency scans were carried out upon cooling from 383 K down to 273 K, in steps of 10 K.

A Quatro Cryosystem (Novocontrol Technologies GmbH) was used to control the temperature with a stability of $\pm 0.2 \text{ K}$ for both low and high frequency domains.

c. Data analysis. In order to access the time scale of each of the four processes expressed in the Nac-MBA ($\epsilon_e = 50\%$) system, their temperature dependencies, the shape parameters, and the dielectric strength, the isothermal dielectric spectra (ϵ' and ϵ'') were fitted with a sum of Havriliak–Negami model functions⁵⁶ and a conductivity contribution for ϵ'' , written as follows:

$$\begin{aligned} \epsilon^*(\omega) &= \epsilon'(f) - i\epsilon''(f) \\ &= \epsilon_\infty + \sum_k^n \left[\frac{\Delta\epsilon_k}{(1 + i(2\pi f \tau_{\text{HN}k})^{\alpha_{\text{HN}k}})^{\beta_{\text{HN}k}}} \right] - i \left(\frac{\sigma_{\text{dc}}}{2\pi f \epsilon_0} \right)^N \end{aligned} \quad (3)$$

where σ_{dc} is the specific dc-conductivity; ϵ_0 the permittivity of the vacuum ($\epsilon_0 = 8.854 \times 10^{-12} \text{ F m}^{-1}$); f the frequency; N gives the exponent of the frequency dependence of ϵ'' ; k sums over the different relaxation processes, τ_{HN} is a characteristic relaxation time with regards to the frequency of maximal loss f_{max} ; ϵ is the dielectric relaxation strength of the process under investigation; and ϵ_∞ the high frequency limit of the real permittivity $\epsilon'(f)$. α_{HN} and β_{HN} are fractional shape parameters which detail the symmetric and asymmetric broadening of the complex dielectric response in such a way that $0 < \alpha_{\text{HN}}$, and $\alpha_{\text{HN}}\beta_{\text{HN}} \leq 1$.¹⁰ From the derived values of τ_{HN} , α_{HN} , and β_{HN} , a model free relaxation time τ of each relaxation process is given by:

$$\begin{aligned} \tau &= \frac{1}{2\pi f_{\text{max}}} \\ &= \tau_{\text{HN}} \left[\sin\left(\frac{\alpha_{\text{HN}}\pi}{2 + 2\beta_{\text{HN}}}\right) \right]^{\frac{-1}{\alpha_{\text{HN}}}} \left[\sin\left(\frac{\alpha_{\text{HN}}\beta_{\text{HN}}\pi}{2 + 2\beta_{\text{HN}}}\right) \right]^{\frac{-1}{\alpha_{\text{HN}}}} \end{aligned} \quad (4)$$

2.5 Molecular dynamics simulations (MD)

Molecular dynamics (MD) simulations have been performed using the DL_POLY package⁵⁷ and the GAFF force field (General Amber Force Field).⁵⁸ This force field was chosen due to its capability of reproducing successfully a large number of experimental data of low molecular weight molecules.⁵⁹ As recommended for the GAFF force field,⁵⁸ atomic partial charges were calculated from *ab initio* computations using the Gaussian 03 programme⁶⁰ at the HF/6-31G* level with the restrained electrostatic potential (RESP) fitting approach. For the electrostatic interactions, a pairwise damped shifted method developed by Wolf⁶¹

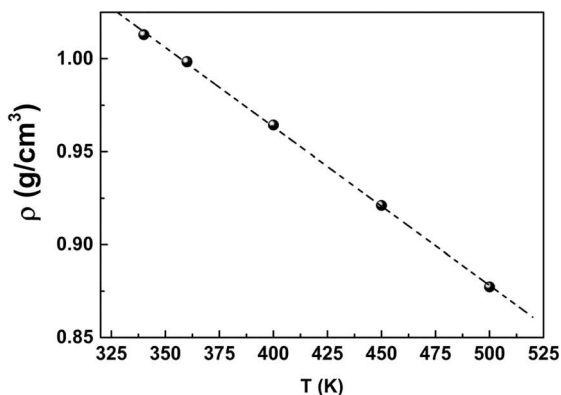


Fig. 2 Temperature evolution of the density of Nac-MBA (ee = 50%) determined from MD simulations.

was used. For both van der Waals and electrostatic interactions, the same cutoff radius of 10 Å was employed. Periodic boundary conditions were applied in all directions. The time step to integrate Newton's equation of motion was chosen to be 0.001 ps. The modelled system possesses a total number of $N = 64$ molecules composed of 48 $S(-)$ Nac-MBA and 16 $R(+)$ Nac-MBA molecules in order to obtain an enantiomeric excess of 50%. Simulations have been conducted either in the NPT or NVT statistical ensemble where P is the pressure, T the temperature and V the volume. Pressure and temperature were controlled with a Nosé–Hoover barostat and thermostat respectively. All NPT simulations were realized at atmospheric pressure. The Nosé–Hoover thermostat and barostat relaxation times have been set at 0.2 and 2.0 ps respectively. The equilibrated volume of the simulation box during the NPT simulation was considered to compute the average density of the system and used to perform the subsequent production simulation in the NVT ensemble. MD simulations were performed at five temperatures: 500 K, 450 K, 400 K, 360 K and 340 K. The equilibration/production times range from 10/200 ns to 20/800 ns from the highest to the lowest investigated temperature. The Nac-MBA densities determined in the present study are shown in Fig. 2. The monotonic behavior of the density as function of the temperature confirms that the system is equilibrated over the simulated times. The calculated density of the liquid extrapolated to a low temperature slightly below the glass transition temperature ($\rho(235 \text{ K}) = 1.1 \text{ g cm}^{-3}$) is consistent regarding the crystalline counterpart: $\rho = 1.13 \text{ g cm}^{-3}$.⁴⁷ Indeed, typically, the density of the glassy state is above 90% of the density of the crystal^{62–64} (i.e. $\rho = 1.017 \text{ g cm}^{-3}$).

3. Results and discussion

3.1 Thermal behavior characterization of Nac-MBA by TMDSC and FSC

Fig. 3a shows conventional DSC thermograms of a physical mixture of Nac-MBA (ee = 50%) for the first (curve 1) and the second (curve 2) heating scans at 2 K min^{-1} . When heating the crystalline powder mixture, three successive endotherms are evidenced and associated with the eutectoid ($T_{\text{eutectoid}} = 338 \text{ K}$),

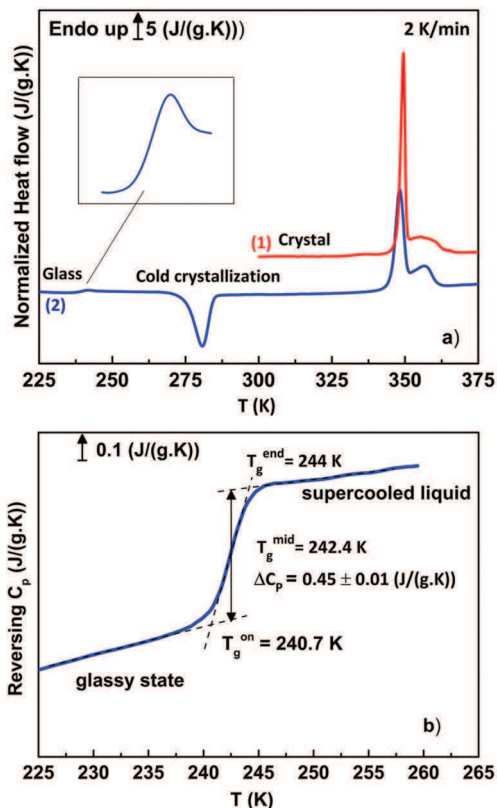


Fig. 3 (a) Thermal behavior (normalized total heat flow versus temperature) of Nac-MBA (ee = 50%) during heating at 2 K min^{-1} (standard DSC); (b) reversing specific heat capacity (C_p) as a function of temperature (at 2 K min^{-1}) in the glass transition domain (TMDSC).

eutectic ($T_e = 348 \text{ K}$) and liquidus ($T_L = 353 \text{ K}$) phenomena, respectively. At the eutectoid temperature, the physical mixture of both enantiomers (conglomerate) converges towards a co-crystal of both enantiomers (racemic compound). These results are in good agreement with the phase diagram between both enantiomers of Nac-MBA proposed in the work of Druot *et al.*⁴⁷ During liquid quenching from 383 K down to 203 K at *circa* 70 K min^{-1} (not shown) no sign of crystallization is observed. The subsequent heating scan (curve 2) shows the characteristic heat flow step for the calorimetric glass transition at *circa* 240 K along with the typical enthalpy recovery peak (zoom in insert). It is proof that an amorphous glass has been obtained during the earlier stage of melt quenching. Therefore, under this condition, Nac-MBA can be considered as a good glass forming liquid. Upon further heating well above T_g , cold-crystallization of the supercooled liquid is evidenced at $T_{\text{Cr}}^{\text{on}} = 273 \text{ K}$ ($\Delta H_{\text{Cr}} = 70 \pm 5 \text{ J g}^{-1}$). This exothermal peak is followed by a double endothermic event related to the eutectic and liquidus events of the corresponding racemic compound. No thermal event revealed the existence of the conglomerate equilibrium. Consequently, from the amorphous glassy state Nac-MBA (ee = 50%) evolves towards metastable equilibrium.

TMDSC allows one to measure the heat capacity and kinetic components (usually referred to as reversing and nonreversing components) of the total heat flow signal obtained in

conventional DSC.⁶⁵ Fig. 3b depicts the reversing specific heat capacity obtained for amorphous Nac-MBA upon heating at 2 K min^{-1} : the thermal glass transition region is very narrow with onset temperature $T_g^{\text{onset}} = 240.7 \text{ K}$ and T_g determined from the mid-step position $T_g^{\text{mid}} = 242.4 \text{ K}$. The heat capacity change at T_g is $\Delta C_p = 0.45 \pm 0.01 \text{ (J (g K)}^{-1})$. It is worth pointing out that while the crystallization ability is strongly impacted by the enantiomeric concentration (forthcoming communication), the glass transition temperature and ΔC_p are independent of the enantiomeric excess.⁵⁰

Fast scanning calorimetry is used to characterize the glass transition in terms of the variation of the fictive temperature over a wide range of cooling rates. The fictive temperature concept was introduced by Tool and Eiclitin⁶⁶ and defines the temperature at which any properties related to the structural relaxation are at the equilibrium state. Fig. 4 depicts the temperature evolution of the normalized heat flow during heating at rate $q_h = 1500 \text{ K s}^{-1}$, after several cooling scans with a rate (q_c) ranging from 5 K s^{-1} up to 1500 K s^{-1} . The enthalpy recovery peak observed in the glass transition region shifts towards higher temperatures and its magnitude increases with a decreasing cooling rate as classically observed in the literature for physical aging phenomena (for increasing aging time).^{67–69} When $q_c = q_h = 1500 \text{ K s}^{-1}$, T_g is shifted toward higher temperatures by more than 10 K compared to standard DSC results obtained for $q_h = 2 \text{ K min}^{-1} = 0.033 \text{ K s}^{-1}$. This shift is the expression of the kinetical character of the glass transition phenomenon observed for such a kind of thermal protocol.⁷⁰ The fictive temperature (T_f) calculation was performed according to the equal area rule method⁷¹ (details on the T_f calculation procedure are described in ref. 52). The change in the fictive temperature at variable cooling rates can be used to describe the temperature dependence of the structural α -relaxation.^{67,72,73} The empirical approach proposed by Frenkel–Kobeko–Reiner (FKR)⁷² illustrates the link between the cooling rate $q_c \text{ (K s}^{-1})$ and the structural relaxation time $\tau \text{ (s)}$ expressed as follows:

$$q_c \tau = C \quad (5)$$

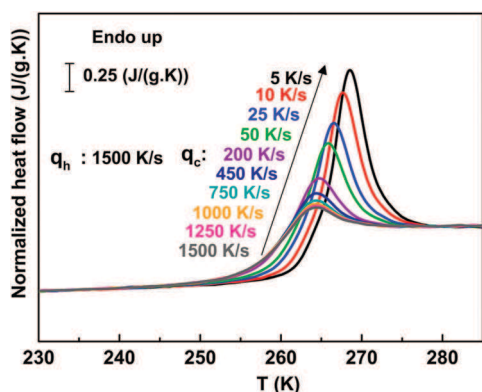


Fig. 4 FSC heating curves of Nac-MBA obtained at $q_h = 1500 \text{ K s}^{-1}$ after cooling from the supercooled liquid state down to the glassy state at cooling rate q_c ranging from 5 K s^{-1} to 1500 K s^{-1} .

where C (Kelvin) is a shift factor usually assume to be a constant.^{67,74} Consequently it should be considered that:

$$\log(q_c) = -\log(\tau) + \log(C) \quad (6)$$

This proposal is generally used to combine DSC and/or FSC data with features of the dynamic glass transition as probed by heat capacity or dielectric relaxation spectroscopy measurements.^{67,74–77} Superposition of the temperature dependence of the cooling rate and the dielectric α -relaxation time will be reported in the relaxation map (Fig. 9a); Section 3.2.2.

3.2 Molecular mobility of Nac-MBA (ee = 50%) probed by DRS

As highlighted by calorimetric results, amorphous glass Nac-MBA (ee = 50%) can be obtained by melt quenching. For dielectric characterization of the glassy and supercooled liquid state near and above T_g , the amorphous sample was prepared *ex situ* to guarantee a sufficiently high cooling rate in order to avoid crystallization. Measurements of the complex permittivity $\epsilon^*(f)$ were then performed isothermally, during heating, in the temperature range [153 K, 273 K] with a frequency scan from 0.1 Hz to 2 MHz for each selected temperature. Isothermal, high frequency (1 MHz–1 GHz) measurements of $\epsilon^*(f)$ were carried out when cooling the liquid from 383 K down to 283 K with regards to accessing the molecular mobility at higher temperatures in the supercooled and liquid state (see Experimental Section 2.4 for details).

3.2.1 Identification and analysis of dipolar relaxations.

The temperature dependence of the real permittivity ϵ' at some representative frequencies (taken from the isothermal dielectric data acquired upon heating) is shown in Fig. 5a. Near the calorimetric glass transition a frequency dependent step increase is observed. For temperatures higher than 260 K a steep decrease is visible in $\epsilon'(T)$. This drop in the dielectric permittivity is frequency independent and represents the manifestation of cold-crystallization. Melt crystallization was also observed at *circa* 273 K during the isothermal high frequency (RF) measurements (not shown). Therefore, in the following only the dielectric spectra obtained for the fully amorphous samples will be taken for analysis and discussion (*i.e.*, data taken at $260 \text{ K} < T < 283 \text{ K}$ are excluded). As shown in the inset of Fig. 5a, a very intense dielectric loss ϵ'' response is observed in the supercooled liquid, associated with the frequency dependent step ϵ' increase when the sample is heated from the glassy state. A close up of the $\epsilon''(T)$ trace at the lowest measured frequency (0.1 Hz) is depicted in Fig. 5b. A quick analysis of this spectrum using two Gaussian functions gives clear evidence for two relaxations: a very low intensity peak with a maximum at $T_{\text{max}} = 240.9 \text{ K}$ and a predominant one at $T_{\text{max}} = 246.3 \text{ K}$. For further information on these processes, Fig. 5c shows the first temperature derivative of the heat capacity $C_p'(T)$ curve. The real part of the complex heat capacity (C_p') of a system is related to the reversing heat capacity measured from TMDSC.^{15,78,79} The C_p' curve shown in the inset of Fig. 5c was obtained by TMDSC during heating at 0.5 K min^{-1} with an oscillation period of 60 s ($f = 1.7 \times 10^{-2} \text{ Hz}$). The use of such scanning conditions allows a thermal treatment (and time scale) that reasonably compares

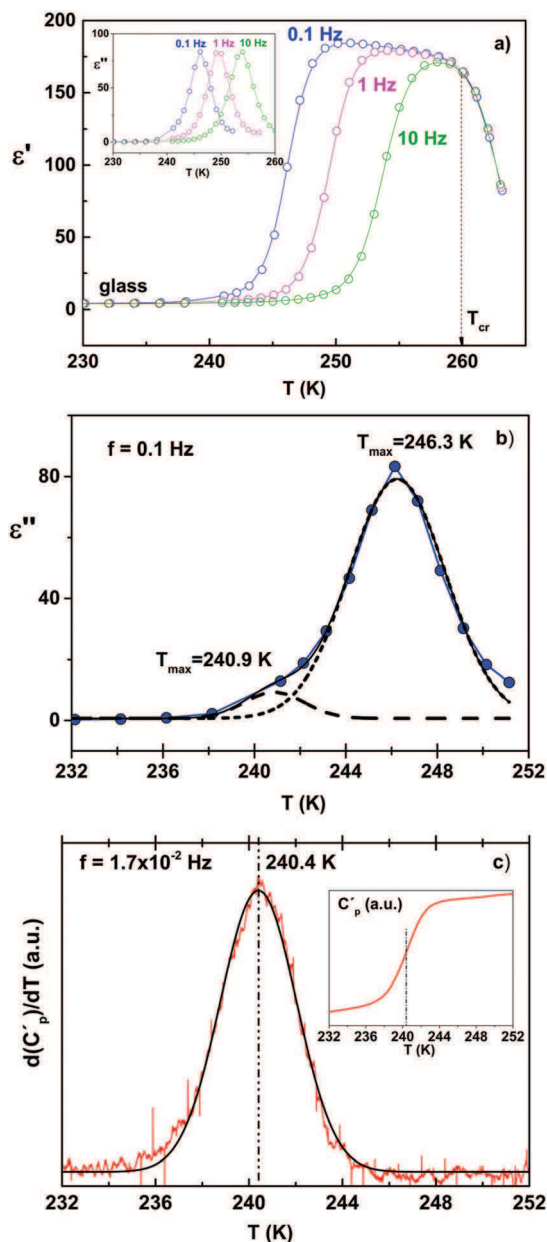


Fig. 5 (a) Temperature dependence of the real part of the complex permittivity (ϵ') and dielectric loss ϵ'' (insert) of Nac-MBA ($\epsilon_e = 50\%$) for the indicated frequencies. (b) $\epsilon''(T)$ for $f = 0.1$ Hz (circles) in the glass transition temperature range [232–252 K]. Solid line – global fit using two Gaussian functions (dashed lines). (c) First temperature derivative ($d(C_p')/dT$) of the C_p' curve shown in the inset (reversing heat capacity obtained by TMDSC upon heating at 0.5 K min^{-1} with temperature oscillation period 60 s = 1.7×10^{-2} Hz). Solid line: Gaussian curve fit to $d(C_p')/dT$ data.

to the dielectric relaxation experiments (equilibrium isothermal measurements were performed with temperature steps that correspond to an average heating rate of around 0.3 K min^{-1}). The temperature derivative of the $C_p'(T)$ curve (proportional to the imaginary component of the heat capacity, C_p'') is perfectly described by a single Gaussian function with a full width at half maximum (FWHM) of ~ 3.9 K and centered at $T_{\text{max}} = 240.4$ K. This temperature corresponds to the middle temperature of the

sigmoidal shaped $C_p'(T)$, *i.e.*, the kinetic glass transition temperature ($T_g^{\text{mid}} = 240.4 \pm 0.5$ K). The low temperature shoulder in the $\epsilon''(T)$ trace ($T_{\text{max}} = 240.9$ K; FWHM = 3 K) is clearly associated with the measurable change of heat capacity and therefore it is recognized as the signature of the structural (primary) α -relaxation. In spite of its high dielectric magnitude, the high temperature relaxation ($T_{\text{max}} = 246.3$ K, FWHM = 5 K) shows no calorimetric activity. Similar features are observed for hydrogen bonded liquids where a dominant Debye-like process (D -process) slower than the smaller α -relaxation is observed.^{31,32,38,41}

For the Nac-MBA system here studied the high amplitude relaxation is also identified as a D -process taking into account that its dielectric loss frequency dependency can be well described by a single Debye function as it is illustrated later on (Fig. 7b).

Fig. 6a depicts the dielectric loss spectra as a function of the frequency for Nac-MBA at given temperatures below the glass transition temperature. The asterisks are visual guides delimiting three clearly distinct dispersion regions labelled α -, β - and “ γ ”, in order of increasing frequency. As expected, at temperatures close to the dynamic glass transition ($T_g^{\text{mid}} = 240$ K; $f \sim 2 \times 10^{-2}$ Hz) the high frequency tail of the α -relaxation becomes visible in the available frequency range. At higher frequencies than the α -relaxation, a secondary β -process appears as a shoulder that clearly shifts towards higher frequencies as the temperature increases. Deep in the glassy state, the β -relaxation seems to leave the

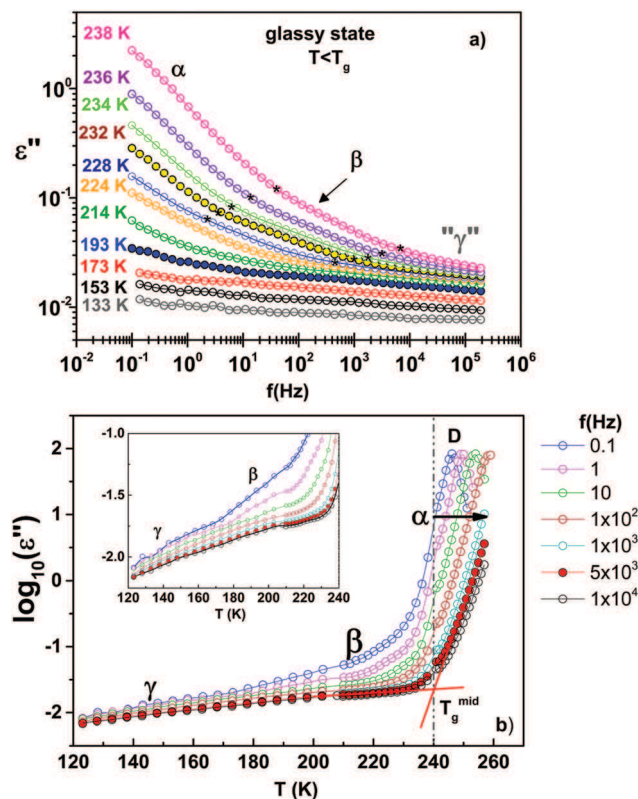


Fig. 6 (a) Frequency dependence of dielectric loss ϵ'' of glassy Nac-MBA ($\epsilon_e = 50\%$) at the indicated temperatures. Lines connect data points. (b) Temperature dependence of $\log_{10}(\epsilon'')$ at indicated frequencies (data taken from isothermal data). The insert shows a close up for $T < T_g^{\text{mid}} = 240$ K.

frequency range and only a very broad dispersion (“ γ ”-relaxation) remains. Fig. 6b shows the isochronal plot of $\log(\epsilon'')$ at chosen frequencies that gives further evidence for the appearance of this broad “ γ ”-relaxation at lower temperatures than the β -relaxation (see also the close up in the insert). For frequency $f = 5 \times 10^3$ Hz a crossover between the straight lines drawn to qualitatively describe the temperature dependence of $\epsilon''(T)$ of the β - and α -process occurs at *circa* 240 K, close to the glass transition temperature, T_g^{mid} . This feature is an indication of a Johari–Goldstein β -relaxation.⁸⁰

Fig. 7a and b show illustrative dielectric spectra (ϵ' and ϵ'' respectively) as a function of the available frequency range in

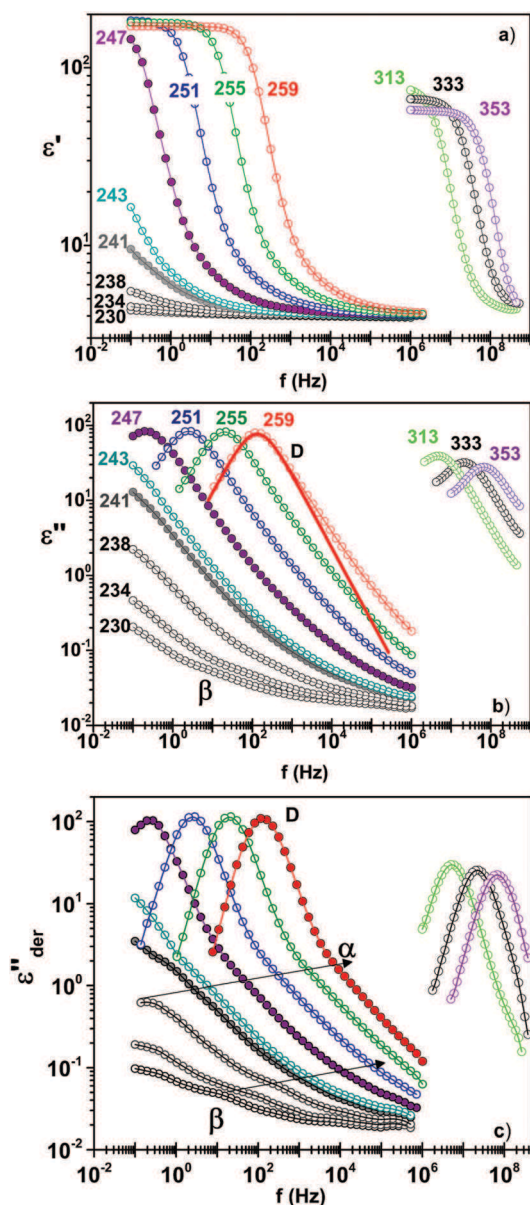


Fig. 7 Frequency dependence of (a) the real permittivity ϵ' , (b) dielectric loss and (c) conduction free dielectric loss ϵ''_{der} in the available frequency region [0.1 Hz–1 GHz] for the indicated temperatures given in Kelvin. Lines connect data points. In panel (b) the conductivity tail observed at lower frequencies than D-relaxation is omitted; the red solid line is the result of fitting a Debye function to the dielectric loss spectra at 259 K.

the glassy state slightly below T_g and in the supercooled liquid state. The slower D-relaxation visible as a step in ϵ' or as a very intense dielectric response ϵ'' (almost 90% of the dielectric strength) arises at temperatures above 246 K. At $T > 253$ K the dc conductivity (not shown for clarity reasons) rises at the lower frequency side of the D-process. In Fig. 7b it is shown that for $T = 259$ K a Debye curve (solid red line) matches only the low frequency side $f < 10^3$ Hz of the $\epsilon''(f)$ spectrum. The faster relaxation previously identified as the α -relaxation is somewhat obscured under the high-frequency flank of the large amplitude D-process. In order to improve the frequency resolution of the overlapping dielectric loss peaks, the derivative method developed by Wübbenhorst and van Turnhout⁸¹ is applied:

$$\epsilon''_{\text{der}} = -\frac{\pi}{2} \frac{\partial \epsilon'(f)}{\partial \ln(2\pi f)} \quad (7)$$

This method has the advantage of considerably improving the resolution of overlapping peaks and also suppressing Ohmic conduction because in that case ϵ' is independent of frequency.⁸¹ Fig. 7c shows that the α -relaxation appears much more clearly from the derivative expression in the intermediate frequency range between the slower D-process and the faster β -process. The conduction free dielectric loss ϵ''_{der} data were analyzed with a sum of derivative HN-functions in order to obtain the relaxation times corresponding to the frequency of maximal dielectric loss (f_{max}) for the D- and α -relaxations. The calculated parameters were then used as starting values for a fitting procedure resulting in a reliable description of the raw data using a sum of Debye ($\alpha_{\text{HN}} = 1$, $\beta_{\text{HN}} = 1$) and Cole–Cole ($\beta_{\text{HN}} = 1$) model functions (eqn (3)). For high temperatures, a dc conductivity contribution was also added to describe the raw dielectric loss data at the lower frequency side of the D-process.

An illustrative example of the fitting procedure used for a semi-quantitative analysis of the current data is given in Fig. 8 for $T = 259$ K. The D-process for $T > 246$ K is well described by a Debye model function ($\alpha_{\text{HN}} = 1$, $\beta_{\text{HN}} = 1$) corresponding to a

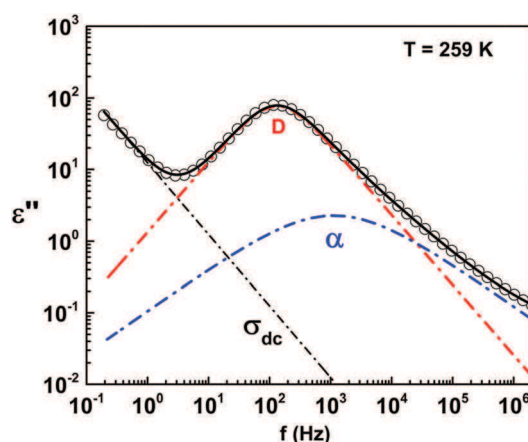


Fig. 8 Fitting procedure of the dielectric loss peak in the supercooled liquid at 259 K. The dash-dot lines represent the individual fitting functions (Cole–Cole for the α -relaxation and Debye for the D-process). Solid lines are the total fit functions (see text for details).

single exponential behavior in the time domain. Concerning the structural α -relaxation ($T > 241$ K) the parameter that quantifies the symmetric broadening remains constant in the supercooled liquid domain ($\alpha_{\text{HN}} = 0.59 \pm 0.01$). Normally, the fitting procedure permits one to derive information about the shape parameters, the dielectric strength and the relaxation time of the different processes. In the present case such a fitting procedure is somehow challenging and daring regarding poorly resolved or overlapping relaxation phenomena, and low magnitude processes. The uncertainties of the width parameters (and dielectric strengths) and their temperature dependencies obtained from the fits, especially for the β and γ relaxations, are rather large and must be taken as indicative (see the ESI†). The temperature dependence of the relaxation times is now presented and discussed.

3.2.2 Relaxation map. The temperature dependence of the relaxation time of all the four detected processes (Debye, α , β and γ)

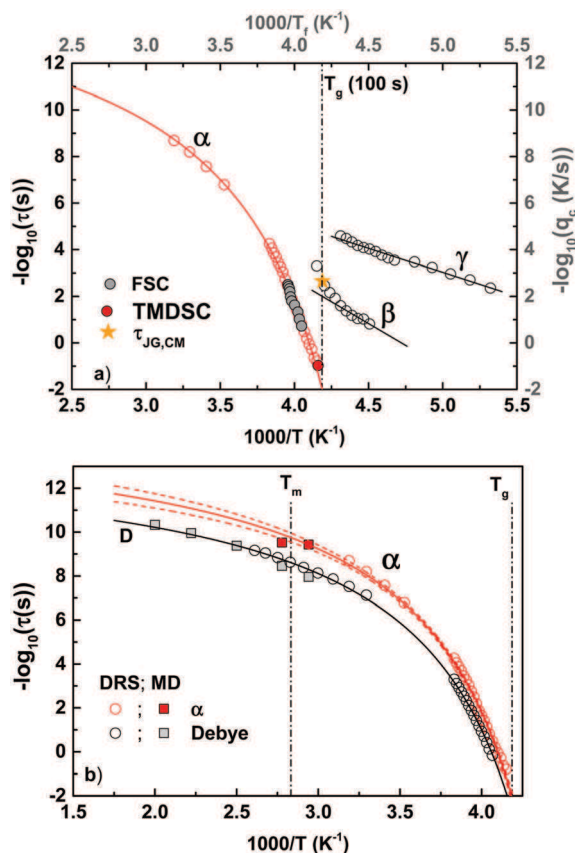


Fig. 9 (a) Relaxation map ($-\log\tau$ vs. $1000/T$) for the α -, β - and γ -relaxations of Nac-MBA probed by DRS (vertical left-hand axis). The red filled circle corresponds to the kinetic glass transition temperature ($T_g^{\text{mid}} = 240.4$ K; $\tau = 9.5$ s). The orange star is the JG relaxation time calculated at T_g using the CM (eqn (10)). The cooling rate ($-\log q_c$) as a function of the inverse of the fictive temperature (T_f) determined from FSC (filled grey circles) is shown on the vertical right-hand axis. (b) Relaxation map for the α - and Debye-like relaxations detected in the supercooled (above T_g) and liquid (above T_m) states from DRS (open circles) and MD simulations (filled squares). Solid lines are fits of the Arrhenius and VFTH equation to the corresponding data. Dashed lines in panel (b) are the 95% confidence limits of the VFTH fit to the α -relaxation.

Table 1 Fit parameters of the Arrhenius and VFTH functions used to describe the temperature evolution of the relaxation time of γ - and β -secondary relaxations and α - and D-processes respectively

$T < T_g$	E_a (kJ mol $^{-1}$)	τ_∞ (s)	
γ -Process	39.4 ± 1.5	$(6.6 \pm 4.5) \times 10^{-14}$	
β -Process	71.8 ± 8.0	$(5.37 \pm 5.36) \times 10^{-17}$	
$T > T_g$	B (K)	τ_∞ (s)	T_0 (K)
α -Process VFTH (DRS)	1310 ± 90	$(1.3 \pm 0.5) \times 10^{-14}$	203 ± 2
VFTH (DRS + MD)	1123 ± 66	$(8 \pm 2) \times 10^{-14}$	207 ± 2
D-Process VFTH	1024 ± 38	$(2.0 \pm 0.2) \times 10^{-12}$	209 ± 1

is summed up in the relaxation map ($-\log\tau$ vs. $1/T$) shown in Fig. 9. For the sake of simplicity and clarity, the Arrhenius plot will be analyzed from the glassy state towards the supercooled liquid. The evaluated parameters from the applied model functions (Arrhenius and VFTH) used to describe the temperature dependence of the relaxation times of the various processes are summarized in Table 1.

Molecular mobility below T_g : γ - and β -relaxations. As generally observed for localized, non-cooperative motions observed in the glassy state, the relaxation time of both γ - and β -processes follows a linear temperature dependence of $\log\tau$ vs. $1000/T$ well described by the Arrhenius relation:

$$\tau(T) = \tau_\infty \exp\left(\frac{E_a}{RT}\right) \quad (9)$$

where τ_∞ is the pre exponential factor, E_a the activation barrier energy and R the ideal gas constant. Given the value of the activation barrier energy of the γ -process ($E_a^\gamma \sim 39$ kJ mol $^{-1}$) it is reasonable to suggest that this secondary relaxation may originate from intramolecular, small angular fluctuations of polar side groups of Nac-MBA molecules that could persist deep in the glassy state. Nevertheless, it should also be mentioned that small amounts of impurities can also be at the origin of such a manifestation.⁸²

The higher activation energy found for the β -process ($E_a^\beta \sim 72$ kJ mol $^{-1}$) can be compatible with a complete rotation of the whole molecule as suggested for the β Johari–Goldstein (β_{JG}) process when analyzed in the framework of the Coupling Model (CM).⁸³

The temperature evolution of τ_β strongly deviates from Arrhenius behavior at the vicinity of T_g . This peculiar change of $\tau_\beta(T)$ has been highlighted for many glass formers,^{12,78,84,85} and it is recognized as a manifestation of the β_{JG} -process. According to the CM, the β_{JG} -process is considered as located near an independent or primitive motion (that implies the rotation of the whole molecule) precursor of the structural α -relaxation. The relaxation time of the β_{JG} process is approximately the same as that of the characteristic time of the primitive motion (τ_0) and correlated to τ_α through the following equation:

$$\tau_{\text{JG}}(T) \approx \tau_0(T) = t_c^n [\tau_\alpha(T)]^{1-n} \quad (10)$$

where n is the coupling parameter ($n = 1 - \beta_{\text{KWW}}$) and t_c is the time characterizing the crossover from independent to cooperative fluctuations proven to be close to $t_c = 2 \times 10^{-12}$ s for molecular glass formers.⁸⁶ From the experimental data it is very difficult to estimate a β_{KWW} value due to the poor frequency resolution of the α -relaxation in the dielectric loss spectrum. Though, a value $\beta_{\text{KWW}} = 0.66$ can be estimated from the obtained HN shape parameters of the structural α -relaxation ($\alpha_{\text{HN}} = 0.59$ and $\beta_{\text{HN}} = 1$) using the empirical relation proposed by Alegria and coworkers:⁸⁷

$$\beta_{\text{KWW}} \approx (\alpha_{\text{HN}}\beta_{\text{HN}})^{\frac{1}{1.23}} \quad (11)$$

Taking into account the β_{KWW} value in the CM relation and $\tau_\alpha = 100$ s at T_g , a value of $\tau_{\text{JG}}(T_g) = 2.22 \times 10^{-3}$ s is obtained. This value is in good agreement with the relaxation time derived from the analysis of the dielectric loss data as shown in Fig. 9a. We must note that the most obvious manifestation of this secondary relaxation (a weak shoulder in the dielectric loss peak) takes place in a very narrow temperature range (almost 15 K). These difficulties increase the uncertainties for a direct confirmation of the β_{JG} nature of this slower secondary process. Therefore, empirical approaches such as the proposal of Ngai and Capaccioli⁸⁸ can be applied:

$$\frac{E_a}{RT_g} = 2.303(2 - 13.7n - \log \tau_\alpha) \quad (12)$$

In the present case, the ratio $E_a/RT_g \sim 31.7$ is approximately identical to the second term of eqn (12), $2.303(2 - 13.7n - \log \tau_\alpha) \sim 29.8$. The apparent correlation of τ_β with τ_α , its change at T_g and the relationship of the activation energy of the β -process in the glassy state with T_g suggest that the detected β -relaxation in Nac-MBA is a genuine Johari–Goldstein β -process.

Molecular mobility above T_g : α -relaxation and the Debye-like process. Fig. 9a includes data obtained from TMDSC (red full circle) and FSC (gray full circles) techniques allowing comparison with the dielectric α -relaxation time τ_α (red open circles). For the FSC data, a vertical shift factor (after the FKR relation (eqn (5)), $\log C = 0.67 \pm 0.12$ or $C = (4.7 \pm 1.3)$ K, is necessary in order to superimpose the temperature dependence of the cooling rate ($-\log(q_c)$ vs. $1/T_f$) and the temperature behavior of the α -relaxation time ($-\log(\tau_\alpha)$ vs. $1/T$). For the temperature range common to calorimetric and dielectric techniques ([240 K; 253 K] – the TMDSC raw point is also included), a strong similarity of the slope of the two sets of data is clearly evidenced which without a doubt confirms the evaluation of τ_α using the fitting procedure described previously. The nonlinearity of the temperature dependence (or super-Arrhenius behavior) of the α -relaxation time is often described by the empirical Vogel–Fulcher–Tamman–Hesse (VFTH) equation given by:^{89–91}

$$\tau(T) = \tau_\infty \exp\left(\frac{B}{T - T_0}\right) \quad (13)$$

where τ_∞ is the value of the relaxation in the high temperature limit, B is an empirical parameter representative of the material that accounts for the deviation from linearity and T_0 is the

so-called Vogel temperature or ideal glass transition temperature ($0 \text{ K} < T_0 < T_g$). In the present case of Nac-MBA, the experimental data alone (Fig. 9a) or when combined with MD simulations (Fig. 9b) are fairly well described by a single VFTH function (see Table 1) with physically acceptable values of the pre-exponential factor corresponding to the phonon lifetime ($\tau_\infty \sim 10^{-14}$ – 10^{-13} s). Note that the VFTH fit allows one to estimate, for $\tau_\alpha = 9.5$ s, a temperature $T_\alpha(9.5 \text{ s}) = 241.3 \pm 0.3$ K which agrees well with $T_g^{\text{mid}} = 240.4 \pm 0.5$ K obtained from the specific heat capacity curve (TMDSC) at the equivalent frequency (~ 0.02 Hz and heating rate 0.5 K min^{-1}). The dielectric glass transition temperature $T_g^{\text{DRS}}(100 \text{ s}) = 238.8 \pm 0.4$ K is obtained by extrapolating the VFTH fit to the relaxation time $\tau = 100$ s.

Usually, the temperature evolution of the α -relaxation time of all glass formers does not express the same deviation from an Arrhenius behavior near T_g . The quantification of this deviation is at the origin of the distinction between fragile and strong systems. This deviation near T_g can be quantified by the so called fragility (or steepness) index m defined as follows:⁹²

$$m = \left[\frac{d \log \tau_\alpha}{d(T/T_g)} \right]_{T=T_g} \quad (14)$$

A glass former is considered as strong when $m \leq 30$ and fragile when $m \geq 100$. For the particular case where $30 < m < 100$ the liquid can be considered as an intermediate glass former. Combining eqn (13) and (14), m can be expressed as:

$$m = \frac{BT_g}{\ln 10(T_g - T_0)^2} \quad (15)$$

Considering the values of B and T_0 reported in Table 1 (for DRS and DRS + MD data sets) an average value of $m = 111 \pm 7$ is obtained, allowing one to classify Nac-MBA as a fragile glass former. The secondary amide Nac-MBA here studied appears to be a much more fragile system than *N*-ethylacetamide and its mixtures with *N*-methylformamide for which a fragility index $m = 65$ has been reported.³¹

As depicted in Fig. 9b, where DRS and MD data obtained in the supercooled liquid and liquid state are combined, the temperature dependence of the D-process relaxation times, τ_D , also can be described by a VFTH equation. The obtained values of the B parameter and of the Vogel temperature T_0 much resemble the ones of VFTH used to describe the temperature dependence of τ_α (Table 1). These similarities between both relaxations could possibly mean that the D-process may be controlled or governed by the α -relaxation.¹² The non-Arrhenius temperature dependence of τ_α is highly correlated with non-Debye relaxation dynamics. However the Debye-like process is not prone to any dispersion of the relaxation time and consequently cannot originate from the same microscopic phenomena as the α -process.^{31,93} The ratio of the two times scales $\tau_D/\tau_\alpha = 8$ at T ($\tau_D = 100$ s) = 241 K (~ 2 K above T_g^{DRS}); near the melting temperature T_m (~ 30 at $T = 340$ K from MD) and for $T \rightarrow \infty$, $\tau_D/\tau_\alpha = 25$. The obtained ratio is in agreement with those observed in *N*-ethylacetamide and its mixture with *N*-methylformamide,^{31,32} and some monohydroxy alcohols.^{36,41,94}

The microscopic origin of the D-process and its implications in the dielectric response of the investigated Nac-MBA system ($\epsilon_e = 50\%$) are probed by MD simulations and presented in the following section.

3.3 MD simulation investigations

3.3.1 Static dipolar properties. The individual dipole moment of a given molecule at time t is calculated from the classical expression $\vec{\mu}(t) = \sum_{\alpha=1}^{N_a} q_{\alpha} \vec{r}_{\alpha}(t)$ where q_{α} and $\vec{r}_{\alpha}(t)$ are respectively the fixed charge localized on atom α and its position at time t , and $N_a = 25$ is the number of atoms in the considered Nac-MBA molecule $C_{10}H_{13}NO$. Fixed charges are directly taken from the *ab initio* calculations (see Section 2.5 MD simulation details). In the present investigation, the average dipole moment $\langle \mu \rangle$ of Nac-MBA molecules computed from MD is found to be about 3.93 ± 0.01 Debye in the liquid state, and does not significantly vary with temperature. The symbol $\langle \rangle$ indicates an average over both time and molecules. It should be noted that this value is close to the value 3.74 Debye directly obtained from the *ab initio* calculations of a single molecule in the gas phase (see Section 2.5).

Dipolar correlations are well described by the so-called Kirkwood correlation factor G_K given by the following equation⁹⁵

$$G_K = 1 + (N - 1) \langle \vec{\mu}_i \cdot \vec{\mu}_j \rangle / \langle \mu^2 \rangle \quad (16)$$

where $\vec{\mu}_i$ is the dipole moment of the molecule i , $\langle \mu^2 \rangle$ the average dipole moment, and $\langle \vec{\mu}_i \cdot \vec{\mu}_j \rangle$ indicates an average over distinct pairs of molecules ($i \neq j$). The Kirkwood correlation factor accounts for the orientational correlation of neighboring dipoles. Parallel and antiparallel dipole orientation lead to $G_K > 1$ and $G_K < 1$, respectively. If orientations of individual dipoles are completely random, one finds $G_K = 1$. The Kirkwood correlation factor G_K was calculated at different temperatures from eqn (16) and it is shown in Fig. 10. The Kirkwood correlation factor monotonically increases from about 1.6 at $T = 500$ K to about 2.6 at $T = 340$ K.

A Kirkwood factor G_K greater than 1 is often found for monohydroxy alcohols^{25,43,96,97} and secondary amides^{31,32} for

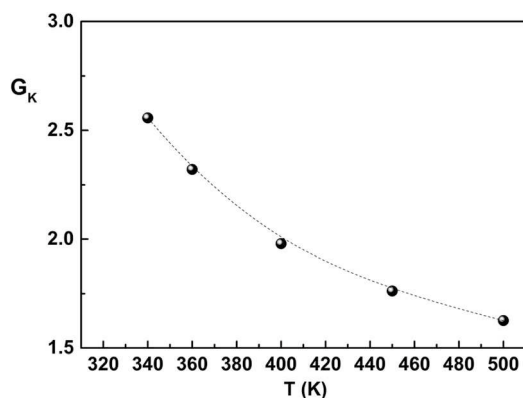


Fig. 10 Temperature evolution of the Kirkwood correlation factor G_K of Nac-MBA ($\epsilon_e = 50\%$) determined from MD simulations.

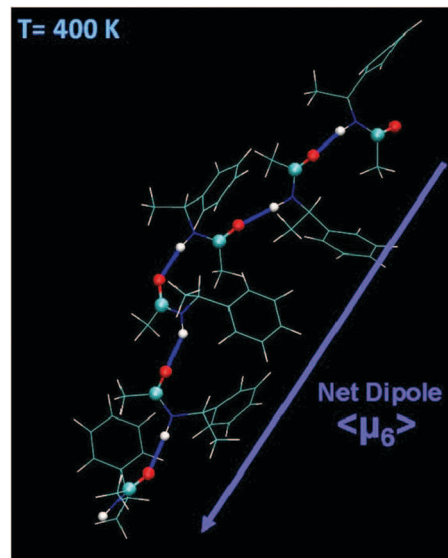


Fig. 11 Snapshot extracted from an MD simulation run at $T = 400$ K showing an HB aggregate composed of $n = 6$ Nac-MBA molecules. This HB aggregate possesses a linear shape and the net dipole $\langle \mu_6 \rangle$ of this aggregate is also schematically represented. Intermolecular HB are displayed as bold lines.

which values may range from 3 up to 4. It is interpreted as the capability of these liquids to form HB associating structures as linear chains showing HB aggregates with parallel dipole orientation. This type of HB associations has been often detected in the present MD investigations from snapshots of instantaneous configurations of the system, and will be discussed below. An example of an $n = 6$ Nac-MBA molecule HB aggregate is displayed in Fig. 11. It should be also noted that the G_K values increase with decreasing temperature suggesting an increasingly parallel correlation of dipoles which can be seen as a precursor of the crystalline structure that may ultimately form as observed many times in HB molecular liquids.^{12,98} The crystalline structure of Nac-MBA suggests that the strongest intermolecular link is a HB between $N-H \cdots O$ atoms with $d(N-O) = 2.87$ Å, $d(H \cdots O) = 2.10$ Å; and $(N-H \cdots O) = 171.8$ deg. The structure reveals infinite syndiotactic linear chains of H-bonded molecules alternately parallel to $\langle 110 \rangle$ and $\langle 1-10 \rangle$ in successive (004) slices. More details about the crystalline structure can be found in the work of Druot *et al.*⁴⁷

In other words, the latter hypothesis is consistent with the main feature of the crystalline structure (being the steric accessibility of the NH group leading to the presence of infinite linear H-bond chains of molecules between $N-H \cdots O$ atoms).⁴⁹ Although in the liquid or supercooled liquid state these infinite intermolecular associations cannot be envisaged (lack of long range order), it is very likely that as temperature fluctuation increases the number of molecules implicated in these associations diminishes. The high dielectric intensity values may emanate from the linear nature of the H-bonding chains and be linked to the number of molecules involved in these intermolecular associations.

3.3.2 Dynamical dipolar properties. Molecular mobility can be probed by the time dependence of the total electric dipole moment $\vec{M}(t)$ at time t .⁹⁹ The total electric dipole moment is defined as $\vec{M}(t) = \sum_{i=1}^N \vec{\mu}_i(t)$ where $\vec{\mu}_i(t)$ is the individual dipole moment of the molecule i at time t and $N = 64$ is the total number of molecules. In a first approximation, the complex frequency dependent permittivity $\varepsilon^*(f) = \varepsilon'(f) - i\varepsilon''(f)$ measured experimentally by DRS is actually proportional to the Fourier transform of the time-dependent correlation function $\Phi_M(t) = \langle \vec{M}(t) \cdot \vec{M}(0) \rangle$ of the total dipole moment.¹¹ This function allows probing the collective dynamics of Nac-MBA dipoles and has been calculated at different temperatures (see Fig. 12). The long time behavior of the $\Phi_M(t)$ functions is dominated by a single exponential decay which can be well fitted with $\sim \exp[-t/\tau_D^{(MD)}]$, where $\tau_D^{(MD)}$ is the characteristic time associated with this long time decay. This behavior is well in line with the Debye like process observed by DRS. The single exponential law allowed us to reproduce the evolution of $\Phi_M(t)$ almost over the whole investigated time domain except at relatively short times ($10 < t < 100$ ps) where an additional fast relaxational process is present (see Fig. 12). This fast process possesses a very low intensity and a reliable characterization is difficult from the present MD data. It has thus just been taken into account considering an additional law $\sim \exp\left[-\left(t/\tau_{\text{fast}}^{(MD)}\right)^{\beta_{\text{fast}}^{(MD)}}\right]$ in order to reproduce the behavior of the $\Phi_M(t)$ function over the complete investigated time range. $\beta_{\text{fast}}^{(MD)} \approx 0.82$ is found to provide a reasonable adjustment in the fitting procedures.

The characteristic times $\tau_D^{(MD)}$ and $\tau_{\text{fast}}^{(MD)}$ obtained at different temperatures have been represented in Fig. 9b for comparison with the DRS experimental data. It clearly shows that the characteristic times determined from MD simulations are in

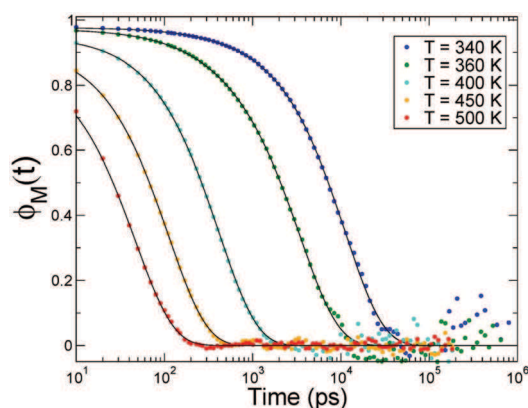


Fig. 12 Time-dependence of the total dipole correlation function $\Phi_M(t) = \langle \vec{M}(t) \cdot \vec{M}(0) \rangle$ for HB aggregates made of Nac-MBA represented at different temperatures: $T = 340, 360, 400, 450,$ and 500 K. The solid lines indicate a fit with the function $\Phi_M(t) = A_D^{(MD)} \exp[-t/\tau_D^{(MD)}] + A_{\text{fast}}^{(MD)} \exp\left[-\left(t/\tau_{\text{fast}}^{(MD)}\right)^{\beta_{\text{fast}}^{(MD)}}\right]$ where the indexes “D” and “fast” refer to the long time single exponential decay (D-process) and to the fast relaxational process ($10 < t < 100$ ps) respectively (see text).

very fair agreement respectively with the relaxation times of the D- and α -processes obtained from DRS experiments. Both processes are separated by about one to 1.5 decades in time and closely follow each other in the investigated temperature domain very much like the behavior observed in monohydroxy alcohols and secondary amides.

3.3.3 Hydrogen bonding structures. HB statistics allow determining the population of different HB associating structures and probing the structure of the investigated liquid with the aim to clarify experimental and numerical dipolar properties. The investigated molecule Nac-MBA possesses both a $-\text{NH}$ and a $\text{C}=\text{O}$ group from which it may form intermolecular HBs (see Fig. 11). In the present study, two Nac-MBA molecules are considered to be H-bonded if (i) the nitrogen-oxygen distance is less than 3.4 \AA and (ii) the $(\text{O} \cdots \text{H}-\text{N})$ angle is larger than 150 deg. This criterion is classically used in MD simulations and allows including more deformed and weaker HBs in statistics.¹⁰⁰

The fraction P_n of HB aggregates composed of n Nac-MBA molecules detected on average during the MD simulation is displayed in Fig. 13 at the highest $T = 500$ K and the lowest $T = 340$ K investigated temperatures. A monotonic trend of the HB statistics is found from 500 K down to 340 K and data obtained at $450, 400$ and 360 K are not shown for clarity. Fig. 13 clearly shows that a large variety of HB aggregates are theoretically possible ranging from an isolated molecule ($n = 1$) to very large aggregates made of $n \approx 15$ molecules. Additional even

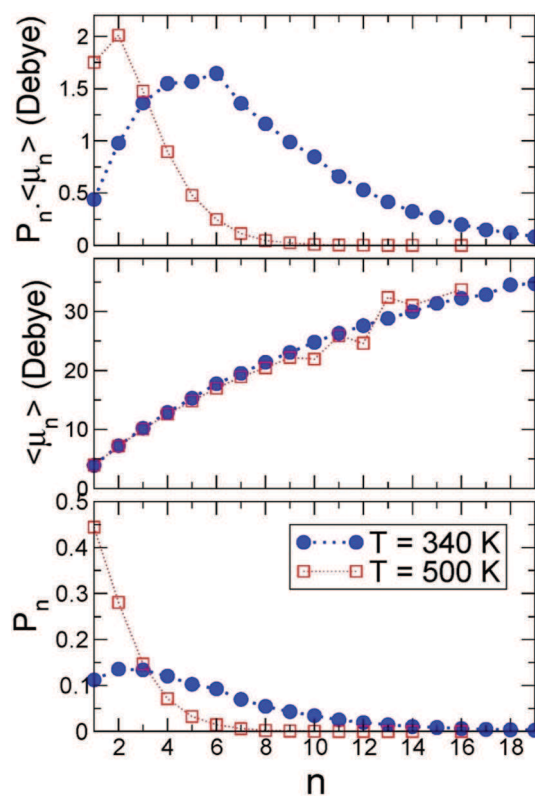


Fig. 13 Evolution of the population P_n (bottom), the average net dipole $\langle \mu_n \rangle$ (middle) and the product $P_n \cdot \mu_n$ (top) for HB aggregates made of n Nac-MBA molecules at $T = 340$ (circles) and 500 K (squares).

larger associated structures could be also transiently observed but their fraction remains really very small at all investigated temperatures. As expected from results obtained on dipolar correlations in the present study, the dominant intermolecular HB association originates from the formation of a linear chain. As an example, a snapshot of a $n = 6$ HB aggregate is displayed in Fig. 11. Upon decreasing temperature, the fraction of isolated molecules ($n = 1$) and dimers ($n = 2$) progressively decreases. The population of trimers ($n = 3$) remains stable while the population of $n > 3$ aggregates increases. At the lowest investigated temperature $T = 340$ K, associations as dimers ($n = 2$) and trimers ($n = 3$) are seen as the most probable structures. However, it may be speculated that the trend found in the investigated temperature range will continue somehow at lower temperatures at which larger structures $n > 3$ might become the most probable. It is confirmed by simply plotting the number of molecules n corresponding to the maximum of P_n as a function of temperature (data not shown). This evolution shows a monotonic increase of n upon decreasing temperature. Additional MD simulations are clearly required, which unfortunately extends beyond the scope of this study due to the difficulty to equilibrate liquid states at temperatures below $T = 340$ K in MD because of the slow dynamics of the dominant D process (see below).

In addition to the population P_n of a given HB aggregate of size n , the average total dipolar moment $\langle \mu_n \rangle$ for this aggregate may also be computed (see Fig. 13). The evolution of $\langle \mu_n \rangle$ as a function of n clearly shows that $\langle \mu_n \rangle$ increases with n , which is well in line with the linear nature of the HB aggregates (see the snapshot in Fig. 11) and the Kirkwood correlation factor $G_K > 1$ (see Fig. 10). Cyclic aggregates would cause $\langle \mu_n \rangle$ to decrease or even to go to zero. Interestingly, it may be also mentioned that the evolution of $\langle \mu_n \rangle$ is quite temperature-independent. All $\langle \mu_n \rangle$ data at $T = 340$ and 500 K overlap onto the same curve as well as $T = 360, 400$ and 450 K data (data not shown). It suggests that the same types of association may potentially form at all temperatures whose exact conformation – the linear chain above all – does not change very much with temperature. From both P_n and $\langle \mu_n \rangle$, it is also possible to calculate the product $P_n \cdot \langle \mu_n \rangle$ which provides an estimation of the “dipolar weight” of an aggregate made of n molecules. At $T = 340$ K, although the population of aggregates made of $n = 4, 5$ or 6 molecules is weaker than $n = 2$ or 3 , they could contribute to a larger extent to the dipolar response since they possess a total higher dipole moment.

4. Conclusions

Molecular mobility investigations in the amorphous Nac-MBA system were achieved by combining experimental and simulation tools such as DRS, FSC and MD simulations covering over 12 decades in the frequency window. Like many glass formers, Nac-MBA revealed a complex relaxational landscape. But interestingly a low frequency high intensity Debye-like process in the supercooled and liquid states is observed by DRS and MD simulations, similarly to monohydroxy alcohols and secondary amides.

A secondary β -relaxation is detected in the glassy state and presents some characteristics (including good agreement of its characteristic time at T_g with that predicted from the CM model) that suggest that it is a genuine Johari–Goldstein relaxation type.

Due to the high amplitude of the dominant D-relaxation, the visualization and localization of the α -relaxation in the frequency dependence of dielectric loss data seems fastidious. Somehow, the derivative method applied to experimental raw ϵ'' data permitted improving the frequency resolution of the α -process. The temperature dependence (fictive temperature) of the cooling rate performed by FSC mimics with excellent agreement $\tau_\alpha(T)$ in the common probed temperature range. $\tau_\alpha(T)$ follows a single VFTH temperature evolution and the evaluated dielectric T_g^{DRS} agrees well with the kinetic T_g^{mid} from TMDSC. The deviation from the Arrhenius behavior at T_g measured by the fragility index ($m = 111 \pm 7$) revealed that Nac-MBA can be classified as a fragile glass forming liquid.

The relaxation time of the highly intense monodisperse D-process that appears at lower frequencies in comparison with the structural relaxation is well described by a VFTH law and the fit parameters show some similarities with that of α -relaxation. This may be an indication that the dynamics of the D-process is influenced by the α -relaxation. The Debye-like process contributes almost 90% of the global dielectric polarization and does not present a calorimetric signature.

The Debye like process is clearly observed from MD simulations and its characteristic relaxation times τ_D are in very good agreement with high frequency DRS measurements confirming the validity of the calculations.

MD simulations also allowed us to evidence in the liquid state the existence of HB aggregates of different size n involving dimers, trimers, tetramers (*e.g.*, $n = 2, n = 3$, and $n = 4$) and so on which can be mainly described as HB linear chains. As the temperature decreases, longer H-bonded chains become more probable. It is suggested that this trend could persist even in the supercooled liquid state and that HB linear chains of finite size could be thus seen as precursors of the future crystalline structure to grow composed of infinite HB chains.

HB linear chains possess parallel dipole orientation consistently with the Kirkwood correlation factor $G_K > 1$ like the behavior reported for monohydroxy alcohols and secondary amides. Upon decreasing temperature, the Kirkwood correlation factor G_K increases well in line with the formation of longer H-bonded linear chains. Effective “super-dipoles” are actually generated by these chains and contribute to the dielectric response observed experimentally. Although longer HB chains are less probable than shorter chains, they could contribute to a larger extent to the dipolar response since they possess a higher “super-dipole” moment. Interestingly, the value of the “super-dipole” of a given HB linear chain of size n does not vary much with temperature implying that the “linearity” of these chains remains similar at all temperatures. This result nicely confirms that the hydrogen bond induces very strong directional intermolecular interactions which are absent in other non-associated liquids.

Globally, the results presented here for the secondary amide NAC-MBA reinforced and confirmed the idea proposed in the literature for amides and monohydroxy alcohols that the high intensity single exponential dielectric response originates from its rich microstructure due to hydrogen bonds. In the present study, only one excess enantiomeric ratio has been investigated, $ee = 50\%$; it should be interesting to investigate other ratios to evaluate the impact of chirality on the Debye process which possibility could lead to additional insights into its still unclear origin.

Conflicts of interest

There are no conflicts to declare.

Acknowledgements

The authors are grateful to FEDER and Region Normandie for the financial support of this work through the FEDER MACHI project. This project has received funding from the Interreg 2 Seas program 2014-2020 co-funded by the European Regional Development Fund under subsidy contract 2S01-059_IMODE. The authors acknowledge the use of the facilities of the CRI (Villeneuve d'Ascq, France) where calculations were carried out.

References

- C. A. Angell, Glass-Formers and Viscous Liquid Slowdown since David Turnbull: Enduring Puzzles and New Twists, *MRS Bull.*, 2008, **33**, 544–555.
- P. G. Debenedetti, *Metastable Liquids: Concepts and Principles*, Princeton University Press, 1996.
- R. Richert and A. Blumen, *Disorder Effects on Relaxational Processes*, Springer, Berlin, Heidelberg, 1994, pp. 1–7.
- M. D. Ediger, C. A. Angell and S. R. Nagel, Supercooled Liquids and Glasses, *J. Phys. Chem.*, 1996, **100**, 13200–13212.
- C. A. Angell, K. L. Ngai, G. B. McKenna, P. F. McMillan and S. W. Martin, Relaxation in glassforming liquids and amorphous solids, *J. Appl. Phys.*, 2000, **88**, 3113–3157.
- K. L. Ngai, Dynamic and thermodynamic properties of glass-forming substances, *J. Non-Cryst. Solids*, 2000, **275**, 7–51.
- E. Donth, *The Glass Transition: Relaxation Dynamics in Liquids and Disordered Materials*, Springer Science & Business Media, 2013.
- M. Descamps and J.-F. Willart, in *Disordered Pharmaceutical Materials*, ed. R. Descamps, Wiley-VCH Verlag GmbH & Co. KGaA, 2016, pp. 1–56.
- F. Stickel, E. W. Fischer and R. Richert, Dynamics of glass-forming liquids. II. Detailed comparison of dielectric relaxation, dc-conductivity, and viscosity data, *J. Chem. Phys.*, 1996, **104**, 2043–2055.
- F. Kremer and A. Schönhals, *Broadband Dielectric Spectroscopy*, Springer, Berlin, Heidelberg, 2003, pp. 99–129.
- P. Lunkenheimer, U. Schneider, R. Brand and A. Loidl, Glassy dynamics, *Contemp. Phys.*, 2000, **41**, 15–36.
- A. R. Brás, J. P. Noronha, A. M. M. Antunes, M. M. Cardoso, A. Schönhals, F. Affouard, M. Dionisio and N. T. Correia, Molecular Motions in Amorphous Ibuprofen As Studied by Broadband Dielectric Spectroscopy, *J. Phys. Chem. B*, 2008, **112**, 11087–11099.
- B. Schammé, M. Mignot, N. Couvrat, V. Tognetti, L. Joubert, V. Dupray, L. Delbreilh, E. Dargent and G. Coquerel, Molecular Relaxations in Supercooled Liquid and Glassy States of Amorphous Quinidine: Dielectric Spectroscopy and Density Functional Theory Approaches, *J. Phys. Chem. B*, 2016, **120**, 7579–7592.
- K. Grzybowska, K. Adrjanowicz and M. Paluch, in *Disordered Pharmaceutical Materials*, ed. R. Descamps, Wiley-VCH Verlag GmbH & Co. KGaA, 2016, pp. 301–360.
- B. Rijal, L. Delbreilh and A. Saiter, Dynamic Heterogeneity and Cooperative Length Scale at Dynamic Glass Transition in Glass Forming Liquids, *Macromolecules*, 2015, **48**, 8219–8231.
- G. Floudas, M. Paluch, A. Grzybowski and K. Ngai, *Molecular Dynamics of Glass-Forming Systems: Effects of Pressure*, Springer-Verlag, Berlin, Heidelberg, 2011.
- The Scaling of Relaxation Processes*, ed. F. Kremer and A. Loidl, Springer International Publishing, 2018.
- E. W. Fischer, E. Donth and W. Steffen, Temperature dependence of characteristic length for glass transition, *Phys. Rev. Lett.*, 1992, **68**, 2344–2346.
- A. Saiter, L. Delbreilh, H. Couderc, K. Arabeche, A. Schönhals and J.-M. Saiter, Temperature dependence of the characteristic length scale for glassy dynamics: Combination of dielectric and specific heat spectroscopy, *Phys. Rev. E: Stat., Nonlinear, Soft Matter Phys.*, 2010, **81**, 041805.
- B. Rijal, J. A. Soto Puente, B. Atawa, L. Delbreilh, K. Fatyeyeva, A. Saiter and E. Dargent, Correlated and cooperative motions in segmental relaxation: Influence of constitutive unit weight and intermolecular interactions, *Phys. Rev. E*, 2016, **94**, 062502.
- M. A. Floriano and C. A. Angell, On the relaxation between debye and nonexponential relaxation in supercooled monohydric alcohols and water: A solution study, *J. Chem. Phys.*, 1998, **91**, 2537.
- U. Kaatzte, Dielectric and structural relaxation in water and some monohydric alcohols, *J. Chem. Phys.*, 2017, **147**, 024502.
- W. Dannhauser, Dielectric Study of Intermolecular Association in Isomeric Octyl Alcohols, *J. Chem. Phys.*, 1968, **48**, 1911–1917.
- C. Hansen, F. Stickel, T. Berger, R. Richert and E. W. Fischer, Dynamics of glass-forming liquids. III. Comparing the dielectric α - and β -relaxation of 1-propanol and o-terphenyl, *J. Chem. Phys.*, 1997, **107**, 1086–1093.
- O. E. Kalinovskaya and J. K. Vij, The exponential dielectric relaxation dynamics in a secondary alcohol's supercooled liquid and glassy states, *J. Chem. Phys.*, 2000, **112**, 3262–3266.
- D. Fragiadakis, C. M. Roland and R. Casalini, Insights on the origin of the Debye process in monoalcohols from dielectric spectroscopy under extreme pressure conditions, *J. Chem. Phys.*, 2010, **132**, 144505.
- G. Power, M. Nagaraj, J. K. Vij and G. P. Johari, Debye process and dielectric state of an alcohol in a nonpolar solvent, *J. Chem. Phys.*, 2011, **134**, 044525.

- 28 S. P. Bierwirth, J. Bolle, S. Bauer, C. Sternemann, C. Gainaru, M. Tolan and R. Böhmer, *The Scaling of Relaxation Processes*, Springer, Cham, 2018, pp. 121–171.
- 29 S. J. Bass, W. I. Nathan, R. M. Meighan and R. H. Cole, Dielectric Properties of Alkyl Amides. II. Liquid Dielectric Constant and Loss, *J. Phys. Chem.*, 1964, **68**, 509–515.
- 30 R. G. Wassink and P. Bordewijk, Dielectric relaxation of some amides in carbon tetrachloride, *Adv. Mol. Relax. Interact. Processes*, 1978, **13**, 299–308.
- 31 L.-M. Wang and R. Richert, Identification of dielectric and structural relaxations in glass-forming secondary amides, *J. Chem. Phys.*, 2005, **123**, 054516.
- 32 C. Gainaru, S. Bauer, E. Vynokur, H. Wittkamp, W. Hiller, R. Richert and R. Böhmer, Dynamics in Supercooled Secondary Amide Mixtures: Dielectric and Hydrogen Bond Specific Spectroscopies, *J. Phys. Chem. B*, 2015, **119**, 15769–15779.
- 33 M. Rams-Baron, Z. Wojnarowska, M. Dulski, A. Ratuszna and M. Paluch, Evidence of slow Debye-like relaxation in the anti-inflammatory agent etoricoxib, *Phys. Rev. E: Stat., Nonlinear, Soft Matter Phys.*, 2015, **92**, 022309.
- 34 M. T. Ottou Abe, N. T. Correia, L.-C. Valdes, J. M. B. Ndjaka and F. Affouard, Local molecular organizations of ibuprofen, flurbiprofen and ketoprofen in the liquid phase: Insights from molecular dynamics simulations, *J. Mol. Liq.*, 2015, **205**, 74–77.
- 35 M. T. Ottou Abe, N. T. Correia, J. M. B. Ndjaka and F. Affouard, A comparative study of ibuprofen and ketoprofen glass-forming liquids by molecular dynamics simulations, *J. Chem. Phys.*, 2015, **143**, 164506.
- 36 L.-M. Wang and R. Richert, Debye Type Dielectric Relaxation and the Glass Transition of Alcohols, *J. Phys. Chem. B*, 2005, **109**, 11091–11094.
- 37 H. Huth, L.-M. Wang, C. Schick and R. Richert, Comparing calorimetric and dielectric polarization modes in viscous 2-ethyl-1-hexanol, *J. Chem. Phys.*, 2007, **126**, 104503.
- 38 C. Gainaru, R. Figuli, T. Hecksher, B. Jakobsen, J. C. Dyre, M. Wilhelm and R. Böhmer, Shear-Modulus Investigations of Monohydroxy Alcohols: Evidence for a Short-Chain-Polymer Rheological Response, *Phys. Rev. Lett.*, 2014, **112**, 098301.
- 39 A. Kudlik, C. Tschirwitz, S. Benkhof, T. Blochowicz and E. Rössler, Slow secondary relaxation process in supercooled liquids, *EPL*, 1997, **40**, 649.
- 40 G. P. Johari, O. E. Kalinovskaya and J. K. Vij, Effects of induced steric hindrance on the dielectric behavior and H bonding in the supercooled liquid and vitreous alcohol, *J. Chem. Phys.*, 2001, **114**, 4634–4642.
- 41 R. Böhmer, C. Gainaru and R. Richert, Structure and dynamics of monohydroxy alcohols—milestones towards their microscopic understanding, 100 years after Debye, *Phys. Rep.*, 2014, **545**, 125–195.
- 42 T. Hecksher, Communication: linking the dielectric Debye process in mono-alcohols to density fluctuations, *J. Chem. Phys.*, 2016, **144**, 161103.
- 43 U. Kaatz, R. Behrends and R. Pottel, Hydrogen network fluctuations and dielectric spectrometry of liquids, *J. Non-Cryst. Solids*, 2002, **305**, 19–28.
- 44 L. P. Singh and R. Richert, Watching hydrogen-bonded structures in an alcohol convert from rings to chains, *Phys. Rev. Lett.*, 2012, **109**, 167802.
- 45 R. Minami, K. Itoh, H. Takahashi and K. Higasi, A theoretical approach to the dielectric relaxation of liquid alcohols, *J. Chem. Phys.*, 1980, **73**, 3396–3397.
- 46 C. Gainaru, R. Meier, S. Schildmann, C. Lederle, W. Hiller, E. A. Rössler and R. Böhmer, Nuclear-Magnetic-Resonance Measurements Reveal the Origin of the Debye Process in Monohydroxy Alcohols, *Phys. Rev. Lett.*, 2010, **105**, 258303.
- 47 S. Druot, M. N. Petit, S. Petit, G. Coquerel and N. B. Chanh, Experimental Data and Modelling of the Interactions in Solid State and in Solution between (R) and (S) N-Acetyl- α -Methylbenzylamine. Influence on Resolution by Preferential Crystallization, *Mol. Cryst. Liq. Cryst. Sci. Technol., Sect. A*, 1996, **275**, 271–291.
- 48 E. Brown and M. Moudachirou, Agents de dédoublement. 2. Synthèse d'arylréthanés de l'acide (S)-lactique et leur utilisation dans le dédoublement de bases racémiques, *Tetrahedron*, 1994, **50**, 10309–10320.
- 49 S. Druot Houlemare, *Influence des interactions homo- et heterochirales lors du dedoublement par cristallisation preferentielle de deux derives de l'alpha-methylbenzylamine: le n-acetamide et le chloroacetate*, Caen, 1999.
- 50 B. Atawa, N. Couvrat, G. Coquerel, E. Dargent and A. Saiter, Chirality impact on physical ageing: An original case of a small organic molecule, *Mater. Lett.*, 2018, **228**, 141–144.
- 51 G. V. Poel, D. Istrate, A. Magon and V. Mathot, Performance and calibration of the Flash DSC 1, a new, MEMS-based fast scanning calorimeter, *J. Therm. Anal. Calorim.*, 2012, **110**, 1533–1546.
- 52 B. Atawa, N. Couvrat, G. Coquerel, E. Dargent and A. Saiter, Impact of chirality on the Glass Forming Ability and the crystallization from the amorphous state of 5-ethyl-5-methylhydantoin, a chiral poor glass former, *Int. J. Pharm.*, 2018, **540**, 11–21.
- 53 G. Schaumburg, Novocontrol introduces high quality low cost interdigitated comb electrodes, *Dielectrics Newsletter* 2006, December Issue.
- 54 Z. Chen, A. Sepúlveda, M. D. Ediger and R. Richert, Dielectric spectroscopy of thin films by dual-channel impedance measurements on differential interdigitated electrode arrays, *Eur. Phys. J. B*, 2012, **85**, 268.
- 55 A. Dhotel, Z. Chen, J. Sun, B. Youssef, J.-M. Saiter, A. Schönhals, L. Tan and L. Delbreilh, From monomers to self-assembled monolayers: the evolution of molecular mobility with structural confinements, *Soft Matter*, 2014, **11**, 719–731.
- 56 S. Havriliak and S. Negami, A complex plane representation of dielectric and mechanical relaxation processes in some polymers, *Polymer*, 1967, **8**, 161–210.
- 57 THE DL POLY 2 USER MANUAL – PDF, <http://docplayer.net/14320255-The-dl-poly-2-user-manual.html>, accessed May 31, 2018.
- 58 J. Wang, R. M. Wolf, J. W. Caldwell, P. A. Kollman and D. A. Case, Development and testing of a general amber force field, *J. Comput. Chem.*, 2004, **25**, 1157–1174.

- 59 C. Caleman, P. J. van Maaren, M. Hong, J. S. Hub, L. T. Costa and D. van der Spoel, Force Field Benchmark of Organic Liquids: Density, Enthalpy of Vaporization, Heat Capacities, Surface Tension, Isothermal Compressibility, Volumetric Expansion Coefficient, and Dielectric Constant, *J. Chem. Theory Comput.*, 2012, **8**, 61–74.
- 60 M. Frisch, G. Trucks, H. Schlegel, G. Scuseria, M. Robb, J. Cheeseman, J. Montgomery, T. Vreven, K. Kudin, J. Burant, J. Millam, S. Iyengar, J. Tomasi, V. Barone, B. Mennucci, M. Cossi, G. Scalmani, N. Rega, G. Petersson, H. Nakatsuji, M. Hada, M. Ehara, K. Toyota, R. Fukuda, J. Hasegawa, M. Ishida, T. Nakajima, Y. Honda, O. Kitao, H. Nakai, M. Klene, X. Li, J. Knox, H. Hratchian, J. Cross, V. Bakken, C. Adamo, J. Jaramillo, R. Gomperts, R. Stratmann, O. Yazyev, A. Austin, R. Cammi, C. Pomelli, J. Ochterski, P. Ayala, K. Morokuma, G. Voth, P. Salvador, J. Dannenberg, V. Zakrzewski, S. Dapprich, A. Daniels, M. Strain, O. Farkas, D. Malick, A. Rabuck, K. Raghavachari, J. Foresman, J. Ortiz, Q. Cui, A. Baboul, S. Clifford, J. Cioslowski, B. Stefanov, G. Liu, A. Liashenko, P. Piskorz, I. Komaromi, R. Martin, D. Fox, T. Keith, A. Laham, C. Peng, A. Nanayakkara, M. Challacombe, P. Gill, B. Johnson, W. Chen, M. Wong, C. Gonzalez and J. Pople, *Gaussian 03, Revision C.02*, 2004.
- 61 D. Wolf, P. Keblinski, S. R. Phillpot and J. Eggebrecht, Exact method for the simulation of Coulombic systems by spherically truncated, pairwise $r - 1$ summation, *J. Chem. Phys.*, 1999, **110**, 8254–8282.
- 62 B. C. Hancock and G. Zografi, Characteristics and Significance of the Amorphous State in Pharmaceutical Systems, *J. Pharm. Sci.*, 1997, **86**, 1–12.
- 63 S. L. Shamblin, L. S. Taylor and G. Zografi, Mixing behavior of colyophilized binary systems, *J. Pharm. Sci.*, 1998, **87**, 694–701.
- 64 M. Naoki, K. Ujita and S. Kashima, Pressure-volume-temperature relations and configurational energy of liquid, crystal, and glasses of D-sorbitol, *J. Phys. Chem.*, 1993, **97**, 12356–12362.
- 65 *Modulated Temperature Differential Scanning Calorimetry: Theoretical and Practical Applications in Polymer Characterisation*, ed. M. Reading and D. J. Hourston, Springer Netherlands, 2006.
- 66 A. Q. Tool and C. G. Eicitlin, Variations Caused in the Heating Curves of Glass by Heat Treatment¹, *J. Am. Ceram. Soc.*, 1931, **14**, 276–308.
- 67 A. Dhotel, B. Rijal, L. Delbreilh, E. Dargent and A. Saiter, Combining Flash DSC, DSC and broadband dielectric spectroscopy to determine fragility, *J. Therm. Anal. Calorim.*, 2015, **121**, 453–461.
- 68 A. Saiter, C. Devallencourt, J. M. Saiter and J. Grenet, Thermodynamically “strong” and kinetically “fragile” polymeric glass exemplified by melamine formaldehyde resins, *Eur. Polym. J.*, 2001, **37**, 1083–1090.
- 69 A. Saiter, M. Hess, N. A. D'Souza and J. M. Saiter, Entropy and fragility in vitreous polymers, *Polymer*, 2002, **43**, 7497–7504.
- 70 Y. P. Koh, S. Gao and S. L. Simon, Structural recovery of a single polystyrene thin film using Flash DSC at low aging temperatures, *Polymer*, 2016, **96**, 182–187.
- 71 C. T. Moynihan, P. B. Macedo, C. J. Montrose, C. J. Montrose, P. K. Gupta, M. A. DeBolt, J. F. Dill, B. E. Dom, P. W. Drake, A. J. Easteal, P. B. Elterman, R. P. Moeller, H. Sasabe and J. A. Wilder, Structural Relaxation in Vitreous Materials, *Ann. N. Y. Acad. Sci.*, 2006, **279**, 15–35.
- 72 J. E. K. Schawe, Vitrification in a wide cooling rate range: The relations between cooling rate, relaxation time, transition width, and fragility, *J. Chem. Phys.*, 2014, **141**, 184905.
- 73 Y. Z. Chua, G. Schulz, E. Shoifet, H. Huth, R. Zorn, J. W. P. Scmelzer and C. Schick, Glass transition cooperativity from broad band heat capacity spectroscopy, *Colloid Polym. Sci.*, 2014, **292**, 1893–1904.
- 74 J. E. K. Schawe, Measurement of the thermal glass transition of polystyrene in a cooling rate range of more than six decades, *Thermochim. Acta*, 2015, **603**, 128–134.
- 75 A. Hensel, J. Dobbertin, J. E. K. Schawe, A. Boller and C. Schick, Temperature modulated calorimetry and dielectric spectroscopy in the glass transition region of polymers, *J. Therm. Anal.*, 1996, **46**, 935–954.
- 76 A. Hensel and C. Schick, Relation between freezing-in due to linear cooling and the dynamic glass transition temperature by temperature-modulated DSC, *J. Non-Cryst. Solids*, 1998, **235–237**, 510–516.
- 77 S. Weyer, A. Hensel, J. Korus, E. Donth and C. Schick, Broad band heat capacity spectroscopy in the glass-transition region of polystyrene, *Thermochim. Acta*, 1997, **304–305**, 251–255.
- 78 A. C. Rodrigues, M. T. Viciosa, F. Danède, F. Affouard and N. T. Correia, Molecular Mobility of Amorphous S-Flurbiprofen: A Dielectric Relaxation Spectroscopy Approach, *Mol. Pharmaceutics*, 2014, **11**, 112–130.
- 79 A. Yildirim, P. Szymoniak, K. Sentker, M. Butschies, A. Bühlmeier, P. Huber, S. Laschat and A. Schönhals, Dynamics and ionic conductivity of ionic liquid crystals forming a hexagonal columnar mesophase, *Phys. Chem. Chem. Phys.*, 2018, **20**, 5626–5635.
- 80 E. Kaminska, M. Tarnacka, O. Madejczyk, A. Chrobok, K. Kaminski and M. Paluch, Observation of the nearly constant loss in super rigid saccharides: in search of a hidden crossover in dynamics deep in the glassy state, *Phys. Chem. Chem. Phys.*, 2016, **18**, 8901–8910.
- 81 M. Wübbenhorst and J. van Turnhout, Analysis of complex dielectric spectra. I. One-dimensional derivative techniques and three-dimensional modelling, *J. Non-Cryst. Solids*, 2002, **305**, 40–49.
- 82 Q. Viel, L. Delbreilh, G. Coquerel, S. Petit and E. Dargent, Molecular Mobility of an Amorphous Chiral Pharmaceutical Compound: Impact of Chirality and Chemical Purity, *J. Phys. Chem. B*, 2017, **121**, 7729–7740.
- 83 K. L. Ngai, An extended coupling model description of the evolution of dynamics with time in supercooled liquids and ionic conductors, *J. Phys.: Condens. Matter*, 2003, **15**, S1107.
- 84 K. Adrjanowicz, Z. Wojnarowska, P. Włodarczyk, K. Kaminski, M. Paluch and J. Mazgalski, Molecular mobility in liquid and glassy states of Telmisartan (TEL) studied by Broadband Dielectric Spectroscopy, *Eur. J. Pharm. Sci.*, 2009, **38**, 395–404.

- 85 M. Paluch, C. M. Roland, S. Pawlus, J. Ziolo and K. L. Ngai, Does the Arrhenius Temperature Dependence of the Johari–Goldstein Relaxation Persist above T_g ?, *Phys. Rev. Lett.*, 2003, **91**, 115701.
- 86 K. L. Ngai and M. Paluch, Classification of secondary relaxation in glass-formers based on dynamic properties, *J. Chem. Phys.*, 2003, **120**, 857–873.
- 87 F. Alvarez, A. Alegría and J. Colmenero, Interconnection between frequency-domain Havriliak-Negami and time-domain Kohlrausch-Williams-Watts relaxation functions, *Phys. Rev. B: Condens. Matter Mater. Phys.*, 1993, **47**, 125–130.
- 88 K. L. Ngai and S. Capaccioli, Relation between the activation energy of the Johari–Goldstein β relaxation and T_g of glass formers, *Phys. Rev. E: Stat., Nonlinear, Soft Matter Phys.*, 2004, **69**, 031501.
- 89 H. Vogel, Das Temperaturabhängigkeitsgesetz der Viskosität von Flüssigkeiten, *Phys. Z.*, 1921, **22**, 645–646.
- 90 G. S. Fulcher, Analysis of Recent Measurements of the Viscosity of Glasses, *J. Am. Ceram. Soc.*, 1925, **8**, 339–355.
- 91 G. Tammann and W. Hesse, Die Abhängigkeit der Viskosität von der Temperatur bei unterkühlten Flüssigkeiten, *Z. Anorg. Allg. Chem.*, 1926, **156**, 245–257.
- 92 R. Böhmer, K. L. Ngai, C. A. Angell and D. J. Plazek, Nonexponential relaxations in strong and fragile glass formers, *J. Chem. Phys.*, 1993, **99**, 4201–4209.
- 93 L.-M. Wang and R. Richert, Dynamics of glass-forming liquids. IX. Structural versus dielectric relaxation in monohydroxy alcohols, *J. Chem. Phys.*, 2004, **121**, 11170–11176.
- 94 A. Mandanici, W. Huang, M. Cutroni and R. Richert, Dynamics of glass-forming liquids. XII. Dielectric study of primary and secondary relaxations in ethylcyclohexane, *J. Chem. Phys.*, 2008, **128**, 124505.
- 95 C. J. F. Böttcher, *Theory of Electric Polarization*, Elsevier, Amsterdam, 2nd edn, 1973, pp. 9–58.
- 96 S. S. N. Murthy and M. Tyagi, Experimental study of the high frequency relaxation process in monohydroxy alcohols, *J. Chem. Phys.*, 2002, **117**, 3837–3847.
- 97 S. Pal, B. Bagchi and S. Balasubramanian, Hydration Layer of a Cationic Micelle, C10TAB: Structure, Rigidity, Slow Reorientation, Hydrogen Bond Lifetime, and Solvation Dynamics, *J. Phys. Chem. B*, 2005, **109**, 12879–12890.
- 98 P. Derollez, A. Hédoux, Y. Guinet, F. Danède and L. Paccou, Structure determination of the crystalline phase of n-butanol by powder X-ray diffraction and study of intermolecular associations by Raman spectroscopy, *Acta Crystallogr., Sect. B: Struct. Sci., Cryst. Eng. Mater.*, 2013, **69**, 195–202.
- 99 F. Affouard and N. T. Correia, Debye Process in Ibuprofen Glass-Forming Liquid: Insights from Molecular Dynamics Simulation, *J. Phys. Chem. B*, 2010, **114**, 11397–11402.
- 100 A. Lerbret, P. Bordat, F. Affouard, M. Descamps and F. Migliardo, How Homogeneous Are the Trehalose, Maltose, and Sucrose Water Solutions? An Insight from Molecular Dynamics Simulations, *J. Phys. Chem. B*, 2005, **109**, 11046–11057.